TARGETING THE FORMYL PEPTIDE RECEPTOR 1 FOR TREATMENT OF GLIOBLASTOMA

D. S. AHMET

PHD

UNIVERSITY OF BRADFORD

2021

Targeting the formyl peptide receptor 1 for treatment of glioblastoma

Djevdet Sarper AHMET

Submitted for the degree of

Doctor of Philosophy

Faculty of Life Sciences

University of Bradford

2021

Abstract

Djevdet Sarper Ahmet

Targeting the formyl peptide receptor 1 for treatment of glioblastoma

Keywords: Formyl peptide receptor 1, annexin-A1, glioblastoma, spheroid, drug discovery, synthetic medicinal chemistry

Background and Aims Gliomas account for over half of all primary brain tumours and have a very poor prognosis, with a median survival of less than two years. There is an urgent and unmet clinical need to develop new therapies against glioma. Recent reports have indicated the overexpression of FPR1 in gliomas particularly in high grade gliomas. The aim of this project was to identify and synthesise small molecule FPR1 antagonists, and to demonstrate a proof of principle in preclinical *in vitro* and *in vivo* models that small molecule FPR1 antagonism can retard expansion of glioma.

Methods A number of small molecule FPR1 antagonists were identified by *in silico* design, or from the literature and then were prepared using chemical synthesis. FPR1 antagonists were evaluated *in vitro* for their ability to abrogate FPR1-induced cellular responses in a range of models including calcium mobilisation, cell migration, and invasion. The efficacy of FPR1 antagonist ICT12035 *in vivo* was assessed in a U-87 MG subcutaneous xenograft model.

Results Virtual high throughput screening using a homology model of FPR1 led to the identification of two small molecule FPR1 antagonists. At the same time chemical synthesis of two other antagonists, ICT5100 and ICT12035 as well as their analogues were carried out. The FPR1 antagonists were assessed in calcium flux assay which gave an insight into their structure-

activity relationship. Further investigation of both ICT5100 and ICT12035 demonstrated that both small molecule FPR1 antagonists were effective at abrogating FPR1-induced calcium mobilisation, migration, and invasion in U-87 MG *in vitro* models in a dose-dependent manner. ICT12035 is a particularly selective and potent inhibitor of FPR1 with an IC_{50} of 37.7 nM in calcium flux assay. Additionally, it was shown that the FPR1 antagonist ICT12035 was able to arrest the growth rate of U-87 MG xenografted tumours in mice.

Conclusion The results demonstrate that targeting FPR1 by a small molecule antagonist such as ICT12035, could provide a potential new therapy for the treatment of glioblastoma.

Acknowledgements

I wish to express my gratitude to my supervisors Dr. K. Afarinkia and Dr. S. Shnyder for their continued support and guidance throughout the project. I would also like to thank Dr. V. Vinader for her invaluable assistance in and out of the lab. I am also very thankful for the financial support from Yorkshire Cancer Research.

Special Thanks must go to fellow students and staff of the Institute of Cancer Therapeutics whose expertise and advice helped make this project possible.

A huge thank you to all my family and friends for supporting me and most importantly pushing me to succeed.

Abbreviations

5-FU	5-Fluorouracil
7TM	7-Trans Membrane
Ac	Acetyl
PKB	Protein Kinase B
ANXA1	Annexin A1
ATCC	American Type Culture Collection
BBB	Blood Brain Barrier
BBTB	Blood Brain-Tumour Barrier
Bcl-2	B-Cell Lymphoma 2
BCNU	Bis-Chloroethylnitrosourea / Carmustine
bFGR	Basic Fibroblast Growth Factor
BSA	Bovine Serum Albumin
C5aR	Complement Component 5a Receptor
CHIPS	Chemotaxis Inhibitory Protein of Staphylococcus Aureus
Calcd.	Calculated
CNS	Central Nervous System
COPD	Chronic Obstructive Pulmonary Disorder
COSY	Homonuclear Correlation Spectroscopy
CT	Computed Tomography
CXCL	C-X-C Chemokine Ligand
CXCR	C-X-C Chemokine Receptor
CXCR4	C-X-C chemokine Receptor Type 4
DAB	3,3-Diaminobenzidine

DAPI	4′,6-Diamidino-2-phenylindole
DCM	Dichloromethane
DIPEA	Diisopropylethylamine
DMF	Dimethylformamide
DMPK	Drug Metabolism and Pharmacokinetics
DNA	Deoxyribonucleic Acid
EC	Endothelial Cell
ECACC	European Collection of Authenticated Cell Cultures
ECM	Extracellular Matrix
EDTA	Ethylenediaminetetraacetic Acid
EGF	Epidermal Growth Factor
EGFR	Epidermal Growth Factor Receptor
EPAS-1	Endothelial PAS Domain-Containing Protein 1
ERK	Extracellular Signal-Regulated Kinase
Et	Ethyl
FC	Flow Cytometry
FCS	Foetal Calf Serum
FFPE	Formalin-Fixed Paraffin-Embedded
fMLF	Formyl Methionyl Leucyl Phenylalanine
FPR	Formyl Peptide Receptor
FPR1	Formyl Peptide Receptor 1
FPR2	Formyl Peptide Receptor 2
FPR3	Formyl Peptide Receptor 3
GBM	Glioblastoma Multiforme

GFAP	Glial Fibrillary Acidic Protein
GPCR	G-Protein Coupled Receptor
GPCR-7TM	G-protein coupled seven-transmembrane domain receptor
GSC	Glioma Stem Cell
h	Hour
HATU	1-[Bis(Dimethylamino)Methylene]-1H-1,2,3-Triazolo[4,5-B]Pyridinium 3-Oxid Hexafluorophosphate
HBTU	(2-(1H-Benzotriazol-1-Yl)-1,1,3,3-Tetramethyluronium Hexafluorophosphate
HIF	Hypoxia Inducible Factor
HIF-1-α	Hypoxia-Inducible Factor 1-Alpha
HMQC	Heteronuclear Multiple-Quantum Correlation
HPLC-MS	High Performance Liquid Chromatography- Mass Spectrometry
HRMS	High Resolution Mass Spectrometry
ICT	Institute Of Cancer Therapeutics
IDH1	Isocitrate Dehydrogenase (NADP(+)) 1
IF	Immunofluorescent
IHC	Immunohistochemistry
IL-8	Interleukin 8
IP	Intraperitoneal
IP3	1,4,5-Inositol Triphosphate
IR	Infrared Spectroscopy
JNK	C-Jun N-Terminal Kinase
LCMS	Liquid Chromatography-Mass Spectrometry

MAPK	Mitogen-Activated Protein Kinases
Me	Methyl
MGMT	Methylguanine Methyltransferase
MMP	Matrix Metalloproteinases
MOE	Molecular Operating Environment
MRI	Magnetic Resonance Imaging
MS	Mass Spectrometry
MTT	3-(4,5-Dimethylthiazol-2-Yl)-2,5-Diphenyltetrazolium Bromide
MW	Molecular Weight
NF1	Neurofibromin 1
NFκB	Nuclear Factor Kappa-Light-Chain-Enhancer of Activated B Cells
NIH	National Institute of Health
NMR	Nuclear Magnetic Resonance
NOESY	Nuclear Overhauser Effect Spectroscopy
NSCs	Neural Stem Cells
p38	p38 Mitogen-Activated Protein Kinases
PBS	Phosphate Buffer Solution
PDB	Protein Data Bank
PDGFRA	Platelet-Derived Growth Factor Receptor Alpha
pet ether	Petroleum Ether boiling point fraction 60-80 °
PKPD	Pharmacokinetics/Pharmacodynamics
Pr	Propyl
RBL	Rat Basophilic Leukaemia
rt	Room Temperature

SAR	Structure Activity Relationship
scRNA-seq	Single-Cell Ribonucleic Acid Sequencing
SD	Standard Deviation
SDF-1	Stromal cell-derived factor 1
siRNA	Small Interfering Ribonucleic Acid
Src	Proto-Oncogene Tyrosine-Protein Kinase
STAT3	Signal Transducer and Activator of Transcription 3
THF	Tetrahydrofuran
TKI	Tyrosine Kinase Inhibitors
TLC	Thin Layer Chromatography
TMZ	Temozolomide
VEGF	Vascular Endothelial Growth Factor
vHTS	Virtual High-Throughput Screen
WHO	World Health Organisation
XRD	X-Ray Diffraction

Publications

This page lists publications that were published as a result of the work presented in this thesis.

Journal Articles

- **Ahmet, D.S.**, H.A. Basheer, A. Salem, D. Lu, A. Aghamohammadi, P. Weyerhäuser, A. Bordiga, J. Almeniawi, S. Rashid, P.A. Cooper, S.D. Shnyder, V. Vinader, and K. Afarinkia, Application of small molecule FPR1 antagonists in the treatment of cancers. Scientific Reports, 2020. 10(1): p. 17249.[1]

Conference Posters

- **Ahmet, D.S.**, M.V. Vinader, S. Shnyder, X.W. Bian, L.H. Patterson, and K. Afarinkia, Targeting the formylpeptide receptor-1 for treatment of glioma, in Yorkshire Cancer Research Annual Meeting. 2013: Harrogate.[2]
- **Ahmet, D.S.**, M.V. Vinader, S. Shnyder, X.W. Bian, L.H. Patterson, and K. Afarinkia, Targeting the formylpeptide receptor-1 for treatment of glioma, in RSC North-East Section Annual Meeting. 2014: Hull, UK.[3]
- **Ahmet, D.S.**, M.V. Vinader, S. Shnyder, X.W. Bian, L.H. Patterson, and K. Afarinkia, Targeting the formylpeptide receptor-1 for treatment of glioma, in Gordon Research Council Conference (Chemotactic Cytokines). 2014: West Dover Vermont USA.[4]

Table of Contents

List of Figures

List of Schemes

List of Tables

1. CHAPTER 1: An introduction to glioblastoma and the formyl peptide receptor 1

1.1. Introduction

Malignant glioma, the most common sub-type of primary brain tumour, is one of the deadlier human cancers. High-grade malignant gliomas are fast growing, neurologically destructive, invasive and patients suffer from a very poor prognosis. Current treatments include cytotoxic chemotherapy, radiotherapy, and surgery either on their own or in combination. However, despite even the highest levels of treatment intervention (tumour resection, radiotherapy and concomitant chemotherapy), the patients diagnosed with the most aggressive manifestation, Glioblastoma Multiforme (GBM) have a median survival time of just under 14.6 months.[5-8] The dismal prognosis of these tumours is due to their ability to diffusely infiltrate into surrounding brain tissue. Many individual tumour cells are able to infiltrate normal brain parenchyma escaping therapeutic interventions such as neurosurgery, radiation and chemotherapy and it has even been suggested that a single tumour cell remaining after treatment, would be able to initiate new tumour growth.[5, 8-10] Therefore, new and more efficient therapies are urgently needed. In this chapter, an overview of glioma and currently available treatment modalities will be covered, and the evidence from the literature that supports the hypothesis linking necrosis and the formylpeptide receptor axis to the malignancy of gliomas will be provided.

1.2. Cancer

Cancer is one of the leading causes of death in developed countries. In 2015-2017, in the UK alone, there were 367,167 new cases of cancer diagnosed and 164,901 deaths from cancer.[11] Cancer is not just one disease, but a name given to a group of related diseases. In all types of cancer, the disease is characterised by uncontrolled cell division. Under normal circumstances, when cells become old or damaged, they would die and be replaced as needed. With cancer however, this process breaks down. Old or damaged cells end up surviving when they should die, and new cells form when they are not needed. The complex mechanisms underpinning the transition from normal cell to cancer cell to tumour/malignancy has been previously rationalised into a selection of traits recognised across all cancers. These “Hallmarks of Cancer” were first articulated by Weinberg and Hanahan.[12] The six original hallmarks encompassed sustained proliferation, the evasion of growth suppressors, activation of invasion and metastasis, enabling replicative immortality, inducing angiogenesis, and resisting cell death.[12] Since publication of these original hallmarks, our knowledge of cancer biology has been further expanded, and so have the hallmarks to include two new enabling characteristics; genome instability and mutation, and tumour-promoting inflammation.[13] Also, two emerging hallmarks have been recognised, deregulation of cellular energetics, and avoidance of immune recognition/surveillance.[13]

Treatment of cancer involves a multidisciplinary approach with teams of surgeons, radiotherapists and oncologists working towards a single goal. Surgeons will remove the bulk of the tumour and where possible resect

enough tissue to give a clear border of cancer free cells, though sometimes, tumours may be inoperable due to location, or cancer cells might be missed due to invasion or micro metastasis. Radiotherapists use high energy radiation sources to cause DNA damage to the cancer cells and elicit cellular death as a result. Chemotherapeutic agents are cancer drug therapies used to treat broad ranges of cancer. In the First and Second World Wars, soldiers exposed to mustard gas experienced decreased levels of leukocytes, this observation led to the use of nitrogen mustard as the first chemotherapeutic agent to treat lymphomas in 1943.[14] Following on from the development of alkylating agents, the dihydrofolate reductase inhibiter methotrexate was discovered, which in 1948 successfully showed leukaemia remission in children.[14] The drug 5-fluorouracil (5-FU) was developed for the treatment of solid tumours in the 1950s and still remains an important chemotherapeutic agent against colorectal, breast and head & neck cancers.[14, 15]

There have been significant advances made for treatment of cancers such as leukaemia, lymphoma, prostate carcinomas, low grade breast cancers. In these cases, earlier detection of cancer leads to even better survival rates.[14] The response to current therapies for lung, high grade breast, colorectal, pancreatic and high-grade neurological cancers remains poor and is often used to prolong life instead of curing the disease (palliative care).[14]

Chemotherapeutics often give rise to toxicity in normal tissue, limiting the dose that can be used, and chemoresistance develops in the cancer causing the drugs to ultimately fail to reduce mortality rates. As our understanding of the underlying biology of these cancers and chemoresistance mechanisms broadens, so does the approach to treatment modalities. The need for new

therapies that selectively target cancer cells over healthy tissue and avoid drug resistance is widely recognised. Novel therapeutics that target the vital hallmarks for cancer survival and progression are being developed along with improved drug delivery methods, surgical techniques, and combination therapies.

Necrosis is an important hallmark for some aggressive cancers, and associates with hypoxia, inflammation, and angiogenesis responses.[16-18]

Hypoxia refers to a substantial and non-transient drop below physiological level of oxygen and is common in many malignant tumours. Hypoxia occurs due to inadequate blood supply. This is the result of the increased distance that oxygen must diffuse due to rapid tumour expansion and dysregulated or dysfunctional vascularisation.[19] Hypoxia leads to a number of phenotypic changes in cells. For instance, it is suggested to lead to acquisition of epithelial to mesenchymal transition phenotype, increasing cell mobility and metastasis.[19] Hypoxia can also affect cancer cell metabolism and contribute to therapy resistance by inducing cell quiescence. [19-21] Furthermore, hypoxia and necrosis have been increasingly associated with tumour stem cell populations and tumour invasion and are both poor prognostic markers of patient survival.[16, 19, 22-24]

1.3. Glioblastoma

Gliomas were thought to be cancers of the glial cells. Glia surround and support neurons in the central nervous system (CNS) and outnumber them by 3 to 1. The glial cells are subdivided, based on their function, into astrocytes, oligodendrocytes, and ependymocytes (Figure 1).

The cell of origin of gliomas remains a topic of controversy and debate in cancer research.[25-28] The cell of origin refers to the “normal” cell that develops the initial cancer promoting genetic traits. In several cancers, the cells of origin are suggested to be immature, proliferating cells and this is demonstrated in animal models of colon, breast, lung, and other cancers.[29] Evidence supports the idea that neural stem cells (NSCs), oligodendrocyte precursor cells (OPCs), and NSC-derived astrocytes could be the cells of origin of glioma.[25-28]

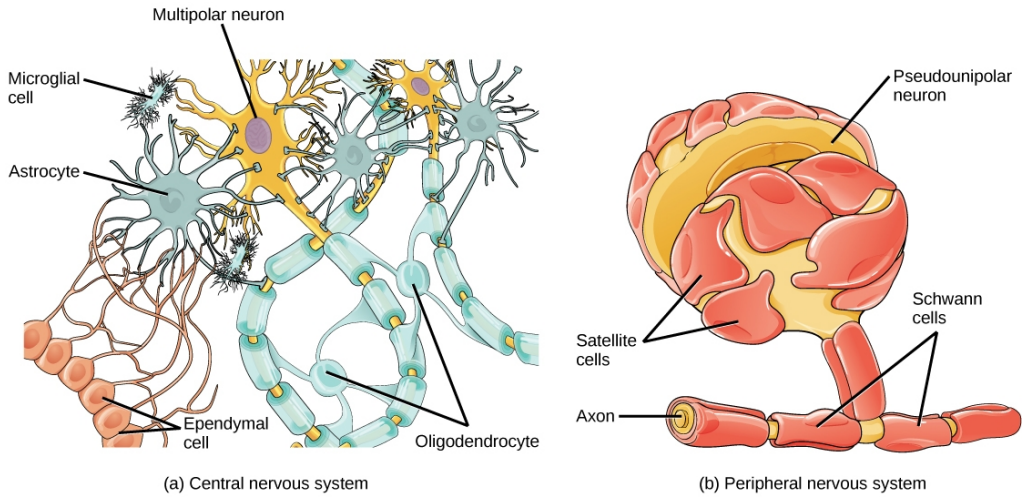

Figure 1 A cartoon depicting the arrangement of glial cells around a neuron.[30]

Gliomas are the most frequent primary brain tumours and despite decades of research into the area, prognosis remains bleak. The World Health Organisation (WHO) classifies gliomas into four grades of malignancy, based primarily on the histology of excised tissue. Grade I apply to neoplasms of low

proliferative potential with a possible cure following surgical resection.[9] Grade II neoplasms are generally of low proliferative levels with some infiltrative activity. They often recur after treatment and tend to progress to higher grades.[9] WHO grade III denotes tumours with histological evidence of malignancy, including nuclear atypia, vigorous mitotic activity and high angiogenic activity.[9] The designation WHO grade IV, also known as glioblastoma multiforme or GBM, refers to cytologically malignant, mitotically active, necrosis prone neoplasms demonstrating an aggressive proliferative and infiltrative capacity with high levels of vascularisation.[9] At this stage the cancer shows high levels of heterogeneity, with regions of pseudopalisading necrosis and haemorrhage (Figure 2), pleomorphic nuclei and cells, and micro vascular proliferation.[5] The cancer is genetically heterogenous with multiple gene deletions, amplifications and point mutations.[5] Unfortunately, GBM, the most aggressive grade IV neoplasm, is also the most clinically observed glioma/astrocytoma with an incidence of 3-6 in 100,000. [6, 7, 9]

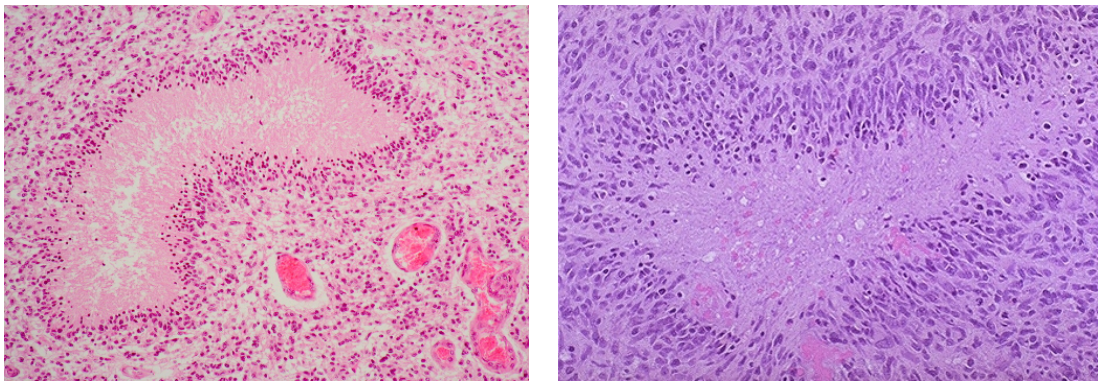

Figure 2 An example of pseudopalisading with necrosis of neoplastic cells in a GBM[31]

Most patients diagnosed with GBM do not survive past a year and essentially none have long term survival prospects with a median survival at the time of writing of under 14.6 months. Only 25 % of patients diagnosed with GBM survive more than one year and 5 % of patients surviving more than 5

years.[32] Due to this, more and more intricate and creative therapies for GBM have been proposed over the last half-century.

1.3.1. Clinical presentation of glioblastoma

The clinical history of patients diagnosed with GBM is generally quite short (<3 months in ~50 % of patients).[33] The common symptoms that lead to a patient seeking further help, and henceforth diagnosis, can include general symptoms of intra cranial pressure such as headaches, nausea, vomiting and cognitive impairment.[33-35] The patients could also present with slowly progressive neurological deficit, usually motor weakness.[35] Neurological symptoms could also be more focal and reflect the location of the tumour including but not limited to visual impairment, sensory loss, hemiparesis and aphasia.[35] Initial diagnostic tools can include a computed tomography (CT) or magnetic resonance imaging (MRI) scans.[36] Imaging by magnetic resonance imaging (MRI), grade II and III astrocytoma demonstrate hyper intense T2-weighted signal abnormalities indicating vasogenic-oedema as a response to the diffuse infiltration by individual tumour cells (Figure 3A).[37] Lower grade tumours tend to expand the surrounding brain but show mild or no contrast enhancement, suggesting an intact BBB and a lack of necrotic foci.[37-39] Growth rates of low grade glioma tend to be low with increases in diameter in the range of 2 to 4 mm/year.[37, 40, 41] The histopathological features of low-grade astrocytoma reflect the imaging properties. Glioma cells show diffuse infiltration, leading to architectural distortion and oedema.[42, 43] As the astrocytoma advances through from grade II to grade III, nuclear anaplasia

and proliferative capacity increases leading to a more densely cellular tumour with a higher level of malignant potential.[37, 44]

In the transition to GBM, the tumour dynamics drastically change. Radial growth rates can accelerate to values nearly 10 time that of grade II astrocytoma.[37, 40, 41] MRI reveals a central contrast enhancing component emerging from within the infiltrative tumour with rapid expansion outwards causing a much larger T2-weighted signal abnormality in the periphery of the tumour (Figure 3B).[37-39]

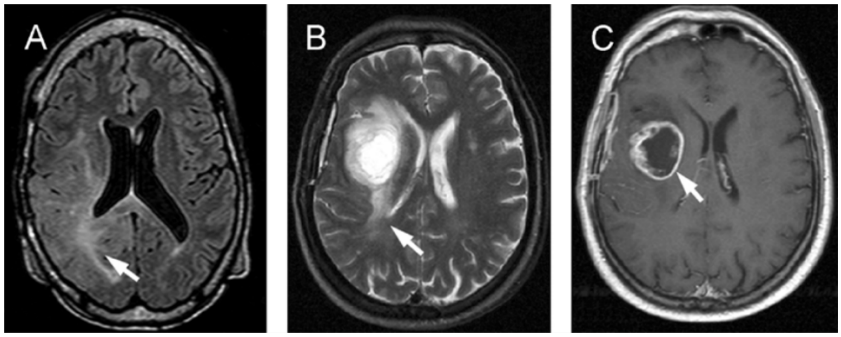

Figure 3 Examples MRI images of GBM. Anaplastic astrocytoma (AA, WHO Grade III) and GBM (WHO grade IV) have distinct growth patterns as demonstrated on magnetic resonance imaging (MRI). (A) Axial MRI of AA shows expansion of the involved brain and increased signal intensity on FLAIR imaging, reflecting the vasogenic edema that arises in response to infiltrating tumor cells (white arrow). After the administration of contrast agents, most AAs demonstrate modest or no enhancement resulting from an intact blood-brain barrier and a lack of central necrosis. (B) Axial MRI of GBM also demonstrates hyperintense regions at the tumor periphery on T2-weighted imaging, indicative of diffusely infiltrating cells (white arrow). (C) A distinguishing feature is the emergence of a central contrast-enhancing component, which contains a necrotic center and a leading edge that rapidly expands outward (white arrow).[37] J Neuropathol Exp Neurol | Copyright © 2006 by the American Association of Neuropathologists, Inc.

Most importantly for this study are the histopathologic features that distinguish GBM from its lower grade counterparts; the occurrence of foci of necrosis (Figure 3C) within the tumour mass with evidence of cellular pseudopalisades (“Pseudopalisading necrosis”) and the presence of microvascular hyperplasia, a form of angiogenesis, morphologically recognised as the proliferation of ECs with newly sprouted vessels.[45, 46]

1.3.2. Current treatment modalities for glioblastoma

1.3.2.1. Surgery

Surgery is an important modality both for diagnosis (through histopathological analysis of excised tissue) and treatment through removal of the bulk of the tumour mass. Though effective at removing the bulk of the tumour mass and generally improving quality of life for the patient, surgery does not provide a definitive cure and is restricted to those tumours that can be accessed.[8] The diffuse nature of GBM cell infiltration into surrounding tissue often makes it difficult to eliminate microscopic disease despite macroscopic gross-total resection.[47] There is a chance after resection of the main tumour mass, for the cancer to recur. [47-50] Studies have shown that about 80% of GBM recurrence after tumour resection occurs as a continuous growth within 2 cm from the border of the original tumour.[49, 50] The extent to which the tumour is resected may play an important role in the chance of recurrence.[49, 51]

Furthermore, complications may arise during the resection if there is damage to healthy tissue due to the brain's limited capacity for self-repair. The surgeon must consider location of the tumour and quality of life of the patient as to how aggressive they can be when resecting the tumour. Therefore, in the case of GBM, a 90 % threshold for tumour resection without compromising the functional pathways of the patient is the realistic goal for the surgeon.[48]

1.3.2.2. Radiotherapy

In addition to surgery, radiotherapy has been the cornerstone of treatment for GBM. For inoperable tumours, radiotherapy can be one of the only options. Radiotherapy “kills” cancer cells by focusing ionising radiation on to the cancer cells, causing DNA damage resulting in cell death. It is argued that highly proliferative cancer cells are more sensitive than the surrounding normal cells for DNA damage.[52]

Radioresistance has been observed in GBM with the theory that hypoxic but viable cells within the tumour are less likely to receive lethal damage from the radiation. In attempts to overcome the radioresistance in GBM, hypoxic cell sensitising agents such as metronidazole have been utilised. The studies failed to show any significant improvement in survival time over the conventional techniques.[53] Higher doses of radiation have been investigated to overcome radioresistance. However, due to side effects of radiation toxicity, radiation therapy necrosis and oedema, the clinical benefit is insignificant.[53, 54]

Delivery and type of radiation has been a key area of focus for development with improvements in imaging of tumours. The standard of care of radiographic characterisation of GBM is magnetic resonance imaging (MRI), which is a widely utilised examination in the diagnosis and post-treatment management of patients with GBM. Advanced MRI methods are being developed and used to further characterise GBM. Methods such as dynamic susceptibility contrast (DSC), dynamic contrast enhancement (DCE).[55-57]The ability to clearly define the tumour/normal tissue border (the margin zone) has allowed for a more accurate delivery of radiotherapy.[54]

1.3.2.3. Chemotherapy

In attempts to improve the duration of survival, chemotherapy regimens are augmented with concomitant adjuvant radiotherapy.[53, 58] The main chemotherapeutic agent in the clinic for treatment GBM is temozolomide (TMZ) a DNA-alkylating agent. TMZ is a prodrug in the sense that it is biologically inactive until metabolised in the body to produce the biologically active drug. The prodrug activation of TMZ can be seen in Figure 4.

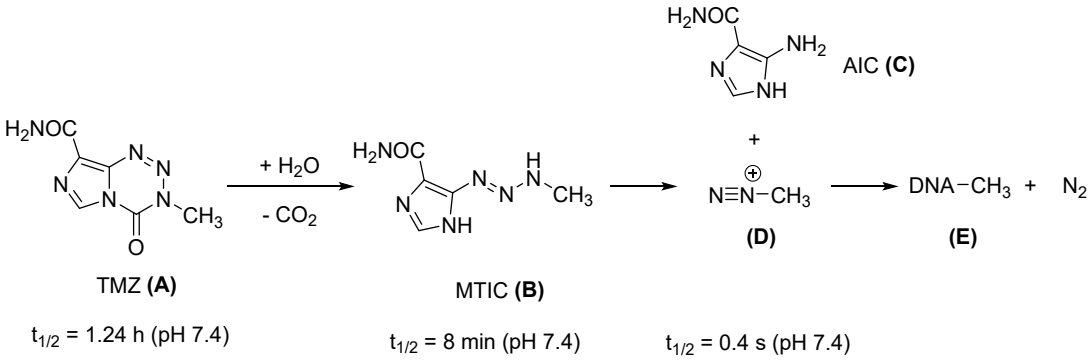

*Figure 4 Prodrug Activation of Temozolomide. Under neutral or alkaline conditions, TMZ **(A)** undergoes a hydrolytic ring opening. This gives the first significant intermediate, the open chain triazine MTIC **(B)**. This activated intermediate **(B)** fragments to produce AIC **(C)** and methyl diazonium ions **(D)**, the latter of which then reacts with nucleophilic sites on DNA, causing methylation **(E)**.*

A study published in 2002 investigated the use of TMZ concurrently with adjuvant radiotherapy and were able to demonstrate a median survival of 16 months with the combined treatment.[58] However, at least 50 % of patients treated with TMZ show no response to the drug, this is primarily down to the expression of O^6-methylguanine-DNA methyltransferase (MGMT) in GBM cells.[36, 59] MGMT is a DNA repair enzyme. The cytotoxicity of TMZ is mediated by its ability to add methyl groups at the O^6 and N^7 sites on guanine and N^3 site on adenine in genomic DNA.[59] Methylation of the O^6 site of guanine leads to the insertion of thymine instead of cytosine during DNA replication which can lead to cell death; MGMT protein acts to reverse the methylation of the O^6 position of guanine (Figure 5).[59]

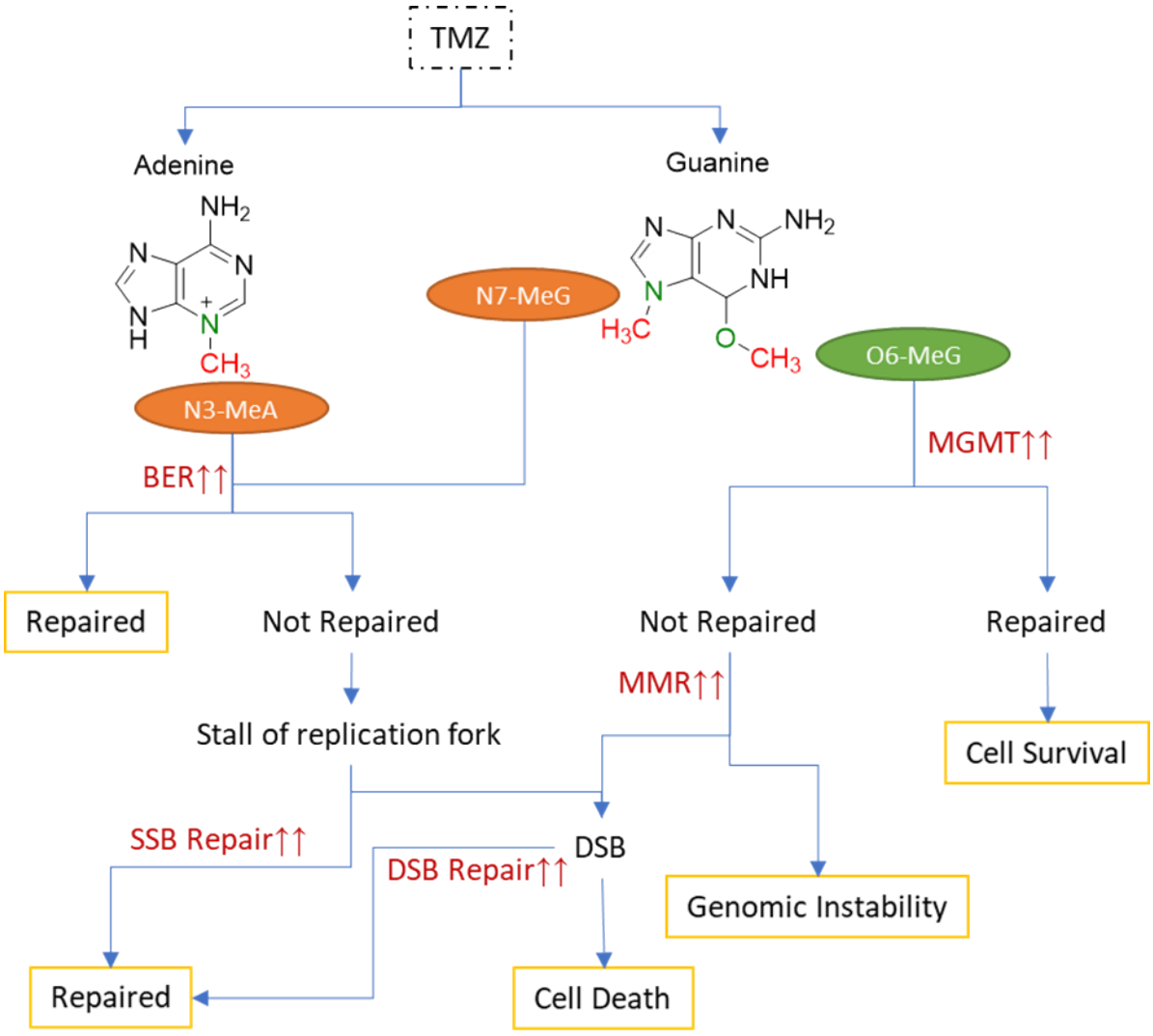

Figure 5 Temozolomide function and activated DNA repair pathway. Temozolomide (TMZ) is converted to 5-3-(methyltriazen-1-yl) imidazole-4-carboximide at physiologic pH followed by degradation to a methyl diazonium cation (see Figure 4), which transfers a methyl group to adenine and guanine of DNA. The most common sites of methylation are N7-methylguanine (N7-MeG) followed by N3-methyladenine (N3-MeA) and O6-methylguanine (O6-MeG). When active MGMT is present, O6-MeG is repaired without cytotoxicity. If MGMT is inactive, not expressed or does not have the potential to completely repair the methylation of O6-MeG, unrepaired O6-MeG undergoes repair by a cycle of mismatch repair (MMR) inducing cell death by causing double-strand breaks (DSB). Incorrect function of MMR leads to amplified genomic instability. N7-MeG and N3-MeA are repaired by base excision repair (BER) pathway. If the repair is unsuccessful, the alkylated bases cause a replication stall, collapsing the replication fork and generating single-strand breaks (SSB) and ultimately, DSBs leading to cell death. There is a possibility that the SSB and DSB repair pathways are activated, further diminishing the cytotoxic effects of TMZ.[60] Figure adapted from Complex DNA repair pathways as possible therapeutic targets to overcome temozolomide resistance in GBM.[60]

Cancer stem cells have been implicated in the progression and recurrence of GBMs. Glioma Stem Cells (GSCs – discussed in section 1.3.4.2) may cause resistance to TMZ. GSCs, identified by stem cell markers were shown to express high levels of MGMT protein, and had strong tumour resistance to

TMZ.[61, 62] Additionally, TMZ preferentially killed GSCs in MGMT-negative cell lines.[63, 64]

More recently, several new treatments, particularly tyrosine kinase inhibitors (TKI's) bevacizumab (vascular endothelial growth factor [VEGF] inhibitor), nimotuzumab (Epidermal Growth Factor Receptor [EFGR] inhibitor), as well as non-selective TKI's have been investigated, but their initial promise does not appear to have translated to the clinic where they fail due to both upfront and acquired resistance.[65-70] Another chemotherapeutic strategy to tackle recurrence of GBM is the use of intraoperative delivery of carmustine (BCNU) intravenously or by the implantation of a carmustine wafer (Gliadel) directly to the site of tumour resection; this technique is demonstrated to prolong survival in a number of studies.[48, 71, 72] However, BCNU is counteracted by the same resistance mechanism as TMZ and so maintains the same shortfalls.[73]

Due to the limitations of current therapies for glioma, as discussed above, there is an urgent need for novel approaches to treatment of glioma.

1.3.2.4. Barriers to drug delivery

The standard treatment for GBM is surgery. This approach is limited by the aggressiveness of GBM, characterised by the infiltration into surrounding tissue and extensive vascularisation. Hence, tumour resection is coupled with radiation therapy and/or chemotherapy. Effective treatment of GBM with conventional chemotherapies is disrupted by developed drug resistance. Further to this, because of the variably disrupted tumour blood supply, effective drug delivery to the required sites of action is difficult. In addition to

the low efficacy of current drugs, drug delivery via the circulatory system in hindered by physical barriers, the blood brain barrier (BBB) and the blood-tumour barrier (BTB).[74, 75] The BBB (Figure 6) is an anatomical and biochemical interface in the CNS between the blood and neural tissue, a barrier to protect the brain from potentially harmful substances in the systemic circulation.

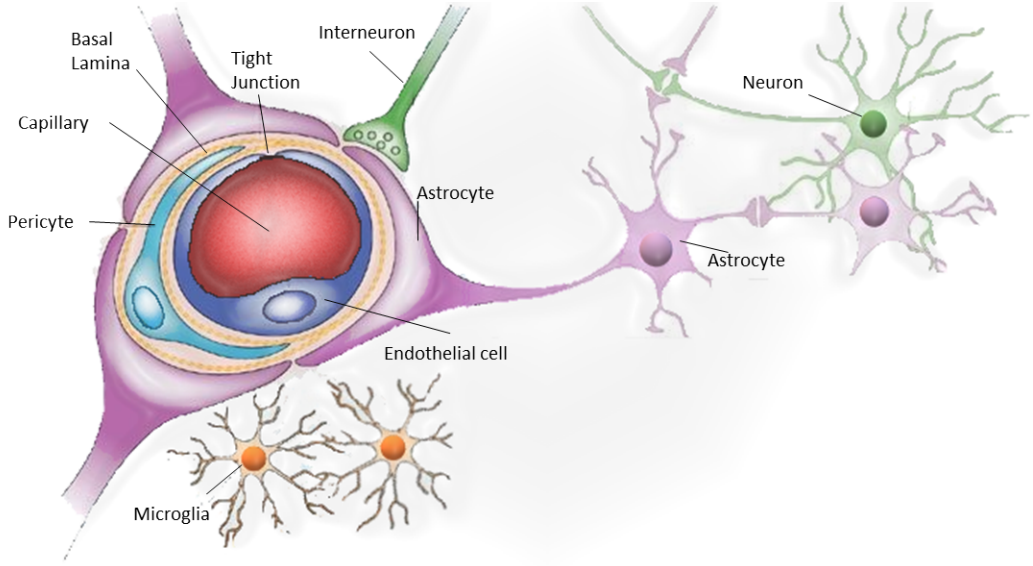

Figure 6 The blood-brain barrier (BBB). The BBB is formed by capillary endothelial cells surrounded by basal lamina and astrocytic feet, pericytes and microglial cells. Reprinted from Adv Drug Deliv Rev, 64(7), Chen Y, Liu L. Modern methods for delivery of drugs across the blood–brain barrier. 640–665., Copyright (2006), adapted and reprinted with permission from Elsevier.[76]

This physical barrier significantly limits the accumulation of hydrophilic drugs due to the lipophilic nature of the barrier.[74] The BBTB exists between the brain tumour tissue and the micro-vessels, and is formed of specialised endothelial cells (ECs), limiting the paracellular delivery of most hydrophilic drugs to the tumour tissue.[74] Several studies focus primarily on overcoming the difficulties faced with drug delivery to GBM, with promising results encompassing nanoparticle delivery methods and BBB disruption via ultrasound techniques or use of pharmacological agents.[74, 75, 77, 78] Ultimately,

when it comes to designing new drugs to treat GBM, considerations must be made to overcome the deficits encountered with drug delivery.

More recently, clinicians and researchers have begun to use more personalised therapies dictated by several factors including previous therapies the patient has received, their age and Karnofsky score.[79, 80] Molecular diagnostics have been used to better predict which therapies will benefit a certain patient group.[79, 80] Recent studies implicate cell surface chemotactic receptors and their corresponding ligands as key players orchestrating the aggressive nature of high grade gliomas. [81-86]

1.3.3. Necrosis

1.3.3.1. Types of cell death

Cell death is the irreversible degeneration of vital cellular functions culminating in a loss of cellular integrity. The mechanisms whereby dead cells and their fragments are disposed of have been historically classified under three forms:

- Type I cell death or apoptosis, exhibiting cytoplasmic shrinkage, chromatic shrinkage, nuclear fragmentation, and the formation of vesicles which are taken up by cells with phagocytic activity and degraded within lysosomes.
- Type II cell death or autophagy, displaying extensive cytoplasmic vacuolisation and similarly to apoptosis, culminating in phagocyte uptake and lysosome degradation.
- Type III cell death or necrosis, with no distinct features of the previous two types, the cells terminate with the disposal of cellular debris in the absence of phagocyte or lysosome activity.[87]

Apoptosis has traditionally been recognised as regulated cell death or programmed cell death which is a natural process resulting in the controlled disposal of cellular debris by phagocytic activity. Necrosis however is generally considered uncontrolled and is characterised by morphological changes such as disruption and breakdown of the plasma membrane resulting in the release of intracellular contents into the extracellular milieu.[87]

Necrotic cell death stimulates a host inflammatory response.[88] When cells die and undergo necrosis, the tissue site is rapidly infiltrated by leukocytes.[88-90] Microbial infection at a site of injury can stimulate a potent inflammatory response. However, inflammation can also be stimulated through sterile injury (without microbial presence) by release of proinflammatory factors by necrotic cells.[90] The signals that drive the sterile inflammatory immune response are normally contained within the interior of the cell and released into the extracellular domain when the cell loses integrity of it's plasma membrane. This indiscriminate inflammatory response helps to ensure adequate host defence.

The inflammatory responses to cell injury can be considered a "double-edged sword". Primarily, the response is to protect and help heal injured tissue. On the other hand, they can cause further tissue damage and disease.[90] Molecules generated to kill microbes such as reactive oxygen species and proteases are released from live and dying leukocytes, damaging and killing surrounding healthy cells.

In some situations where there is sterile tissue damage, inflammation has a higher negative cost to the host, doing more harm than good.[90] This has been demonstrated in experimental models of myocardial infarctions and toxic

damage to liver where tissue damage is reduced by the depletion of neutrophils or blocking of factors leading their accumulation.[90-93] Another study has shown that wound healing is prolonged by neutrophilic inflammation.[94]

Tissue damage from inflammation is not limited to acute responses and neutrophils. Macrophage chronic inflammatory infiltrates can also damage normal/healthy cells and is thought to underlie the pathogenesis of many chronic diseases e.g. autoimmune diseases, chronic obstructive pulmonary disease, and Alzheimer's disease.[90] Further to this, the links between cancer and chronic inflammation have been widely investigated.[95, 96] The association between the development of cancer and inflammation has long been appreciated.[95-97] There is evidence to suggest inflammation and immune responses may inhibit the development of cancer.[97] On the other hand, some forms of chronic inflammation have been directly linked to tumorigenesis.[97-99] Pre-malignant tumours can be "wound-like" causing an inflammatory response, mediating angiogenesis, tissue invasion and metastasis.[97, 100-102]

As understanding of cell death continues to progress, novel mechanistic pathways that orchestrate cell death are being characterised leading to a better understanding and reclassification of the underlying mechanics of cell death. Apoptosis and necrosis are common hallmarks of cancers with the latter being a particularly negative prognostic marker for several cancers.[103]

1.3.3.2. Necrosis in glioblastoma

Necrosis has long been recognised as a hallmark GBM, a key prognostic marker when defining the progression from a grade III neoplasm to a grade IV; with previous research looking at the molecular pathways to necrosis and the development in diagnostic imaging techniques specifically focused on the non-invasive detection of necrosis.[7, 9, 35, 37, 54, 104-106] Some clinical observations suggest that necrosis has a negative impact on survival.[37, 104]

Necrotic foci within the tumour can be formed as result of vaso-occlusion and intravascular thrombosis during the rapid and uncontrolled growth of the tumour, leading to hypoxic and nutrient starved cells.[104, 107-109] The model hypothesises a sequence that begins with the infiltration of astrocytoma of moderate to high cellularity, vascular occlusion associated with intravascular thrombosis leads to hypoxic regions forming around compromised vasculature. Outward migration of tumour cells away from hypoxic regions creates a peripherally moving wave (pseudopalisade) with central necrosis (Figure 2). The secretion of hypoxia-inducible, proangiogenic factors such as VEGF and interleukin 8 (IL-8) from the pseudopalisading cells causes an angiogenic response creating microvascular proliferation adjacent to the central hypoxia.[110] The movement/ invasion of cells and remodelling of the extracellular matrix (ECM) is facilitated through the release of matrix metalloproteinase (MMP) enzymes MMP2, MMP9 and MMP13.[111, 112] The tumour cells are accelerated outwards towards new vasculature. The growth properties of GBM reflect a union of these microscopic processes and the result, a peripherally expanding tumour with a large degree of central necrosis and microvascular hyperplasia.

Another theory instigates disruption of the tumour necrosis factor apoptosis pathway, promoting necrosis over apoptosis as the final mode of cell death.[104] Tumour necrosis also results from certain treatment modalities, including radiation therapy necrosis.[53, 104, 113, 114] Both therapy and tumour induced necrosis share many features with tissue necrosis observed during bacterial infection, including a key role for the formyl peptide receptor 1 (FPR1).

Necrosis can induce an inflammatory response in the tumour. Pro-inflammatory activity of dead cells occurs from a variety of intracellular molecules that are released as cell permeability breaks down during necrotic cell death. These molecules have been termed damage associated molecular patterns (DAMPs) or alarmins. Alarmins are defined functionally by their ability to trigger innate immunity, promote chemotaxis and stimulate antigen specific responses.[115] Excessive necrosis during tumour development may infer a more aggressive phenotype due to the stimulatory role of necrosis induced inflammation.[103] A study by J. C. Lin *et al.* suggests that inflammation promotes tumour cell proliferation and increases GBM invasion through interaction between intercellular adhesion molecule-1 (ICAM1) and Musashi-1 (MSI1).[116] This study is supported by observations by M. Papale *et al.* that hypoxia is important for GSCs maintenance, but also for guiding GSCs response to external necrosis.[24] Migration of GSCs was induced *in vivo* by necrotic extract. [24] Interestingly, surgical resection and biopsy of the tumour has potential to induce local recruitment of monocytes/macrophages, which can subsequently increase tumour progression of remaining tumour cells.[24, 117, 118] National Institute for Health and Care Excellence (NICE) guidelines recommend after surgery, the patient is treated with radiotherapy followed up

by adjuvant TMZ.[119] Radiotherapy following tumour resection is to kill any remaining cancer cells and prevent recurrence. However, radiotherapy can cause radiation necrosis, stimulating inflammation at the resection site, and blood vessel related radiation damage leading to hypoxic stress.[120-122] As previously mentioned, GSCs respond to necrosis and inflammation, and so the presence of radiation necrosis may drive disease progression/ recurrence.

1.3.3.3. Necrosis and tumour aggression

At the centre of cancer treatment is the induction of tumour cell death which is achieved by various methods such as radio- and chemotherapy. The necrosis present in GBM is indicative of cell death, however, this type of cell death is not desirable in tumours. Clinical observations suggest that the presence of necrosis in GBM has a negative impact on survival.[104-106, 123] In one study looking at necrosis as a prognostic factor in GBM, 88 % of patients with GBM presented with tumour necrosis, furthermore the GBM patients absent of tumour necrosis predicted longer survival times.[123] Patients without tumour necrosis had a median survival of 12.5 months, the patients presenting with tumour necrosis had a median survival of 10.9 months.[123] However, the two year survival of patients with and without tumour necrosis did not present with a statistically significant result. Another study identified the degree of tumour necrosis measured by MRI to have an inverse correlation to patient survival (Figure 7).[124] These findings were confirmed in a more comprehensive study of prognostic factors relating to survival in GBM.[125]

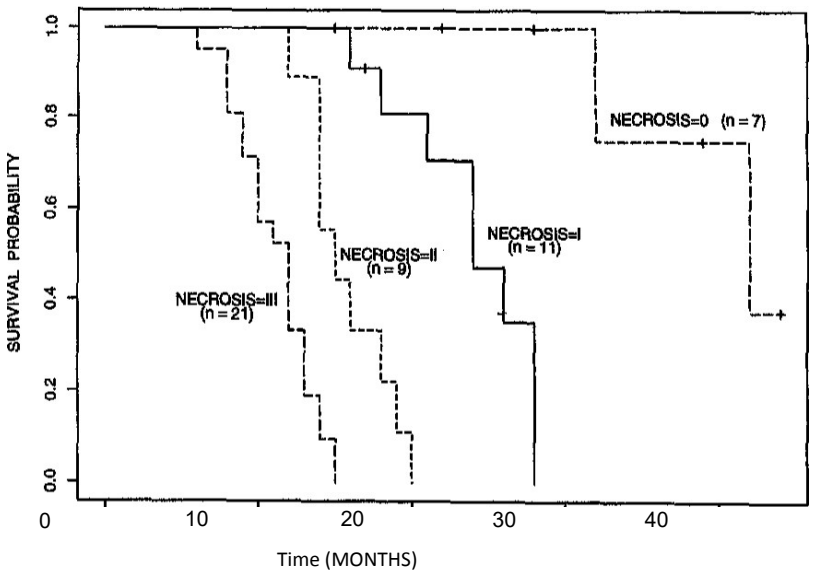

Figure 7 Graph of survival probabilities of GBM patients by degree of magnetic resonance imaging (MRI)-based tumour necrosis. Necrosis=0, no necrosis apparent on the MRI scan. Necrosis=I, necrosis amounts to less than 25 % of the tumour volume. Necrosis=II, necrosis amounts to 25 to 50 % of the tumour volume. Necrosis=III, necrosis amounts to over 50 % of the tumour volume.[104]

1.3.4. Tumour heterogeneity and the tumour microenvironment in GBM

1.3.4.1. The GBM microenvironment

The brain tumour microenvironment is emerging as a critical regulator of cancer progression and aggression with several approaches currently in preclinical and clinical studies to target the microenvironment in brain tumours as a potential therapeutic.[126] Solid cancers like GBM appear to hijack resident and infiltrating non-tumour cells and exploit the existing ECM and interstitial fluids to progress and survive.[127] The glioma microenvironment consists not only of glioma cells, but an intricate network of encompassing different cell types ECs, microglia, astrocytes), stromal components and soluble factors and the extracellular matrix.[128] GBM cells infiltrating through the brain parenchyma (invasion) is a complex process driven by direct interaction with the ECM; the cells must interact and remodel the ECM through the release of MMP enzymes including MMP2, MMP9 and MMP13.[111, 112, 128] The effects of MMPs on GBM

progression amplify through interactions with other features of the GBM microenvironment including cell receptors, ECM components and other soluble factors.[129]

One of the more important features of GBM relating to the presence of necrotic foci are the hypoxic environments that are recognised as a driving force for tumour progression, invasion, and tumour cell survival and resistance to chemotherapy and radiotherapy. Hypoxia in GBM is a result of increased cell proliferation linked to erratic tumour neovascularisation and vasculature occlusion leading to poor oxygen diffusion.[20] Hypoxia in regions of the tumour stimulates the expression of transcription factors hypoxia inducible factor (HIF), hypoxia-inducible factor 1-alpha (HIF-1-α) and endothelial PAS domain-containing protein 1 (EPAS-1 [formally known as HIF-2-α]); the master regulators of the hypoxia adaptive response.[20] Hypoxia is also well known to regulate a many proangiogenic, pro-invasion and proinflammatory factors including carbonic anhydrase IX, VEGF, MMPs, integrin β3, IL-8/CXCL8, C-X-C chemokine receptor type 4 (CXCR4), Stromal cell-derived factor 1 (SDF-1) and annexin A1 (ANXA1).[20, 130-132] Targeting the hypoxic niche in GBM as a combinatorial therapy could bring light to new therapies for GBM while supporting the existing therapies that ultimately fail due to developed resistance relating to hypoxia.

1.3.4.2. Molecular GBM heterogeneity

A significant obstacle challenging the development of effective GBM therapeutics include tumour heterogeneity.[133-135] The incomplete understanding of GSCs, which give rise to chemotherapy and radiotherapy

resistance, and cancer recurrence, only contribute further to these challenges.[61, 136, 137] Heterogeneity between GBM patients was established through genomic and transcriptomic analyses by The Cancer Genome Atlas (TCGA) research network.[133, 138] Analysis of whole-tumour transcriptomic data, primarily extracted from differentiated cells, showed that GBM could be originally grouped into four main subtypes: proneural; neural; classical; and mesenchymal.[139] These four subtypes were characterised by an 840 gene signature (210 genes per type), with gene abnormalities in Platelet-Derived Growth Factor Receptor (PDGFRA), Isocitrate Dehydrogenase (NADP(+)) 1 (IDH1), EGFR, and Neurofibromin 1 (NF1).[139] The gene signatures of normal brain cell types were shown to have a strong relationship between GBM subtypes.[139] More recently, the neural subtype has been dropped from the classification of subtypes.[140] The neural subtype had been previously associated with the tumour margin where normal neural tissue is more likely to be detected.[140, 141] Using a 500 gene signature, the proneural and neural subtypes defined by Verhaak's 840 gene signature now form a single subtype (proneural/neural subtype).[142]

Another layer of complexity arises from the presence of a subpopulation of GBM cells that have stem cell properties.[143, 144] The idea of cancer stem cells stems from our understanding of "normal" stem cells, the cells must exhibit the ability of self-renewal and to produce differentiated progeny.[145] GSCs do exhibit these properties. GSCs can propagate tumours from one host to another, and they can develop to form brain cancers in orthotopic xenograft models that recapitulate the original tumour.[143, 146] The GSC population, though relatively small in comparison to the bulk of the tumour mass, is

relevant clinically. Studies have shown GSCs to have a higher resistance to radiotherapy compared to non-GSCs due to a series of cellular factors including an increased DNA repair capacity.[147-149] As previously mentioned, GSCs have a higher capacity to resist TMZ (and other DNA alkylating agents) chemotherapy through the MGMT DNA repair pathway. [61, 62, 150, 151]Tumour heterogeneity poses a major challenge to cancer diagnosis and treatment. Cells within the same tumour may express different genetic signatures or phenotypic states. Single-cell RNA sequencing (scRNA-seq) has enabled gene expression to be studied at an unprecedented resolution.[152] scRNA-seq is helping to better understand intratumoural heterogeneity by profiling cell-to-cell variability on a genomic scale. This is of particular importance in GBM as tumour heterogeneity is increasingly appreciated as a determinant of treatment failure and disease recurrence.[153] A recent study used scRNA-seq to show that GBM recapitulated normal neurodevelopmental hierarchy and suggested the use of this hierarchal map to identify therapeutic targets specific to GSCs.[133] scRNA-seq is increasing being used as a tool to understand the link between poor prognosis or recurrence of GBM and tumour heterogeneity, and more precise classification of GBM in the clinic.[154, 155]

1.3.4.3. 3D-multicellular spheroids as an *in vitro* model of the tumour microenvironment

3D *in vitro* cell culture models can simulate *in vivo* tumour microenvironments better than 2D cultures and are being increasingly used to study tumour cell biology and to test potential new therapeutics. It has been shown that 2D cell culture models are not suitable models for recapitulating

the microenvironment of solid tumours.[156-158] Cells in 2D culture are less likely to exhibit stem cell properties, and do not mimic the microenvironmental stress (hypoxia/necrosis) or ECM components, and cell-cell interactions.[159] This has led to a large deviation in drug sensitivities between *in vitro* and *in vivo* clinical studies.[159]

Indeed, glioma cells when grown *in vitro* as a 3D structure, either on a "scaffold" or as a multicellular spheroid have been shown to better mimic the tumour microenvironment.[156, 158] The tumour cells in 3D culture demonstrated greater levels of differentiation, quiescence as well as enhanced chemotherapeutic resistance with larger populations of glioma stem cells and an upregulation of O^6-methylguanine DNA methyltransferase (MGMT) over cells grown in 2D culture.[156] Dependant on the needs of the researcher and the method used, 3D multicellular spheroids can be obtained in a multitude of dimensions; larger spheroids in particular (starting from 400-500 μm in diameter) are characterised by a ring of proliferation on the periphery of the spheroid, an internal quiescent zone caused by limited oxygen and nutrient diffusion and a necrotic central core resembling the heterogeneity observed in solid *in vivo* tumours.[160]

1.4. Formyl Peptide Receptor 1 (FPR1)

There is a large body of research that suggests that malignancy in glioma is orchestrated by cell surface chemotactic receptors, with a particular emphasis on formyl peptide receptor 1 (FPR1).[81-84, 161, 162] The human genome encodes for three formyl peptide receptors (FPRs), the most common being FPR1.[162] This is followed by formyl peptide receptor 2 (FPR2) which is expressed by neutrophils, monocytes, eosinophils, macrophages, synovial fibroblasts, and airway and intestinal epithelium.[162] Formyl peptide receptor 3 (FPR3) which is detected on monocytes but not macrophages.[162] The FPRs belong to the Class A of the G-protein coupled seven-transmembrane domain receptor (GPCR-7TM) super family.[162] GPCR-7TMs comprise of an extracellular N-terminus followed by seven helical domains in a "serpentine" formation enclosed within the cell membrane, and an intracellular C-terminus which binds to a G-protein complex.[162] G-protein coupled receptors (GPCRs) generally detect/interact with molecules in the extracellular region and activate intracellular signal transduction ultimately leading to a cellular response. In Class A GPCRs, the principal interactions between receptor and ligand occur within the extracellular region of the 7TM domain.

Chemoattractant GPCRs participate in essential homeostasis as well as pathophysiological processes in humans, including inflammation, development, haematopoiesis, wound healing and host defence against pathogens.[162] The human GPCR FPR1 was originally detected as a high affinity binding site on human neutrophils in 1976.[162] FPR1 was found to bind to N-formyl-methionyl-leucyl-phenylalanine (fMLF), a formylated peptide product of gram-negative bacteria, mediating leukocyte chemotaxis and

activation.[162] Activation of FPR1 regulates the infiltration of phagocytes, particularly neutrophils to sites of inflammation in response to tissue derived chemoattractant ligands.[162] Though the exact causes of high grade glioma have not been identified, an accumulating body of evidence suggests the possibility that glial cells undergo genetic mutations that promote a malignant transformation giving the cells the ability to sense growth signals present in the microenvironment by over-expressed cell surface receptors.[163, 164] The receptors that are over-expressed include receptors for EGFR and basic fibroblast growth factor (bFGR).[84, 165] As well as growth factor receptors, the role of chemoattractant GPCRs has been recognised, these include the chemokine receptor CXCR4 and more importantly for this study, FPR1. FPR1, through interaction with the endogenous ligand ANXA1, is able to transactivate EGFR in GBM cells to mediate cell growth, migration and the production of angiogenic factors (Figure 8).[81, 84, 166] The activation of EGFR results in an increase of transcription factors, including Nuclear Factor Kappa-Light-Chain-Enhancer of Activated B Cells (NFκB), Signal Transducer and Activator of Transcription 3 (STAT3) and HIF-1-α.[83] Both STAT3 and HIF-1-α have been implicated in the transcriptional gene coding for VEGF, and the activation of FPR1 has been shown to lead to an increase in VEGF, as well as other important promoters of cancer and metastasis such as the matrix metalloproteinases MMP2 and MMP9.[82, 84, 166, 167]

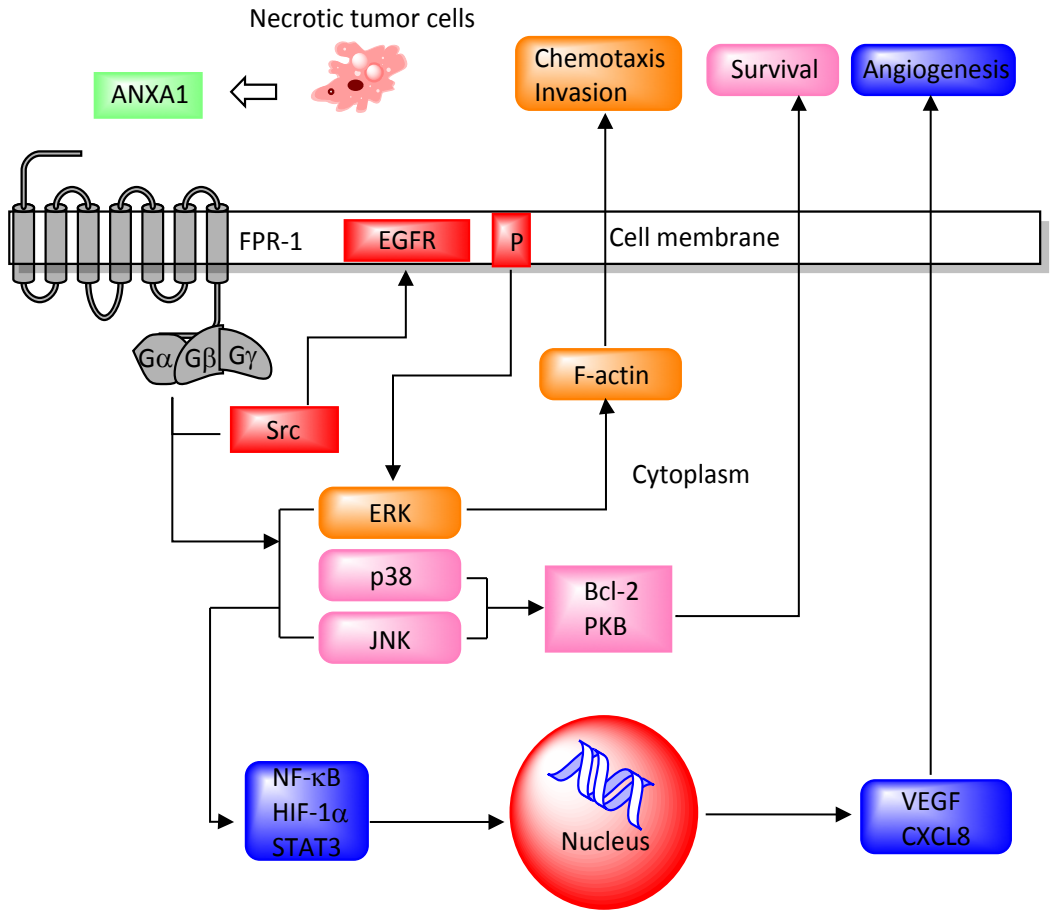

Figure 8 The signalling pathway of FPR1 in human GBM. FPR1 on GBM is activated by tumour and host derived agonists, of which include ANXA1 which is released by necrotic tumour cells. Agonist binding to the receptor activates the regulatory molecules ERK1/2, JNK, MAPK and p38, and transcription factors NFκB, STAT3 and HIF-1-α to enhance invasion, growth and angiogenic factors. FPR1 function in GBM is partially mediated by EGFR through a Src kinase dependent transactivation pathway. Intracellular signalling pathways between the two receptors help drive the malignant behaviour of the GBM tumour.[84]

1.4.1. FPR1 Structure and Binding Properties

FPR1 was the first neutrophil GPCR to be cloned and sequenced. It comprises of a "serpentine" structure consisting of a 350-residue protein with seven hydrophobic segments.[168, 169] A subsequent study further elucidated the structure of FPR1 as a 7-helical transmembrane receptor with an extracellular N-terminus and three loops exposed for ligand interaction and an intracellular C-terminus and the remaining loops contained within the cytoplasm for intracellular signalling (Figure 9).[168, 170] The binding site within the FPR1

molecule for the agonist ligand fMLF had been previously investigated by use of site directed mutagenesis and fMLF analogues (Figure 9).[171] The formamide group of fMLF hydrogen bonds to both Asp-106 and Arg-201, while the COOH-terminal of fMLF ion paired with Arg-205, an area that is favoured by small ligands in the Class A GPCR family.[171, 172]

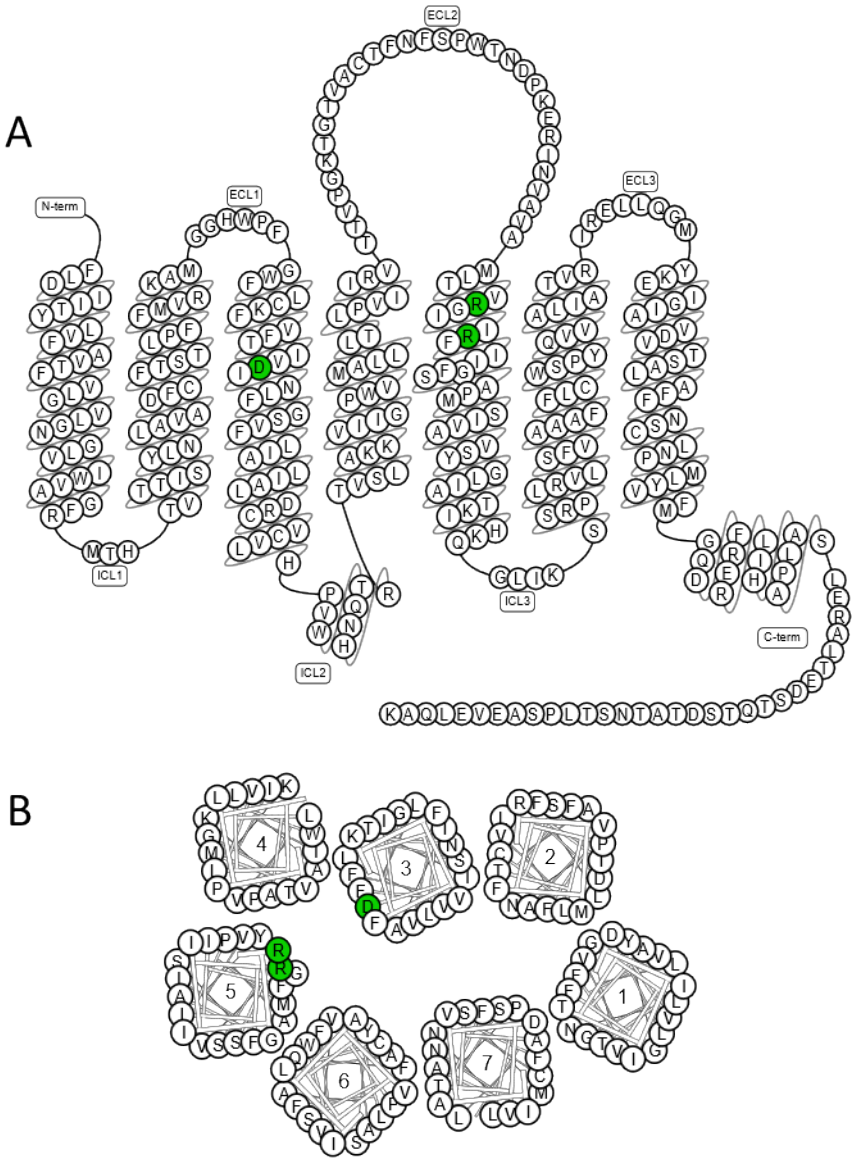

Figure 9 The sequence and predicted structure of FPR1 with key fMLF binding residues labelled (green). (A) side view of the "serpentine" structure (ECL=extracellular, ICL=intracellular). (B) Top down view of the FPR1 structure showing the binding pocket for FPR1. (generated from, http://gpcrdb.org/protein/FPR11_human/).

1.4.2. Expression of FPR1 in High Grade Glioma

FPR1 was detected in high grade human glioma primary specimens. 33 surgically removed gliomas of various grades were examined, with a 78 % positive rate in grade III anaplastic astrocytoma and a 100 % occurrence in grade IV GBM.[83, 84, 86] This was contrasted by a much lower incidence of just 15 % positive for FPR1 in the lesser aggressive grade II astrocytoma.[83, 84] More importantly, FPR1 has been shown to be highly (and functionally) expressed by GSC subpopulations, identified by the expression of the stem-cell marker CD133.[82, 167, 173, 174] These GSCs expressing both CD133 and FPR1 were shown to be more invasive, tumorigenic and stronger promoters of angiogenic factors than those that do not express FPR1.[82, 167, 173, 174] FPR1 expression in CD133 positive cells has also been associated with the self-renewal properties of the GSCs and is lost in differentiated cells.

One of the major problems with the efforts to understand the cancer biology of glioma is that commonly available cell line models for glioma are poor in recapitulating the features of the disease. This is in fact a problem for the study of FPR1. For example, although FPR1 expression is strong in clinical tissue, Walenkamp has shown that patient derived immortalised cell lines originating from these clinical tissues lose their expression of FPR1 in culture, although interestingly they regain the FPR1 expression if re-implanted into mice.[175] In other words, expression of FPR1 is induced within the tumour microenvironment through mechanisms which are yet unknown.

There are many cell lines used in preclinical investigations of new glioma therapies including but not limited to the human glioma cell lines; U-87 MG, U251, LN229, T98G and the rat cell line C6. Some studies prefer or require

the use of primary cell lines established directly from patient material to maintain a closer profile to the source material.

U-87 MG cell line, derived from a female GBM patient, is widely used. The use of this cell line is not without controversy. U-87 MG was established in 1966 at the Uppsala University in Sweden, using tissue derived from a 44-year-old woman with aggressive GBM.[176] However, a study released in 2016 has noted that the current U-87 MG line in general circulation and available from the ATCC has a Y chromosome suggesting the source tissue for the current U-87 MG is from a male patient.[176] The U-87 MG line from ATCC was compared to the archival U-87 MG stored at Uppsala University and found that it was not a match, suggesting that at some point between Uppsala and the ATCC, there was a mix-up with the samples.[176] However, the gene expression showed that the current U-87 MG cell line still possibly originated from a brain tumour and so studies still reflect brain-cancer biology.[176]

1.4.3. FPR1 and Angiogenesis in GBM

A hallmark for the progression of malignant tumours is the increase in angiogenesis, which is attributed to the production of angiogenic factors by tumour and stromal cells. One of the pathologic features that distinguish GBM from lower-grade glioma is microvascular proliferation. Several studies have indicated that in the comparison of perfusion in normal cortical tissue and perfusion in glioma tissue, perfusion in the malignant glioma tissue is decreased and variable.[104, 177, 178] This observation is somewhat contradictory as GBM are among the most angiogenic and vascularised human tumours.[179] However, where 95 % of normal cortical capillaries exhibit red blood cell

perfusion, on average, only 50-70 % of newly formed glioma vessels exhibit perfusion with decreased levels towards the centre of larger tumours triggering hypoxic conditions and necrosis. Interestingly, the hypoxic transcription factor HIF-1-α enhances the transcription of the most potent angiogenic factor produced in solid tumours;[45, 180, 181] VEGF, which not only induces cell migration and tubule formation but also increases micro vascular permeability that facilitates dissemination of tumour cells.[82, 180, 182] By blocking VEGF either with antibodies or with VEGF withdrawal in experimental models, apoptosis of ECs occurred and tumour growth was inhibited.[84, 183, 184] Interestingly, a study has demonstrated that activation of FPR1 in GBM cells increases the production of VEGF along with other angiogenic factors including CXCL8, this indicates a correlation between FPR1 expression/activation and increased angiogenesis/ vascularisation in GBM.[84]

1.4.4. FPR1 promotes cell survival in GBM cells

The function of FPR1 in glioma has been studied and many of the subsequent pathways from FPR1 activation closely relate to GBM cell proliferation and survival.[86] Studies have shown *in vitro*, the stimulation of FPR1 supports the survival and proliferation of GBM cells in culture medium supplemented with a low concentration of serum through increased cellular levels of Bcl-2, an anti-apoptotic protein.[84, 86] Activation of FPR1 also increased the phosphorylation of nuclear factor-κB (NF-κB), STAT3 and HIF-1-α.[84] Phosphorylation controls transcription in a gene-specific matter regulating stability, nuclear localisation, transactivation and protein-protein interaction in these transcription factors.[185-187] NF-κB is a transcription factor

that regulates several genes associated with cellular processes in GBM, including proliferation, differentiation, cell motility and survival.[188] The role of STAT3 in GBM is critical in mediating tumorigenesis, tumour progression and suppression of anti-tumour immunity.[189] HIF-1-α as previously mentioned is a recognised as a driving force of invasion and survival, and vital in tumour resistance to chemotherapy and radiotherapy.

1.4.5. FPR1 promotes invasion in GBM cells

A critical characteristic of high-grade glioma and in particular GBM is the high rate of growth and the aggressive and diffuse rate of invasion into surrounding normal tissue.[82, 167] The invasion of GBM was studied *in vivo* by subcutaneous implantation into nude mice of both $FPR1^+$ and $FPR1^-$ clones isolated from the U-87 MG cell line.[82] The $FPR1^+$ clone had a greater rate of invasion into surrounding tissue in comparison to the $FPR1^-$ cells.[82] Also, transfection of the human *FPR1* gene into the $FPR1^-$ G3 U-87 MG subclone resulted in a more invasive phenotype.[82] The $FPR1^+$ tumours were also observed to grow more rapidly and there was an increase in the release of MMPs, key mediators in ECM remodelling and are implicated in the assistance of the break-out of tumour cells from the primary site.[82]

1.4.6. FPR1 and the endogenous ligand ANXA1

The activation of FPR1 *in vivo* suggests an endogenous agonist is present in the tumour microenvironment. To investigate the link between FPR1 and necrosis, a necrotic supernatant was generated from U-87 MG cells and primary glioma tissue.[86] The cells were artificially necrotised by cycled freezing and thawing.[86] The necrotic supernatant of U-87 MG cells and primary tumour tissue was shown to increase motility and trigger an influx of calcium in a calcium flux assay in U-87 MG cells.[86] A desensitization assay with fMLF and the necrotic supernatant demonstrated that the agonist contained within the necrotic supernatant may interact with FPR1.[86] Further studies on the necrotic supernatant identified ANXA1 as the critical protein for activation of FPR1.[85] For clinical relevance, ANXA1 expression had been investigated in human primary tumours and of 102 cases tested, 42 % of Grade II, 100 % Grade III and 88 % of Grade IV stained positive for ANXA1.[85, 175]

Removal of ANXA1 by immunoadsorption from the necrotic supernatant diminished the ability of the necrotic supernatant to promote GBM cell growth, invasion and colony formation *in vitro*.[85] Knockdown of ANXA1 by small interfering RNA (siRNA) dramatically reduced the tumorigenicity of GBM cells in nude mice.[85] Knockdown of both FPR1 and ANXA1 further reduced the tumorigenicity of GBM cells.[85] Like FPR1, ANXA1 appears to be more highly expressed in higher grade gliomas.[190, 191] However, ANXA1 is an intracellular protein while FPR1 is activated in the extracellular region. This suggests that ANXA1 must be released into the extracellular region to interact with FPR1. One suggestion is that ANXA1 is released during necrosis of tumour cells.[85] This is supported by the fact that one key characteristic of GBM tumours is the

presence of hypoxia induced multifocal necrosis.[9, 131, 192] This would support the hypothesis that FPR1 activation promotes the survival and expansion of GBM via the tumour microenvironment.[131, 164, 192] The occurrence of necrosis suggests a region where oxygen and nutrients are low, thus there is the requirement by the adjacent cells to migrate, source new supplies of nutrients and oxygen via the formation of new vasculature and to resist apoptosis.[193] It is suggested that the pseudopalisading cells adjacent the necrotic foci in GBM represent an actively migrating cell population moving away from an area of central thrombosis. (Figure 2).[107, 110, 193]

1.4.7. FPR1 Transactivates EGFR

Epidermal growth factor (EGF) has been implicated as one of the more important growth stimulating protein in a variety of malignant tumours.[166, 194-198] Human GBM cells have been shown to also express the EGF receptor (EGFR) as well as FPR1.[84, 199, 200] Around 40-60 % of clinical cases of GBM contain EGFR gene amplification.[84, 165] The two receptors have intracellular pathways directly linking them (Figure 8). The pathway through which FPR1 transactivates EGFR has been identified to be through intracellular signalling rather than FPR1 causing EGF production, and thus EGFR is activated devoid of its corresponding ligand.[84, 165] Depletion of EGFR does not completely suppress the tumorigenicity of GBM cells, though an almost complete abrogation of GBM tumour growth was achieved when both FPR1 and EGFR were knocked down in xenograft models.[84, 165] This suggests the activation of FPR1 is able to support tumour growth through non-EGFR pathways. This

highlights the requirement of concomitant therapies to tackle the disease from multiple angles.

1.4.8. FPR1 as a pharmacological target

FPR1 plays an important role in the progression of diseases including inflammation and malignancies. Based on the evidence presented above, in high grade glioma such as grade IV GBM, FPR1 has been implicated as a vital component in the driving force behind the aggressive nature of the disease, all by activation of the receptor through the endogenous ligand ANXA1 which is released in hypoxic/necrotic regions. While a multi-pronged approach may be the best mode of action targeting hypoxia, EGFR and FPR1; FPR1 takes focus in this study. There is a need for selective and potent small molecule antagonists of FPR1 that have a suitable PKPD profile for penetrating the blood brain barrier.

1.4.9. Known FPR1 Antagonists

Having previously been identified as a key player in inflammatory diseases and more recently a key player in glioma progression, it is not surprising that several FPR1 antagonists have already been identified. Small-molecule, selective antagonists of FPR1 are critical as probes to help with understanding the disease progression and for acting as a platform for potential future therapies. There is an increasing interest in the FPR1 signalling pathway in a multitude of biological mechanisms, from the innate immune response to disease progression and so the number of synthetic and natural FPR1

antagonists appearing in current literature is increasing.[168, 201-207] A selection of FPR1 antagonists is shown in Figure 10.

Cyclosporines

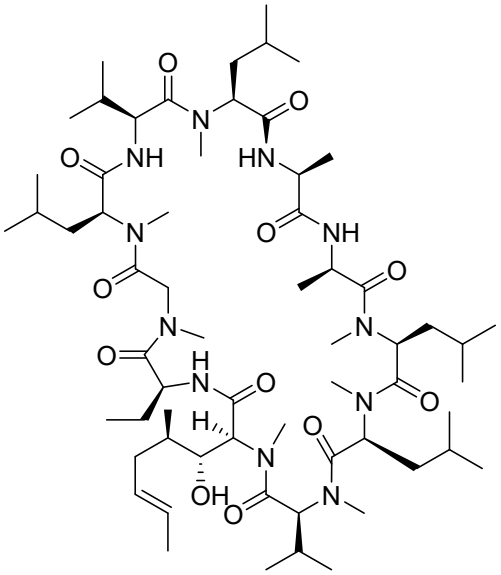

(1)

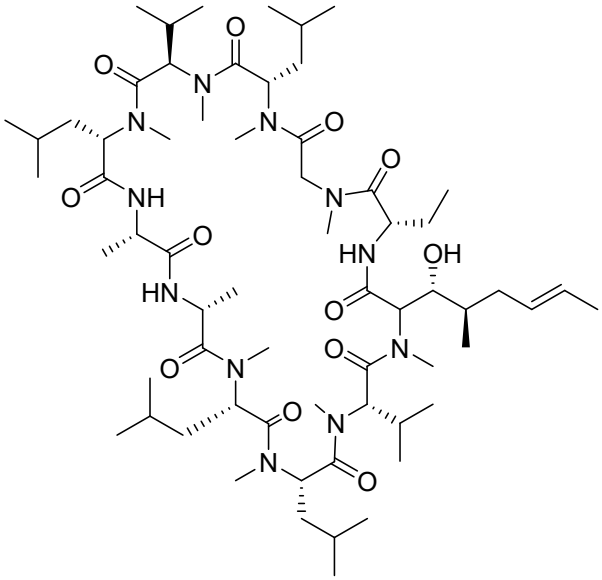

(2)

fMLF derivatives

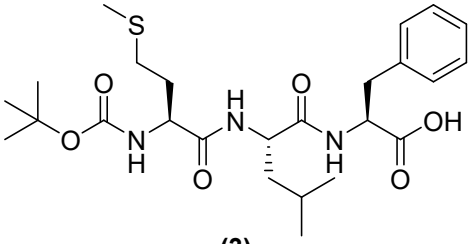

(3)

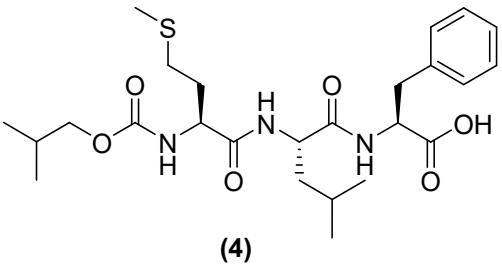

(4)

Small molecule non-peptides

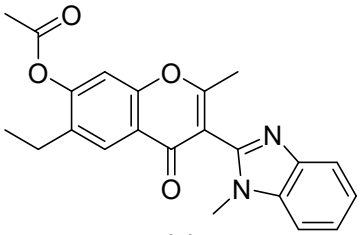

(5)

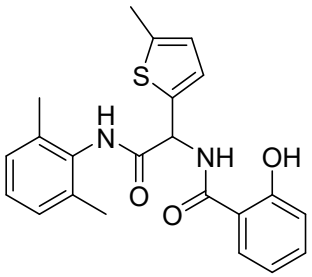

(6)

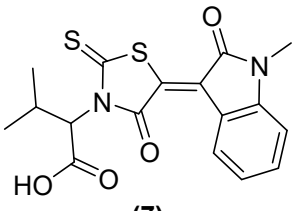

(7)

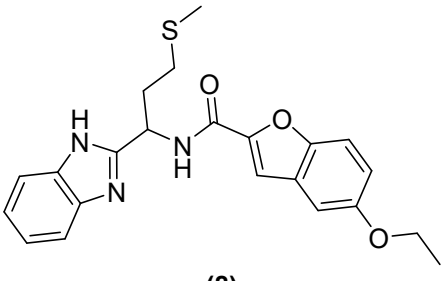

(8)

*Figure 10 A selection of FPR1 antagonists from the literature. **(1)** Cyclosporin A. **(2)** Cyclosporin H. **(3)** t-Boc-MLF. **(4)** i-Boc-MLF. **(5)** 3570-0208. **(6)** A Diamide. **(7)** A Sulphinpyrazone. **(8)** Methionine Benzimidazole. FPR1 antagonist activity can be seen in Table 1.*

Some of the most potent, receptor specific FPR1 antagonists described are the naturally derived hydrophobic peptides, cyclosporine A **(1)** and H **(2)**.[208-210] Cyclosporine A and H were shown to displace [^{3}H]-fMLF in FPR1 transfected rat basophilic leukaemia (RBL) cells with half-maximal inhibitory concentration (IC_{50}) values of 1.8 μM and 100 nM respectively, though did not exhibit inhibitory effects on FPR2 mediated cellular functions.[211, 212]

Table 1 FPR1 antagonist activities of selected compounds fMLF-induced response inhibited in vitro.

	Compound	pIC_{50}	Reference
(1)	Cyclosporin A	6.2[a]	212
(2)	Cyclosporin H	7.0[a]	212
(3)	*t*-Boc-MLF	5.9[b]	205
(4)	*i*-Boc-MLF	6.6[b]	205
(5)	Compound 5 (ICT5100)	5.0[c]	213
(6)	Compound 6	6.4[d]	214
(7)	Compound 7	5.0[c]	206
(8)	Compound 8	6.3[d]	214
(9)	ICT7005 (R = H)	6.4[e]	215
(10)	ICT7009 (R = CH_3)	7.1[e]	215
(11)	ICT12035	8.4[e]	216

[a] Antagonist was evaluated as inhibition of fMLF induced Ca^{2+} mobilization in RBL-hFPR1 cells.
[b] Antagonist was evaluated as inhibition of fMLF-induced superoxide anion release in human neutrophils.
[c] Antagonist was evaluated as inhibition of fMLF induced Ca^{2+} mobilization in U937-hFPR1 cells.
[d] Antagonist was evaluated as inhibition of fMLF induced Ca^{2+} mobilization in human neutrophils.
[e] Antagonist was evaluated as inhibition of fMLF induced Ca^{2+} mobilization in HEK-hFPR1 cells.
(-hFPR1 = transfected with human FPR1)

Chemotaxis inhibitory protein of *Staphylococcus aureus* (CHIPS), a 121-residue (14.1 kDa) naturally derived protein excreted by several strains of *S. aureus*, was reported as an antagonist for FPR1 and the complement component 5a receptor (C5aR). Radiolabelled CHIPS bound to FPR1 had a

reported binding affinity (K_d) of ~ 35 nM indicating direct binding of CHIPS to FPR1 but also inhibited the binding and receptor activation of *N*-formylated peptide agonists.[211, 217]

Another category of antagonist includes analogues of the formylated peptide fMLF. While fMLF is an agonist for FPR1, by replacement of the formyl group with *t*-Boc **(3)**, *i*-Boc **(4)** or a carbobenzoxy (cbz) group, molecules which exhibit antagonist properties for FPR1 were obtained with *i*-Boc-MLF **(4)** being the most potent of the three.[205, 210, 211]

Small molecule non-peptide FPR1 antagonists, both natural and synthetic make up another class of compounds investigated, including but not exhausting flavonoids, isoflavones, coumarins, pyrazoles, and their synthetic derivatives. Chemical structures of selected FPR1 antagonists are shown in Figure 10. Of these, the 4*H*-chromen-4-one 3570-0208 **(5)** (ICT5100), identified by Young *et al*. in a high throughput screen for FPR1 antagonists, was able to abrogate the FPR1/fMLF response with an IC_{50} in the micromolar range and had promise for modification and optimisation.[206, 207]

Another study looking at inflammatory disease and chronic obstructive pulmonary disorder identified a family of pyrazole analogues that demonstrated FPR1 antagonism. The most promising of these molecules identified in the study were ICT7005 **(9)** [215] and ICT7009 **(10)** [215], although following intravenous administration to Sprague-Dawley rats, ICT7009 **(10)** was shown to have a higher plasma clearance than what was previously predicted.[215] Though these compounds would be useful tools for primary investigations, compounds with more robust PKPD profiles and higher efficacy would be required for *in vivo* proof of concept studies. Identified in an

optimisation study of ICT7009 (**10)**, ICT12035 **(11)**[216] was identified and reported to possess a more robust DMPK profile and higher levels of FPR1 inhibition; a more suitable candidate for *in vivo* studies in the effect of antagonism of the FPR1 receptor in the progression on GBM. The structures of ICT7005 **(9)**, ICT7009 **(10)** and ICT12035 **(11)** are shown in Figure 11.

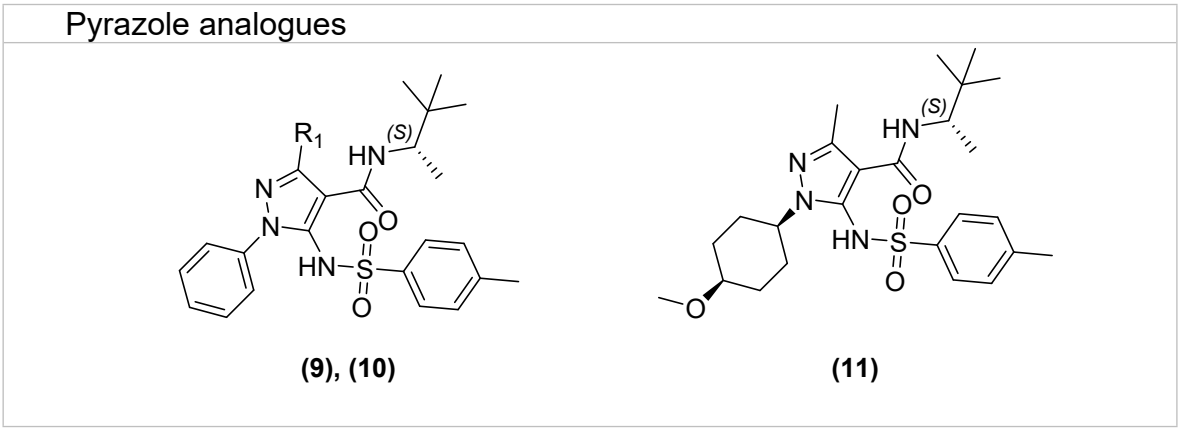

*Figure 11 FPR1 antagonists ICT7005 **(9)**, ICT7009 **(10)** and ICT12035 **(11)** identified from a COPD study.*[215, 216] ***(9)*** *R = H.* ***(10)*** *R = CH_3.*

1.5. Previous work

1.5.1. Identification of FPR1 antagonists from *in silico* high-throughput screening

This section describes work originally carried out by Dr. V. Vinader which was then built upon and optimised as part of this PhD. FPR1 belongs to the GPCR super family. All GPCRs comprise of an extracellular N-terminus followed by seven helical domains in a "serpentine-like" formation enclosed within the cell membrane, and an intracellular C-terminus which binds to a G-protein complex. GPCRs detect/interact with molecules in the extracellular region and activate intracellular signal transduction leading to a cellular response. In Class A GPCRs, to which FPR1 belongs, the principal interactions between receptor and ligand occur within the upper (extracellular) domain of the 7TM receptor. To identify potential antagonists for a protein using molecular modelling software, it is first required to model the desired protein either using X-ray crystallography data of the protein, or by creating a homology model if the crystal data are not available (as is currently the case with FPR1). A homology model takes the protein sequence of the desired protein and searches a database for template protein with a solved crystal structure and with the closest number of residue-matches (homology). The target protein sequence is then constructed onto the known protein structure and any unfavourable interactions between the side chains are minimised using the software. Using this homology model or data from site directed mutagenesis, a specific binding pocket can be located and virtual libraries of "drug-like" molecules docked in this target pocket. From this search a database of virtual "hits" listed in order of scoring functions such as predicted

binding affinity. The most promising of these virtual molecules can be either purchased or synthesised, and then tested *in vitro* to determine the nature of the compound's pharmacological interaction with the receptor protein.

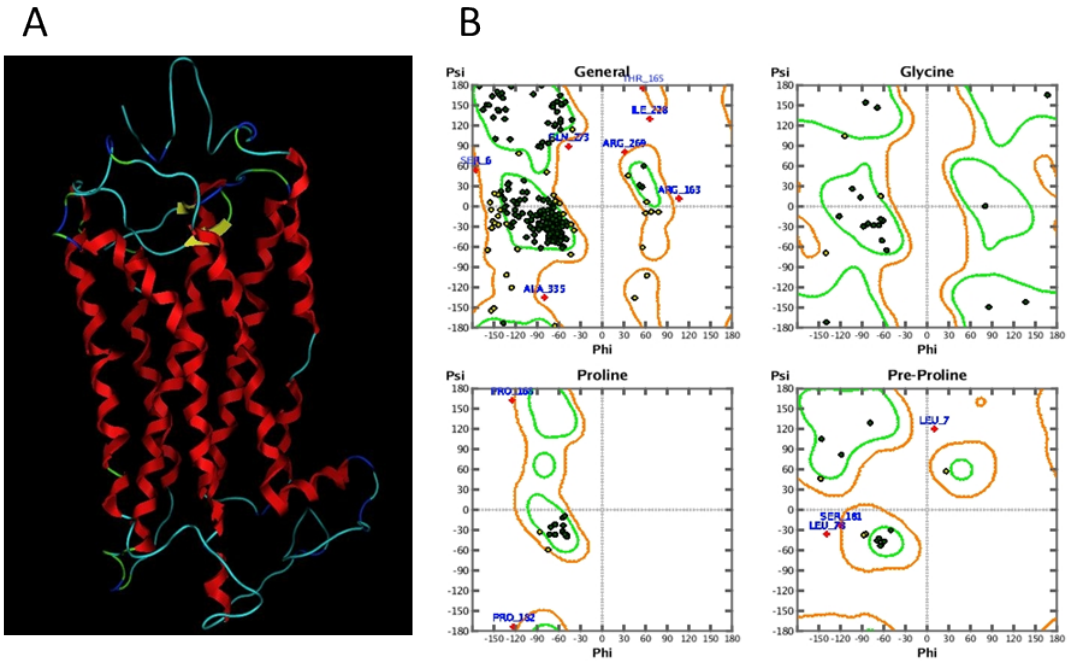

Figure 12 ***(A)*** *The homology model of FPR1 based on the bovine bathorhodopsin receptor 2G87.* ***(B)*** *The Ramachandran plot for the homology model showing all favourable and unfavourable interactions.*

An X-ray crystal structure was not available for FPR1 at the time of writing. Several homology models of the FPR1 receptor were constructed based around a dozen templates that Molecular Operating Environment 2009 (MOE.09) software package identified as having close homology to the FPR1 sequence. The model based on bovine bathorhodopsin (PDB code 2G87) was selected as the best model at the time of this analysis (Figure 12A). The model was checked (Ramachandran plot) (Figure 12B), the conformation modified and globally re-minimised. The process was repeated iteratively until all unfavourable interactions with the 7TM region were neutralised. The key residues within the 7TM of FPR1 responsible for binding to fMLF had been previously identified through site directed mutagenesis studies and the use of

analogues of known formyl peptide agonists. The binding region was defined based on a previous study using site directed mutagenesis to identify the key binding residues for the protein-ligand interaction between FPR1 and fMLF. The residues from the study include Asp-106 and Arg-201, and Arg-205.[171] Additionally, the residues Ile-107, Phe-110, Ala-153, Leu-156 and Thr-157 were included to define the binding pocket for *in silico* screening, all of the additional residues sit adjacent to the mutagenesis study residues (Figure 13).

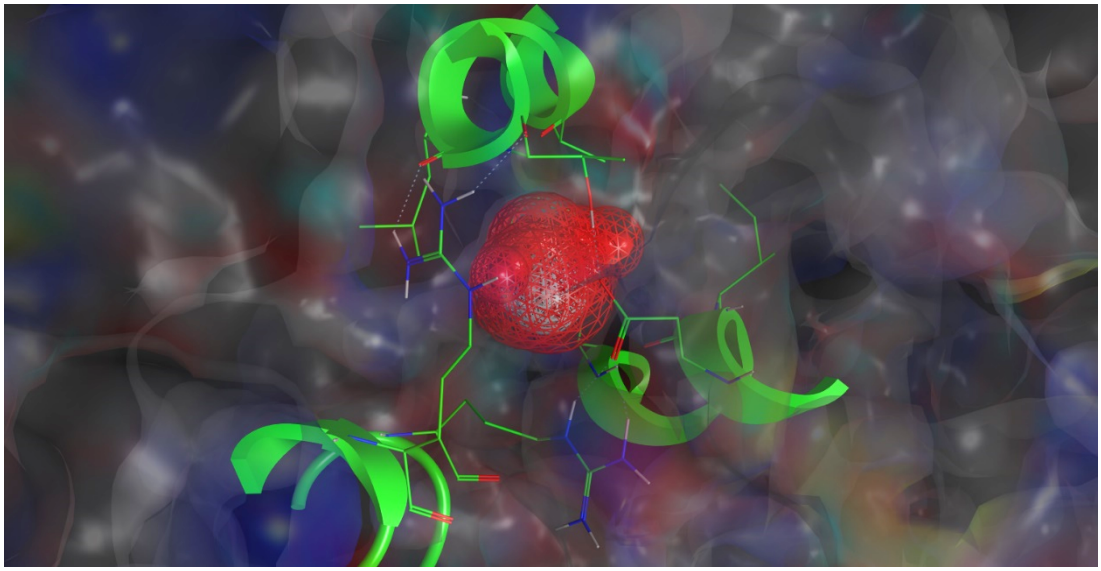

Figure 13 The defined binding pocket within the homology model of FPR1 for the pharmacophore search. (green) selected residues defining the binding site. (red spheres) The calculated binding space as predicted by Molecular Operating Environments Site Finder function.

ICT5100 **(5)** and a selection of other small molecule antagonists were docked within the homology model, the energies minimised, and the best fit identified. Key binding interactions of the antagonist to the receptors were elucidated allowing the identification of structural modifications that may result in an improvement in binding. The predicted *in silico* interactions of ICT5100 **(5)** were shown to correlate with the measured inhibition within *in vitro* functional assays confirming the integrity of the homology model.

A virtual high throughput screen (vHTS) was carried out on libraries of 170,424 “drug-like” molecules, compliant with Lipinski’s rules (molecular weight ≤ 500, ≤ 5 hydrogen-bond donors, ≤ 10 hydrogen-bond acceptors, CLogP ≤ 5) including the Maybridge Screening Collection. The Maybridge Screening Collection library, a collection of over 56,000 highly diverse “hit-like”, “lead-like” and “drug-like” compounds was used as a virtual source of potential antagonists. Several virtual “hits” were identified. A selection of “hits” with the highest predicted binding affinities were selected to be synthesised, to then be tested *in vitro* for their ability to abrogate the cellular response to FPR1 activation. Two molecules, ICT-5093 **(15)** and ICT-5106 **(18)** were selected. Under my supervision and guidance, compounds ICT-5093 **(15)** and ICT-5106 **(18)** were independently synthesised by Mr Faisal Bajwa and Mrs. Shohreh Jafarinejad respectively (Scheme 1, Scheme 2) for further biological evaluation (for data, see Figure 28F).

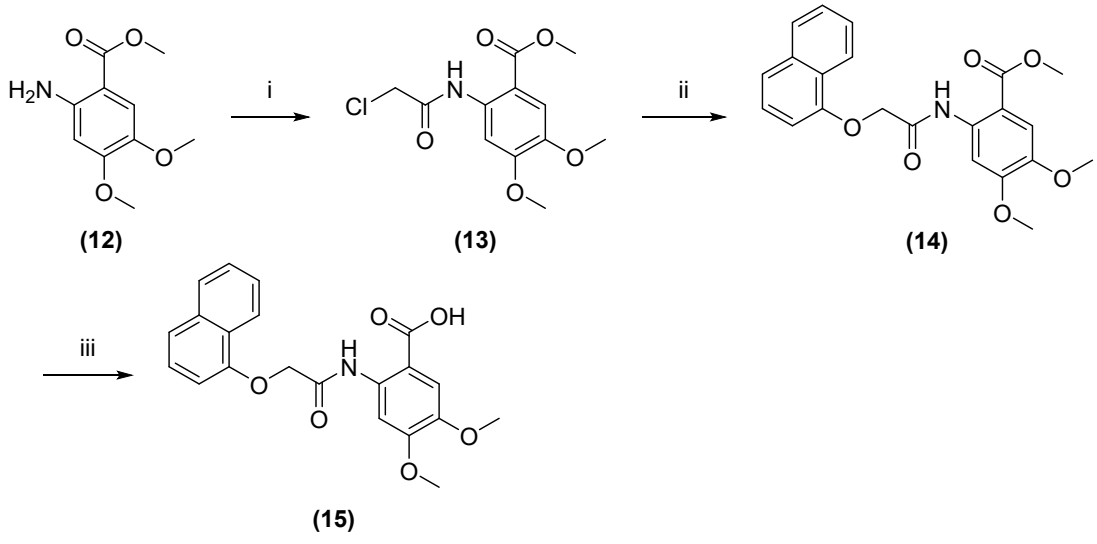

*Scheme 1 Synthetic route for ICT-5093 **(15)**. (i) chloroacetyl chloride, Et_3N, DCM, stir 12h. (ii) 1-napthol, KCO_3, DMF, reflux 80°C 24h. (iii) KOH, THF, rt 24h.*

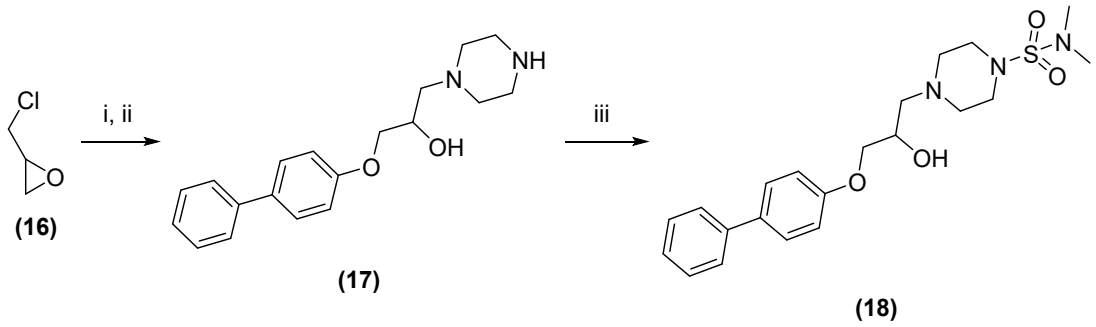

Scheme 2 Synthetic route for ICT-5106 ***(18)****. (i) 4-phenylphenol, $NaHCO_3$, reflux, 15h. (ii) Piperazine (4 eq), EtOH, 50 °C, 2h. (iii) $N(CH_3)_2SO_2Cl$, Et_3N, DMF.*

ICT-5093 **(15)** and ICT-5106 **(18)** both demonstrated an ability to abrogate the fMLF induced FPR1 activation in U-87 MG cells, however, the efficacy of these compounds was lower than compounds previously identified in the literature. These compound classes deserve further investigation through structure activity relationships and have potential for a vast array of structural modifications. However, time on the project was better focused on synthesising and characterising compounds with lower IC_{50} values for the abrogation of FPR1 activation cellular response.

1.6. The Project Aims

The fundamental goal of this project was to demonstrate through preclinical proof of principle that the administration of the FPR1 antagonists identified through this project can retard expansion of glioma *in vivo* suggesting their potential as a new therapy for GBM.

1.6.1. FPR1 antagonist synthesis

In this study, the aim was to synthesise small molecule compounds with selectivity for the inhibition of FPR1 activation in glioma cells. Compounds were identified from the literature, and by *in silico* design. Compounds were synthesised, and then spectroscopically characterised to confirm their structure. The goal was to identify compounds that were able to abrogate FPR1 activation in glioma cells. The compounds were not to be cytotoxic as cells must remain viable for a true indication of FPR1 specific inhibition.

1.6.2. FPR1 antagonist *in vitro* testing

Initially compounds were tested *in vitro* for cytotoxicity using a cell viability assay. If compounds were not cytotoxic, they were then tested *in vitro* for their ability to inhibit FPR1 activation by an FPR1 agonist. To achieve this aim, *in vitro* assays appropriate to GPCRs and adherent glioma cell lines were employed.

Small molecule FPR1 antagonists' performance was based on no/low cytotoxicity, and low IC_{50} values (a lower IC_{50} indicates the compound can inhibit FPR1 at lower concentrations). Compounds with desired inhibition and cytotoxicity were carried forward into *in vitro* metabolism and *in vivo* biodistribution studies.

1.6.3. FPR1 antagonist *in vivo* efficacy

FPR1 antagonists that did not show metabolism and demonstrated appropriate biodistribution were then assessed in an *in vivo* xenografted glioma mouse model. *In vivo* GBM models were administered FPR1 antagonists and tumour growth rate measured.

1.6.4. Investigation a link between FPR1 and the hypoxic/necrotic niche in GBM

Further to the study of FPR1 antagonism, we began to explore the relationship between FPR1 and the hypoxic/necrotic niche in GBM. In this area of the project, expression of FPR1 was explored under hypoxia. The relationship between FPR1 activation and necrotic glioma cells was also investigated in *in vitro* models.

2. CHAPTER 2: Identification and synthesis of small molecule FPR1 antagonists

2.1. Introduction to Chapter 2

In this chapter, the identification and synthesis of several small molecule FPR1 antagonists are described. To evaluate the role of FPR1 in high grade glioma, we required small molecule FPR1 antagonists as chemical tools to evaluate the role and significance of the protein in models of disease progression. The goal was to demonstrate that a small molecule antagonist that blocks the function of FPR1 in high grade glioma, can lead to a therapeutic option for the treatment of this aggressive cancer. At the onset of this investigation, there were only a few known FPR1 antagonists in the literature (Figure 10) with little information on selectivity and very little on FPR1 and its relationship to glioma. The idea of using small molecule antagonists of FPR1 as a therapeutic treatment for high grade glioma was therefore novel. The reasoning behind using small molecules was that the molecule could be modified to be more drug-like with the ability to balance ability to antagonise FPR1, toxicity, and distribution (particularly important for crossing the blood brain barrier, BBB). I identified several series of compounds both known in the literature and identified through our own vHTS screening. Though some of the compounds identified from the literature stated FPR1 antagonism in a desirable range (micromolar to nanomolar IC_{50}), some were not “drug-like” and thus not ideal as a starting point for drug discovery. The following chapter describes the identification and synthesis of the small molecule antagonists used in this project.

2.2. The synthesis of ICT5100 (5)

In the previous section (**1.5.1**), we outlined *de novo* discovery of FPR1 antagonists (Identified by Dr. V. Vinader, and synthesised F. Bajwa, S. Jafarinejad). Although this approach supported the discovery of novel FPR1 antagonist chemotypes which could be drug-like and BBB penetrant (based on software informed predictions), we expected the potency optimisation to be a long process. To be able to develop and validate assays to confirm the potential of FPR1-antagonists as a glioma therapy, existing FPR1 antagonist molecules were investigated.

Young *et al.* in collaboration with the National Institutes of Health Molecular Library Screening Network, implemented a flow cytometry based high throughput screening approach to identify selective small molecule FPR1 and FPR2 ligands.[206, 207] They measured the ability of a library of 24,304 small molecules (from NIH Small Molecule Repository) to displace a fluorescein labelled high affinity peptide ligand of FPR1, FPR2 or both.[206, 207] In this assay, 181 compounds showed >30 % inhibition, of which 34 had selective binding inhibition constants (Ki) ≤ 4 μM for FPR1. A second round of analysis and screening was performed to identify compounds with greater potency. The active compounds from the initial screen were evaluated to identify common structural motifs that correlated with activity. 1,276 compounds were selected through structure-activity-relationship analysis of the initial set of active compounds and the combined library was screened in a single concentration HTS assay; using flow cytometry to measure the compounds competitive binding properties against a high-affinity fluorescent ligand for binding to human FPR1.[207] After several screening steps, the hypothesized chemotype

family structure had been confirmed with all but one of the selected compounds demonstrating selective activity for the FPR1 receptor, the most potent of the compounds identified was the novel small molecule FPR1 antagonist 3570-0208 (ICT5100**, (5)**) (Scheme 3).

The small molecule FPR1 antagonist ICT5100 **(5)** was synthesised for this project and tested for its efficacy in functional FPR1 assays. The literature was sourced for a method to synthesise ICT5100 **(5)** and similar benzimidazole substituted chromone species. A route based on a method previously reported by Frasinyuk for the synthesis of benzimidazole analogue of isoflavones was adopted and modified.[218] ICT5100 **(5)** was synthesised based on this method as outlined in Scheme 3.[218]

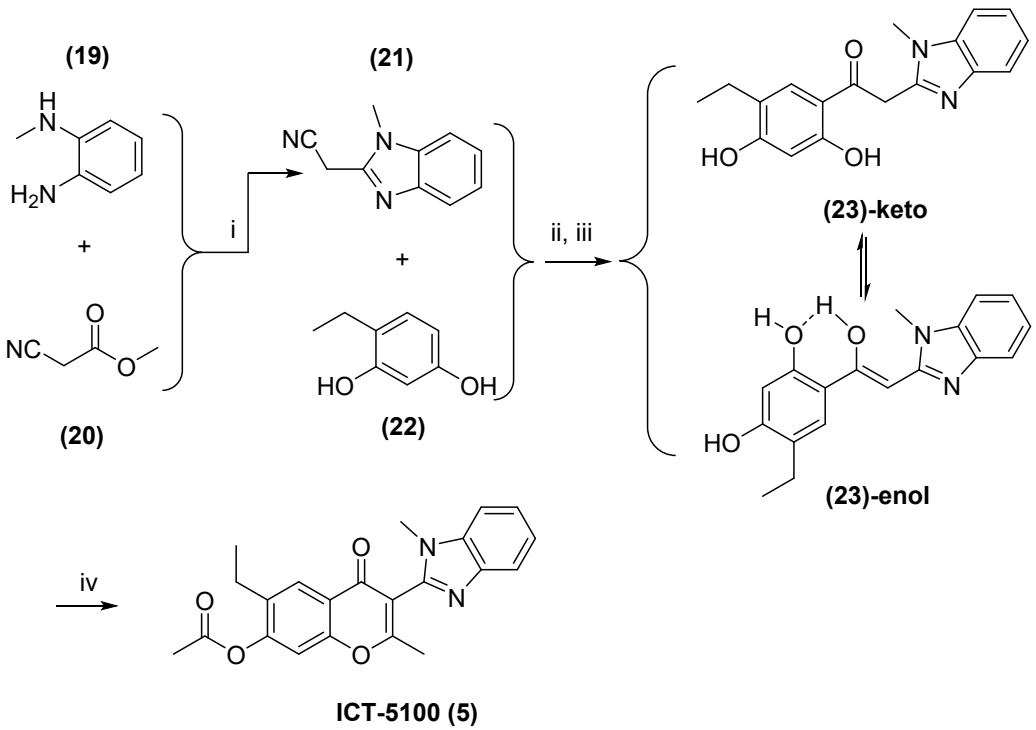

*Scheme 3 Synthetic route for ICT-5100 **(5)** (i) reflux 3h. (ii) $BF_3.OEt_2$, HCl gas, 60 °C, 16h. (iii) H_2O, reflux. (iv) Ac_2O, pyridine, rt, 24h.*

The first step in the synthetic pathway for the preparation of ICT5100 **(5)** was the synthesis of the benzimidazole **(21)**. While the compound was commercially available, in order to obtain substantial quantities required for further steps in the synthesis of this and related analogues, I decided to synthesise the benzimidazole according to the literature method proposed by Mckinnon.[219] The starting compounds *N*[1]-methylbenzene-1,2-diamine **(19)** and methyl cyanoacetate **(20)** were heated under reflux together without solvent. A condensation reaction between the two amino groups and the methyl ester forms the desired benzimidazole **(21)**. Purification by column chromatography afforded the desired benzimidazole **(21)** as a light brown/green solid. NMR analysis shows two singlet peaks at 4.50 and 3.72 ppm that integrate to 2H and 3H which correspond to -C$\underline{H}_2$- and -NC$\underline{H}_3$ respectively. Two sets of multiplets at 7.55 and 7.20 ppm integrating to 4 protons in total correspond to the aromatic protons of the benzene ring. The proton NMR integration correlated with the calculated number of protons in the desired product. The number of carbon signals detected in the carbon NMR also correlated to the calculated number of carbon environments giving evidence to the fact that **(21)** had been synthesised.

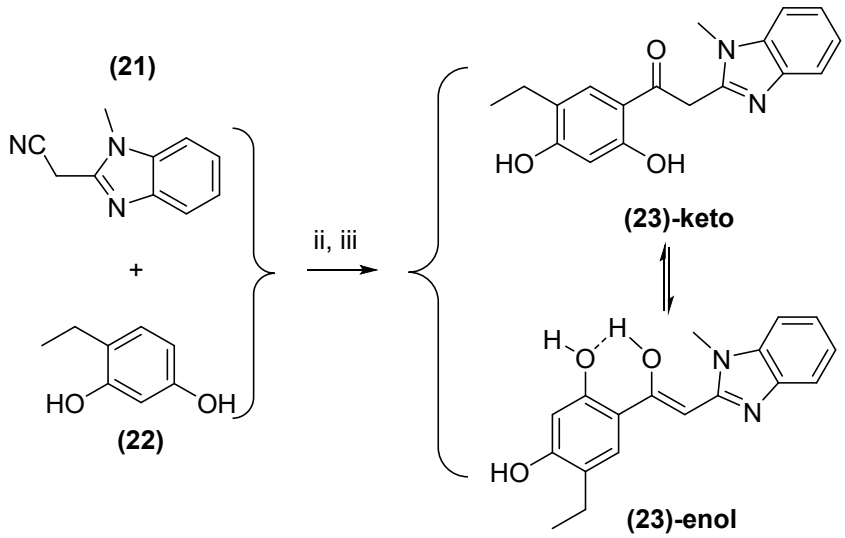

*Scheme 4 Synthesis of compounds **(23)-keto/enol** (i) $BF_3.OEt_2$, HCl gas, 60 °C, 16h. (ii) H_2O, reflux.*

The intermediate compounds **(23)-keto/enol** were made by reacting benzimidazole **(21)** with commercially available 4-ethylresorcinol **(22)** under modified Hoesch reaction conditions (Scheme 4).[218] In a pressure tube, the Lewis acid trifluoroboron etherate was added to **(21)** and **(22)** and hydrogen chloride gas was bubbled through the reaction mixture for a minute before the pressure tube was sealed and heated at 60 °C for 18 hours. After allowing the reaction mixture to cool to room temperature, distilled water was added, and the reaction mixture was heated under reflux for 2 h to ensure complete hydrolysis of the imine intermediate (see mechanism, Scheme 5). Upon cooling, the solution was neutralized, and was filtered and dried to afford the desired product as an off-white solid.

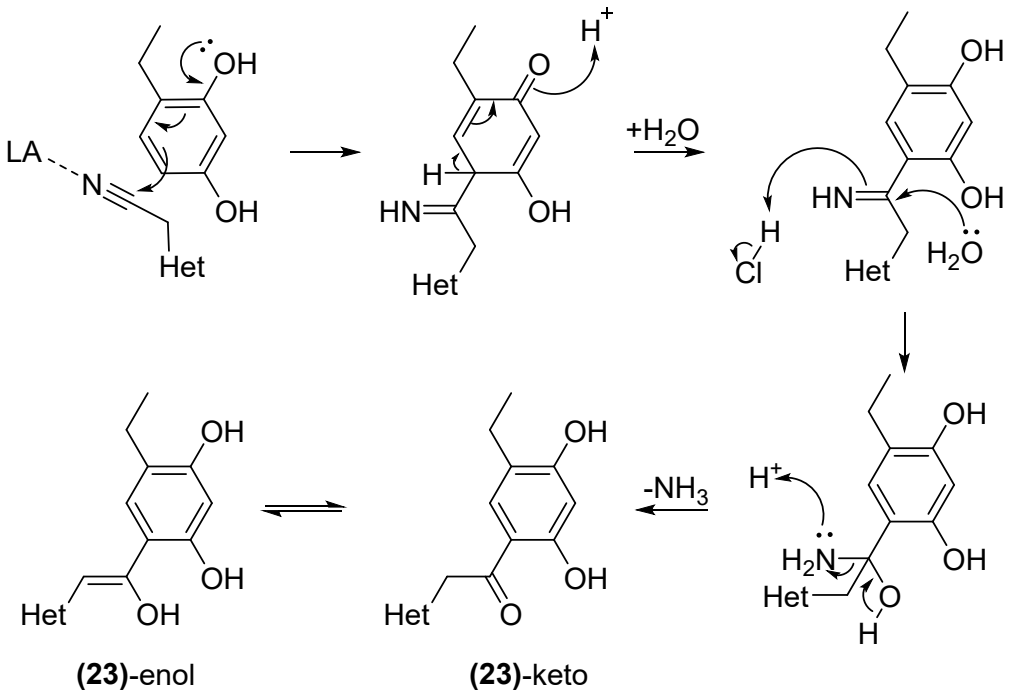

(23)-enol **(23)**-keto

Scheme 5 Modified Hoesch reaction mechanism. LA = Lewis acid, Het = heterocycle

NMR analysis suggests the presence of both -keto and -enol forms in compound **(23)**. The evidence for this tautomerism included the doubling of peaks of the hydroxyl groups (Figure 13). Integral intensity of the aromatic protons of the phenol section of the molecule supports the presence of tautomerism. In deuterated dimethyl sulfoxide, the molecule is enolized by around 85 %, as shown by the ratios of the 4-OH peaks at 10.09 (1H) and 9.97 (0.09H) ppm for the enol and ketone respectively (see Figure 14). This observation of tautomerism was confirmed in the original literature for the synthesis of similar species.[218]

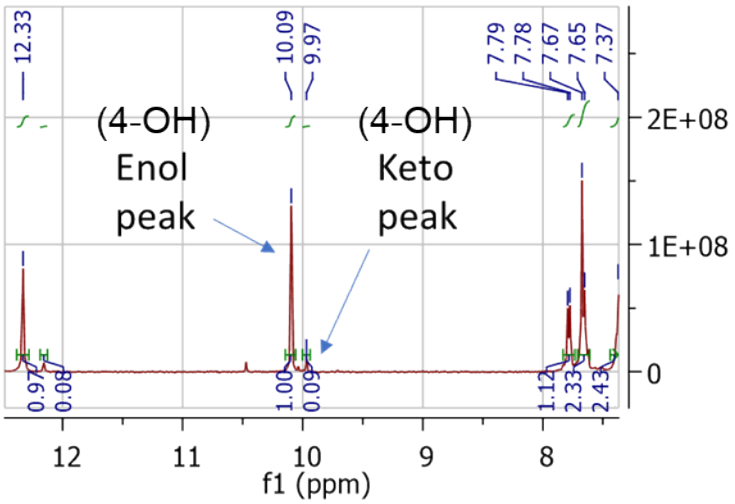

*Figure 14 Expanded section of the proton NMR of **(23)** showing the enol and keto 4-OH peaks.*

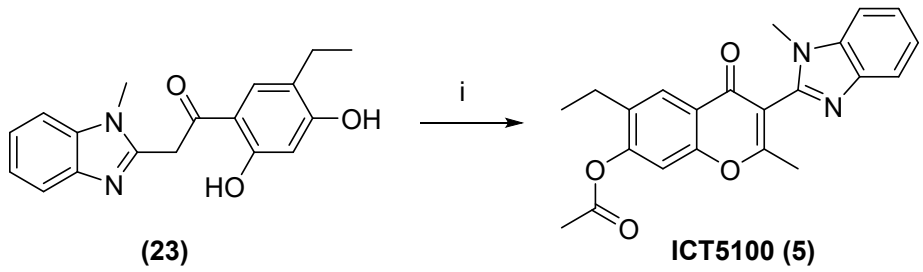

*Scheme 6 The final synthetic step for ICT5100 **(5)**. (i) Ac_2O, pyridine, rt, 24h.*

The final step in the synthesis of ICT5100 **(5)** was to perform a cyclisation of compound **(23)** to form the final chromone structure. To **(23)** in anhydrous pyridine was added acetic anhydride and the mixture was stirred at 40 °C overnight. It was found that it is important that the reagents are particularly dry or the reaction proceeds with only very low yield. After cooling to room temperature, the solution was poured over ice and the solid that had formed was filtered off, washed with water, and dried. Crystallisation from hexane gave compound **(5)** as an off-white solid. From the proton NMR spectrum of the product, we observe a loss of the hydroxyl group proton peaks observed in the proton NMR of compound **(23)** at 10.09 ppm. Further evidence for fact that the chromone **(5)** had been produced results from the proton NMR

spectrum measured in deuterated chloroform, multiplet peaks were found in the range of 7.21-8.05 ppm with an integration of 6 protons corresponding to the aromatic protons of the benzimidazole substituent and the chromone ring. Peaks were also found in the alkyl range a with triplet and a quartet (1.19 ppm, t, 3H; 2.59 ppm, q, 2H, J= 7.5 Hz for both) splitting pattern indicative of the R-CH_2CH_3 group. A peak at 3.59 ppm (s, 3H) corresponds to the -NCH_3 of the benzimidazole group, while the two singlets at 2.32 and 2.39 ppm (both 3H) indicate the protons of the aryl and acyl groups respectively. The carbon NMR spectrum indicates 22 carbon environments present which corresponds to the number of carbons present in the compound. All peaks in the proton and carbon NMR were assigned indicating the desired product was formed and so was carried through for biological assessment.

2.3.1. Analogues of ICT5100 (5)

Using the Chembridge Online Chemical Store (www.hit2lead.com) and the structure of ICT5100 **(5)** as a search parameter, several compounds were identified in the Chembridge screening compound library with similar structural properties to ICT5100 **(5)**. These compounds were purchased in small quantities to screen for biological activity alongside ICT5100 **(5)** with the intention of understanding structure activity relationship for the chromone series.

The SAR of ICT5100 **(5)** was based around modifications to the groups on the 4*H*-chromene-2-one core as depicted in Figure 15. By modification of these sites, the aim was to identify what structural modifications would improve potency and biological stability.

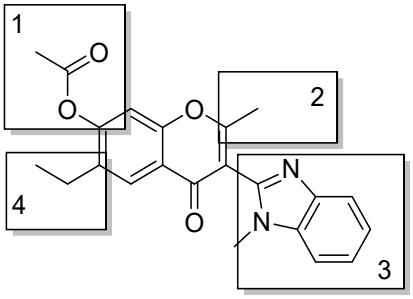

*Figure 15 SAR modification sites of ICT5100 **(5)***

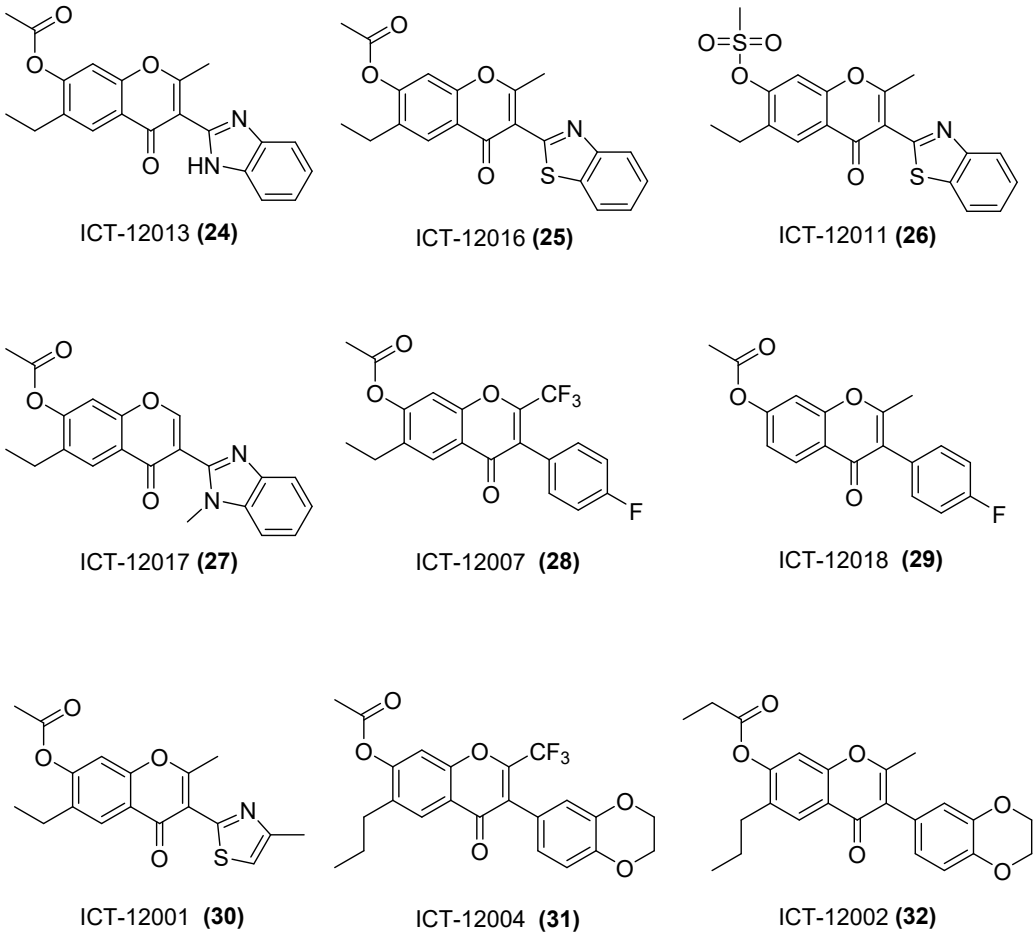

ICT-12013 **(24)**

ICT-12016 **(25)**

ICT-12011 **(26)**

ICT-12017 **(27)**

ICT-12007 **(28)**

ICT-12018 **(29)**

ICT-12001 **(30)**

ICT-12004 **(31)**

ICT-12002 **(32)**

*Figure 16 Chembridge ICT5100 analogues **(24)-(32)**.*

The Chembridge compounds were tested initially at two concentrations in the calcium flux assay (Table 2) on U-87 MG cells in response to fMLF. The compounds tested were selected according to meeting solubility criteria. The compounds should dissolve in dimethyl sulfoxide (DMSO) to achieve a maximum concentration of 10 μM and must remain dissolved when diluted in phosphate buffer solution. Of the compounds purchased, **(24) – (32)** (Figure

16) had the required solubility and were tested at the highest concentrations, between 10-100 μM and a 10-fold dilution for the second dilution between 1-10 μM.

*Table 2 Tabulated data for FPR1 antagonist IC_{50} values for calcium mobilisation assay data for compounds **5** and **24-32**.*

Compound	Antagonist pIC_{50} against fMLF
ICT5100 **(5)**	5.3
ICT12013[a] **(24)**	<4
ICT12016[a] **(25)**	NA
ICT12011[a] **(26)**	<4
ICT12017[a] **(27)**	4-5
ICT12007[a] **(28)**	<4
ICT12018[a] **(29)**	<4
ICT12001[a] **(30)**	<4
ICT12004[a] **(31)**	<4
ICT12002[a] **(32)**	<4

Compounds tested at two concentrations in HTS screen of focused library of ICT5100 analogues. NA – no antagonism or antagonism below the highest soluble concentration.

Of the ICT5100 **(5)** analogues selected from the Chembridge database, only compound **(27)** demonstrated similar antagonism to compound **(5)**. Interestingly, the only modification between **(5)** and **(27)** is the replacement of the methyl group in position 2 (Figure 15) with a hydrogen.

While the ICT5100 SAR investigation was active, a research article was released. The paper extensively investigated the SAR of the 4H-chromone scaffold for the antagonism of FPR1 in FPR1-HL60 cells and human neutrophil

cells.[220] 100 analogues of the 4*H*-chromone **(5)** were included in the study looking at antagonism, binding and selectivity for FPR1 over the other FPR receptors.[220] The stand out compound from the study was “compound 10” **(33)** which demonstrated selectivity for FPR1 and had the highest FPR1 antagonist activity of the study.

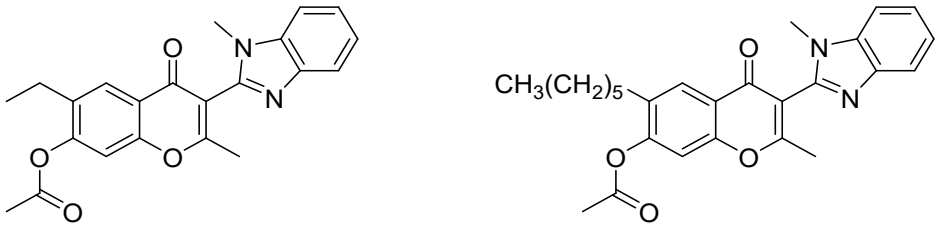

*Figure 17 The structures of ICT5100 **(5)** and "compound 10" **(33)***

From the research article, for the antagonism of FPR1 in HL60(FPR1) cells, **(33)** demonstrated an IC_{50} = 0.31 μM, whereas ICT5100 **(5)** in the same study had an IC_{50} = 1.4 μM.[220] Interestingly, approaching a 10-fold increase in antagonism activity was observed from **(5)** to **(33)** by extending the alkyl side chain. The ability of this compound class to antagonise FPR1 activation has demonstrated potential for further optimisation. However, the focus of this study was shifted towards a class of molecules that have demonstrated greater FPR1 antagonist potential. A class of pyrazole compounds have previously demonstrated FPR1 antagonism with lower IC_{50} values and scope for further structural modification, and so were the next compounds to be investigated.

2.3. The synthesis of pyrazoles ICT7005 (9) and ICT7009 (10)

Morley *et al.* of AstraZeneca released a paper identifying a pyrazole series they had been investigating as potential drug candidates for the treatment of Chronic Obstructive Pulmonary Disorder (COPD) by targeting the FPR1 pathway.[215] Previous compounds investigated by the group, including a benzimidazole and a diamine proved too lipophilic to possess the desired DMPK and physicochemical properties to be of value as a drug candidate for COPD, and so they further pursued the pyrazole series.[214] Through high throughput screening, a series of pyrazoles had been identified and an SAR analysis performed on select compound scaffolds.[214, 215] From the work of Morley *et al.*, several key pyrazole candidates were identified to be used to further investigate the biology of FPR1 in GBM. It was decided to synthesise a selection of the compounds from the study which demonstrated the lowest IC_{50} values for the inhibition of FPR1 activation.

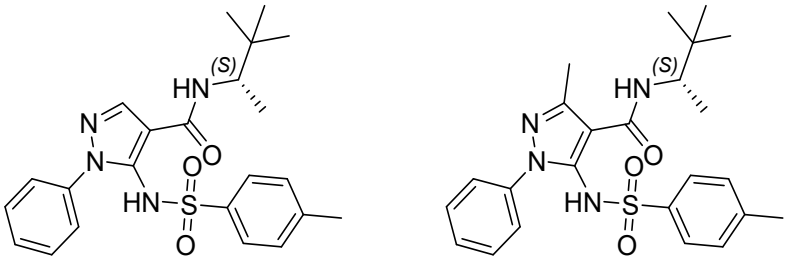

(9) **(10)**

*Figure 18 The structures of ICT7005 **(9)** and ICT7009 **(10)**.*

The first compounds synthesised from the series were **(9)** (ICT7005) and **(10)** (ICT7009) (see Figure 18). Both ICT7005 **(9)** and ICT7009 **(10)** were found to have similar or slightly better FPR1 inhibition compared to ICT5100 **(5)**, but since their synthesis was relatively straight forward, we felt they will be a good starting point for this study. ICT7005 **(9)** is similar in structure to ICT7009 **(10)** but lacks the methyl substituent in the 3-position of the pyrazole

scaffold. Assessment of their relative potency would therefore establish the importance of a methyl substituent in this position. A general synthetic route was adopted for the synthesis of the pyrazole analogues as proposed in Scheme 7.[215]

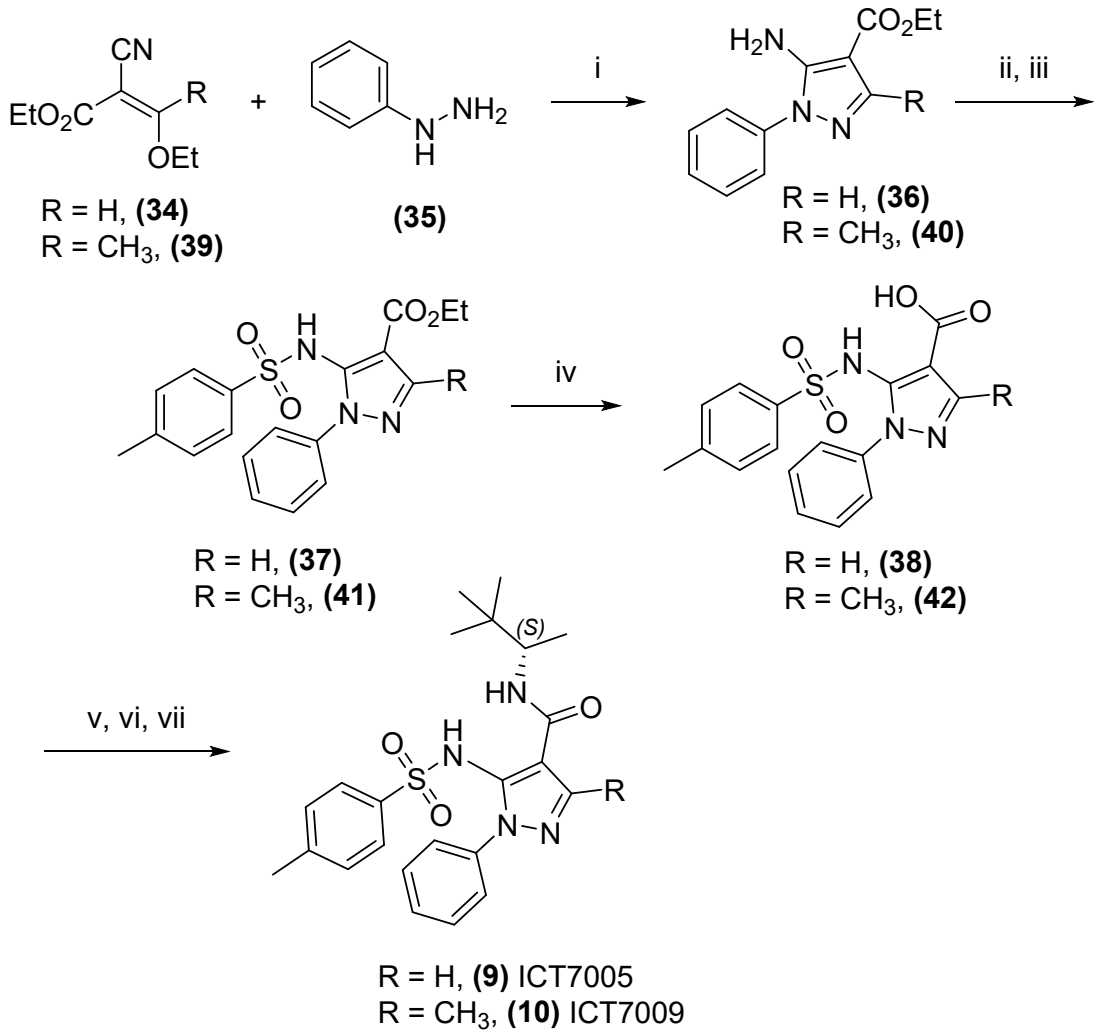

*Scheme 7 A synthetic route for the pyrazole compounds **(9)** and **(10)**. (i) Ethanol, triethylamine, nitrogen atm, reflux 18 h. (ii) 0 °C, anhydrous THF, NaH (iii) tosyl chloride, rt 18 h. (iv) Ethanol, H_2O, $LiOH.H_2O$, reflux 16 h. (v) DMF, diisopropylamine, argon atm, rt, 10 mins. (vi) HATU/HBTU, 20 min. (vii) (s)-3,3-dimethyl-2-butylamine, rt, 16 h.*

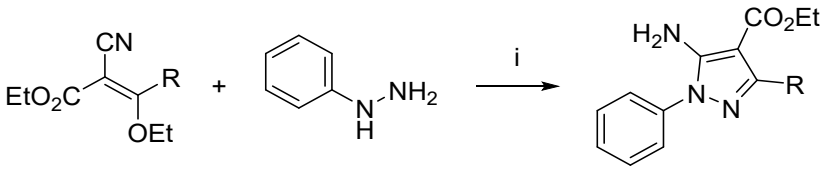

(34) R= H
(39) R= CH_3

(35)

(36) R= H
(40) R= CH3

Scheme 8 The first synthetic step in the synthesis of pyrazoles ICT7005 ***(9)*** *and ICT7009* ***(10)*** *(i) Ethanol, triethylamine, nitrogen atm, reflux 18 h.*

The first step of the synthesis uses the reaction of mono-substituted hydrazines with ethyl-2-cyano-3-ethoxyacrylate **(34)** as observed in Scheme 8, providing the pyrazole without the methyl substituent in the 3-position; or with ethyl-2-cyano-3-ethoxycrotonate **(39)**, giving the pyrazole with a 3-methyl substituent. The condensation reaction was carried out in ethanol under reflux conditions. A proposed mechanism is outlined in Scheme 9.

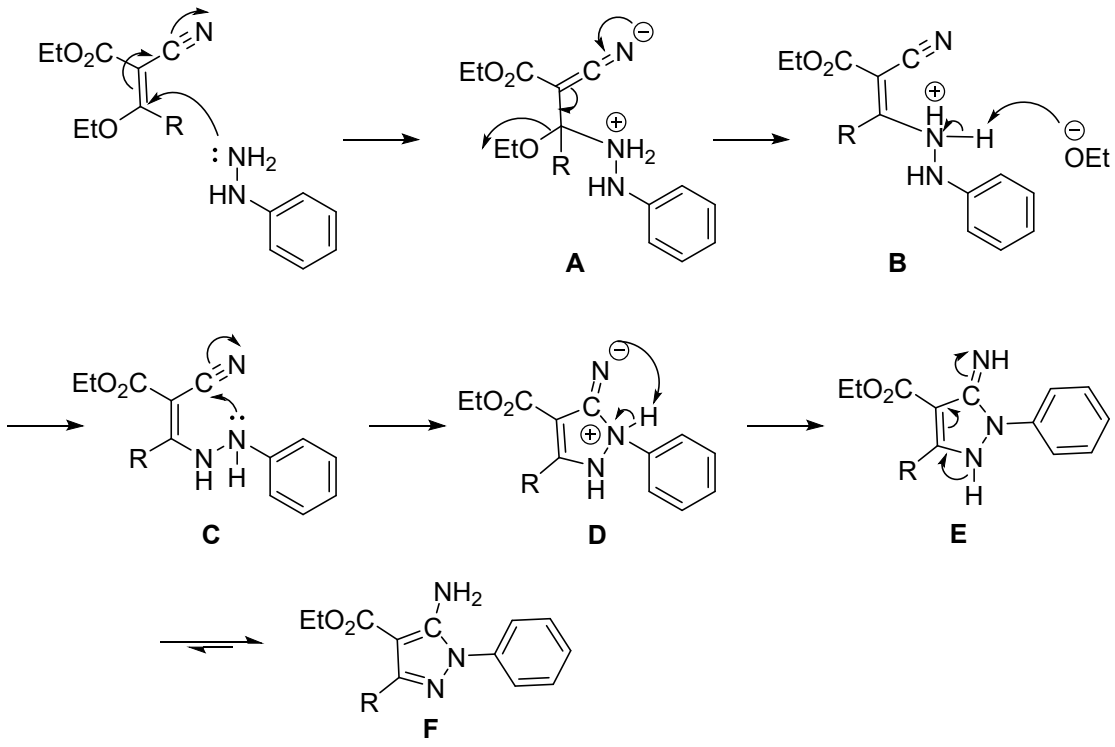

*Scheme 9 A mechanism for formation of the pyrazole ring. Michael addition to ethyl-2-cyano-3-ethoxyacrylate occurs with the lone pair of the -NH_2 in the hydrazine as a nucleophile to form the intermediate **(A)**. Ethanol is lost to form intermediate **(B)**. The ethoxy ion extracts a proton from the ammonium ion to produce intermediate **(C)**. At this point, intermolecular cyclisation occurs through the lone pair of the secondary amine -NH-Ph group attacking the carbon of the cyano group to produce intermediate **(D)**. Migration of the ammonium proton to the imine occurs to form intermediate **(E)**, followed by aromatic driven hydrogen migration to yield the final 5-aminopyrazole **(F)**.*

The final product of the reaction was recrystallised from ethanol to form small white crystals. The structures of the products were confirmed by proton and carbon NMR. From the proton NMR spectrum, the multiplet at 7.50 ppm (4H) corresponds to the *ortho* and *meta* protons of the benzene ring, the multiplet at 7.37 ppm (1H) corresponds to the para positioned proton of the ring. A broadened peak at 5.31 ppm (2H) is indicative of the protons of the amine group. A quartet and triplet at 4.30 ppm (J=7.1Hz, 2H) and 1.37 ppm (J=7.1Hz, 3H) correspond to the ethyl ester group. Additionally, the key difference between compounds ICT7005 **(9)** and ICT7009 **(10)** is the presence of a methyl group on C-3 for compound **(10)**. The peak for the methyl group of **(10)** is observed in the proton NMR as a singlet at 2.41 ppm (3H), while the signal for the heterocyclic proton of **(9)**, because it is aromatic, appears in the

aromatic region as a singlet at 7.78 ppm (1H). The ^{13}C NMR supported this assignment, with peaks corresponding to 10 and 11 magnetically non-equivalent carbons for compounds **(9)** and **(10)** respectively. Due to the symmetry of the benzene ring, 2 less peaks than expected were observed for the *ortho* and meta carbons of the benzene ring, instead, the peaks at 129.9 and 124.0 ppm integrate to 2 carbons each and thus increasing the tally for carbons to 12 and 13 for compounds **(9)** and **(10)** respectively. The assignments were confirmed by HMQC, and COSY NMR experiments and the calculated mass correlated with the high-resolution mass spectrometry results. The compounds were carried through to the next step of the synthesis without further purification.

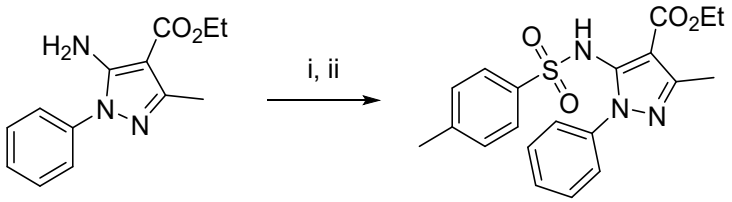

(36) R= H
(40) R= CH_3

(37) R= H
(41) R= CH_3

*Scheme 10 Tosylation of the amine of **(36)/(40)** to form compound **(37)/(41).** (i) 0 °C, anhydrous THF, NaH (ii) tosyl chloride, rt 18 h.*

The next step in the synthesis was the tosylation of the 5-aminopyrazole to form the subsequent sulphonamide via a nucleophilic substitution with tosyl chloride (Scheme 10). In the initial attempts to synthesise the desired compounds, to a solution of **(36)/(40)** in anhydrous pyridine as the solvent and base, added tosyl chloride under nitrogen and the reaction was heated at 100 °C for 24h. However, analysis of the reaction mixture showed that large amounts of starting material remained whilst the tosyl chloride had been depleted. Additional portions of tosyl chloride were added as well as 4-dimethylaminopyridine (as a nucleophilic catalyst) in attempt to drive the

reaction forward. On work up and purification only low yields of the desired product were isolated. As this step was early in the synthetic pathway to the final desired compound, higher yields were required to take enough material through to subsequent steps. An alternate method was planned using sodium hydride as a stronger base with the hope for a higher yielding and cleaner reaction (Scheme 11).

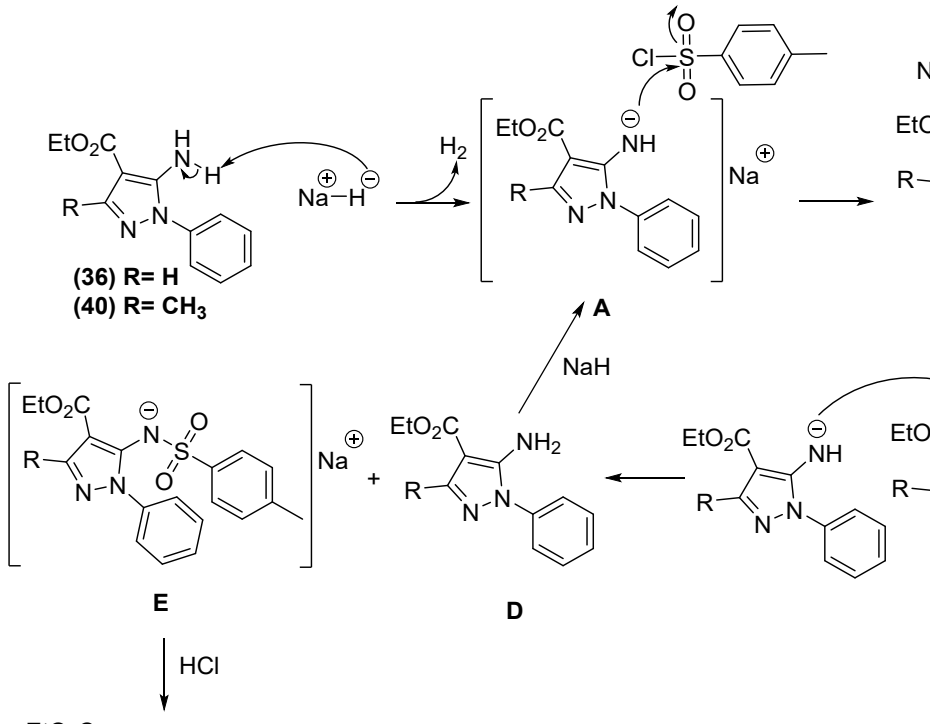

*Scheme 11 Mechanism for the amine tosylation using sodium hydride as the base. The 5-aminopyrazole **(36)/(40)** from the previous step was added to a suspension of sodium hydride in anhydrous THF, an evolution of gas from the reaction mixture indicated that the hydride had deprotonated the amine group to produce the salt intermediate **(A)**. On addition of the tosyl chloride to the reaction mixture, the sulphur of the tosyl undergoes nucleophilic attack from the nitrogen anion to form intermediate **(B),** and subsequently, elimination of sodium chloride, formed the desired product **(C)**. However, the NH of the sulphonamide product is more acidic than the NH_2 of the starting material. As a result, pyrazole **(A)** would accept a proton from **(C)** to reform the starting pyrazole **(D)** and the sulphonamide salt **(E)**. An additional portion of sodium hydride regenerates product **(A)** from **(D)**. An acidic/aqueous workup of product **(E)** produces the desired product **(F)**.*

The amine tosylation step required two equivalents of sodium hydride. This is because the sulphonamide product has an -NH- group which is more acidic than the $-NH_2$ of the starting material. As the reaction proceeds, any pyrazole-NH^- from the starting material would take a proton from the pyrazole-$NHSO_2Ar$ to regenerate the pyrazole-NH_2 starting material and [Pyrazole-$NSO_2Ar]^-Na^+$. To ensure the reaction goes to completion, the reaction would require 2 equivalents of sodium hydride to allow the regeneration of the pyrazole-NH^- intermediate. After an acidic-aqueous work up of the reaction, the [Pyrazole-$NSO_2Ar]^-Na^+$ is converted back to the desired Pyrazole-$NHSO_2Ar$. The product of the reaction was purified by flash chromatography to afford an orange solid. Proton and carbon NMR were used to confirm the desired product had been obtained.

As with the previous step of the experiment, similar peaks were observed in the proton and carbon NMR spectrum. A quartet (4.05 ppm, 2H) and triplet (1.23 ppm, 3H) indicate the alkyl group of the ester. For compound **(37)**, the aromatic proton of the pyrazole can be located as a singlet at 7.89 ppm, while a singlet at 2.40 ppm integrating to 3 protons corresponds to the methyl attached to the pyrazole for compound **(41)**. The introduction of the tosyl group to the molecule brings in new signals to the proton NMR spectrum in the aromatic region, and thus, to better assign the NMR data, 2D NMR experiments were used to identify ^1H-^1H and ^1H-^{13}C coupling signals.

A peak at 2.39/2.38 ppm for **(37)/(41)** respectively indicates the methyl- of the tosyl group. COSY NMR data for compound **(37)** indicates coupling signals between the tosyl methyl peak and the aromatic proton multiplet peaks at 7.17 (2H) and 7.43 (5H) ppm indicating the remaining 4 protons of the tosyl

aromatic ring. Coupling signals can also be observed between the multiplet peaks at 7.65 (3H) and 7.43 (5H) indicating overlapping peak signals for the aromatic protons These peaks indicate the phenyl aromatic protons. The integration leaves one proton unaccounted for. For compound **(37)**, the proton NMR spectrum reveals a singlet signal at 7.89 ppm (1H) which also demonstrates coupling to a carbon in the ^{1}H-^{13}C HMQC NMR, indicating the aromatic proton of the pyrazole. The remaining proton within the aromatic region would indicate the proton of the sulphonamide.

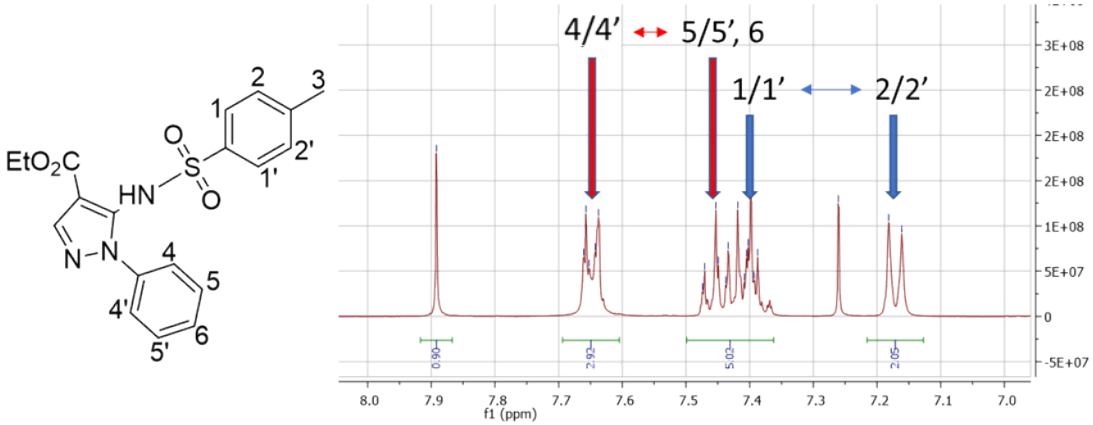

*Figure 19 Proton NMR expansion of the aromatic region for compound **(37)** indicating peak signal coupling (derived from 2D COSY spectrum).*

For compound **(41)** however, the proton signal at 7.79 ppm does not correlate to a carbon in the ^{1}H-^{13}C HMQC NMR indicating that this signal corresponds to the proton of the sulphonamide. From the previous step, the broadened peak around 5.31 ppm (2H) indicating the amine had disappeared from the spectrum of the new compound suggesting further evidence for the fact the desired product has been formed. Overall, the proton NMR spectrum integrates to 19H and 21H for **(37)** and **(41)** respectively. The carbon NMR spectra gave signals indicating 15 and 17 non-magnetically equivalent carbon atoms which corresponds to the predicted numbers for **(37)** and **(41)** respectively. The mass spectrometry data gave m/z $[M+H]^{+}$ **(37)** = 386.1170

and **(41)** = 400.1322 which correlates to the calculated $[M+H]^+$ of the desired compounds.

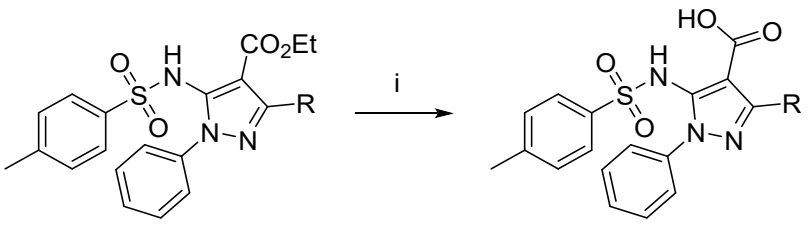

(37) R= H
(41) R= CH_3

(38) R= H
(42) R= CH_3

*Scheme 12 The base catalysed hydrolysis of compounds **(37)** and **(41)** to produce **(38)** and **(42)** respectively. (i) Ethanol, H_2O, $LiOH.H_2O$, reflux 16 h.*

The next step in the synthesis was the hydrolysis of the ester group to a carboxylic acid (Scheme 12). The reaction proceeded via a base catalysed ester hydrolysis employing aqueous lithium hydroxide. The product of the previous step **(37)/(41)** dissolved in ethanol was added to a solution of lithium hydroxide monohydrate (excess) in distilled water and heated under reflux for 16 hours. The suggested mechanism for the base catalysed hydrolysis can be observed in Scheme 13**.**

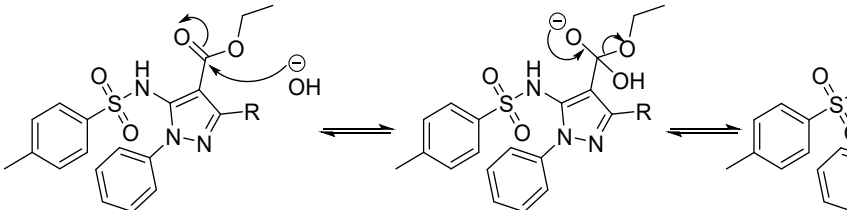

*Scheme 13 Mechanism for the base catalysed ester hydrolysis of **(37)/(41)**. The process is started by the attack of the nucleophile hydroxide ion on the electrophilic carbon of the ester, forming a new σ-bond between the carbon and hydroxide and subsequently breaking the π-bond of the carbonyl to form the intermediate **(A)**. The negative charge of the oxygen will then move back to reform the π-bond (energetically more favourable state) and the -OEthyl anion leaving group to form the desired compound intermediate **(B)**. Each step of the reaction is reversible, however, the equilibrium is driven towards forming desired compound because under basic conditions, once the ester has been hydrolysed to the carboxylic acid any remaining anions either $[OEthyl]^-$ or $[OH]^-$ can deprotonate the acid to generate the carboxylate intermediates **(C)/(D)** which are no longer reactive. By neutralising the reaction mixture with aqueous acid, the carboxylic acid is regenerated to give the desired product **(E)**.*

Analysis of the proton NMR spectrum run in deuterated methanol through comparison to the starting material shows a loss of the ethyl ester proton signals. The number of carbon signals correlated to the predicted number of non-magnetically equivalent carbon atoms for both compounds. The mass spectrometry data m/z $[M+H]^+$ **(38)** = 358.0857 and **(42)** = 372.1013 correlates to the calculated $[M+H]^+$ value supporting the evidence that the product had been synthesised.

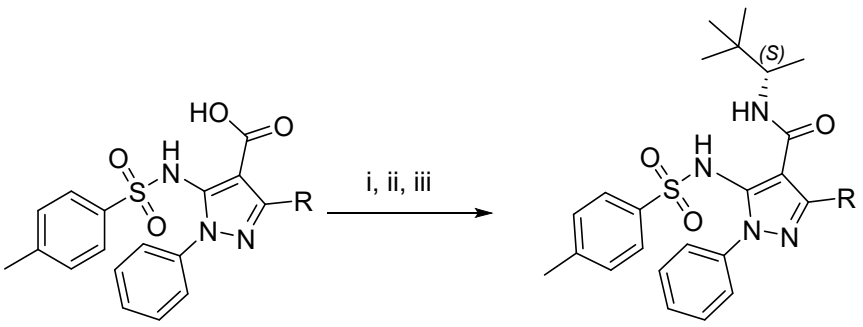

(38) R= H
(42) R= CH_3

(9) R= H
(10) R= CH_3

*Scheme 14 Formation of the amides **(9)** and **(10)** under peptide coupling conditions. (i) DMF, diisopropylamine, argon atm, rt, 10 mins. (ii) HATU/HBTU, 20 min. (iii) (s)-3,3-dimethyl-2-butylamine, rt, 16 h.*

The final step in the synthesis of the pyrazole compounds was to convert the carboxylic acid group to the corresponding amide under peptide coupling conditions (Scheme 14). The reagents used for the coupling were HATU and Hunigs base (DIPEA) and the chiral amine (*S*)-3,3-dimethyl-2-butylamine. The (*S*) configuration of the final compound was noted to have greater antagonism of the FPR1 receptor over the (*R*) isomer.[215] To a solution of the pyrazole was added Hunig's base followed by HATU and then (*S*)-3,3-dimethyl-2-butylamine and stirred at room temperature for 16h. HATU exists as two isomers, the uronium salt and the guanidinium salt, the suggested mechanism for the coupling using the uronium salt is displayed in Scheme 15.[221, 222]

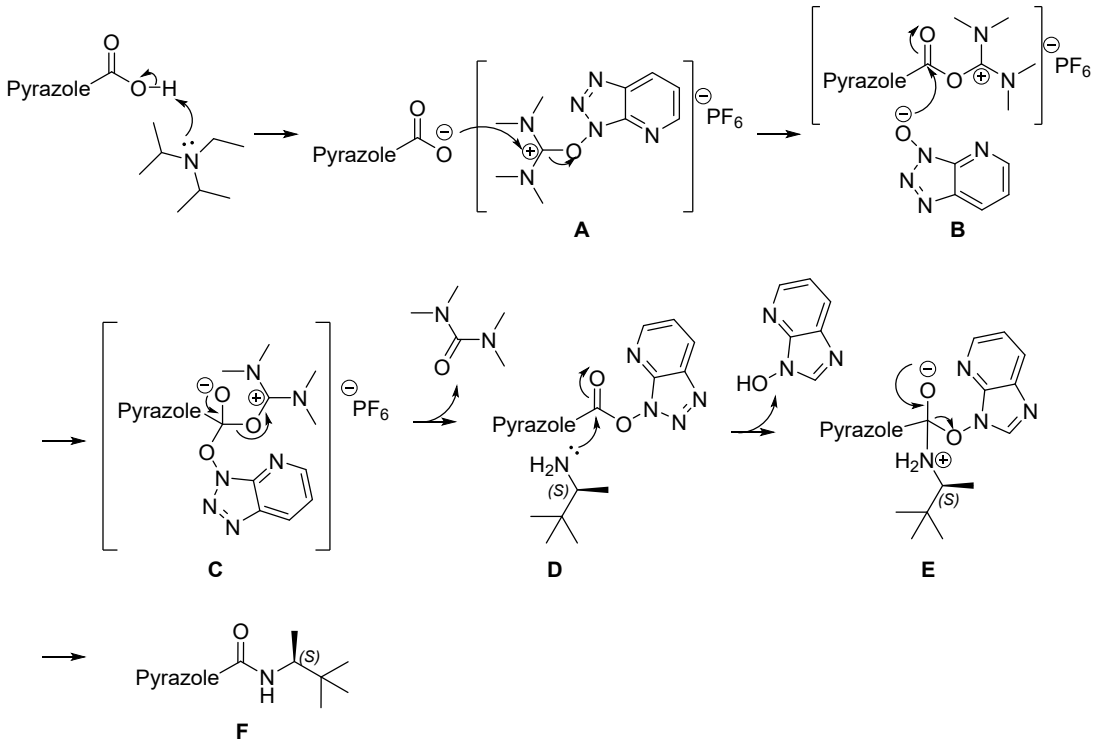

*Scheme 15 Formation of the amide under peptide coupling conditions using HATU and Hunig's base. Initially, the carboxylic acid is deprotonated by attack of the lone pair of Hunig's Base to form intermediate **(A)**. The carboxylate anion proceeds to attack HATU to form the O-acyl(tetramethyl) isouronium salt **(B)** while eliminating an OAt anion. The OAt anion attacks the C=O group of the isouronium salt to form the OAt-active ester intermediate **(C)** followed by the elimination of tetramethylurea to form intermediate **(D)**. On adding (S)-3,3-dimethyl-2-butylamine as the nucleophile, the lone pair of the nitrogen attacks the C=O of intermediate **(D)** and to form intermediate **(E)**, the subsequent loss of the HOAt leaving group leads to the formation of the desired acylated product **(F)**.*

The reaction mixture was quenched with water, and the pH adjusted to 1 with aqueous hydrochloric acid, following solvent extraction, the compound was purified by flash chromatography with an ethyl acetate/petroleum solvent system. The reaction yielded a white compound with around 95 % yield, the assignment of final product was confirmed by NMR and mass spectrometry and sent for biological evaluation.

The proton NMR confirmed the desired compounds had been synthesised, peaks were observed that are concurrent with the groups carried over from the intermediate starting material. The proton signal at 8.79 ppm (1H) corresponds to the -NH of the sulphonamide. The peaks at 7.30 and 6.98 ppm (2H each) correspond to the aromatic protons of the tosyl group while the remaining

peaks in the aromatic region 7.36 (2H) and 7.28-7.17 (3H) correspond to the aromatic protons of the N-Benzene group. The doublet at 5.99 ppm (1H) in the proton NMR does not correlate to a carbon atom in the HMQC spectrum, suggesting along with the chemical shift that the proton is bound to another heteroatom, in this case, the nitrogen of the amide. The signal at 3.79 ppm (1H, J = 9.5, 6.9 Hz) is a doublet of quartets, indicating that this proton signal originates from the proton adjacent the amide; the splitting pattern due to the proton's vicinity to the single amide proton and the 3 protons of the adjacent methyl group of which gives an adjacent doublet peak at 0.95 ppm (3H, J = 6.8 Hz). The remaining peaks, two singlets at 2.38 (3H) and 2.26 (3H) correspond to the methyl groups of the pyrazole and the tosyl group respectively, while the singlet at 0.80 ppm (9H) accounts for the remaining 9 protons of the t-butyl group. From the carbon NMR, 17 and 18 carbon signals were detected correlating to the predicted number of non-magnetically equivalent carbon atoms for both **(9)** and **(10)** respectively. The mass spectrometry data m/z $[M+H]^+$ **(9)** = 441.1946 and **(10)** = 455.2107 correlates to the calculated $[M+H]^+$ value supporting the evidence that the products had been synthesised.

2.4. The synthesis of pyrazoles ICT12028 (60) and ICT12035 (11)

As the biological characterisation progressed with ICT7005/9, further work was released by Morley *et al.* focusing on FPR1 for inflammatory disease.[216]

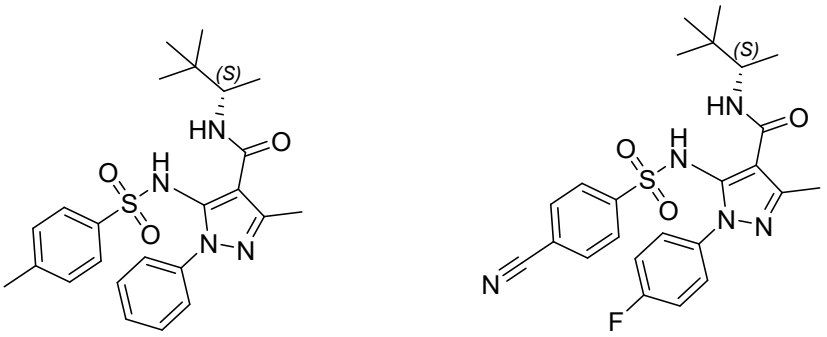

(10) **(43)**

*Figure 20 The chemical structures of compounds **(10)** and **(43)**.*

Continuing from their previous work on compounds targeting the FPR1 receptor with a focus on the innate immune response and COPD, Morley *et al.* explored further the lead discovery and optimisation of pyrazole analogues.[215, 216] Morley *et al.* carried through the compounds **(10)** and **(43)** (Figure 20) as the most promising lead candidates and investigated the *in vivo* PK parameters in rat.[216] From this base, a SAR investigation to the discovery of pyrazoles **(11)** and **(44)** (Figure 21).

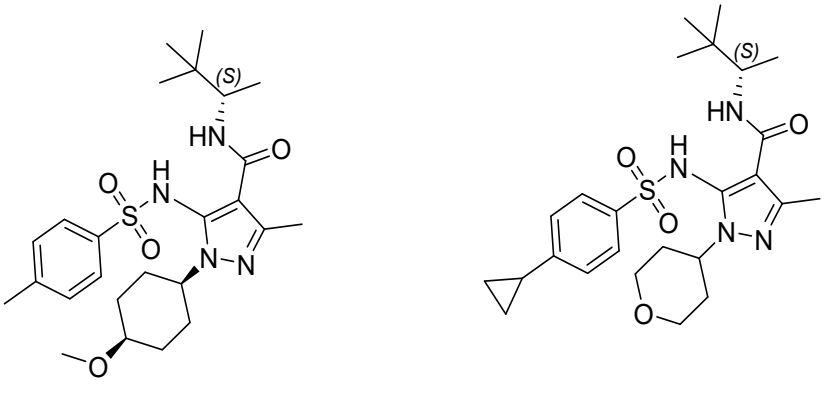

(11) **(44)**

*Figure 21 The chemical structures of compounds **(11)** and **(44)**.*

Compound **(11)** (ICT12035) had a reported FPR1 IC_{50} of 4 nM (pIC_{50} = 8.4) whereas **(44)** had a reported IC_{50} of 158 nM (pIC_{50} = 6.8).[216] ICT12035 **(11)**

had a lower IC_{50} value compared to compound **(44)** and so was selected to be synthesised as a tool compound to be used to further investigate the therapeutic benefits of antagonising the FPR1 receptor in high-grade glioma.

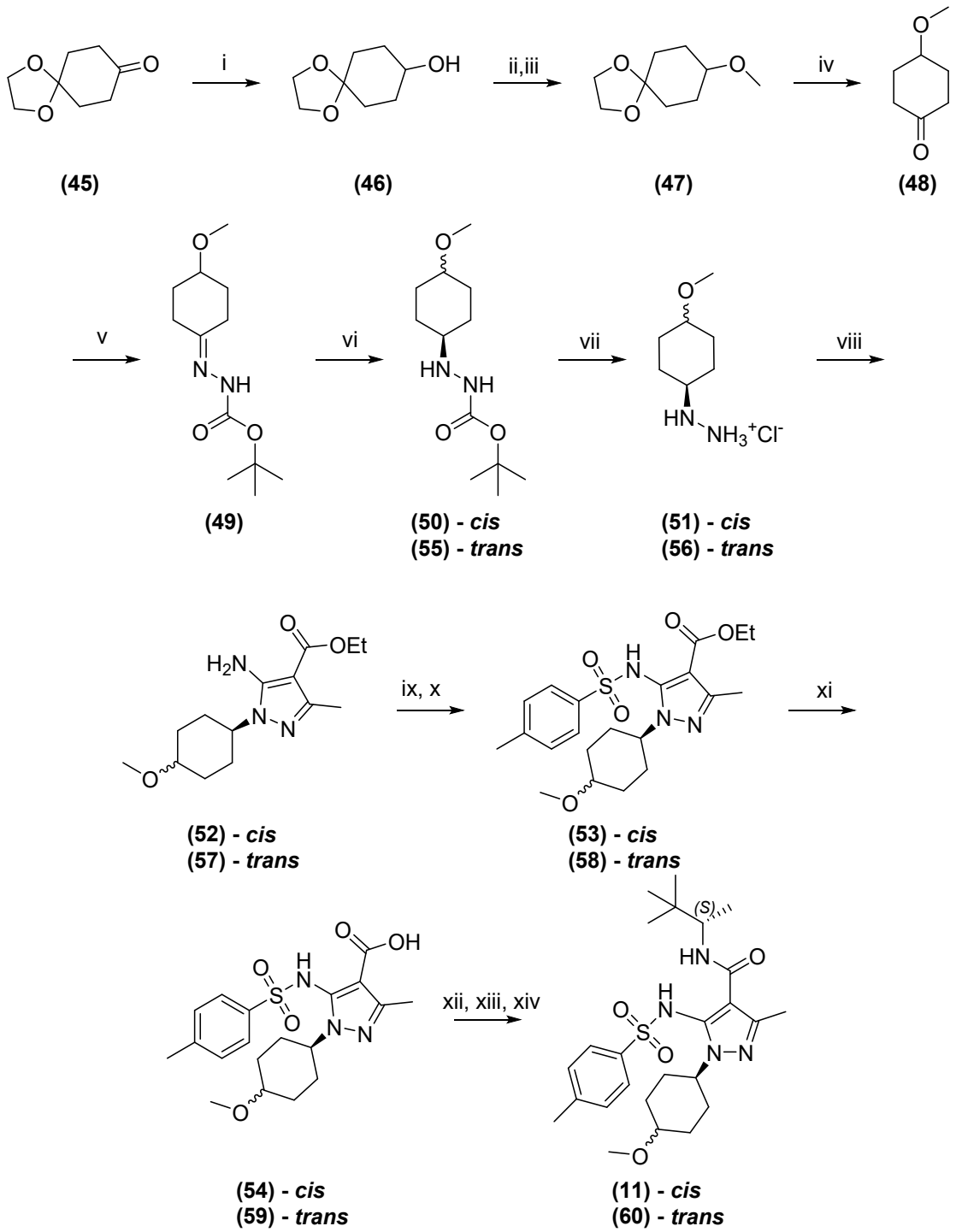

Scheme 16 The full synthetic pathway for ICT12035 ***(11)*** *and ICT12028* ***(60)****. (i) $NaBH_4$, ethanol, nitrogen atm, rt, 24 h. (ii) NaH, THF, 0 °C - rt, 0.5 h. (iii) MeI, rt, 24 h. (iv) THF, HCl (5M), rt, 16 h. (v) MeOH, tert-*butyl carbazate*, rt, 2 h. (vi) Acetic acid, H_2O, $NaBH_3CN$, rt, 16 h. (vii) Dioxane, HCl (5M), rt, 1 h. (viii) Ethanol, triethylamine, ethyl-2-cyano-3-ethoxycrotonate, nitrogen atm, reflux 18 h. (ix) 0 °C, anhydrous THF, NaH (x) tosyl chloride, rt 18 h. (xi) Ethanol, H_2O, $LiOH.H_2O$, reflux 16 h. (xii) DMF, diisopropylamine, argon atm, rt, 10 mins. (xiii) HATU/HBTU, 20 min. (xiv) (s)-3,3-dimethyl-2-butylamine, rt, 16 h.*

ICT12035 **(11)** was the *cis*-diastereoisomer, the decision was made to synthesise both diastereoisomers to allow investigation of the biological properties between the two compounds. Morley *et al.* included the *trans*-diastereoisomer **(60)** in their study, however, under the conditions of their experiments the diastereoisomer was deemed inactive, this claim was to be investigated.[216] The first step was to synthesise the mono-substituted hydrazine **(51)/(56)** as proposed in Scheme 16. Followed by the reaction of the hydrazine with ethyl (E)-2-cyano-3-ethoxycrotonate to form the pyrazole **(52)/(57)** and the subsequent steps towards the final compounds **(11)/(60)**. The full synthetic pathway is proposed in Scheme 16. It was expected under the reaction conditions proposed, during step vi, both diastereoisomer hydrazines would be synthesised. From this point, the reactions would be carried out in parallel towards the final products.

According to the synthetic route proposed in Scheme 16, the first step was to reduce commercially available 1,4-dioxaspiro[4,5]decan-8-one **(45)** to the corresponding alcohol **(46)**. The mild reducing agent sodium borohydride was used with ethanol as the protic solvent. On addition of sodium borohydride to **(45)**, a hydride ion attacks the carbon of the carbonyl shifting the charge towards oxygen of the carbonyl. The lone pair of the oxygen proceeds to extract a hydrogen from ethanol forming the alcohol product. Sodium borohydride was used in a slight excess to accommodate for the degradation of the reducing agent, the reaction was stirred for 24 h under nitrogen to reduce atmospheric moisture and decrease degradation. The reaction solvent was removed under reduced pressure to afford a cloudy oil, the oil was

dissolved in dichloromethane and sodium hydroxide solution (2M) added to neutralise the reaction mixture. The organic phase was collected and dried over magnesium sulphate and the solvent removed to afford the product as a clear oil.

The proton NMR spectrum confirmed the desired compound had been synthesised, peaks were observed in the shift regions concurrent with the proton environments of the desired compound. Due to symmetry in the molecule, we observe less peaks to the number of proton groups on the molecule, where there are 8 groups of protons, we only observe 5 different proton environments, this is subsequently reflected in the integration of the peaks in the proton NMR spectrum with a total integration of 14H which equates to the desired number of protons. The multiplet at 3.91 ppm (4H) is indicative of the 1,3-dioxolane protecting group, the peak integrates to 4 protons and the COSY NMR experiment indicates no coupling to another proton environment. Multiplet peaks in the ranges of 1.96 – 1.73 (4H) and 1.71 – 1.51 (4H) correlate to the protons of the cyclohexane. Two peaks are observed with an integration of one proton each, a split peak at 3.78 ppm and a broad peak at 1.42 ppm, these would equate to the proton adjacent the alcohol group and the proton of the alcohol group. To decipher the assignment between the two, COSY and HMQC experiments were utilised, the split peak at 3.78 ppm (1H) demonstrates coupling to the protons of the cyclohexane in the COSY NMR spectrum while also demonstrating coupling in the HMQC ^{1}H-^{13}C experiment. The broad peak at 1.42 ppm (1H) demonstrates no coupling in both COSY and HMQC experiments. This information confirms the assignment of the peak at 3.78 ppm to the proton of the cyclohexane adjacent

to the alcohol group while the peak at 1.42 ppm corresponds to the proton of the alcohol group. The carbon NMR further supports the confirmation the desired product had been synthesised, we observe the expected 5 carbon peaks indicative of the 5 carbon non-magnetically equivalent carbon atoms observed in the desired molecule. The compound was carried through to the next step of the synthesis without further purification.

The next step in the synthesis was the methylation of the alcohol group of **(46)** to form **(47)**. Sodium hydride was used as a strong hydride donor. On addition of sodium hydride to the intermediate alcohol **(46)** dissolved in tetrahydrofuran (THF), the hydride ion attacks and deprotonates the alcohol group to form the sodium salt, and hydrogen gas which was vented from the reaction. Subsequent addition of methyl iodide to the reaction mixture leads to attack of the methyl of methyl iodide by the lone pair of the deprotonated alcohol. This forms the desired product and eliminates sodium iodide. The reaction was quenched with methanol and water and the subsequent mixture extracted with ethyl acetate. The organic phase was extracted from the reaction mixture, dried over magnesium sulphate and the solvent removed under reduced pressure to afford a yellow oil. TLC of the product indicated impurities and starting material were still present in the reaction product. The yellow oil was purified by flash chromatography. The final product **(47)** was isolated as a yellow oil with a relatively good yield of 70 %.

The proton NMR spectrum confirmed the desired compound had been synthesised though peaks were also observed for residual ethyl acetate indicating that the solvent had not been completely removed before the NMR

experiments were run. A multiplet peak at 3.91 ppm (4H) again corresponds to the acetal group while the multiplet peaks at 1.86 - 1.45 ppm (8H) correspond to the protons of the cyclohexane. There has been a loss of the broad singlet at 1.42 ppm of the starting material corresponding to the alcohol proton, while the peak for the proton of the cyclohexane adjacent the alcohol remains at 3.31 ppm (1H). Overlapping the peak at 3.31 ppm is a new singlet peak at 3.33 ppm (3H), with the integration to 3 protons and lack of coupling, this peak is indicative of the desired -OMethyl group. Along with the assignments of the proton NMR spectrum, the carbon NMR confirms a new carbon environment for the product in comparison to the starting material spectrum. The compound was carried through to the next step of the synthesis after excess solvent was removed by leaving the product under a high vacuum.

At this point in the synthesis, the -OMethyl group of the molecule was complete so focus moved towards forming the mono substituted hydrazine portion of the molecule, para to the -OMethyl. The first step of forming the hydrazine was to deprotect the carbonyl group which is currently protected with an acetal group. A standard acetal deprotection method was utilised, a strong aqueous hydrochloric acid solution (5M) was added to the intermediate product **(47)** dissolved in THF and stirred at room temperature for 16h. The acetal group is transformed to the desired ketone, the pH of the reaction mixture was adjusted to 10 with sodium hydroxide solution (2M) and organic products were extracted with ethyl acetate. The organic extract was dried over

magnesium sulphate and the solvent removed to afford a yellow oil with a yield of 91 %.

The proton and carbon NMR spectra confirmed the desired compound **(48)** had been synthesised. A multiplet peak at 3.63 ppm (1H) corresponds to the proton adjacent the -OMethyl group while the remaining protons of the cyclohexane are represented by 4 multiplet peaks at 2.58, 2.28, 2.11 and 1.97 ppm (2H each). The -OMethyl peak resides at 3.43 ppm (3H). Further evidence for the fact the desired product had been synthesised was the loss of the acetal group peaks from the proton and carbon NMR spectra, multiplet peaks were no longer observed in the 3.91 ppm region where the peak was observed for the starting material. The proton NMR spectrum integrates to 12 protons while the carbon NMR spectrum indicates 5 carbon non-magnetically equivalent carbon atoms which correlates to the desired product. A quaternary carbon signal at 211 ppm was also detected in the carbon NMR, HMQC indicated this carbon lacked proton carbon coupling and the chemical shift suggests that this carbon peak indicates a ketone. The compound was carried through to the next step of the synthesis without further purification.

With the ketone unprotected, the next step was to replace the ketone with a BOC protected hydrazone species which subsequently will be reduced to form the BOC-hydrazine analogue. On addition of *tert*-butyl carbazate to a solution of 4-methoxycyclohexan-1-one **(48)** dissolved in methanol, the *tert*-butyl carbazate undergoes a condensation reaction with the ketone group of **(48)**. The lone pair on the primary nitrogen of the hydrazine attacks the carbon of the ketone group followed by H-migration and subsequent loss of one water

molecule and formation of the hydrazone analogue. The reaction progress was monitored to completion with TLC. On complete conversion of the starting material, the organic solvent was removed under reduced pressure leaving the product and the water side product as an oil. The oil was dissolved in ethyl acetate, dried over magnesium sulphate and the solid residue removed by filtration. The organic solvent was then removed under reduced pressure to afford a white crystalline product with a yield of 99 %.

The proton NMR spectrum confirmed the desired compound **(49)** had been synthesised. Peaks were observed that are concurrent with the groups carried over from the intermediate starting material **(48)**. Peaks were also observed that were indicative of residual solvent in the NMR product indicating that the product was not completely dried. Assignment of the proton NMR spectrum used COSY and HMQC NMR experiments. In the proton NMR spectrum, the peak at 3.48 ppm (1H) is consistent with the proton adjacent the -OMethyl group. A peak at 3.36 ppm (3H) corresponds to the protons of the -OMethyl group. The protons of the cyclohexane demonstrate a similar peak pattern to the intermediate starting material with multiplet peaks at 2.55, 2.35, 2.16 and 1.84 ppm, however the integration for the peaks is 1H, 2H, 1H and 4H respectively as opposed to each multiplet integrating to 2H each as the starting material did, this observation suggests a conformation change in the cyclohexane ring and could be a result of steric hinderance caused by the bulky BOC-hydrazone group. A peak was observed at 7.51 ppm (1H), with no coupling effect observed in the HMQC NMR spectrum, this peak is indicative of the -NH- group of the BOC-hydrazone. A large peak was also observed at 1.50 ppm (9H), the integration of 9 protons and the lack of coupling indicates

this peak belongs to the *tert*-butyl group of the BOC-hydrazone. The total proton NMR integration of 22 protons correlates to the number of protons of the desired product. The carbon NMR indicates 8 different carbon non-magnetically equivalent carbon atoms within the product, with symmetry in the cyclohexane and *tert*-butyl sections of the molecule, this correlates to the expected peak numbers for the carbon NMR spectrum. The compound was carried through to the next step of the synthesis after excess solvent was removed by leaving the product under a high vacuum.

At this stage in the reaction scheme, the hydrazone **(49)** was reduced to the corresponding hydrazine prior to the removal of the BOC protecting group to reveal the desired mono-substituted hydrazine. The reduction product of this reaction resulted in both the *cis* **(50)** and *trans* **(55)** isomers. The reducing agent used for the reduction was sodium cyanoborohydride. To a solution of the hydrazone in acetic acid and water was added in small portions sodium cyanoborohydride. Sodium cyanoborohydride acted as a strong hydride donor, the hydride ion attacked the carbon of the imine to drive the reduction forward. The isomer formed is dependent on the direction of attack, whether the hydride attacks from above or below the molecule. Under basic conditions, the reaction would subsequently eliminate the hydrazine, and thus, the reaction is run under acidic conditions. After stirring at room temperature for 16h, the reaction mixture was neutralised with sodium hydroxide solution (2M) and extracted with dichloromethane. The organic extract was dried over magnesium sulphate and the solvent removed under reduced pressure to afford the product as a yellow oil. The proton NMR of the crude oil indicated

that the *cis* and *trans* isomers had been produced in a near 50:50 ratio. TLC indicated that the two products, though chemically similar, resolved separately meaning it was possible to isolate the isomers at this stage. The two isomers were purified by column chromatography. The resolution between the two isomers was low and due to the nature of the chemical groups of the molecules, there were considerable levels of tailing within the column. This meant the products had to be purified over several columns to ensure both isomers were isolated pure. The *cis* isomer was less polar than the *trans* isomer and so eluted first. Both isomers were isolated, and the samples sent for characterisation to confirm the products.

The NMR spectrum for both isomers showed similarities. The conformational differences between the two isomers were indicated by significant chemical shift differences, particularly for the cyclohexane ring. Proton assignments were confirmed using a combination of ^{13}C, COSY and HMQC NMR experiment data.

*Table 3 Proton chemical shift assignments for **(50)** and **(55)***

^{1}H Chemical Shift (ppm)	**(50)** *cis*	**(55)** *trans*
1-CH	2.89	2.83
2/6-CH_2	1.53, 1.86	1.13, 1.92
3/5-CH_2	1.53, 1.86	1.26, 2.06
4-CH	3.33	3.15
4-OCH_3	3.29	3.36
1-NH	3.86	3.97
7-NH	6.05	6.03
8-*t*-butyl	1.45	1.48

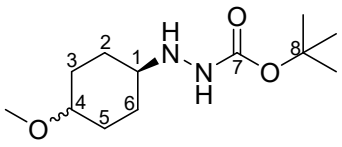

Before the cyclisation step could occur to form the pyrazole analogue, the BOC-hydrazine had to be deprotected to produce the free hydrazine derivative.

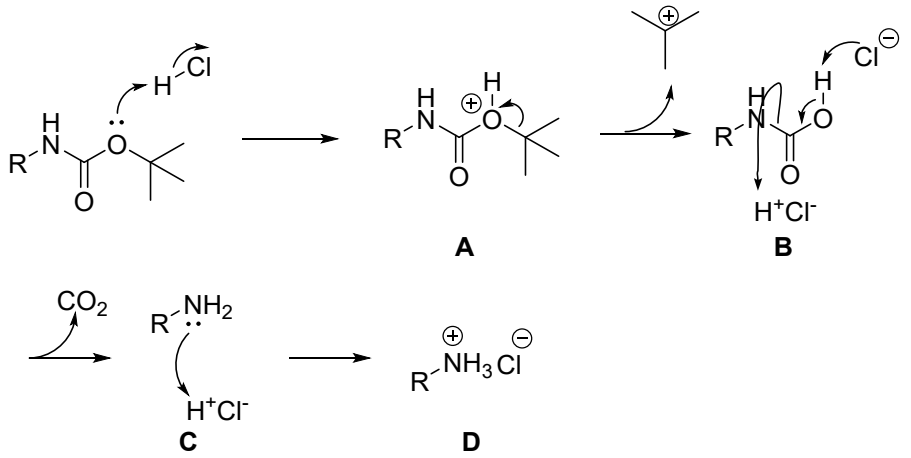

Scheme 17 The mechanism for the deprotection of BOC-hydrazine to form the free hydrazine.

For the deprotection, strong hydrochloric acid solution (5M) was used as a proton donor. The mechanism for the deprotection of BOC-hydrazine is demonstrated in Scheme 17. On addition of the hydrochloric acid solution to the BOC-hydrazine intermediate dissolved in dioxane, the *tert*-butyl carbamate oxygen becomes protonated to form intermediate **A**. This is followed by the elimination of the *tert*-butyl cation to produce the carbamic acid intermediate **B**. Deprotonation of the alcohol of the carbamic acid results in the loss of carbon dioxide and the subsequent protonation to form the free amine intermediate **C**. Under acidic conditions however, the amine undergoes further protonation to provide the product as the chloride salt. TLC indicated that all starting material had been consumed, and the reaction solvent was removed under reduced pressure to afford the product as white flaky crystals. During the initial attempt to deprotect the hydrazine, after deprotection, the chloride salt product was then neutralised to produce the free hydrazine. However, while relatively stable under anhydrous conditions, the free hydrazine showed

signs of decomposition when exposed to air/moisture. Therefore, the compound was carried through to the next step in the synthesis as the chloride salt.

The reaction was carried out in parallel with the *cis* and *trans* isomers. As the compounds remained as the chloride salt, the products were carried forward to the next step without further purification. The NMR spectrum of the crude *cis* isomer product revealed peaks consistent with the desired product while the *tert*-butyl peak of the starting material no longer remained.

*Table 4 Proton chemical shift assignments for **(51)***

^{1}H Chemical Shift (ppm)	**(51)** *cis*
1-CH	3.00-3.16
2/6-CH_2	1.69-1.57, 2.03
3/5-CH_2	1.55-1.48, 1.87
4-CH	3.47
4-OCH_3	3.31
1-NH	N/A[1]
1-NH$\underline{NH_3}$	N/A[1]

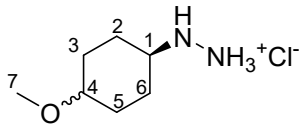

[1] no peak for NH observed when spectrum run using deuterated methanol.

Hereon, the synthetic route used to produce ICT7005/9 **(9)**/**(10)** was used. In the cyclisation step to form the pyrazole a modification to the procedure had to be made to account for the fact the hydrazine was being introduced as the chloride salt. The pyrazole was formed directly from the hydrazine chloride salt **(51)/(56)** as the free amine proved to be less stable if formed prior to the synthesis. The free amine was formed *in situ* with the addition of one equivalent of base to the reaction mixture. To a solution of the hydrazine salt **(51)**/**(56)** dissolved in ethanol was added triethylamine followed by ethyl-2-cyano-3-ethoxycrotonate and set to reflux. TLC was used to determine the end

of the reaction. On complete consumption of the starting material, the reaction was cooled, the organic solvent removed under reduced pressure to afford an orange solid. As a side product to neutralising the hydrazine chloride salt, triethylamine hydrochloride was produced and remained in the reaction product. To remove the triethylamine hydrochloride the product was dissolved in THF. The organic components of the reaction dissolved while the triethylamine hydrochloride salt precipitated out and was removed by filtration. The supernatant was collected, the solvent removed under reduced pressure and the resulting oil dissolved in ethyl acetate. TLC indicated several impurities remained in the crude product. HCl solution (4M) was added to the organic mixture to generate the amine chloride salt of the product. The aqueous phase was isolated, the pH adjusted to 14 with sodium hydroxide solution (4M) and extracted with dichloromethane. The organic phase of the resultant mixture was isolated, dried over magnesium sulphate and filtered, the solvent removed to afford an orange oil. The resulting oil was purified by flash chromatography. The yellow oil product was then recrystallised from hot petroleum ether and diethyl ether to afford large white crystals. The products **(52)**/**(57)** were confirmed by proton and carbon NMR experiments and carried through to the next step of the synthesis without further purification. Proton assignments (Table 5) were confirmed using a combination of ^{13}C, COSY and HMQC NMR experiment data.

*Table 5 Proton chemical shift assignments for **(52)** and **(57)***

^{1}H Chemical Shift (ppm)	**(52)** *cis*	**(57)** *trans*
1-CH	3.77	3.69
2/6-CH_2	2.23, 1.68	1.99
3/5-CH_2	2.12, 1.46	2.22, 1.38
4-CH	3.47	3.24
4-OCH_3	3.31	3.37
7-CH_3	2.32	2.33
9-NH_2	5.04	5.02
10-OCH_2CH_3	1.33, 4.26	1.33, 4.27

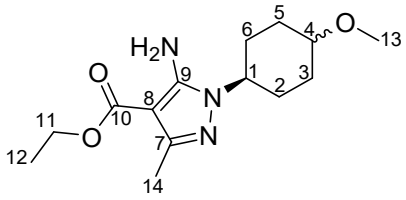

The tosylation step of the reaction scheme was carried out under the same conditions as for ICT7005/9. The products **(52)**/**(57)** of the previous step in the synthesis were reacted with *p*-toluenesulfonylchloride dissolved in anhydrous THF with sodium hydride as the base. The reaction was quenched as previously described, and the reaction mixture was extracted with sodium hydroxide solution (2M). Under basic conditions, the product becomes a basic salt with the sodium cation, and thus dissolves in the aqueous phase. After an acidic-aqueous work up of the reaction, the [Pyrazole-NSO_2Ar]$^{-}$ Na^{+} is converted back to the desired Pyrazole-$NHSO_2Ar$. The product of the reaction was obtained as a yellow oil. The oil was purified by column chromatography. After removal of the solvent, the product was obtained as clear crystals. The products **(53)**/**(58)** were confirmed by proton and carbon NMR and carried through to the next step of the synthesis without further purification. Proton assignments (Table 6) were confirmed using a combination of ^{13}C, COSY and HMQC NMR experiment data.

*Table 6 Proton chemical shift assignments for **(53)** and **(58)***

^{1}H Chemical Shift (ppm)	**(53)** *cis*	**(58)** *trans*
1-CH	4.68	4.65
2/6-CH_2	2.25, 1.75	2.01
3/5-CH_2	1.57, 2.12	1.41, 2.19
4-CH	3.50	3.27
4-OCH_3	3.34	3.38
7-CH_3	2.29	2.29
9-NH	7.41	7.40
10-OCH_2CH_3	1.14, 3.88	1.14, 3.89
12/16-CH	7.49	7.49
13/15-CH	7.20	7.21
14-CH_3	2.39	2.40

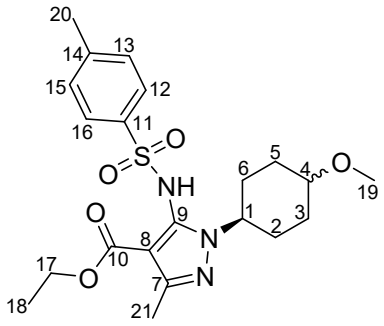

The hydrolysis step of the reaction scheme was carried out under the same conditions as for ICT7005/9. The product **(53)**/**(58)** of the previous step was heated under reflux with an excess of lithium hydroxide monohydrate dissolved in ethanol and water for 16h. TLC was used to confirm the starting material had been consumed. The reaction was cooled, and the pH adjusted to 1 with hydrochloric acid solution (4M). The organic phase was collected, dried over magnesium sulphate and the solvent removed to afford the product as a white solid with good yield (99 %). Analysis of the proton NMR run in deuterated chloroform by comparison to the starting material shows a loss of the ethyl ester proton signals. The *trans* product **(59)** was confirmed by proton NMR (Table 7) and carried through to the next step of the synthesis without further purification.

*Table 7 Proton chemical shift assignments for **(59)**.*

^{1}H Chemical Shift (ppm)	***(54)** cis*	***(59)** trans*
1-CH	4.64	4.62
2/6-CH_2	1.54, 1.71	2.04
3/5-CH_2	2.07, 2.19	1.99, 2.20
4-CH	3.47	3.28
4-OCH_3	3.31	3.38
7-CH_3	2.35	2.34
9-NH	8.62	5.30
12/16-CH	7.51	7.51
13/15-CH	7.15	7.19
14-CH_3	2.27	2.34

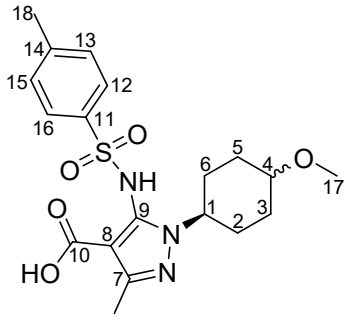

The final step in the synthesis of the pyrazole compounds **(11)** and **(60)** was to convert the carboxylic acid group to the corresponding amide under peptide coupling conditions used previously for ICT7005/9. The carboxylic acid group of the intermediate **(54)**/**(59)** was coupled to the chiral amine (S)-3,3-dimethyl-2-butylamine using HATU and DIPEA as the coupling reagents. The product of the reaction was purified by flash chromatography to afford the compound as a white powder after solvent removal. The final products **(11)**/**(60)** were confirmed by NMR spectrometry. X-ray crystallography of the *cis* isomer **(11)** was obtained to confirm the absolute stereochemistry of the compound. The X-ray crystal structure (Figure 22) confirms that in the *cis* -isomer **(11)**, the cyclohexane exists in the chair conformation with -OMe in the axial position. Para to the -OMe, the pyrazole bond sits in the equatorial position demonstrating that **(11)** is in fact the *cis* isomer. Both *cis* **(11)** and *trans* **(60)** isomers were sent for biological evaluation. Proton assignments (Table 8) were confirmed using a combination of ^{1}H, ^{13}C, COSY and HMQC

NMR experiment data. The products were further confirmed by high resolution mass spectrometry. The calculated m/z of the [M+H] ion of **(11)** and **(60)** was 491.2647. HRMS found peaks for the [M+H] ion at 491.2687 and 491.2685 for **(11)** and **(60)** respectively. Additionally, in the infrared spectrum for both compounds, peaks are observed at the range of 3320-2750 cm^{-1}. These peaks are indicative of N-H, CONH and C-H groups. Peaks observed in the spectrum around 1600 cm^{-1} suggest the presence of C=O groups.

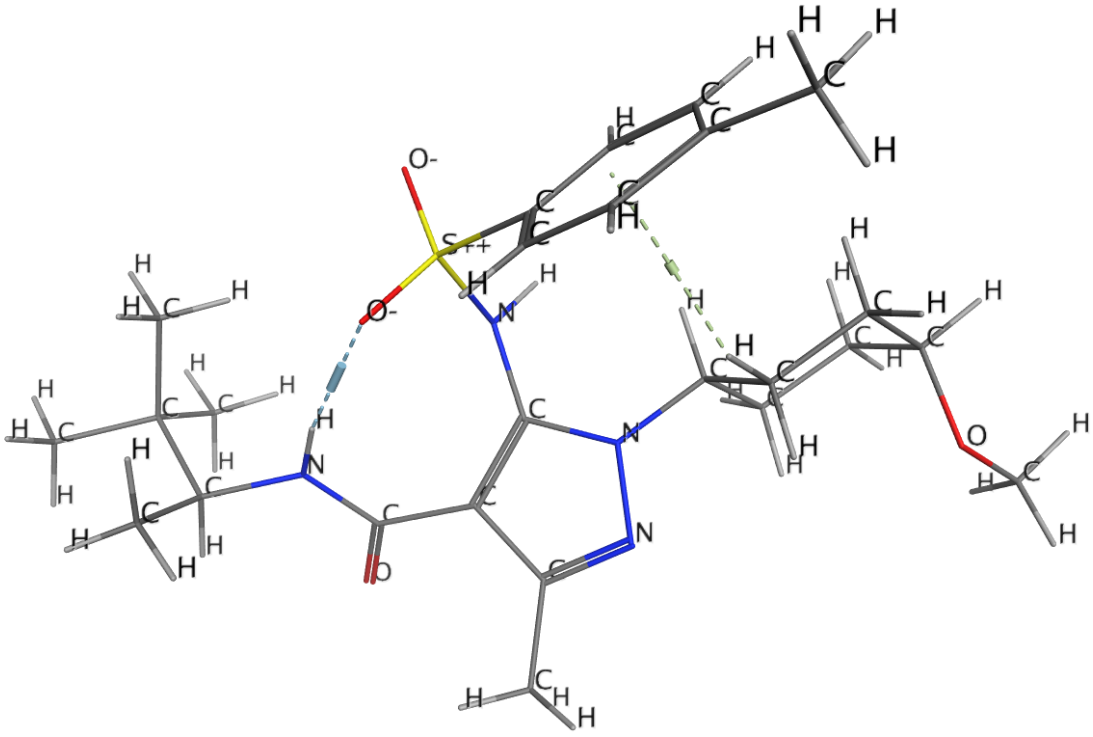

*Figure 22 The X-ray crystal structure for ICT12035 **(11)**. Generated by Prof. I. Scowen. University of Lincoln.*

*Table 8 Proton chemical shift assignments for **(11)** and **(60)***

^{1}H Chemical Shift (ppm)	**(11)** *cis*	**(60)** *trans*
1-CH	4.70	4.66
2/6-CH_2	1.58,2.11	1.97
3/5-CH_2	1.75, 2.22	1.41, 2.18
4-CH	3.50	3.26
4-OCH_3	3.34	3.37
7-CH_3	2.35	2.36
9-NH	8.66	8.61
10-NH	5.19	5.22
12/16-CH	7.54	7.54
13/15-CH	7.17	7.18
14-CH_3	2.33	2.33
19-CH	3.69	3.70
19-CH_3	0.88	0.89
21-*t*-butyl	0.82	0.83

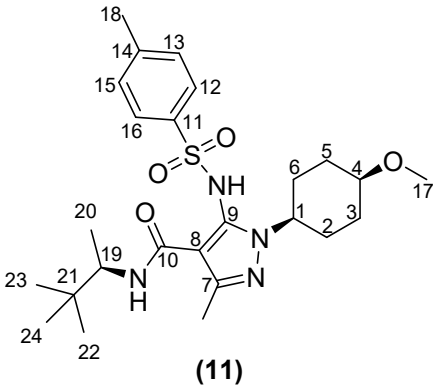

(11)

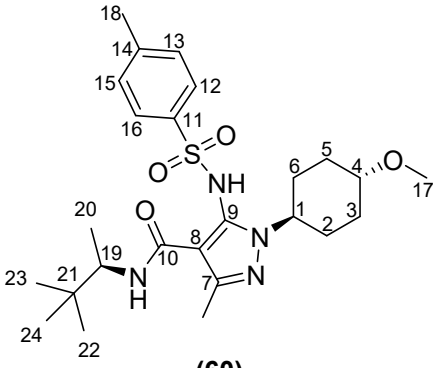

(60)

3. Chapter 3: Biological evaluation of small molecule FPR1 antagonists

3.1. Introduction to Chapter 3

In this chapter, evidence is provided to demonstrate that FPR1 antagonism can retard the expansion of gliomas in preclinical models. As discussed in chapter 1, there is evidence to support a correlation between FPR1 expression and glioma tumour WHO grade.[83, 84, 86] Tumour necrosis is a negative prognostic factor in glioma diagnosis, but also plays a complex role in glioma expansion.[37, 104] Necrotic foci within the tumour can be formed as a result of vaso-occlusion and intravascular thrombosis due to the rapid and dysregulated growth of the tumour, leading to hypoxia and an insufficient nutrient supply. Necrotised cells release cytoplasmic molecules including ANXA1 protein into the extracellular milieu.[85] These molecules are often proinflammatory and recruit leukocytes to the tumour microenvironment. The inflammatory response within the tumour is suggested to both help and hinder tumour expansion.[223] In glioma, ANXA1 and FPR1 expression appears to have a distinct tumour promoting effect.[85] The activation of FPR1 by ANXA1 promotes angiogenesis, proliferation and invasion in a number of cancers including glioma.[224-226] Inhibition of the activation of FPR1 by its endogenous ligands, may have a potential role as a therapy against glioma. To date, small molecule non-peptide FPR1 antagonists have not been investigated as a potential cancer therapy. In chapter 2, the synthesis of small molecule FPR1 antagonists was shown. We set out to provide preclinical proof of principle that a small molecule FPR1 antagonist can have a potential as a therapy for glioma.

3.2. Rationale for compound selection for biological evaluation

In chapter 2, the synthesis of potential FPR1 antagonists is discussed. Every compound went through a process of identification, synthesis, purification, and spectroscopic characterisation. This was a dynamic process with compound identification and synthesis occurring throughout this project. This meant that compounds were introduced at varying stages of the project. See Figure 23 for the order of compound identification and synthesis. Initially, all synthesised compounds were tested for cytotoxicity in U-87 MG cells using an MTT cell viability assay. Compounds were then assessed for their ability to inhibit FPR1 activation by fMLF in a calcium mobilisation assay in U-87 MG cells. The result from the calcium mobilisation assay demonstrated a dose-dependent response from which an IC_{50} was determined. Compounds with lower IC_{50} were sought as these compounds were able to inhibit FPR1 activation at lower concentrations. Compounds with the lowest IC_{50} for FPR1 were carried forward to the advanced stages of the project as they were identified.

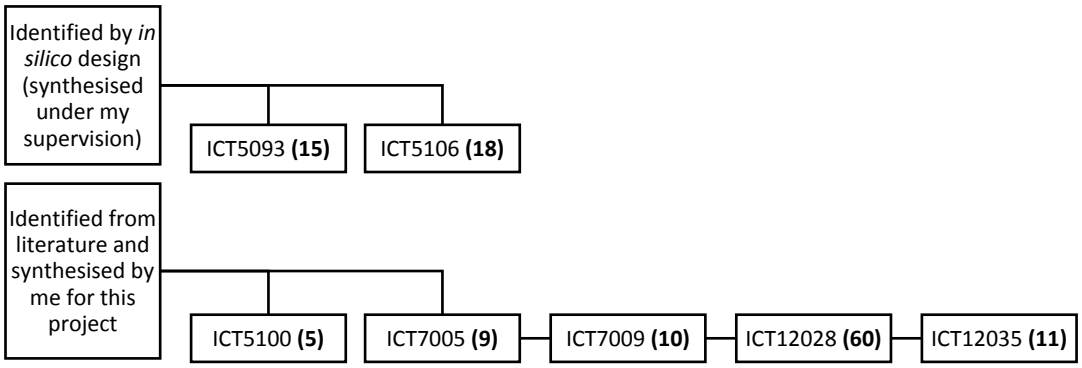

Figure 23 Flowchart demonstrating the timeline of compound synthesis for the project.

Further to this, functional assays were introduced through the project and required optimisation. The requirement for live cell assays in this project were that they demonstrate a functional cellular response to FPR1 activation by an

agonist. It was then demonstrated that using an FPR1 small molecule antagonist, this functional response could be inhibited.

3.3. Expression of FPR1 is elevated in U-87 MG cells in 2D culture under cellular stress (hypoxia/starvation), as well as in the periphery of the hypoxic/necrotic foci of 3D spheroid models and xenografted tissue

U-87 MG was used as a model glioma cell line. This set of experiments was purely qualitative at this stage of the project and was used initially to confirm FPR1 expression in U-87 MG cells. The information presented in this section would act as a basis for future work following this project.

FPR1 expression was confirmed in U-87 MG cells by immunofluorescent (IF) staining and flow cytometry (FC). Positive FPR1 IF staining was observed in 2D-culture slides with FPR1 localisation on the cell membrane (Figure 24A). Positive FPR1 expression was also observed by FC (Figure 24B). Furthermore, it was found that the levels of cell surface expression of FPR1 in U-87 MG cells was influenced by the conditions in which the cells were cultured and grown. FC was used to show that under cellular stress, expression is increased in U-87 MG 2D monolayer cell cultures. U-87 MG cells were cultured as monolayers under normal cell culture conditions (normoxia, 10 % FCS), serum-starved conditions (normoxia, 0 % FCS), and hypoxic conditions (0.1 % O_2, 10 % FCS) (Figure 24B). The expression of FPR1 in U-87 MG cells by FC was quantified relative to the isotype control (Figure 24C). The data suggests FPR1 expression in U-87 MG cells cultured under serum-starved and hypoxic conditions had 1.5-fold and 1.4-fold increase respectively compared to U-87 MG cells cultured under normal conditions. As this was only a single repeat, the experiment required future work to confirm the observation and statistical significance of this result.

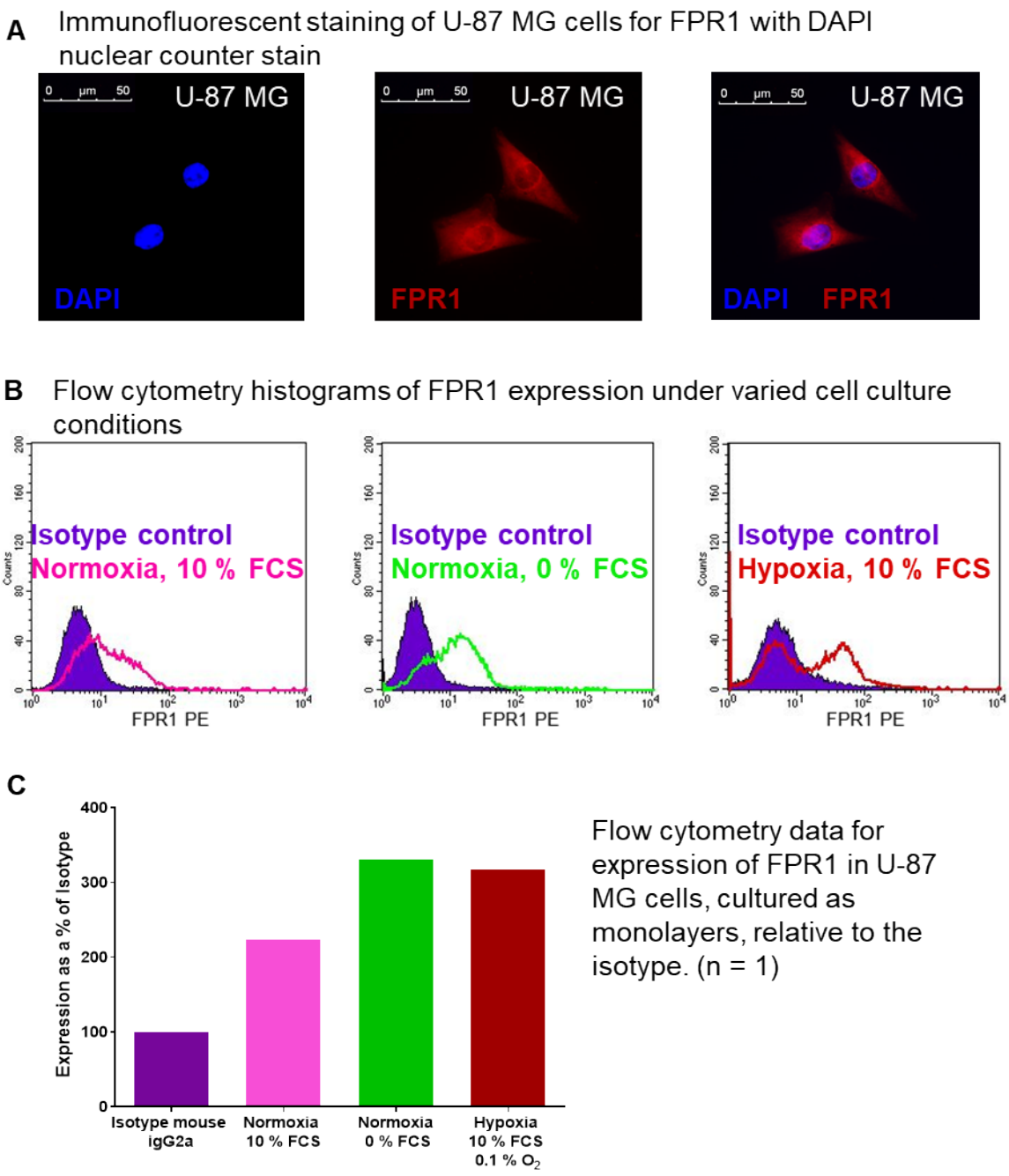

Figure 24 The expression of FPR1 in U-87 MG cells in monolayer cell culture. ***(A)*** *IF staining of formalin-fixed U-87 MG cells FPR1 (red) with DAPI nuclear staining (blue).* ***(B)*** *Expression of FPR1 by FC, histogram data for U-87 MG cells cultured under normal cell culture conditions (normoxia) – 10 % FCS (cyan), normoxia and serum-starved – 0 % FCS (green), and hypoxia (red), purple represents the isotype (igG2a) control.* ***(C)*** *Graphical presentation of quantified FC data comparing expression of FPR1 under different culture conditions. Data is (n = 1) and so purely qualitative at this stage.*

The result of increased FPR1 expression under cellular stress in monolayer culture was reflected in U-87 MG cells grown both in a 3D spheroid model and in xenograft tissue.

U-87 MG spheroids were grown using a spinner flask. The spinner flask culture method creates spheroids by preventing cells in suspension from adhering to a surface and promoting cell-to-cell collisions by constant stirring.[227] To form the spheroids, a well-mixed single cell suspension of U-87 MG cells were added to the flask containing growth media. The media was stirred at a constant speed by a magnetic stirrer and stored in a cell incubator. Maintaining a constant rotation speed was important. Media agitation that was too slow would allow cells to settle and adhere to the flask surface, but too fast could cause cellular damage. Culturing cells as spheroids can create *in vivo*-like microenvironments by formation of gradients of oxygen, nutrients, and growth factors. Gradients of soluble components in the cell culture medium (nutrients, oxygen, growth factors) are formed due to limitations of diffusion created by the spheroid.[228] It was estimated (based on a previous study)[160] that the spheroids would have to be at least 400-500 μm in diameter to show heterogeneity/ hypoxia foci observed in high grade glioma.

FPR1 expression was observed by immunohistochemistry (IHC) in both formalin-fixed paraffin-embedded (FFPE) U-87 MG spheroids (Figure 25A-C) and xenografted U-87 MG tumour (Figure 25D-F). In both the 3D spheroid culture and xenografted tumour, higher levels of FPR1 expression were observed on the periphery of the hypoxic/necrotic foci, of my knowledge, this was a novel observation. The data presented in Figure 25 is qualitative and was to be used for future work investigating the relationship between FPR1

expression and the hypoxic/necrotic niche in GBM. The data indicates the U-87 MG cell line expresses FPR1 in 2D/3D *in vitro* cultures and *in vivo* xenograft tissue and so is a suitable cell line for testing FPR1 antagonists in *in vitro* and *in vivo* models.

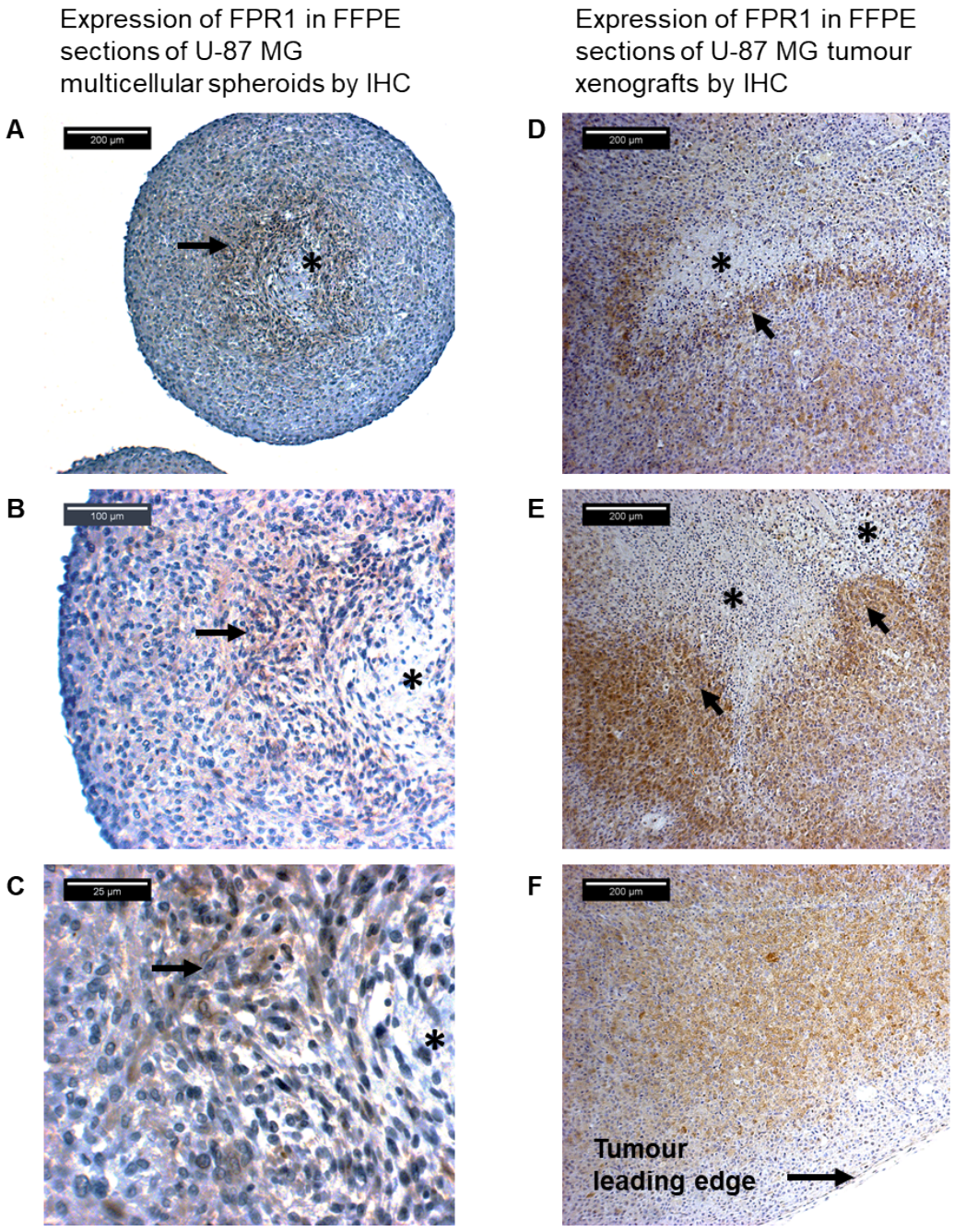

Figure 25 The expression of FPR1 in U-87 MG cells in multicellular spheroid models and xenografted tissue (IHC). ***(A-C)*** *IHC staining of FFPE sections from a U-87 MG multicellular spheroid for FPR1 expression, (*= necrotic foci, arrow= necrotic periphery/hypoxic region).* ***(D-E)*** *IHC staining of FFPE sections from U-87 MG xenograft tumours for FPR1 expression, (*= necrotic foci, arrow= necrotic periphery/hypoxic region).* ***(F)*** *IHC staining of FFPE section from U-87 MG xenograft tumours for FPR1 expression, (arrow= tumour border/leading edge). FPR1 was stained brown using DAB. Basophilic structure of the cells was stained in blue with haematoxylin solution.*

3.4. Small molecule FPR1 antagonists inhibit fMLF induced calcium mobilisation in U-87 MG cells

Calcium (Ca^{2+}) is an essential mineral for life, widely known for its role in bone structure. Free intracellular Ca^{2+} ions also serve as secondary messengers and as a universal signalling molecule.[229-231] Ca^{2+} has been implicated in the regulation of a wide variety of physiological processes, not limited to but including vascular contraction and dilation, hormone secretion, muscle function, cell division and differentiation and other aspects of cellular metabolism.[229] Precise regulation of intracellular Ca^{2+} concentration is required to maintain the signal transduction functions of Ca^{2+}.[229-231] The Ca^{2+} concentration in resting cells is maintained at the range of 100 nM.[229-231] Upon cellular activation, the Ca^{2+} concentration can be elevated as high as 100-fold within miliseconds.[231] The intracellular Ca^{2+} concentration is mediated by one of two ways; by transfer of extracellular Ca^{2+} through calcium channels in the cell membrane, or by release of intracellular Ca^{2+} stores in the endoplasmic reticulum.[231]

Upon the stimulation by ligands, GPCRs including FPR1 transduce extracellular signals into intracellular responses. On activation and subsequent release of the G-proteins, a signal cascade leads to the generation of 1,4,5-inositol triphosphate (IP3). The IP3 binds to IP3-sensitive Ca^{2+} channels on the endoplasmic reticulum causing a release of Ca^{2+} ions from the endoplasmic reticulum into the cytoplasm.[231]

Ca^{2+}-based assays have been used widely for GPCR-targeted drug screening and characterisation.[232] The use of Ca^{2+} sensitive fluorescent probes allows

both qualitative and quantitative analysis of GPCR mediated Ca^{2+} increases in live-cell assays.[232]

Before compounds were assessed for their ability to abrogate Ca^{2+} mobilisation, compound cytotoxicity was measured. This project aims to demonstrate that inhibiting the FPR1 receptor with a small molecule antagonist has therapeutic potential but not through cytotoxic mechanisms. Desirable compounds would inhibit the effects of FPR1 activation but not induce cell death. Compounds were tested against U-87 MG cells in an MTT-based cell viability assay.

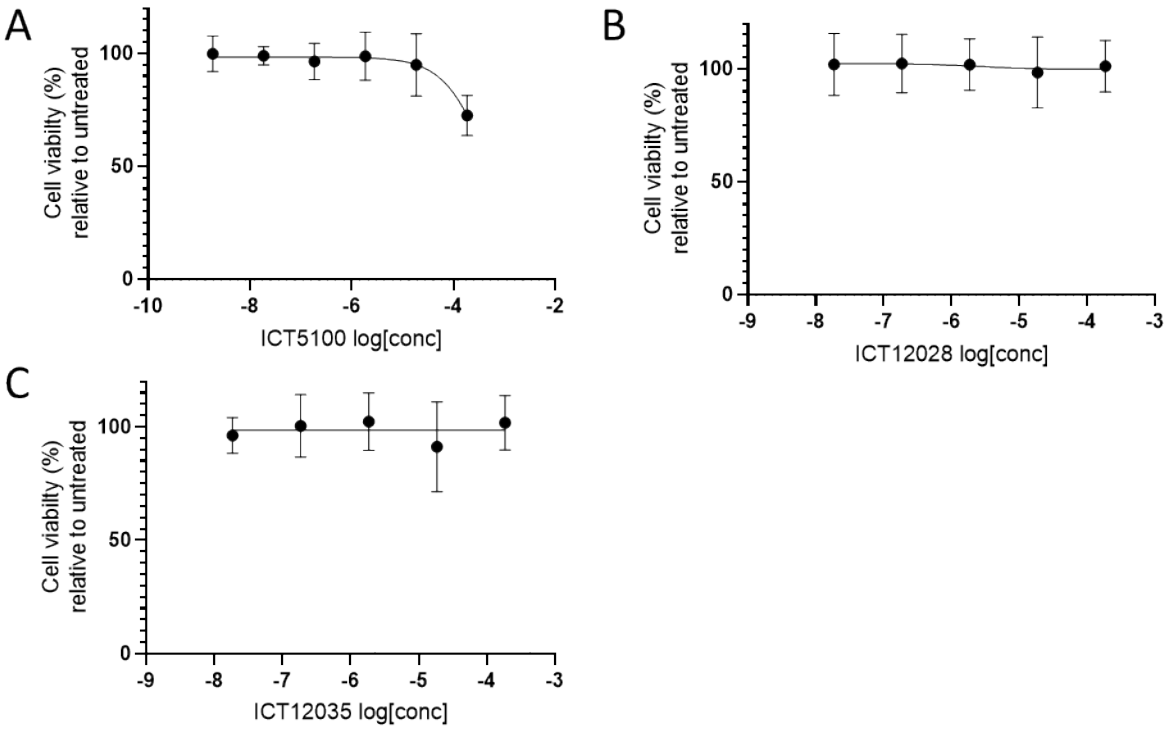

*Figure 26 Dose-response curves for the MTT-based cell viability assay to measure compound cytotoxicity in the U-87 MG cell line. Dose-response curves (normalized to untreated cells) are shown for U-87 MG cells treated with **(A)** ICT5100 **(5)**, **(B)** ICT12028 **(60)**, **(C)** ICT12035 **(11)** for a 24-hour treatment period. Data are means ± SD of three biological replicates.*

Figure 26 shows the dose-response curves for ICT5100 **(5)**, ICT12028 **(60)**, and ICT12035 **(11)**. ICT5100 **(5)** showed some cytotoxicity at the highest concentration tested (185 µM). An IC_{50} could not be determined for ICT5100

(5) due to maximum solubility of the compound in DMSO having been reached. The concentration of DMSO required to dissolve higher concentrations of ICT5100 **(5)** were cytotoxic. ICT12028 **(60)** and ICT12035 **(11)** did not appear to be cytotoxic in against U-87 MG cells at the concentrations tested.

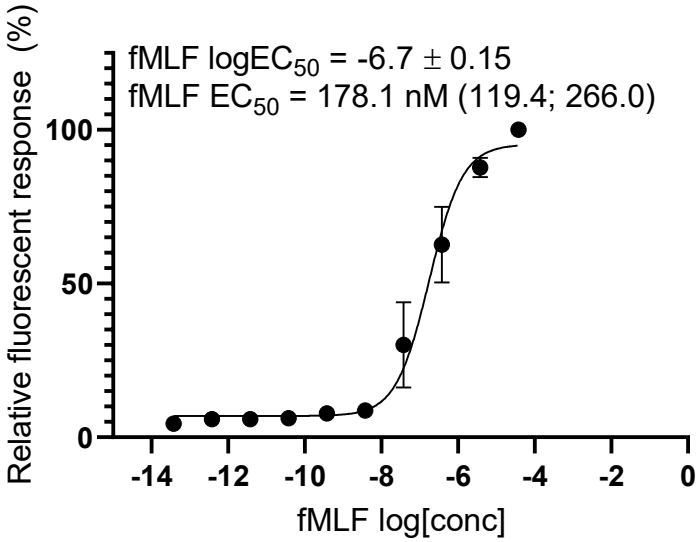

Figure 27 Calcium Flux dose-response curve (normalised to the maximum fluorescent response) for a concentration range of fMLF. The corresponding EC_{50} (half maximal effective concentration) values (nanomolar; with 95% confidence intervals), and $logEC_{50}$ with SD are shown for the U-87 MG cell model. Data are means ± SD of three biological replicates.

A known agonist for FPR1, fMLF was shown to induce calcium mobilisation in U-87 MG cells in a dose-dependent manner (Figure 27) showing that the FPR1 receptor was functionally active. From the calcium mobilisation assay, EC_{50} of fMLF (178.1 nM) in U-87 MG cells was determined. When testing antagonists against fMLF induced FPR1 activation, it was decided to use a concentration close to or above the EC_{50} range. fMLF was used at an assay concentration of 100 nM when calcium mobilisation was run in the antagonist mode.

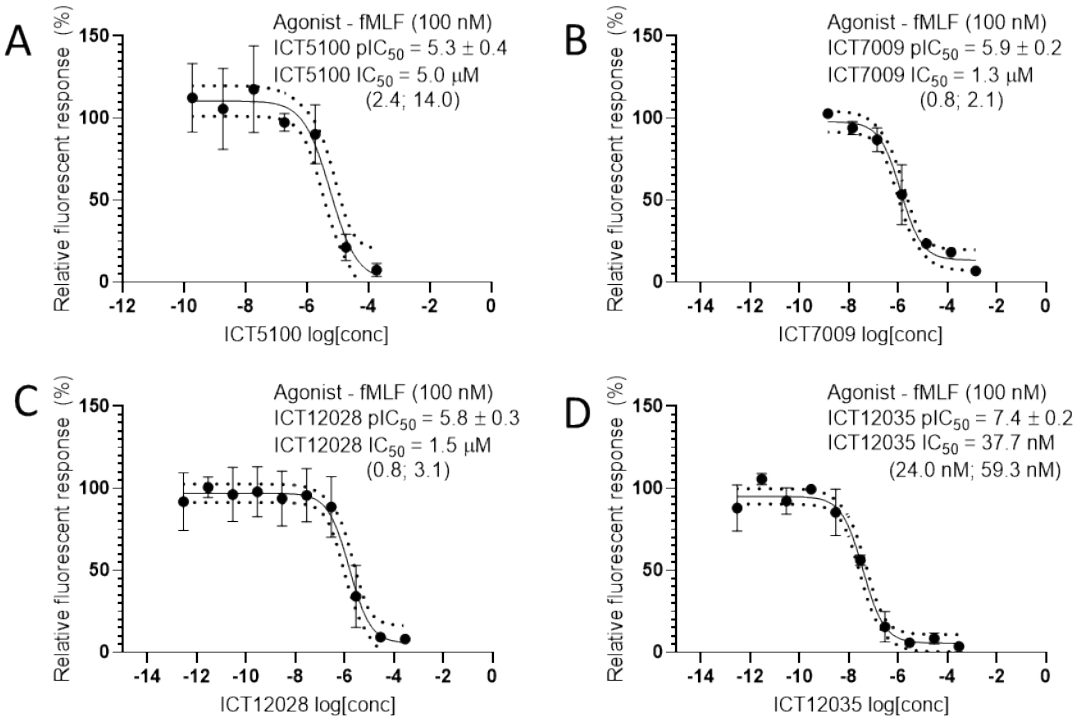

E

Compound	Cytotoxicity pIC_{50} (µM)	Antagonist pIC_{50} against fMLF
ICT5093 **(15)**	N/A[a]	4.6
ICT5100 **(5)**	<4[b]	5.3 ± 0.4
ICT5106 **(18)**	N/A[a]	5.0
ICT7005 **(9)**	3.7[c]	5.2[c]
ICT7009 **(10)**	3.9[c]	5.9 ± 0.2
ICT12028 **(60)**	<4[b]	5.8 ± 0.3
ICT12035 **(11)**	<4[b]	7.4 ± 0.2

Figure 28 Calcium mobilisation assay and cytotoxicity data for FPR1 small molecule antagonists. U-87 MG cells were loaded with Fluo4-NW cell dye causing the cells to fluoresce in response to calcium mobilisation. The FPR1 agonist fMLF causes the release of intracellular calcium which can be measured with a fluorometer. ***(A-D)*** *Dose-response curves (normalised to the maximum fluorescent response) in a calcium mobilisation assay to fMLF (100 nM) in the presence of varying concentrations of FPR1 antagonists* ***(A)*** *ICT5100* ***(5)****,* ***(B)*** *ICT7009* ***(10)****,* ***(C)*** *ICT12028* ***(60)****,* ***(D)*** *and ICT12035* ***(11).*** *The corresponding EC_{50} (half maximal effective concentration) values (micromolar unless otherwise stated; with 95% confidence intervals), and logEC_{50} with SD are shown for the U-87 MG cell model. Hashed line = 95 % confidence interval.* ***(E)*** *Tabulated data for cytotoxicity and FPR1 antagonist IC_{50} values for FPR1 antagonists. [a] Compounds were not tested for cytotoxicity at this stage of the project. [b] The pIC_{50} for cytotoxicity was below 4, lower concentrations could not be tested due to solubility of the compound at these concentrations. [c] These pIC_{50} values were determined by a student supporting the project under my supervision. Data are means ± SD of three biological replicates.*

Furthermore, it was demonstrated that the response to fMLF can be abrogated by selective small molecule FPR1 antagonists. ICT5100 **(5)** reduced fMLF induced calcium mobilisation back to baseline levels at

concentrations above 20 μM with an IC_{50} of 5.0 μM (Figure 28A). From the pyrazole series of FPR1 antagonists, ICT12028 **(60)** (*trans* isomer) had an improved IC_{50} of 1.5 μM over ICT5100 **(5)** (Figure 28C). As previously discussed, Morley *et al.* had described ICT12028 **(60)** as inactive (<30 % FPR1 inhibition at 30 μM) as an FPR1 antagonist.[216] It is demonstrated here that ICT12028 **(60)** is weakly active as an FPR1 antagonist. .[216] ICT12035 **(11)**, the *cis* isomer, recorded the highest efficacy with an IC_{50} 37.7 nM (Figure 28D). Importantly, ICT12028 **(60)** and ICT12035 **(11)** were not cytotoxic to U-87 MG cells at the maximum soluble dose of 100 μM. This shows that the compounds are preventing a cellular response by antagonising FPR1 against fMLF rather than cytotoxic mechanisms. A full table of calcium mobilisation and cytotoxicity data is shown in Figure 28E.

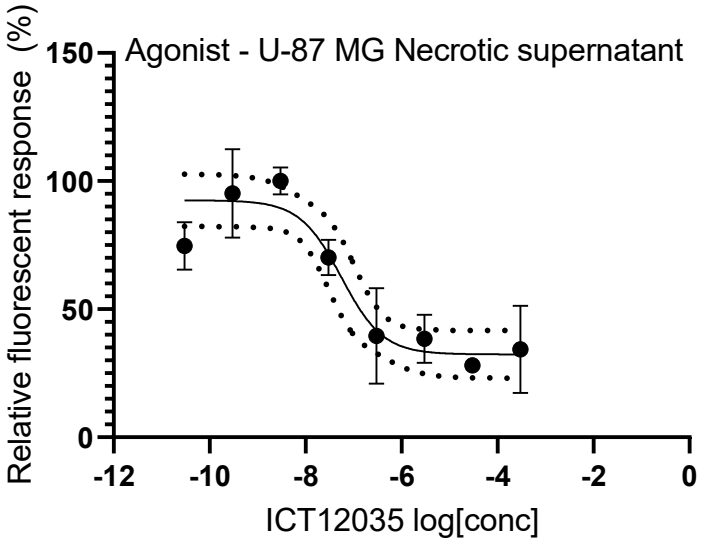

*Figure 29 A dose-response curve of ICT12035 **(11)** in a calcium mobilisation assay of U-87 MG cells responding to a U-87 MG necrotic supernatant. Hashed line = 95 % confidence interval.*

It was also shown that calcium mobilisation could be induced by the necrotic supernatant of U-87 MG cells as discussed previously.[86] The necrotic supernatant was generated by cycling a suspension of U-87 MG cells through a freeze and thaw process. The mixture was centrifuged, and the supernatant

collected by filtration to remove any cellular debris. Here, it was demonstrated that ICT12035 **(11)** was also able to abrogate the calcium mobilisation response induced by necrotic supernatant of U-87 MG cells in a dose dependent manner. (Figure 29). ICT12035 **(11)** was not able to completely abrogate calcium mobilisation back to baseline. This could be due to other factors in the necrotic supernatant that may be triggering calcium mobilisation through a non-FPR1 pathway. This experiment was important in the case of GBM as necrotic foci are a characteristic of this disease. It was important to demonstrate that an FPR1 antagonist could abrogate the response of U-87 MG cells to factors that may exist as a result of necrosis in GBM.

3.5. Small molecule FPR1 antagonists reduce fMLF-induced U-87 MG cell migration through a membrane in a two-chamber chemotaxis assay

Glioma cells migrate through the extracellular space in the brain. Cell migration is a complicated process that involves multiple biologic features. These features include adhesion to the ECM, with concurrent modifications to the ECM in the case of cancer cells and in particular, tumour astrocytes. [233] The cells own motility which involves reorganisation of the actin cytoskeleton. [234] Invasion, which involves the breakdown of matrix proteins by tumour-secreted proteolytic enzymes.[235, 236]

As previously discussed, FPR1 has been associated with a more invasive GBM phenotype. Therefore, it was decided to investigate whether FPR1 activation by an agonist (fMLF) induced an increase in cell migration and could this FPR1 induced migration be abrogated by an FPR1 small molecule antagonist. The antagonists used for this investigation were ICT5100 **(5)**, ICT7009 **(10)**, and ICT12028 **(60)**. At the time when this investigation was carried out, ICT12035 **(11)** had not yet been synthesised. The three compounds used in this investigation had demonstrated FPR1 antagonism in the calcium mobilisation assay.

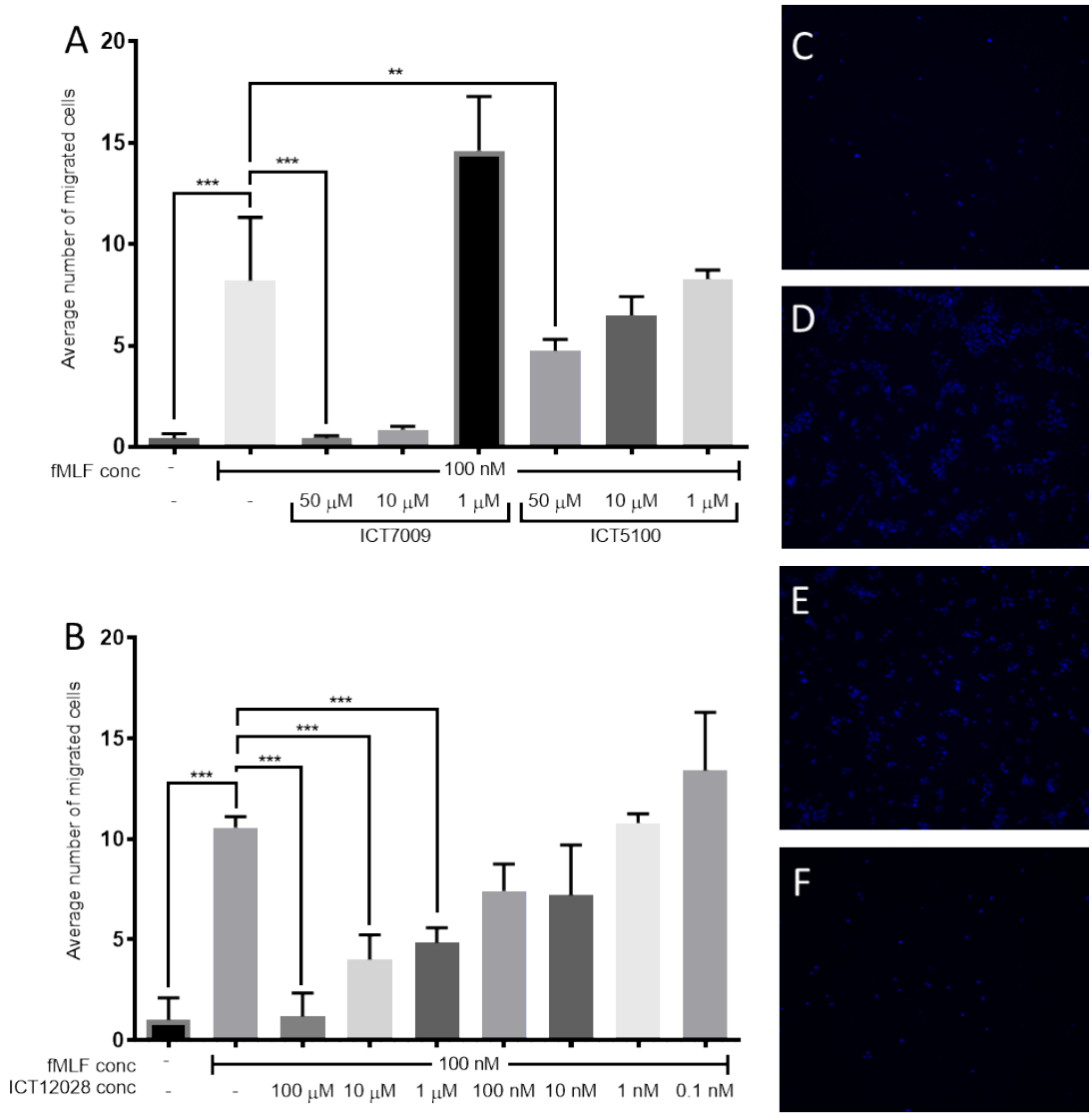

Figure 30 U-87 MG single cell migration through a porous membrane in the Boyden Well chemotaxis assay. ***(A)*** *fMLF induced migration of U-87 MG cells against varying concentrations of the FPR1 antagonists ICT5100* ***(5)*** *and ICT7009* ***(10)****.* ***(B)*** *fMLF induced migration of U-87 MG cells against varying concentrations of ICT12028* ***(60)****.* ***(C – F)*** *Representative images from the Boyden well assay showing fluorescent images of DAPI stained migrated U-87 MG cells.* ***(C)*** *control, no agonist/antagonist.* ***(D)*** *fMLF (9.14 μM).* ***(E)*** *fMLF (9.14 μM)/ ICT5100 (50 μM).* ***(F)*** *fMLF (9.14 μM)/ ICT7009 (50 μM). Data are means ± SD of three biological replicates, **P < 0.005, and ***P < 0.001, Student's t test (two-tailed).*

The fMLF induced migration of U-87 MG cells was investigated using the Boyden two-chamber chemotaxis assay (Figure 30). U-87 MG cells were placed in the upper chamber of the Boyden well. The lower chamber contained buffer or the FPR1 agonist fMLF as negative and positive controls. The well medium also contained either buffer alone or varying concentrations of FPR1 small molecule antagonists. The chambers were separated by a porous

membrane coated in collagen-I. After incubation overnight, the medium was removed from the top chamber of the well insert. The well inserts were transferred to new wells containing ethanol (70 % v/v) to fix the cells. Cells remaining in the top compartment were scraped away using a cotton bud leaving only the cells that have migrated to the lower side of the membrane. The membranes were cut out and mounted (lower side up) onto microscope slides using mounting media (+DAPI). The number of migrated cells were counted using fluorescent microscopy. A minimum of 5 fields were counted and the averages calculated.

By including fMLF in the well, cell chemotaxis towards the lower chamber was increased significantly compared to the control well containing no FPR1 agonist. The fMLF-induced migration was significantly reduced in a dose-dependent manner by compounds ICT5100 **(5)**, ICT7009 **(10)** and ICT12028 **(60)**. At the highest concentrations of FPR1 antagonist, ICT5100 **(5)**, ICT7009 **(10)**, and ICT12028 **(60)** reduced migration through the membrane. However, ICT7009 **(10)** (50 μM) was more effective than ICT5100 **(5)** (50 μM) at reducing fMLF-induced migration. At the lower concentration (1 μM) both ICT5100 **(5)** and ICT7009 **(10)** were no longer effective at reducing fMLF induced migration. Interestingly, ICT7009 **(10)** at the lower concentration (1 μM) appears to increase migration above fMLF control levels. This could suggest a potential agonist effect at lower concentrations, an observation that requires future work. ICT12028 **(60)** was still effective at reducing fMLF induced migration significantly at concentrations of 0.1 – 1 μM. The migration reduction was no longer significant for ICT12028 **(60)** below concentrations of 10 nM.

3.6. Small molecule FPR1 antagonists reduce fMLF-induced invasion of U-87 MG spheroids into a 3D collagen-I matrix

Developing on the 2-chamber assay results, it was decided to investigate whether FPR1 activation in U-87 MG cells would induce invasion and whether that invasion could be inhibited with a FPR1 antagonist. This parallels with the idea previously discussed that GBM cells invade into surrounding ECM of healthy tissue. If factors in the necrotic region activate the FPR1 receptor and drive invasion, antagonism of FPR1 could be used to reduce this effect. When this assay was run, ICT12035 **(11)** had been synthesised and the IC_{50} for FPR1 in U-87 MG cells determined. As ICT12035 had the lowest IC_{50} by this point, it was decided to use it as the tool compound for this assay.

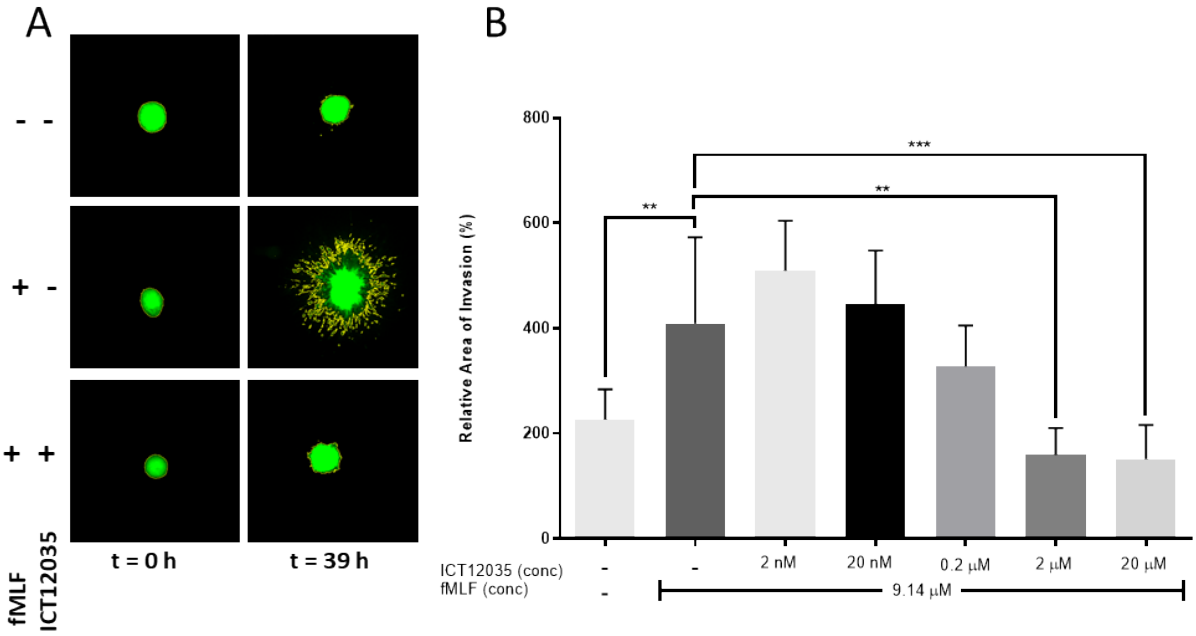

*Figure 31 U-87 MG 3D multicellular spheroid invasion into a collagen matrix. **(A)** Representative fluorescent imaging of U-87 MG spheroids embedded in collagen-I at timepoints 0h and 39h, with and without fMLF (9.14 μM) and/or the FPR1 antagonist ICT12035 **(11)** (20 μM). **(B)** fMLF induced invasion of U-87 MG cells against varying concentrations of ICT12035 **(11)**. All values are expressed as mean ± SD of three biological replicates. **P < 0.01, and ***P < 0.001, student's t test (two tailed).*

The invasion of U-87 MG cells was investigated in a 3D spheroid model in a collagen-I matrix (Figure 31). U-87 MG cells were pre-treated with

fluorescent dye Calcein-AM. This molecule is normally colourless but under the action of esterases inside the live cell, is hydrolysed to a fluorescent dye. U-87 MG multicellular spheroids were formed using the hanging drop method. The spheroids were embedded in a collagen-I matrix (with and without agonist/antagonist) and incubated for 39 h. Images of the spheroids embedded in collagen were taken at two timepoints (t = 0 h and 39 h) using the fluorescent option on the Lumascope 500 (Figure 31A). Images were analysed using the ImageJ software suite.[237] Using ImageJ software, the area of the image covered with green fluorescence (live cells) was determined using the "Threshold Color" selection tool (Figure 32). The calculated area of fluorescence at t = 0 was subtracted from t = 39 h to give the area of invasion. The relative area of invasion (%) was calculated by comparison to the control containing no agonist/antagonist.

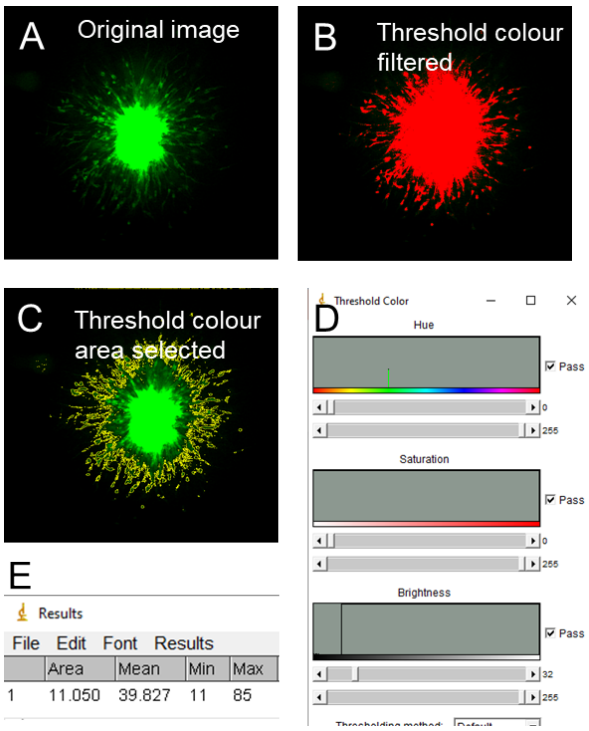

*Figure 32 ImageJ processing for U-87 MG spheroid invasion into collagen. The original image **(A)** was uploaded into ImageJ software. Using the "Threshold Color" selection tool **(D)** the green fluorescence was filtered from the black background to produce image **(B)**. **(C)** The filtered area was then selected (yellow line = border of the selected area). **(E)** The ImageJ "Measure" tool was then used to report the selected area.*

The FPR1 agonist fMLF (9.14 μM) increased the invasion of U-87 MG cells by a 1.8-fold increase relative to the untreated spheroids. Note that a higher concentration of fMLF was used in this assay compared to others in this report. A higher concentration of fMLF was to ensure cells were exposed to the agonist as the assay relied on passive diffusion of the molecule through collagen. The final concentration of agonist that cells are exposed to would be lower due to diffusion through the matrix and into media used to keep assay wells from drying out. The same applies to the antagonist used, again, the antagonist will diffuse through the collagen and into the media. The final antagonist concentration will be diluted. Spheroids exposed to fMLF (9.14 μM) and treated with ICT12035 **(11)** at 20 μM and 2 μM showed significant ($P = <0.05$) reductions in invasion, with 2.2-fold and 2.1-fold decreases in invasion respectively, relative to the spheroids treated with fMLF only (Figure 31B). The antagonist effect of ICT12035 **(11)** began to drop off at concentrations below 2 μM. There was no statistically significant reduction in invasion by ICT12035 **(11)** at 0.2 μM and below. This indicates that the FPR1 agonist fMLF increases the invasion of U-87 MG spheroids into a collagen-I matrix. Furthermore, there is a significant reduction in the fMLF-induced invasion of U-87 MG cells in the presence of the small molecule FPR1 antagonist ICT12035 **(11)**.

3.7. *in vitro* liver metabolism and *in vivo* Pharmacokinetics (PK) of ICT12028 (60).

It is important to understand how a drug behaves when interacting with a biological system. By investigating the metabolism and distribution of a compound in biological systems, a more informed efficacy study could be performed. A basic *in vitro* metabolism investigation of ICT12028 **(60)** was used to investigate the stability of the compound in mouse liver homogenate. At this stage in the project, when this experiment was carried out, ICT12035 was still in the process of being synthesised. ICT12028 **(60)** was predicted to have a similar chemical and metabolic profile to its isomer ICT12035 **(11)**. ICT12028 **(60)** was incubated in mouse liver homogenate (4:1) at 37 °C, over a 5 h period (Figure 33A). Samples of homogenate were taken at hourly timepoints, processed, and analysed by liquid chromatography-mass spectrometry (LCMS). The concentration of ICT12028 **(60)** at each timepoint remained stable throughout the assay incubation period suggesting stability of the compound in the homogenate. The metabolism data was from a single experiment and requires further investigation to confirm the result. Furthermore, a more in-depth metabolism study of ICT12035 **(11)**, the more active isomer of ICT12028 **(60)**, would be beneficial to this study.

An investigation into the tissue distribution of active compounds *in vivo* would determine whether compounds would reach the destination organ in an efficacy study. ICT12028 **(60)** was administered by intraperitoneal (IP) injection at 20 mg/kg to mice bearing xenografted U-87 MG tumours. The *ex vivo* tissue was processed, and then analysed by LCMS to determine the concentration of the parent ICT12028 **(60)**. ICT12028 **(60)** was detected in all

tissues including the target organ (brain) and the U-87 MG xenograft tumour (Figure 33C). Furthermore, at the 4-hour timepoint, the tissue concentration of ICT12028 **(60)** in brain and tumour remained above the IC_{50} for the compound.

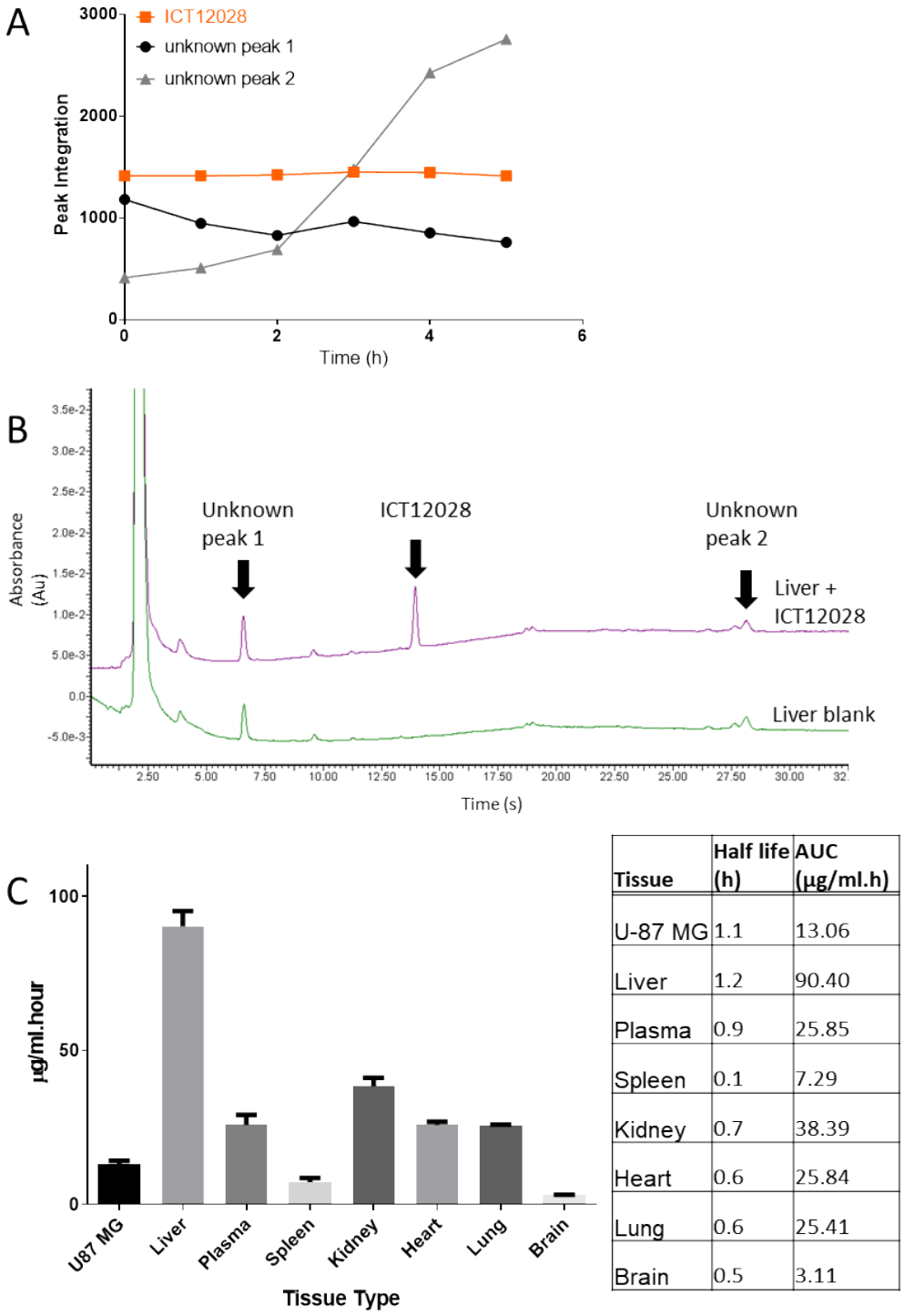

Tissue	Half life (h)	AUC (µg/ml.h)
U-87 MG	1.1	13.06
Liver	1.2	90.40
Plasma	0.9	25.85
Spleen	0.1	7.29
Kidney	0.7	38.39
Heart	0.6	25.84
Lung	0.6	25.41
Brain	0.5	3.11

Figure 33 in vitro liver metabolism and pharmacokinetics (PK) of ICT12028 ***(60)****.* ***(A)*** *in vitro liver metabolism, ICT12028* ***(60)*** *was incubated in mouse liver homogenate (1:4) for 5 h, timepoints were taken each hour. (n=1)* ***(B)*** *Comparison of mouse liver blank and mouse liver dosed with ICT12028* ***(60)*** *to identify baseline peaks.* ***(C)*** *in vivo tissue distribution of ICT12028* ***(60)*** *in mouse calculated from timepoints t= 0 h, 1 h, 4 h after administration of ICT12028* ***(60)*** *(20 mg/kg) by IP injection. (n=2). All values are expressed as mean ± SD of two biological replicates.*

3.8. Antagonism of FPR1 modulates growth of U-87 MG xenoplanted tumour in mice

The following work was carried out by Patricia Cooper (Institute of Cancer Therapeutics, University of Bradford) in support of this project.

A subcutaneous U-87 MG mouse xenograft model was used to investigate the efficacy of the FPR1 small molecule antagonist ICT12035 **(11)**. ICT12035 **(11)** was selected for this investigation because it had demonstrated the lowest IC_{50} for FPR1 in U-87 MG cells in this project and showed no cytotoxicity to U-87 MG cells. A maximum tolerated dose study was performed to determine the maximum dose. ICT12035 **(11)** reduces U-87 MG tumour growth *in vivo* (Figure 34). ICT12035 **(11)** did not show toxic effects *in vivo* up to concentrations of 100 mg/kg when administered via intraperitoneal (I.P.) injection (Figure 34A). Mice were dosed for 5 consecutive days then rested for 2 days. The volume of the tumours were measured for a period of 16 days in total . The maximum tolerated dose (MTD) could not be determined as the limit of solubility of ICT12035 **(11)** in the vehicle (peanut oil) was 100 mg/kg (Figure 34A). ICT12035 **(11)**, however, did not show toxicity at 100 mg/kg/dose.

The *in vivo* efficacy of ICT12035 **(11)** was tested on U-87 MG established tumours grown subcutaneously as xenografts (Figure 34B). One group received ICT12035 **(11)** administered by IP injection at 100 mg/kg/dose on days 0-4. For comparison, the control group was left untreated. Tumour volume was measured by callipers through the experiment and normalised to the respective volume on the initial day of treatment (day 0). 6.1 days tumour growth delay was observed in the ICT12035 **(11)** treated group versus the untreated group. Median relative tumour volume doubling time (RTV2) in

ICT12035 **(11)** treated group and untreated group were 15.5 and 9.4 days; the distributions in the two groups differed significantly (Mann–Whitney U = 8, n1 = n2 = 8, P < 0.05 two-tailed).

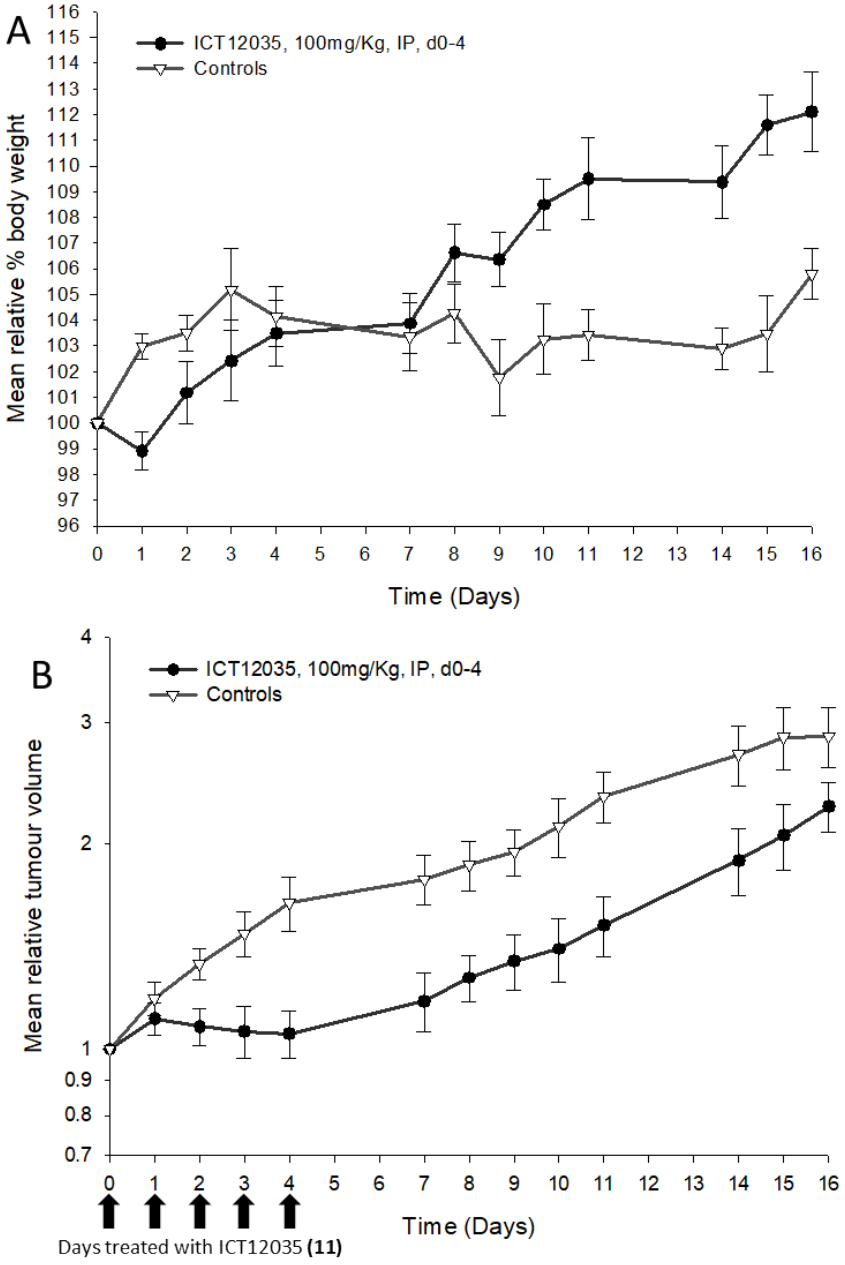

Group	Mean time to RTV2 (days)	Median time to RTV2 (days)	Growth delay (days)	Significance
ICT12035, 100mg/Kg, IP, days 0-4	14.3	15.5	6.1	p<0.05
Untreated controls	9.3	9.4	-	-

*Figure 34 In vivo efficacy study for ICT12035 **(11)** against xenografted U-87 MG tumours. **(A)** In vivo toxicity study of ICT12035 **(11)** at a fixed dose of 100 mg/kg administered by IP injection. **(B)** In vivo efficacy study of ICT12035 **(11)** administered by IP injection on days 0,1,2,3,4 (shown by the black arrows) at 100 mg/kg/dose. Tumour mass was measured by callipers. Mann-Whitney U tests were conducted to determine the statistical significance of differences in growth rate based on tumour doubling time (RTV2) between untreated control and treated groups (U = 8, p <0.05). All values are expressed as mean ± SD of eight biological replicates for each group.*

3.9. Discussion

The biological characteristics of GBM are very distinct in comparison to the lower grade astrocytoma (grade II and III) and indicate a greater step in malignancy. The unique pathologic and neuroimaging features that result from the transition from low grade astrocytoma to high grade GBM give an insight in to the potential mechanisms that drive the increased growth rate of GBM. A proposed model of tumour progression explains the development of "pseudopalisading necrosis", the relationship between pseudopalisades and angiogenesis and the strong correlation between pseudopalisades and the aggressive clinical nature and poor prognosis of GBM.[44, 238-240]

Necrotised glioma cells release cytoplasmic molecules into the extracellular milieu.[85] These molecules are often proinflammatory and recruit leukocytes to the tumour microenvironment. The inflammatory response within tumours is suggested to both hinder and promote tumour progression.[241] FPR1 is highly expressed in human GBM with lower expression in grade III astrocytoma and low to no expression in grade II and I astrocytoma.[175] The supernatant obtained from necrotic GBM cells contains an agonist that interacts with living GBM cells, this agonist has been identified as ANXA1, an endogenous agonist of FPR1.[175] As, previously discussed, double knockdown studies of FPR1 and ANXA1 in U-87 MG cells showed a significant reduction in tumorigenicity in mice.[85] The high level of expression of ANXA1 and FPR1 in primary tissue, and the significant effect of double knockdown of these proteins suggests an important role for the ligand/receptor axis in intensifying the malignant behaviour of GBM. Indeed, the activation of FPR1 by ANXA1 promotes angiogenesis, proliferation, and invasion in several other

cancers,[204, 242, 243] including GBM. [82, 84, 86, 174, 184, 199] It follows that inhibiting the activation of FPR1 by endogenous agonists such as ANXA1 may have a potential role as a therapy against GBM. To date, no small molecule FPR1 antagonists have been investigated as a potential GBM therapy. Several FPR1 antagonists were identified and synthesised, with ICT12035 **(11)** showing greatest FPR1 inhibition. I set out to provide preclinical proof of principle that a small molecule FPR1 antagonist can have potential as a therapy for GBM.

As previously mentioned, the expression of FPR1 is elevated in glioma tissue and the expression correlates with the stage of the tumour. Walenkamp has shown that the expression of FPR1 is regulated under conditions within the tumour microenvironment.[175] The observation (Figure 25) that FPR1 expression is elevated in the periphery of the necrotic/hypoxic foci both in a U-87 MG 3D spheroid model and in U-87 MG xenografted tissue, strengthens the correlation of FPR1 to tumour progression. The periphery of necrotic foci is known to be rich in the hypoxia markers HIF-1-α, carbonic anhydrase IX and a selection of MMPs.[108, 109] Although investigations have not been carried out for the driver for the elevation of FPR1 expression in the periphery of necrotic foci, it can be speculated that it may in part be due to hypoxia. In previous studies, it has been shown that the hypoxic pseudopalisades surrounding necrotic foci and the neighbouring vessels in GBM exert increased levels of SDF-1 [132] in glioma and ANXA1 [130] in prostate cancer; FPR1 expression could be elevated via similar mechanisms. It is important to note that FPR1 is also expressed on macrophages. As previously discussed, FPR1 agonists trigger a chemotactic response in macrophages drawing them to sites of injury.

Patient derived GBM samples expressed high levels of macrophages, representing up to 50 % of the tumour bulk.[244] These tumour-associated macrophages could account for FPR1 expression in GBM. A limitation of this study is the lack of specific macrophage and microglia markers. Evidence from a study released since the initial investigation was carried out supports the idea that macrophages and microglia do populate invading pseudopalisades surrounding necrotic foci in GBM.[245] It cannot then be ruled out that the increase in FPR1 expression surrounding necrotic foci is a result of FPR1 positive macrophage recruitment.

Whilst the expression of FPR1 on U-87 MG cells was significant in showing a role for FPR1 in disease, to test small molecule FPR1 antagonists the receptor on the U-87 MG cells must be functionally active. I demonstrated in monolayer cultures that FPR1 could be activated by the FPR1 agonist fMLF (Figure 28), triggering an increase in the intracellular concentration of cytoplasmic calcium mobilisation (also known as calcium flux) and that this response could be abrogated with small molecule FPR1 antagonists. In this assay, cells are first treated with a cell permeable dye that selectively binds to calcium (Ca^{2+}) cations and in doing so, produces fluorescence. This assay demonstrates the U-87 MG cells directly respond to the FPR1 ligand fMLF. Furthermore, it showed that the fMLF response could be abrogated in U-87 MG cells pre-treated with small molecule FPR1 antagonists, with ICT12035 **(11)** being the greatest inhibiter of FPR1 activation in our collection. The FPR1 antagonists were not however cytotoxic at assay concentrations, so the antagonist effect was not due to cell death. Cells, when treated with an agonist may become “desensitized”. When the receptor has been activated by a ligand

it may become internalised or the agonist ligand may bind blocking further activation. To ensure the antagonists were not in fact acting as agonists, the antagonist small molecules were tested in the calcium flux assay under the agonist setup. None of the small molecule FPR1 antagonists elicited an agonist response in FPR1 cells. Furthermore, to show the relevance of necrosis to FPR1 mediated glioma expansion, ICT12035 **(11)** was used to abrogate the response induced by U-87 MG necrotic supernatant in U-87 MG cells. The calcium mobilisation assay is a common assay for testing the efficacy of GPCR agonists and antagonists. The results observed in this investigation align with the observations in the literature for FPR1 antagonists. The FPR1 agonist fMLF has been shown to elicit a Ca^{2+} response in both GBM cells and neutrophils.[82, 85, 246] Additionally, FPR1 antagonists have been shown to abrogate the fMLF mediated Ca^{2+} response in neutrophils.[215, 246]

GBM cells are known to diffusely infiltrate surrounding brain tissue by active migration either along the white matter tracts, intra-parenchymal or along blood vessels.[247] Interestingly, Ca^{2+} oscillations have been shown to enhance cell migration in a number of cell types including U-87 MG.[248] I have previously shown that FPR1 activation causes Ca^{2+} mobilisation/ intracellular concentration increases. To investigate the hypothesis that FPR1 activation promotes glioma migration *in vitro*, a Transwell migration assay was used. The assay allows for the examination of cell migration across a membrane barrier with 10 μM pores towards higher concentrations of fMLF, an FPR1 peptide agonist. Furthermore, the assay can be used to quantitatively study the efficacy of FPR1 small molecule antagonists on reducing fMLF-mediated migration. Firstly, fMLF-mediated migration was tested. I demonstrate that the

FPR1 agonist fMLF significantly increases cell migration through the porous membrane compared to the assay with no agonist (Figure 30). Furthermore, I show that small molecule FPR1 antagonists ICT5100 **(5)**, ICT7009 **(10)** and ICT12028 **(60)** can abrogate the fMLF-mediated migration in a dose-dependent manner. This assay can show cell chemotaxis towards a higher concentration of a chemoattractant, in this case fMLF. While this assay captures vital cell mobility data, it does not capitulate the cells' ability to migrate or invade through the ECM.

Aggressive glioma invades the surrounding brain tissue making it difficult to remove the entire tumour surgically without removing/ damaging the delicate healthy brain tissue. The invasion of glioma cells across white matter is believed to be one of the major factors responsible for the resistance of these tumours to treatment. Therefore, investigation into FPR1's role in the invasion of glioma cells and the potential to antagonise this invasion with small molecule FPR1 antagonists is essential for the development of a potential therapy. Monolayer cell culture experiments work well for initially characterisation of potential antagonists; however, they do not fully represent the true nature of the cells. 3D-cultures can better simulate *in vivo* microenvironments within the tumour and have been increasingly investigated and used to study tumour cell biology.[160] When applied to drug discovery, 3D-culture *in vitro* studies could provide data that better capitulates clinical tumours over 2D methods.[160] This is of importance for the discovery of new glioma therapies as many potential therapies that show efficacy in preclinical models have failed to perform in the clinic. Previous work has identified that glioma cells grown in 3D collagen scaffold cultures showed closer similarities

to the *in vivo* microenvironment, greater degrees of differentiation and quiescence than cells in 2D-cultures.[156] Furthermore, Walenkamp's work demonstrates the relevance of the microenvironment in regulating FPR1 expression in glioma and so, at least for targeting FPR1, 3D-culture methods could prove more beneficial and relevant.[175] I demonstrate that U-87 MG cells, grown as a 3D-multicellular spheroid (hanging drop method) and embedded into a collagen scaffold, have a significant invasion response when treated with fMLF (Figure 31); furthermore, this response can be abrogated significantly by treatment with the FPR1 antagonist ICT12035 **(11)**. By performing the invasion assay in a 3D environment, the assay better capitulates the cell-cell interactions observed in the tumour environment. Additionally, the collagen matrix acts as a basic ECM to simulate the tissue surrounding the GBM. By introducing a more complex matrix to the assay, we could better mimic the brain/tumour environment. However, in doing so, would increase assay costs, time, and complexity while the collagen model produces enough data for the current investigation.

Knockdown of FPR1 in glioma cells has been shown to reduce the tumorigenicity in *in vivo* glioma models.[85] Prior to an *in vivo* efficacy trial, *in vivo* tissue distribution was investigated to ensure the FPR1 antagonist would reach the target tissue (Figure 33). The FPR1 antagonist ICT12028 **(60)**, the trans isomer of ICT12035 **(11)** was given as a single dose of 20 mg/kg to mice bearing U-87 MG xenograft tumours. The tissue was analysed by LCMS and ICT12028 **(60)** was detected in all tissues analysed. Importantly for this study, the compound was observed in brain and tumour tissue at concentrations exceeding the IC_{50} determined in the calcium mobilisation assay. Furthermore,

a basic *in vitro* metabolism study of ICT12028 **(60)** incubated in liver homogenate suggested the compound was stable in liver for 74 h. While the studies had not been concluded for ICT12035 **(11)**, the data for isomer ICT12028 **(60)** indicated desirable distribution and minimal to no metabolism in liver. This data gives an idea of the potential pharmacokinetics for ICT12035 **(11)**.

An *in vivo* efficacy study to further investigate the therapeutic potential of small molecule FPR1 antagonist ICT12035 **(11)**. The *in vivo* GBM model would better capitulate tumour heterogeneity/ tumour microenvironment over *in vitro* methods. Mice bearing xenografted U-87 MG tumours were treated with ICT12035 **(11)** (100 mg/kg/dose, I.P.) for 5 days. Over the course of the experiment the growth rate for the treated mice was delayed by 6.1 days relative to the untreated group (Figure 34). Positively, no toxic side effects were observed in the mice in a maximum tolerable dose study. The small molecule FPR1 antagonist ICT12035 **(11)** was able to significantly abrogate tumour growth *in vivo* without compromising the overall health of the mice. This observation is consistent with previous reports; mice bearing xenografted tumours were treated with nordy, which is not an antagonist of FPR1 receptor but inhibits the FPR1 protein expression along with the expression of several other proteins; also abrogated the growth of tumours without cytotoxic effects.[249]

For the *in vivo* study, tumours were xenografted into the flank of mice, this gives a “better” representation of the tumour microenvironment over *in vitro* studies and demonstrates the efficacy of therapeutics *in vivo*. It does not however fully capitulate the microenvironment of the brain. An orthotopic

xenograft model, where the cancer cells are implanted or injected into the organ of origin would better simulate the original tumour microenvironment. In the case of glioma, the cancer cells would be implanted into the animal brain.

3.10. Conclusions

A large volume of evidence has supported FPR1 as a critical player in inflammation and inflammatory disease. More recent work instigates FPR1 as also playing a critical role in cancers including but not limited to high-grade glioma.[84, 202, 204, 224, 226, 242, 243] FPR1 is activated by *N*-formylated peptides, derived from either mitochondrial proteins or bacterial peptides.[162] It was also shown that FPR1 was activated by the necrotic supernatant of GBM cells and that ANXA1 was the responsible protein contained within the necrotic supernatant.[85] Both FPR1 and its endogenous ligand ANXA1 show increased expression with higher grades of glioma malignancy,[83, 84, 86, 190] and the tumour microenvironment plays an important role in modulating FPR1 expression and activation.[175]

In this investigation, the relationship between necrosis, hypoxia and FPR1 were explored. It was shown that U-87 MG expressed FPR1 *in vitro* and *in vivo.* This data meant U-87 MG was a suitable cell line to explore the functional relationship of FPR1 and GBM further. Moreover, the data suggests expression of FPR1 increased under hypoxia *in vitro*. Increased expression was also observed in the periphery of the necrotic foci in xenografted tumours, a region known to be hypoxic. The expression of FPR1 adjacent to the necrotic niche is of particular importance as the endogenous agonist for GBM in glioma is released by necrotic GBM cells. Interestingly, necrosis in glioma is a

prognostic marker inferring a more malignant/ aggressive tumour.[37, 104, 123] Furthermore, cellular necrosis can also result from certain treatment modalities for glioma.[53, 104, 113, 114] This raises an interesting hypothesis that associates, in part, a poor clinical outcome of current therapies in glioma, to the activation of FPR1 as a result of those treatments.

During this project, a selection of small molecule FPR1 antagonists were synthesised and characterised. The results of this investigation demonstrate that small molecule FPR1 antagonists can inhibit FPR1 activation in GBM cells *in vitro* and *in vivo*. FPR1 antagonists were shown to reduce FPR1 mediated calcium mobilisation, cell migration and invasion *in vitro*.

The main aim was to demonstrate through preclinical proof of principle that the administration of the FPR1 antagonists identified through this project can retard expansion of glioma *in vivo* suggesting their potential as a new therapy for GBM. The FPR1 antagonist ICT12035 **(11)** was able to cause significant growth delay in an *in vivo* U-87 MG xenograft efficacy experiment. The result of this efficacy study, when carried out, was a novel and significant observation of an FPR1 small molecule antagonist reducing growth rate of GBM xenograft tumours. Given the rising importance of FPR1 in GBM and other cancers, further investigation into small molecule FPR1 antagonists and the FPR1/necrosis relationship could provide opportunities for more efficient treatment modalities.

3.11. Limitations of this study

This body of research showed the potential of small molecule FPR1 antagonists as therapeutic agents for the treatment of GBM. FPR1 activation is shown to mediate several responses *in vitro* while expression of FPR1 confers a more aggressive phenotype. [82, 173, 174] Using FPR1 small molecule antagonists, the responses elicited by FPR1 activation in U-87 MG cells can be abrogated *in vitro* and *in vivo*. This study focused primarily on the U-87 MG cell line for all live cell assays. This is a disadvantage to this study as immortalised cells cannot be considered “normal”. Immortalised cells divide indefinitely and may express unique gene signatures not found in patient derived GBM cultures. U-87 MG may not express relevant attributes or functions of “normal” GBM cells. It is therefore important to expand this study with future work focussing on identifying patient derived cell lines expressing FPR1 to better capitulate the original tumour and clinical presentation of GBM. Additionally, an expanded *in vivo* efficacy study of small molecule FPR1 antagonists could provide vital information. The efficacy study used xenografted U-87 MG tumours in the flank of a mouse. While this model is able to capitulate some of the cell-cell interactions within the tumour, the model is unable to fully recapitulate the multicellular microenvironment in which patient tumour cells reside. Unmanipulated patient-derived tumour cell cultures in an orthotopic brain model would present a more reliable depiction of the tumour features over use of an established cell line in a xenograft flank model.

3.12. Future Work

The efficacy study of ICT12035 **(11)** showed a significant U-87 MG tumour growth delay for the ICT12035 **(11)** treated group relative to the untreated group. However, the mechanism of action had not been fully explored. From this study, it is understood that ICT12035 **(11)** inhibits FPR1 activation. It has also been shown that ICT12035 **(11)** does not induce cytotoxicity in U-87 MG cells. It is therefore important to investigate differences between tumours in the treated and untreated groups. Tumour histology and molecular markers should be investigated. Building on this result, efficacy of small molecule FPR1 antagonists should be investigated in primary patient-derived orthotopic models to better validate FPR1 targeting in GBM.

The PKPD investigation for ICT12035 **(11)** was limited to a prediction based on information from the isomer ICT12028 **(60)**. Investigations need to be carried out to provide a detailed picture of ICT12035 **(11)**. Selectivity of ICT12035 **(11)** should be determined. Before ICT12035 **(11)** is carried forward for further investigation, absorption, distribution, metabolism, and excretion should be determined. A BBB *in vitro* model could be used to investigate blood-brain penetration as the BBB is one barrier to therapy when treating glioma. The results of this work would determine if further structure-activity relationship should be carried out to build on the efficacy and PKPD of ICT12035 **(11)**.

4. Chapter 4: Chemistry Experimental

4.1. General Methods and Instrumentation

Commercially available reagents were used as received without additional purification. All solvents were of reagent grade. Petroleum ether refers to the fraction of petroleum spirit with a boiling point in the range of 60 to 80 °C. Where stated, mixtures of solvents are referred to as percentage volume to volume (v/v) ratios.

Products were typically purified by column chromatography using Merck 9385 silica gel 60 (40-63 μm). Analytical thin layer chromatography (TLC) was conducted on Merck silica gel 60 F254 glass backed plates. Visualisation of the reaction components was accomplished by illumination under short wavelength (254 nm) ultraviolet light or using basic potassium permanganate ($KMnO_4$) stain unless otherwise stated.

Proton Nuclear Magnetic Resonance (^{1}H NMR) spectra were recorded on a BRUKER Advance 400 FT NMR (400 Hz) Spectrometer. Carbon Nuclear Magnetic Resonance (^{13}C NMR) were performed on the same instruments operating at 101 Hz. Chemical shifts are reported in parts per million (ppm/ δ) with internal reference to tetramethyl silane. Coupling constants (*J*) are expressed in Hertz (Hz) and spectra are reported with the following abbreviations: singlet (s), doublet (d), triplet (t), quartet (q), doublet of doublets, (dd), doublet of triplets (dt), multiplet (m) and broad (br).

^{1}H-^{1}H coupling was determined using double quantum-filtered COSY; ^{1}H-^{13}C $^1J_{CH}$ coupling by HMQC experiments.

Routine mass spectra were run on a Micromass Quattro Ultima spectrometer in the electrospray ionisation (ESI). High resolution mass

spectrometry was performed at the National Mass Spectrometry Centre Swansea using MAT95 or MAT900 in the electrospray ionisation (ESI) mode.

Single crystal X-ray diffraction was carried out by Professor Ian J. Scowen (University of Lincoln). All data and experimental method were provided by Professor Ian J. Scowen. Single crystals suitable for X-ray diffraction measurements were mounted on MiTeGen Dual-Thickness MicroMounts and analysed using a Bruker D8 Venture diffractometer with a Photon detection system. Unit cell measurements and data collections were performed at 173 K using Cu Kα radiation (λ = 1.54056 Å). Structure solutions were carried out by direct methods and refinement with SHELXL[250] was finished using the ShelXle software[251]. All non-hydrogen atoms were refined anisotropically, the C–H hydrogen atoms placed in idealized positions and the N–H and O–H hydrogen atoms found from the electron density map and refined with fixed bond distances and thermal parameters riding on the parent atom. Absolute configuration was confirmed.

All chemical structures, calculated mass and chemical names were generated using Perkin Elmer ChemDraw Professional.

4.2. Synthetic Procedures

4.2.1. 2-(1-methyl-1H-benzo[d]imidazol-2-yl)acetonitrile 21

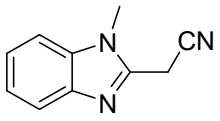

(21)

2-methylaminoaniline **(19)** (3.22 g, 26.4 mmol) and methylcyanoacetate **(20)** (2.61 g, 26.4 mmol) were gently heated under reflux (~180 °C) with no solvent. After 4 h, the reaction was left to cool, affording a black oil. The product was purified by flash chromatography, eluting with 20 % v/v ethyl acetate in petroleum ether to afford 1.20 g (18 %) of a light brown/green solid. NMR experimental data was used to confirm the desired product had been formed.

^{1}H NMR (400 MHz, DMSO) δ 7.55 (m, 2H, Ar H), 7.20 (m, 2H, Ar H), 4.50 (s, 2H CC$\underline{H_2}$C), 3.74 (s, 3H, NC$\underline{H_3}$).

^{13}C NMR (101 MHz, DMSO) δ 145.7, 141.7, 135.9, 122.4, 121.8, 118.8, 116.3, 110.2, 29.8, 17.4.

4.2.2. 1-(5-ethyl-2,4-dihydroxyphenyl)-2-(1-methyl-1H-benzo[d]imidazol-2-yl)ethenone 23-keto/enol

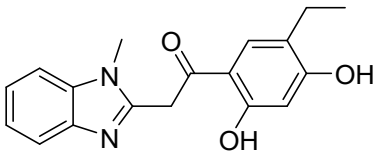

(23)-Keto

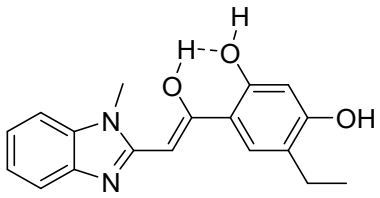

(23)-Enol

In a pressure tube, to 2-(1-methyl-1H-benzo[d]imidazol-2-yl)acetonitrile **(21)** (500 mg, 2.92 mmol) and 4-ethylresorcinol **(22)** (404 mg, 2.92 mmol) was added boron trifluoride diethyl etherate (6 ml). The reaction mixture was immediately saturated with hydrogen chloride gas via bubbling for 1 min and then the pressure tube was sealed. The reaction was stirred at 60 °C for 24 h. The reaction mixture was transferred to a round bottomed flask and was quenched with distilled water (120 ml). The resultant mixture was heated under reflux for 4 h. After cooling, the pH was adjusted to 7 with aqueous ammonia solution (33 % w/v) and the precipitate collected by filtration and dried in a vacuum desiccator to afford 753 mg (79 %) of a green solid. NMR indicated that the desired product was acquired as a 91:9 mix of the enol to keto respectively. This product was carried through without further purification.

(23)-enol

^{1}H NMR (400 MHz, DMSO) δ 12.33 (s, 1H, OH), 10.09 (s, 1H, OH), 7.78 (s, *J* = 7.4 Hz, 1H, C<u>H</u>=C-OH), 7.66 (m, 2H, Ar H), 7.37 (d, J = 5.4 Hz, 2H Ar H), 6.22 (s, 1H Ar H), 6.01 (s, 1H Ar H), 3.87 (s, 3H, NCH_3), 2.48 (q, 2H, $CC\underline{H_2}CH_3$), 1.12 (t, *J* = 7.4 Hz, 3H, $CCH_2C\underline{H_3}$).

^{13}C NMR (101 MHz, DMSO) δ 168.20, 161.32, 157.87, 149.49, 132.13, 130.50, 127.45, 124.95, 123.87, 113.32, 111.17, 109.16, 104.04, 74.75, 30.71, 22.96, 15.23.

4.2.3. 6-ethyl-2-methyl-3-(1-methyl-1H-benzo[d]imidazol-2-yl)-4-oxo-4H-chromen-7-yl acetate 5 [213]

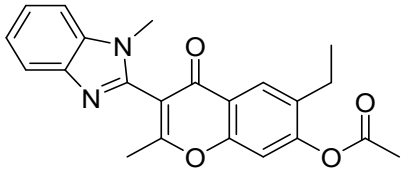

(5)

A solution of **(23)** (150 mg, 0.48 mmol) in anhydrous pyridine (3 ml) was treated with acetic anhydride (2 ml). The resulting solution was stirred at 40 °C overnight. After cooling to rt, the solution was poured over ice and left for 24 h. The crystals formed were collected by filtration, washed with water, and air-dried. Crystallization from hexanes provided **(5)** (117 mg, 65 %) as a white crystalline solid. NMR and mass spectrometry confirmed that the desired product had been obtained.

HRMS m/z (ESI) calcd. for $C_{22}H_{20}N_2O_4H$ 377.1507, found $[M+H]^+$ 377.1502.

^{1}H NMR (400 MHz, $CDCl_3$) δ 8.05 (s, 1H, Ar H), 7.74 (m, 1H, Ar H), 7.34 (m, 1H, Ar H), 7.23-7.27 (m, 2H, Ar H), 7.21 (s, 1H, Ar H), 3.59 (s, 3H, NCH_3), 2.59 (q, J = 7.5 Hz, 2H, $CC\underline{H_2}CH_3$), 2.39 (s, 3H, $O{=}CCH_3$), 2.32 (s, 3H, C-O-CCH_3), 1.19 (t, *J* = 7.5 Hz, 3H, $CCH_2C\underline{H_3}$).

^{13}C NMR (101 MHz, $CDCl_3$) δ 175.0, 168.8, 168.5, 154.5, 153.1, 147.2, 143.0, 135.9, 134.5, 126.3, 122.7, 122.0, 120.9, 119.9, 114.2, 111.4, 109.6, 30.7, 22.9, 20.9, 19.7, 13.8.

4.2.4. Ethyl 5-amino-1-phenyl-1H-pyrazole-4-carboxylate 36

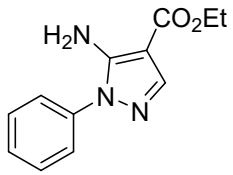

(36)

To a stirred solution of ethyl (*Z*)-2-cyano-3-ethoxyacrylate c**(34)** (10.43 g, 61.7 mmol) dissolved in ethanol (100 ml) was added phenylhydrazine **(35)** (6.07 ml, 61.7 mmol) and heated under reflux under a nitrogen atmosphere. After 18 h, the reaction was left to cool to room temperature. The solvent was removed under reduced pressure to afford an orange solid which was purified by recrystallisation from hot ethanol to give 11.13 g (78 %) of orange/yellow crystals. NMR and mass spectrometry confirmed that the desired product had been obtained.

HRMS (ESI) calcd. for $C_{12}H_{13}N_3O_2H$ 232.1041, found 232.1079 $[M+H]^+$.

^{1}H NMR (400 MHz, $CDCl_3$) δ 7.78 (s, 1H, pyrazole-H), 7.57 – 7.45 (m, 4H, Ar H), 7.44 – 7.35 (m, 1H, Ar H), 5.31 (s, 2H, NH_2), 4.30 (q, J = 7.1 Hz, 2H, $OC\underline{H}_2CH_3$), 1.36 (t, J = 7.1 Hz, 3H, $OCH_2C\underline{H}_3$).

^{13}C NMR (101 MHz, $CDCl_3$) δ 164.8, 149.1, 140.8, 137.7, 129.9, 128.3, 123.9, 96.3, 59.8, 14.7.

4.2.5. Ethyl 5-(4-methylphenylsulfonamido)-1-phenyl-1H-pyrazole-4-carboxylate 37

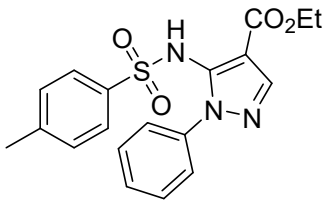

(37)

To a stirred suspension of sodium hydride (60 % dispersion in mineral oil) (302 mg, 7.55 mmol) in anhydrous tetrahydrofuran (3 ml) was added a solution of ethyl 5-amino-1-phenyl-1H-pyrazole-4-carboxylate **(36)** (1.00 g, 4.32 mmol) in anhydrous tetrahydrofuran (2 ml) under an argon atmosphere at 0 °C. After 30 min stirring at 0 °C, a solution of tosyl chloride (1.24 g, 6.49 mmol) in anhydrous tetrahydrofuran (2 ml) was added and the reaction was left to warm to room temperature. After stirring for 18 h, the reaction was quenched with distilled water (10 ml), the pH adjusted to ~1 with 5 % w/v hydrochloric acid and the resultant mixture extracted with dichloromethane (4 x 10 ml). The organic phase was washed with brine, dried over magnesium sulphate, and filtered. The solvent was removed under reduced pressure to afford an orange oil, which was purified by flash chromatography, eluting with 20 % v/v ethyl acetate in petroleum ether to afford 304 mg (18 %) of an orange solid. NMR and HRMS experiments were used to confirm the desired product had been produced.

HRMS (ESI) calcd. for $C_{19}H_{19}N_3O_4SH$ 386.1130, found 386.1170 $[M+H]^+$.

^{1}H NMR (400 MHz, $CDCl_3$) δ 7.89 (s, 1H, pyrazole-H), 7.65 (m, 3H, Ar H, NH), 7.50 – 7.34 (m, 5H, Ar H), 7.17 (d, J = 8.2 Hz, 2H, Ar H), 4.05 (q, J = 7.2 Hz, 2H, $OC\underline{H_2}CH_3$), 2.39 (s, 3H, Ar CH_3), 1.21 (t, J = 7.2 Hz, 3H, $OCH_2C\underline{H_3}$).

^{13}C NMR (101 MHz, $CDCl_3$) δ 162.7, 144.5, 140.4, 138.9, 138.0, 134.7, 129.4, 129.1, 128.3, 127.6, 124.3, 107.8, 60.5, 21.6, 14.2.

4.2.6. 5-(4-methylphenylsulfonamido)-1-phenyl-1H-pyrazole-4-carboxylic acid 38

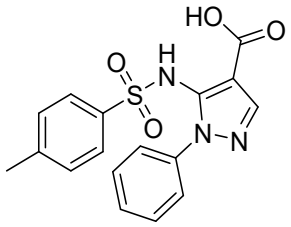

(38)

To a stirred solution of ethyl 5-(4-methylphenylsulfonamido)-1-phenyl-1H-pyrazole-4-carboxylate **(37)** (720 mg, 1.87 mmol) in ethanol (9 ml) was added a suspension of lithium hydroxide monohydrate (314 mg, 7.47 mmol) in distilled water (3 ml) and heated under reflux. After 16 h the reaction was left to cool to room temperature. The pH of the reaction mixture was adjusted to 1-2 with hydrochloric acid solution (6 M). The resultant mixture extracted with dichloromethane (3 x 10 ml). The organic phase was washed with water and brine, dried over magnesium sulphate, and filtered. The solvent was removed under reduced pressure to afford 591 mg (88 %) of a white powder. NMR and HRMS experiments were used to confirm the desired product had been produced.

HRMS (ESI) calcd. for $C_{17}H_{15}N_3O_4SH$ 358.0817, found 358.0857 $[M+H]^+$.

^{1}H NMR (400 MHz, MeOD) δ 7.91 (s, 1H, pyrazole-H), 7.43 (dd, J = 8.1, 1.7 Hz, 2H, Ar H), 7.39 – 7.26 (m, 5H, Ar H), 7.12 (d, J = 8.2 Hz, 2H, Ar H), 2.32 (s, 3H, Ar CH_3).

^{13}C NMR (101 MHz, MeOD) δ 145.2, 142.6, 140.0, 138.1, 138.0, 130.5, 130.0, 129.4, 128.3, 126.3, 112.4, 21.5.

4.2.7. (*S*)-N-(3,3-dimethylbutan-2-yl)-5-(4-methylphenylsulfonamido)-1-phenyl-1H-pyrazole-4-carboxamide 9 [215]

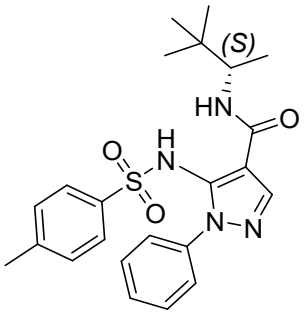

(9)

To a stirred solution of 5-(4-methylphenylsulfonamido)-1-phenyl-1H-pyrazole-4-carboxylic acid **(38)** (559 mg, 1.56 mmol) in dimethylformamide (9 ml) was added diisopropylethylamine (0.82 ml, 4.692 mmol) under an argon atmosphere. After 10 min of stirring, to the reaction was added a solution of HATU (595 mg, 1.56 mmol) in dimethylformamide (2 ml). After a further 20 min stirring (*S*)-3,3-dimethyl-2-butylamine (0.22 ml, 1.56 mmol) was added to the reaction and stirred for 16 h at room temperature. The reaction was quenched with distilled water (30 ml), the pH adjusted to ~1 with 5 % w/v hydrochloric acid and the resultant mixture extracted with ethyl acetate (2 x 30 ml). The organic phase was washed with ammonium chloride solution followed by brine, dried over magnesium sulphate, and filtered. The solvent was removed under reduced pressure to afford a white solid which was purified by flash chromatography, eluting with 30 % v/v ethyl acetate in petroleum ether to afford 532 mg (77 %) of a white powder. NMR and HRMS experiments were used to confirm the desired product had been produced.

HRMS (ESI) calcd. for $C_{23}H_{28}N_4O_3SH$ 441.1916, found 441.1946 $[M+H]^+$.

^{1}H NMR (400 MHz, $CDCl_3$) δ 8.66 (s, 1H, NH), 7.70 (s, 1H, pyrazole-H), 7.57 (m, 2H, Ar H), 7.47 – 7.33 (m, 5H, Ar H), 7.11 (d, *J* = 8.2 Hz, 2H, Ar H), 5.62 (d, *J* = 9.7 Hz, 1H, CHN<u>H</u>), 3.82 (dq, *J* = 9.7, 6.9 Hz, 1H, NHC<u>H</u>CH_3), 2.35 (s, 3H, Ar, CH_3), 1.01 (d, *J* = 6.9 Hz, 3H, CHC<u>H_3</u>), 0.87 (s, 9H, C(C<u>H_3</u>)$_3$) ppm.

^{13}C NMR (101 MHz, $CDCl_3$) δ 161.8, 144.2, 139.1, 137.2, 136.9, 134.9, 129.4, 129.1, 128.2, 127.6, 124.2, 110.0, 52.5, 34.2, 26.2, 21.6, 16.1.

4.2.8. Ethyl 5-amino-3-methyl-1-phenyl-1H-pyrazole-4-carboxylate 40

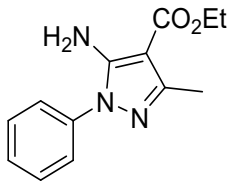

(40)

To a stirred solution of ethyl (*Z*)-2-cyano-3-ethoxybut-2-enoate **(39)** (3.00 g, 16.4 mmol) dissolved in ethanol (40 ml) was added phenylhydrazine **(35)** (1.61 ml, 16.4 mmol) and heated under reflux under a nitrogen atmosphere. After 22 h, the reaction was left to cool to room temperature. The solvent was removed under reduced pressure to afford an orange solid which was purified by recrystallisation from ethanol to give 522 mg (13 %) of fine white crystals. NMR and HRMS experiments were used to confirm the desired product had been produced.

HRMS (ESI) calcd. for $C_{13}H_{15}N_3O_2$ 246.1198, found 246.1236 $[M+H]^+$.

^{1}H NMR (400 MHz, $CDCl_3$) δ 7.56 – 7.42 (m, 4H, Ar H), 7.38 (dd, *J* = 10.9, 4.2 Hz, 1H, Ar H), 5.34 (s, 2H N$\underline{H_2}$), 4.31 (q, *J* = 7.1 Hz, 2H, OC$\underline{H_2}$$CH_3$), 2.41 (s, 3H, CH_3), 1.37 (t, *J* = 7.1 Hz, 3H, $OCH_2C\underline{H_3}$).

^{13}C NMR (101 MHz, $CDCl_3$) δ 165.5, 150.5, 150.1, 137.7, 129.9, 128.0, 124.0, 94.8, 59.7, 14.7, 14.7.

4.2.9. Ethyl 3-methyl-5-(4-methylphenylsulfonamido)-1-phenyl-1H-pyrazole-4-carboxylate 41

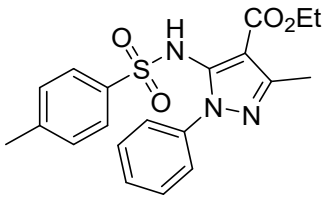

(41)

To a stirred suspension of sodium hydride (60 % dispersion in mineral oil) (134 mg, 3.35 mmol) in anhydrous tetrahydrofuran (3 ml) was added a solution of ethyl 5-amino-3-methyl-1-phenyl-1H-pyrazole-4-carboxylate **(40)** (632 mg, 2.58 mmol) dissolved in anhydrous tetrahydrofuran (3 ml) under an argon atmosphere at 0 °C. After 30 min stirring at 0 °C, a solution of tosyl chloride (639 mg, 3.35 mmol) in anhydrous tetrahydrofuran (3 ml) was added and the reaction left to reach room temperature. After stirring for 2 h, the reaction was quenched with distilled water (3 ml), the pH adjusted to ~1 with 5 % w/v hydrochloric acid and the resultant mixture extracted with dichloromethane (4 x 10 ml). The organic phase was washed with 5 % w/v hydrochloric acid and brine, dried over magnesium sulphate, and filtered. The solvent was removed under reduced pressure to afford a brown oil. The oil was purified by flash chromatography, eluting with 20 % v/v ethyl acetate in petroleum ether to afford 304 mg (18 %) of orange solid. NMR and mass spectrometry confirmed that the desired product had been obtained.

HRMS (ESI) calcd. for $C_{20}H_{21}N_3O_4SH$ 400.1916, found 400.1322 $[M+H]^+$.

^{1}H NMR (400 MHz, $CDCl_3$) δ 7.79 (s, 1H, NH), 7.63 – 7.55 (m, 2H Ar H), 7.46 – 7.31 (m, 5H, Ar H), 7.15 (d, *J* = 8.0 Hz, 2H, Ar H), 4.05 (q, *J* = 7.1 Hz, 2H, $OC\underline{H_2}CH_3$), 2.40 (s, 3H, Tosyl-$C\underline{H_3}$), 2.38 (s, 3H, CH_3), 1.23 (t, *J* = 7.1 Hz, 3H, $OCH_2C\underline{H_3}$).

^{13}C NMR (101 MHz, $CDCl_3$) δ 163.7, 150.3, 144.5, 139.0, 138.7, 135.1, 129.4, 129.1, 128.1, 127.7, 124.5, 105.9, 60.5, 21.7, 14.5, 14.3.

4.2.10. 3-methyl-5-(4-methylphenylsulfonamido)-1-phenyl-1H-pyrazole-4-carboxylic acid 42

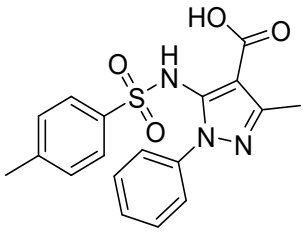

(42)

To a stirred solution of ethyl 3-methyl-5-(4-methylphenylsulfonamido)-1-phenyl-1H-pyrazole-4-carboxylate **(41)** (495 mg, 1.24 mmol) dissolved in ethanol (4 ml) was added a suspension of lithium hydroxide monohydrate (208 mg, 4.96 mmol) in distilled water (3 ml). The reaction mixture was heated under reflux. After 16 h the reaction was left cool to room temperature. The pH of the reaction mixture was adjusted to 1-2 with hydrochloric acid solution (6 M). The resultant mixture was extracted with dichloromethane (3 x 10 ml). The organic phase was washed with water and brine, dried over magnesium sulphate, and filtered. The solvent was removed under reduced pressure to afford 378 mg (82 %) of a white powder. NMR and mass spectrometry confirmed that the desired product had been obtained.

HRMS (ESI) calcd. for $C_{18}H_{17}N_3O_4SH$ 372.0973, found 372.1013 $[M+H]^+$

^{1}H NMR (400 MHz, MeOD) δ 7.44 – 7.21 (m, 7H Ar H), 7.12 (d, *J* = 8.2 Hz, 2H, Ar H), 2.34 (s, 3H, C$\underline{H_3}$), 2.32 (s, 3H, Tosyl-C$\underline{H_3}$).

^{13}C NMR (101 MHz, MeOD) δ 165.6, 152.6, 145.2, 139.9, 138.9, 138.1, 130.8, 130.5, 130.0, 129.9, 129.2, 129.1, 128.3, 126.4, 126.3, 109.7, 21.5, 14.3.

4.2.11. (*S*)-N-(3,3-dimethylbutan-2-yl)-3-methyl-5-(4-methylphenylsulfonamido)-1-phenyl-1H-pyrazole-4-carboxamide 10 [215]

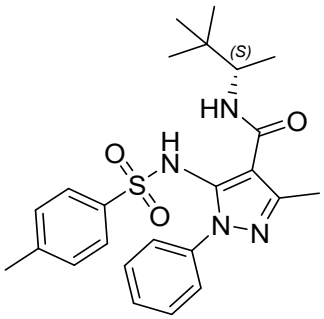

(10)

To a stirred solution of 3-methyl-5-(4-methylphenylsulfonamido)-1-phenyl-1H-pyrazole-4-carboxylic acid **(42)** (307 mg, 0.83 mmol) in dimethylformamide (9 ml) was added diisopropylethylamine (0.43 ml, 2.48 mmol) under an argon atmosphere. After 10 min of stirring, to the reaction was added a solution of HBTU (314 mg, 0.83 mmol) in dimethylformamide (2 ml). After a further 20 min stirring (*S*)-3,3-dimethyl-2-butylamine (0.113 ml, 0.83 mmol) was added to the reaction and stirred for 16 h at room temperature. The reaction was quenched with distilled water (15 ml), the pH adjusted to ~1 with 5 % w/v hydrochloric acid and the resultant mixture extracted with ethyl acetate (2 x 30 ml). The organic phase was washed with ammonium chloride solution followed by brine, dried over magnesium sulphate, and filtered. The solvent was removed under reduced pressure to afford a white solid which was purified by flash chromatography, eluting with 30 % v/v ethyl acetate in petroleum ether to afford 357 mg (95 %) of a white powder. NMR and mass spectrometry confirmed that the desired product had been obtained.

HRMS (ESI) calcd. for $C_{24}H_{30}N_4O_3SH$ 455.2072, found 455.2107 $[M+H]^+$

^{1}H NMR (400 MHz, $CDCl_3$) δ 8.86 (s, 1H, SO_2NH), 7.46 – 7.40 (m, 2H, Ar H), 7.37 (d, *J* = 8.3 Hz, 2H, Tosyl-Ar H), 7.34 – 7.25 (m, 3H, Ar H), 7.05 (d, *J* = 8.2 Hz, 2H, Tosyl Ar H), 6.07 (d, *J* = 9.6 Hz, 1H, NHCHCH$_3$), 3.91 – 3.81 (m, 1H, NHCHCH$_3$), 2.44 (s, 3H, CH_3), 2.33 (s, 3H, Tosyl-CH_3), 1.02 (d, *J* = 6.8 Hz, 3H, NHCHCH_3), 0.88 (s, 9H, C(CH_3)$_3$).

^{13}C NMR δ 162.9, 146.5, 144.0, 138.7, 136.4, 135.4, 129.4, 128.9, 127.76, 127.4, 124.3, 110.2, 52.9, 34.1, 26.2, 21.6, 16.1, 14.7.

4.2.12. 1,4-dioxaspiro[4.5]decan-8-ol 46

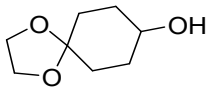

(46)

1,4-dioxaspiro[4.5]decan-8-one **(45)** (20.0 g; 128 mmol) was completely dissolved in ethanol (270 ml) and cooled to 0 °C. Sodium borohydride (5.79 g; 153 mmol) was added to the reaction mixture and stirred under nitrogen at room temperature. After 24 h, most of the solvent was removed and dichloromethane (200 ml) added. The reaction was cooled to 0 °C and sodium hydroxide solution (2 M) added (slowly) to neutralise the reaction. The aqueous phase was extracted with dichloromethane (50 ml x 2). The organic phase was collected and dried over magnesium sulphate, filtered and the solvent removed under reduced pressure to afford 17.83 g (88 %) of **(46)** as a clear oil. NMR spectroscopy was used to confirm the product had been obtained.

^{1}H NMR (400 MHz, $CDCl_3$) δ 4.01 – 3.86 (m, 4H, OC$\underline{H_2}$), 3.78 (ddd, *J* = 18.2, 9.1, 4.9 Hz, 1H, C$\underline{H}$OH), 1.97 – 1.73 (m, 4H, cyclohexane-C$\underline{H_2}$), 1.73 – 1.47 (m, 4H, cyclohexane-C$\underline{H_2}$).

^{13}C NMR (101 MHz, $CDCl_3$) δ 108.4, 68.3, 64.4, 32.2, 31.7.

4.2.13. 8-methoxy-1,4-dioxaspiro[4.5]decane 47

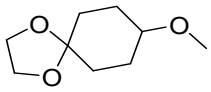

(47)

To a suspension of sodium hydride (60 % in mineral oil) (4.55 g; 114 mmol) in anhydrous tetrahydrofuran (50 ml) under nitrogen at 0 °C was added a solution of 1,4-dioxaspiro[4.5]decan-8-ol **(46)** (15.0 g; 94 mmol) in anhydrous tetrahydrofuran (30 ml) and stirred for 30 min at 0 °C. Methyl iodide (29.51 ml; 474 mmol) was added and the reaction stirred at room temperature. After 3 h the reaction was quenched with methanol and water, followed by the addition of ethyl acetate and water. The organic phase was collected, and the aqueous phase re-extracted with ethyl acetate. The organic phases were combined and dried over magnesium sulphate, filtered and the solvent removed under reduced pressure to afford a yellow oil. The oil was purified by flash chromatography eluting with 30 % v/v ethyl acetate in petroleum ether to afford 11.44 g (70 %) of **(47)** as a yellow oil. NMR spectroscopy was used to confirm the product had been obtained.

^{1}H NMR (400 MHz, $CDCl_3$) δ 3.98 – 3.85 (m, 4H, OC$\underline{H}_2$), 3.38 – 3.20 (m, 4H, C$\underline{H}$OC$\underline{H}_3$), 1.86 – 1.45 (m, 8H, cyclohexane-C$\underline{H}_2$).

^{13}C NMR (101 MHz, $CDCl_3$) δ 108.6, 76.3, 64.4, 55.9, 31.4, 28.3.

4.2.14. 4-methoxycyclohexan-1-one 48

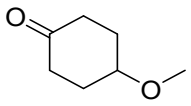

(48)

To a solution of 8-methoxy-1,4-dioxaspiro[4.5]decane **(47)** (11.4 g; 66.4 mmol) in tetrahydrofuran (15 ml) was added hydrochloric acid (50 ml; 5 M) and stirred at room temperature. After 16 h, the pH of the reaction mixture was adjusted to 10 with sodium hydroxide solution (2 M) followed by extraction with ethyl acetate. The organic was collected and dried over magnesium sulphate, filtered and the solvent removed under reduced pressure to afford 7.79 g (91 %) of **(48)** as a yellow oil. NMR spectroscopy was used to confirm the product had been obtained.

^{1}H NMR (400 MHz, $CDCl_3$) δ 3.67 – 3.55 (m, 1H, C<u>H</u>OCH_3), 3.43 (s, 3H, CHOC<u>H_3</u>), 2.66 – 2.18 (m, 4H, cyclohexane-C<u>H_2</u>), 2.18 – 1.85 (m, 4H, cyclohexane-C<u>H_2</u>).

^{13}C NMR (101 MHz, $CDCl_3$) δ 211.3, 74.4, 56.2, 37.2, 30.3.

4.2.15. *Tert*-butyl 2-(4-methoxycyclohexylidene)hydrazine-1-carboxylate 49

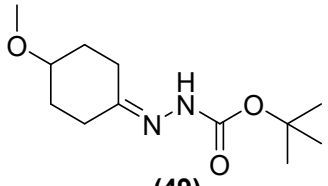

(49)

To a solution of 4-methoxycyclohexan-1-one **(48)** (8.24 g; 66.9 mmol) in methanol (30 ml) was added *tert*-butyl carbazate (8.84 g; 66.9 mmol). The reaction mixture was stirred for 30 min at room temperature. The solvent was removed under reduced pressure to afford a cloudy oil. The oil was dissolved in ethyl acetate (50 ml), dried over magnesium sulphate, and filtered. The remaining solvent was removed under reduced pressure and placed under high vacuum overnight to afford 16.2 g (99 %) of **(39)** as a white crystalline solid. The product was confirmed by NMR spectroscopy in deuterated chloroform.

^{1}H NMR (400 MHz, $CDCl_3$) δ 7.58 (s, 1H, NH), 3.54 – 3.38 (m, 1H, C<u>H</u>OCH_3), 3.34 (s, 3H, CHOC<u>H_3</u>), 2.61 – 2.06 (m, 4H, cyclohexane-C<u>H_2</u>), 1.94 – 1.68 (m, 4H, cyclohexane-C<u>H_2</u>), 1.47 (d, *J* = 13.2 Hz, 9H, *tert*-butyl).

^{13}C NMR (101 MHz, $CDCl_3$) δ 154.8, 153.3, 81.0, 75.7, 56.1, 31.0, 30.6, 30.3, 29.5, 28.4, 21.9.

4.2.16. *Tert*-butyl 2-((1*S*,4*S*)-4-methoxycyclohexyl)hydrazine-1-carboxylate 50 and *tert*-butyl 2-((1*R*,4*R*)-4-methoxycyclohexyl)hydrazine-1-carboxylate 55

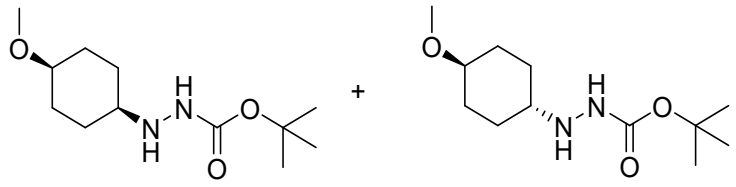

(50) **(55)**

To a stirred solution of tert-butyl 2-(4-methoxycyclohexylidene)hydrazinecarboxylate **(49)** (16.2 g; 66.9 mmol) in acetic acid (75 ml) and distilled water (125 ml) was added sodium cyanoborohydride (5.00 g; 80.28) in small portions (gas evolved – extreme caution, hydrogen cyanide gas). The reaction was stirred overnight at room temperature. After 16 h, the reaction was cooled in an ice bath and the pH adjusted to 7 with sodium hydroxide solution (2 M) (~500 ml). The reaction mixture was extracted with dichloromethane (200 ml x 2), the organic fractions collected and dried over magnesium sulphate and filtered. The solvent was removed under reduced pressure to afford a yellow oil. NMR of the crude oil indicated the cis and trans isomers were formed in ~50:50 ratio. The isomers were isolated by column chromatography, eluting with 20 % v/v ethyl acetate in petroleum ether. The *cis* isomer **(50)** was isolated as 5.54 g (34 %) of white solid. The *trans* isomer **(55)** was isolated as 6.34 g (39 %) of white solid. NMR data was used to confirm the desired products had been produced.

Cis **(50)**

^{1}H NMR (400 MHz, $CDCl_3$) δ 6.05 (s, 1H, NH), 3.86 (s, 1H, NH), 3.33 (dt, *J* = 7.3, 2.7 Hz, 1H, C<u>H</u>OCH_3), 3.29 (s, 3H, CHOC<u>H_3</u>), 2.89 (m, 1H, C<u>H</u>NH), 1.86 (m, 4H, cyclohexane-C<u>H_2</u>), 1.53 (m, 4H, cyclohexane-C<u>H_2</u>), 1.45 (s, 9H, *tert*-butyl).

^{13}C NMR (101 MHz, $CDCl_3$) δ 157.1, 80.5, 75.7, 56.9, 55.6, 28.5, 27.5, 25.9.

Trans **(55)**

^{1}H NMR (400 MHz, $CDCl_3$) δ 6.03 (s, 1H, NH), 3.97 (s, 1H, NH), 3.36 (s, *J* = 6.5 Hz, 3H, CHOC<u>H_3</u>), 3.17 – 3.05 (m, 1H, C<u>H</u>OCH_3), 2.83 (t, *J* = 10.2 Hz, 1H, C<u>H</u>NH), 2.06 (dd, *J* = 12.5, 3.1 Hz, 2H, cyclohexane-C<u>H_2</u>), 1.92 (d, *J* = 11.4 Hz, 2H, cyclohexane-C<u>H_2</u>), 1.48 (s, 9H, *tert*-butyl), 1.26 (m, 2H, cyclohexane-C<u>H_2</u>), 1.13 (m, 2H, cyclohexane-C<u>H_2</u>).

^{13}C NMR (101 MHz, $CDCl_3$) δ 157.1, 80.6, 79.0, 58.0, 56.0, 29.6, 28.9, 28.5.

4.2.17. 2-((1*S*,4*S*)-4-methoxycyclohexyl)hydrazin-1-ium chloride 51

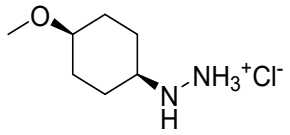

(51)

To a solution of tert-butyl 2-((1*S*,4*S*)-4-methoxycyclohexyl)hydrazinecarboxylate **(50)** (5.4 g; 22.1 mmol) in methanol (30 ml) was added hydrochloric acid in dioxane (30 ml) which was stirred at room temp overnight. The solvent was removed under reduced pressure to afford 3.99 g (99 %) of flaky white crystals. NMR data was used to confirm the desired product had been produced.

^{1}H NMR (400 MHz, MeOD) δ 3.47 (m, 1H, C<u>H</u>OCH$_3$), 3.31 (s, 3H, CHOC<u>H$_3$</u>), 3.16 – 3.00 (m, 1H, C<u>H</u>NH), 2.03 (dd, *J* = 12.7, 2.8 Hz, 2H, cyclohexane-C<u>H$_2$</u>), 1.87 (dd, *J* = 12.5, 3.4 Hz, 2H, cyclohexane-C<u>H$_2$</u>), 1.69-1.57 (m, 2H, cyclohexane-C<u>H$_2$</u>), 1.55– 1.48 (m, 2H, cyclohexane-C<u>H$_2$</u>).

^{13}C NMR (101 MHz, MeOD) δ 74.9, 60.6, 56.1, 28.3, 23.5.

4.2.18. Ethyl 5-amino-1-((1*S*,4*S*)-4-methoxycyclohexyl)-3-methyl-1H-pyrazole-4-carboxylate 52

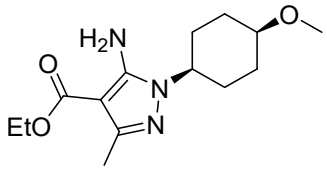

(52)

To a solution of 2-((1*S*,4*S*)-4-methoxycyclohexyl)hydrazin-1-ium chloride **(51)** (3.99 g; 22.1 mmol) and ethyl (*Z*)-2-cyano-3-ethoxybut-2-enoate **(39)** (4.04 g; 22.1 mmol) dissolved in ethanol (50 ml) was added triethylamine (9.25 ml; 66.3 mmol) and heated under reflux overnight. The reaction left to cool, the solvent removed under reduced pressure and tetrahydrofuran (50 ml) added causing the amine salt to crash out of the reaction. The amine salt was filtered off and the supernatant collected, and the solvent removed. The resultant oil was re-dissolved in ethyl acetate (50 ml) and extracted with hydrochloric acid solution (4 M, 50 ml x 3). The aqueous phase was collected, and the pH adjusted to 14 with sodium hydroxide solution (4 M). The resultant aqueous phase was extracted with dichloromethane (100 ml x 3), dried over sodium sulphate, filtered and the solvent removed to afford an orange oil. The product was run quickly through a column, eluting with 40 % v/v ethyl acetate in petroleum ether. The column afforded a yellow oil which was recrystallized from petroleum ether and diethyl ether to afford 2.86 g (46 %) large white crystals. NMR data was used to confirm the desired product had been produced.

^{1}H NMR (400 MHz, $CDCl_3$) δ 5.04 (s, 2H, NH_2), 4.26 (q, *J* = 7.1 Hz, 2H, $OC\underline{H}_2CH_3$), 3.84 – 3.67 (m, 1H, C<u>H</u>-NH), 3.47 (dd, *J* = 8.4, 5.8 Hz, 1H, $C\underline{H}OCH_3$), 3.31 (d, *J* = 8.6 Hz, 3H, $CHOC\underline{H}_3$), 2.32 (s, 3H, CH_3), 2.22 (ddd, *J* = 15.6, 13.1, 3.6 Hz, 2H, cyclohexane-$C\underline{H}_2$), 2.15 – 2.06 (m, 2H, cyclohexane-$C\underline{H}_2$), 1.71 – 1.63 (m, 2H, cyclohexane-$C\underline{H}_2$), 1.46 (ddd, *J* = 11.1, 10.0, 3.1 Hz, 2H, cyclohexane-$C\underline{H}_2$), 1.33 (t, *J* = 7.1 Hz, 3H, $OCH_2C\underline{H}_3$).

^{13}C NMR (101 MHz, $CDCl_3$) δ 165.7, 149.3, 148.5, 94.8, 73.2, 59.4, 56.2, 55.7, 28.7, 25.6, 14.8, 14.7.

4.2.19. Ethyl 1-((1*S*,4*S*)-4-methoxycyclohexyl)-3-methyl-5-((4-methylphenyl)sulfonamido)-1H-pyrazole-4-carboxylate 53

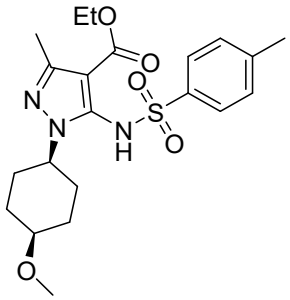

(53)

To a suspension of sodium hydride (60 % in mineral oil; 1.22 g; 30.5 mmol) in anhydrous tetrahydrofuran (30 ml) under argon at 0°C was added a solution of ethyl 5-amino-1-((1*S*,4*S*)-4-methoxycyclohexyl)-3-methyl-1H-pyrazole-4-carboxylate **(52)** (2.86 g; 10.2 mmol) in anhydrous tetrahydrofuran (10 ml) and stirred for 30 minutes. To the stirring reaction was added a solution of tosyl chloride (3.88 g; 20.3 mmol) in tetrahydrofuran (10 ml) and stirred for a further 30 minutes at 0 °C. The reaction mixture left to warm to room temperature and stirred for another 60 minutes followed by the careful addition of ice-cold water (50 ml). The reaction was extracted with sodium hydroxide solution (2 M; 25 ml x 2), the aqueous phase was collected and acidified to pH 1 with hydrochloric acid solution (2 M). The resultant aqueous phase was extracted with dichloromethane (25 ml x 3), dried over magnesium sulphate, filtered and the solvent removed to afford a yellow oil. The crude oil was purified by column chromatography, eluting with 30 % ethyl acetate in petroleum ether. The product was afforded as 810 mg (18 %) of clear crystals. NMR data was used to confirm the desired product had been produced.

^{1}H NMR (400 MHz, $CDCl_3$) δ 7.49 (d, *J* = 8.3 Hz, 2H, Ar H), 7.41 (s, 1H, NH), 7.20 (d, *J* = 8.2 Hz, 2H, Ar H), 4.68 (m, 1H, C<u>H</u>-NH), 3.88 (q, *J* = 7.1 Hz, 2H, OC<u>H$_2$</u>CH_3), 3.50 (d, *J* = 2.6 Hz, 1H, C<u>H</u>OCH_3), 3.34 (s, 3H, CHOC<u>H$_3$</u>), 2.39 (s, 3H, Tosyl-C<u>H$_3$</u>), 2.35 – 2.21 (m, 2H, cyclohexane-C<u>H$_2$</u>), 2.29 (s, 3H, CH_3), 2.12 (d, *J* = 15.0 Hz, 2H, cyclohexane-C<u>H$_2$</u>), 1.75 (d, *J* = 12.6 Hz, 2H, cyclohexane-C<u>H$_2$</u>), 1.66 – 1.51 (m, 2H, cyclohexane-C<u>H$_2$</u>), 1.14 (t, *J* = 7.2 Hz, 3H, OCH_2C<u>H$_3$</u>).

^{13}C NMR (101 MHz, $CDCl_3$) δ 163.7, 149.2, 144.7, 137.5, 134.3, 129.4, 128.1, 103.9, 73.5, 60.0, 57.3, 55.8, 28.7, 26.7, 21.7, 14.6, 14.3.

4.2.20. 1-((1*S*,4*S*)-4-methoxycyclohexyl)-3-methyl-5-((4-methylphenyl)sulfonamido)-1H-pyrazole-4-carboxylic acid 54

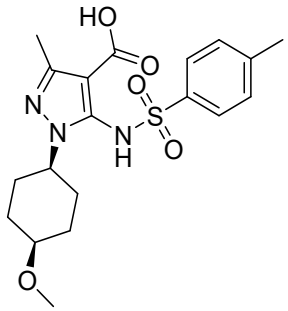

(54)

To a mixture of ethyl 1-((1*S*,4*S*)-4-methoxycyclohexyl)-3-methyl-5-((4-methylphenyl)sulfonamido)-1H-pyrazole-4-carboxylate **(53)** (810 mg; 1.86 mmol) dissolved in ethanol (20 ml) and distilled water (20 ml) was added lithium hydroxide monohydrate (1.4 g; 33.4 mmol). The reaction was heated under reflux. After 16 hours, the reaction was left to cool to room temperature. The pH was adjusted to pH 1 with hydrochloric acid solution (4 M). The mixture was extracted with dichloromethane (50 ml x 3), the organic phase was separated, dried over magnesium sulphate, filtered and the solvent removed to afford 758 mg of an off-white solid (99 %). No further purification steps were performed, and the product was carried forward to the next step of the synthesis. NMR data was used to confirm the desired product had been produced.

^{1}H NMR (400 MHz, $CDCl_3$) δ 7.47 (d, *J* = 8.3 Hz, 2H, Ar H), 7.30 (s, 1H, NH), 7.15 (d, *J* = 8.6 Hz, 2H, Ar H), 4.66 (m, 1H, C<u>H</u>-NH), 3.50 (m, 1H, C<u>H</u>OCH_3), 3.33 (s, 3H, CHOC<u>H_3</u>), 2.33 (s, 3H, CH_3), 2.30 (s, 3H, Tosyl-C<u>H_3</u>), 2.29 – 2.19 (m, 2H, cyclohexane-C<u>H_2</u>), 2.11 (dd, *J* = 14.4, 4.0 Hz, 2H, cyclohexane-C<u>H_2</u>), 1.74 (dd, *J* = 12.3, 3.1 Hz, 2H, cyclohexane-C<u>H_2</u>), 1.55 (m, 2H, cyclohexane-C<u>H_2</u>).

^{13}C NMR (101 MHz, $CDCl_3$) δ 168.0, 150.3, 145.0, 138.3, 134.3, 129.6, 128.1, 102.8, 73.5, 57.6, 55.9, 29.9, 26.7, 21.8, 14.6.

4.2.21. N-((*S*)-3,3-dimethylbutan-2-yl)-1-((1s,4*R*)-4-methoxycyclohexyl)-3-methyl-5-((4-methylphenyl)sulfonamido)-1H-pyrazole-4-carboxamide 11 [216]

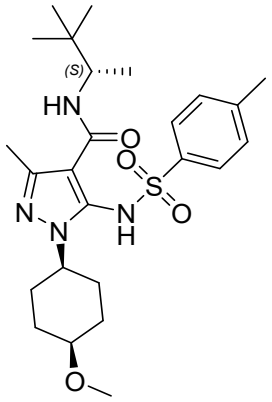

(11)

To a solution of 1-((1*S*,4*S*)-4-methoxycyclohexyl)-3-methyl-5-((4-methylphenyl)sulfonamido)-1H-pyrazole-4-carboxylic acid **(54)** (758 mg; 1.86 mmol) in dimethylformamide (20 ml) was added *N,N*-diisopropylethylamine (972 µL; 5.58 mmol) and stirred for 10 minutes under an argon atmosphere. A solution of HATU (707 mg; 1.86 mmol) in dimethylformamide (5 ml) was added to the reaction mixture and stirred for a further 30 minutes. To the reaction (*S*)-(+)-3,3-dimethyl-2-butylamine (254 µL; 1.86 mmol) was added and stirred for 16 hours at room temperature under argon. The reaction was quenched with distilled water (25 ml), acidified to pH 1 with hydrochloric acid solution (2 M) and extracted with ethyl acetate (25 ml x 3). The organic phase was washed with hydrochloric acid solution (2M, 25 ml), followed by ammonium chloride solution (25 ml) and brine (25 ml). The organic phase was collected, dried over magnesium sulphate, filtered and the solvent removed to afford a crude white solid. The solid was dissolved into dichloromethane (30 ml) and then filtered to remove insoluble residues. The dichloromethane filtrate was then collected, the solvent removed under reduced pressure to afford a white solid. The

product was purified by column chromatography, eluting with 70 % v/v ethyl acetate in petroleum ether followed by trituration with diethyl ether to afford 480 mg (53 %) of white powder. The final product was confirmed by NMR, HRMS, IR and XRD experimental data.

HRMS (ESI) calcd. for $C_{25}H_{38}N_4O_4SH$ 491.2647, found 491.2687 $[M+H]^+$

^{1}H NMR (400 MHz, $CDCl_3$) δ 8.66 (s, 1H, NH), 7.54 (d, *J* = 8.3 Hz, 2H, Ar H), 7.17 (d, *J* = 8.2 Hz, 2H, Ar H), 5.19 (d, *J* = 9.6 Hz, 1H, NH-CH), 4.70 (m, 1H, CH-NH), 3.69 (dd, *J* = 9.5, 6.8 Hz, 1H, NHCH), 3.51 – 3.48 (m, 1H, $CHOCH_3$), 3.34 (s, 3H, $CHOCH_3$), 2.35 (s, 3H, CH_3), 2.33 (s, 3H, Tosyl-CH_3), 2.29 – 2.15 (m, 2H, cyclohexane-CH_2), 2.15 – 2.06 (m, 2H, cyclohexane-CH_2), 1.81 (d, *J* = 12.4 Hz, 1H, cyclohexane-CH_2), 1.72 (d, *J* = 12.4 Hz, 1H, cyclohexane-CH_2), 1.65 – 1.50 (m, 2H, cyclohexane-CH_2), 0.88 (d, *J* = 6.7 Hz, 3H, NHCHCH_3), 0.82 (s, 9H, *t*-butyl).

^{13}C NMR (101 MHz, $CDCl_3$) δ 163.2, 144.2, 143.6, 138.1, 134.8, 129.4, 128.2, 73.6, 57.2, 55.8, 52.4, 34.0, 28.8, 28.7, 26.9, 26.3, 21.7, 16.2, 15.4.

IR 3328, 2942, 2856, 2826, 2742, 1741, 1598, 1555, 1335, 1156, 1092 cm^{-1}.

X-ray

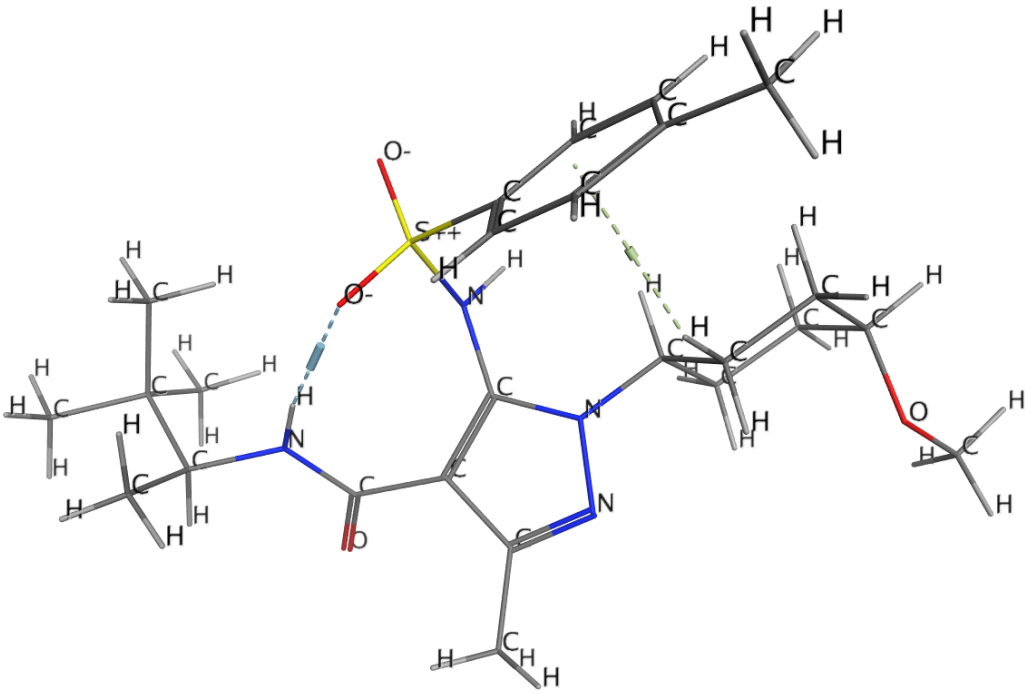

4.2.22. 2-((1*R*,4*R*)-4-methoxycyclohexyl)hydrazin-1-ium chloride 56

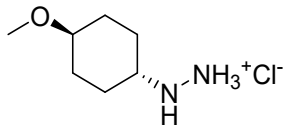

(56)

To a solution of tert-butyl 2-((1*R*,4*R*)-4-methoxycyclohexyl)hydrazinecarboxylate **(55)** (3.5 g; 14.3 mmol) dissolved in methanol (30 ml) was added hydrochloric acid in dioxane (30 ml) and stirred at room temp overnight. The solvent was removed under reduced pressure and the product was stored under high vacuum for 5 h to afford 2.58 g (99 %) of an off-white solid. Thin layer chromatography and an NMR spectrum of the crude product were used to confirm complete conversion of the starting material. The product was carried through to the next step without further analysis.

4.2.23. Ethyl 5-amino-1-((1*R*,4*R*)-4-methoxycyclohexyl)-3-methyl-1H-pyrazole-4-carboxylate 57

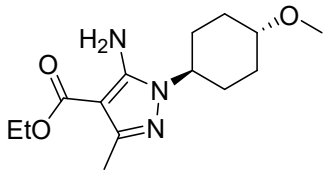

(57)

To a solution of 2-((1*R*,4*R*)-4-methoxycyclohexyl)hydrazin-1-ium chloride **(56)** (4.70 g; 26.0 mmol) and ethyl (*Z*)-2-cyano-3-ethoxybut-2-enoate **(39)** (4.76 g; 26.0 mmol) dissolved in ethanol (50 ml) was added triethylamine (11 ml; 78.0 mmol) and the reaction was heated under reflux overnight. After 16 h the reaction was left to cool to room temperature. The solvent was removed under reduced pressure and tetrahydrofuran (50 ml) added causing the amine salt to crash out of the reaction as a precipitate. The amine salt was filtered off and the supernatant collected, the solvent was removed under reduced pressure. The resultant oil was re-dissolved in ethyl acetate (50 ml) and extracted with hydrochloric acid solution (4 M, 50 ml x 3). The aqueous phase was collected, the pH adjusted to 14 with sodium hydroxide solution (4 M). The resultant aqueous phase was extracted with dichloromethane (100 ml x 3), dried over magnesium sulphate, filtered and the solvent removed under reduced pressure to afford an orange oil. The product was run quickly through a column eluting with 40 % v/v ethyl acetate in petroleum ether to afford a yellow oil. The oil was recrystallized from petroleum ether and diethyl ether to afford 2.92 g (40 %) of large white crystals. NMR data was used to confirm the desired product had been produced.

^{1}H NMR (400 MHz, $CDCl_3$) δ 5.02 (s, 2H, NH_2), 4.27 (q, *J* = 7.1 Hz, 2H, $OC\underline{H}_2CH_3$), 3.69 (ddd, *J* = 15.6, 10.4, 4.9 Hz, 1H, $C\underline{H}OCH_3$), 3.37 (s, 3H, $CHOC\underline{H}_3$), 3.24 (m, 1H, C<u>H</u>-NH), 2.33 (s, 3H, CH_3), 2.22 (d, *J* = 13.1 Hz, 2H, cyclohexane-$C\underline{H}_2$), 2.08 – 1.88 (m, 4H, cyclohexane-$C\underline{H}_2$), 1.40 – 1.25 (m, 2H, cyclohexane-$C\underline{H}_2$), 1.33 (t, *J* = 7.1 Hz, 3H, $OCH_2C\underline{H}_3$).

^{13}C NMR (101 MHz, $CDCl_3$) δ 165.6, 149.4, 148.8, 78.0, 77.4, 59.5, 56.2, 55.0, 30.9, 29.6, 14.8, 14.7.

4.2.24. Ethyl 1-((1*R*,4*R*)-4-methoxycyclohexyl)-3-methyl-5-((4-methylphenyl)sulfonamido)-1H-pyrazole-4-carboxylate 58

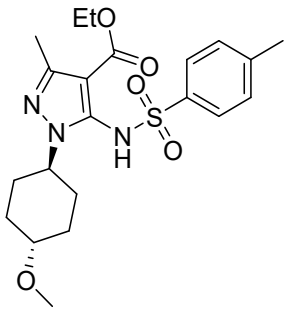

(58)

To a suspension of sodium hydride (60 % in mineral oil; 1.25 g; 30.9 mmol) in anhydrous tetrahydrofuran (30 ml) under argon at 0°C was added a solution of ethyl 5-amino-1-((1*R*,4*R*)-4-methoxycyclohexyl)-3-methyl-1H-pyrazole-4-carboxylate **(57)** (2.90 g; 10.3 mmol) in anhydrous tetrahydrofuran (10 ml) and stirred for 30 minutes. To the stirring reaction was added a solution of tosyl chloride (3.93 g; 20.6 mmol) in tetrahydrofuran (10 ml) which was stirred for a further 30 minutes at 0°C. The reaction mixture was left to warm to room temperature and stirred for another 60 minutes followed by the careful addition of ice-cold water (50 ml). The reaction was extracted with sodium hydroxide solution (2 M; 25 ml x 2), the aqueous phase was collected and acidified to pH 1 with hydrochloric acid solution (2 M). The resultant aqueous phase was extracted with dichloromethane (25 ml x 3), dried over magnesium sulphate, filtered and the solvent removed to afford a yellow oil. The crude oil was purified by column chromatography, eluting with 30 % ethyl acetate in petroleum ether. The product was afforded as 1.89 g (42 %) of clear crystals. NMR data was used to confirm the desired product had been produced.

^{1}H NMR (400 MHz, $CDCl_3$) δ 7.49 (d, *J* = 8.3 Hz, 2H, Ar H), 7.40 (s, 1H, NH), 7.21 (d, *J* = 8.2 Hz, 2H, Ar H), 4.70 – 4.60 (m, 1H, C<u>H</u>-NH), 3.89 (q, *J* = 7.1 Hz, 2H, OC<u>H$_2$</u>CH$_3$), 3.38 (s, 3H, CHOC<u>H$_3$</u>), 3.32 – 3.12 (m, 1H, C<u>H</u>OCH$_3$), 2.40 (s, 3H, Tosyl-C<u>H$_3$</u>), 2.29 (s, 3H, CH_3), 2.24 – 2.15 (m, 2H, cyclohexane-C<u>H$_2$</u>), 2.10 – 1.94 (m, 4H, cyclohexane-C<u>H$_2$</u>), 1.52 – 1.30 (m, 2H, cyclohexane-C<u>H$_2$</u>), 1.14 (t, *J* = 7.1 Hz, 3H, OCH$_2$C<u>H$_3$</u>).

^{13}C NMR (101 MHz, $CDCl_3$) δ 163.5, 149.3, 144.7, 137.8, 134.4, 129.4, 128.1, 104.1, 78.3, 77.2, 60.1, 56.9, 56.1, 30.8, 30.4, 21.7, 14.5, 14.3.

4.2.25. 1-((1*R*,4*R*)-4-methoxycyclohexyl)-3-methyl-5-((4-methylphenyl)sulfonamido)-1H-pyrazole-4-carboxylic acid 59

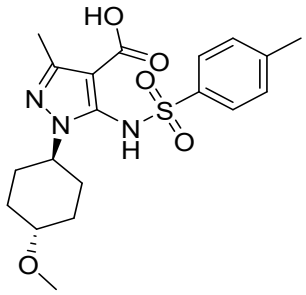

(59)

To a mixture of ethyl 1-((1*R*,4*R*)-4-methoxycyclohexyl)-3-methyl-5-((4-methylphenyl)sulfonamido)-1H-pyrazole-4-carboxylate **(58)** (1.89 g; 4.30 mmol) dissolved in ethanol (20 ml) and distilled water (20 ml) was added lithium hydroxide monohydrate (2.40 g; 57.2 mmol). The reaction was heated under reflux. After 16 hours, the reaction was left to cool to room temperature. The pH was adjusted to pH 1 with hydrochloric acid solution (4 M). The mixture was extracted with dichloromethane (50 ml x 3), the organic phase was separated, dried over magnesium sulphate, filtered and the solvent removed to afford 1.57 g of an off-white powder (89 %). No further purification steps were performed, and the product was carried forward to the next step of the synthesis. NMR data was used to confirm the desired product had been produced.

^{1}H NMR (400 MHz, $CDCl_3$) δ 7.51 (d, *J* = 8.0 Hz, 2H, Ar H), 7.19 (d, *J* = 8.1 Hz, 2H, Ar H), 5.30 (s, 1H, NH), 4.62 (m, 1H, C<u>H</u>-NH), 3.38 (s, 3H, CHOC<u>H$_3$</u>), 3.32 – 3.19 (m, 1H, C<u>H</u>OCH$_3$), 2.34 (d, *J* = 3.0 Hz, 6H, CH$_3$, Tosyl-C<u>H$_3$</u>), 2.20 (d, *J* = 11.7 Hz, 2H, cyclohexane-C<u>H$_2$</u>), 2.04 (d, *J* = 6.3 Hz, 4H, cyclohexane-C<u>H$_2$</u>), 1.50 – 1.31 (m, 2H, cyclohexane-C<u>H$_2$</u>).

^{13}C NMR (101 MHz, $CDCl_3$) δ 168.0, 150.3, 145.0, 138.3, 134.3, 129.6, 128.1, 102.8, 73.5, 57.6, 55.9, 29.9, 26.7, 21.8, 14.6.

4.2.26. N-((*S*)-3,3-dimethylbutan-2-yl)-1-((1*R*,4*S*)-4-methoxycyclohexyl)-3-methyl-5-((4-methylphenyl)sulfonamido)-1H-pyrazole-4-carboxamide 60 [216]

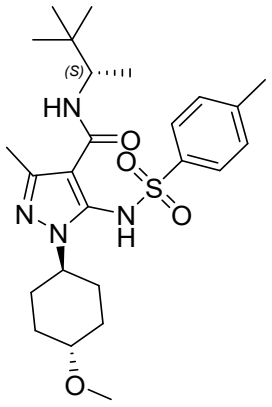

(60)

To a solution of 1-((1*R*,4*R*)-4-methoxycyclohexyl)-3-methyl-5-((4-methylphenyl)sulfonamido)-1H-pyrazole-4-carboxylic acid **(59)** (1.57 g; 3.84 mmol) in dimethylformamide (30 ml) was added *N,N*-diisopropylethylamine (2.00 mL; 11.52 mmol) and stirred for 10 minutes under an argon atmosphere. A solution of HATU (1.46 g; 3.84 mmol) in dimethylformamide (5 ml) was added to the reaction mixture and stirred for a further 30 minutes. To the reaction (*S*)-(+)-3,3-dimethyl-2-butylamine (522 µL; 3.84 mmol) was added and stirred for 16 h at room temperature under argon. The reaction was quenched with distilled water (25 ml), acidified to pH 1 with hydrochloric acid solution (2 M) and extracted with ethyl acetate (25 ml x 3). The organic phase was washed with hydrochloric acid solution (2 M, 25 ml), followed by ammonium chloride solution (25 ml) and brine (25 ml). The organic phase was collected, dried over magnesium sulphate, filtered and the solvent removed to afford a crude white solid. The solid was dissolved into dichloromethane (30 ml) and then filtered to remove insoluble residues. The dichloromethane filtrate was then collected, the solvent removed under reduced pressure to afford a

white solid. The product was purified by column chromatography, eluting with 70 % v/v ethyl acetate in petroleum ether followed by trituration with diethyl ether to afford 1.10 g (58 %) of white powder. The final product was confirmed by NMR, HRMS, and IR experimental data.

HRMS (ESI) calcd. for $C_{25}H_{38}N_4O_4SH$ 491.2647, found 491.2685 $[M+H]^+$

^{1}H NMR (400 MHz, $CDCl_3$) δ 8.61 (s, 1H, NH), 7.54 (d, *J* = 8.3 Hz, 2H, Ar H), 7.18 (d, *J* = 8.2 Hz, 2H, Ar H), 5.22 (d, *J* = 9.5 Hz, 1H, NHCH), 4.66 (m, 1H, CH-NH), 3.70 (dq, *J* = 13.6, 6.8 Hz, 1H, NHCH), 3.37 (s, 3H, $CHOCH_3$), 3.32 – 3.21 (m, 1H, $CHOCH_3$), 2.36 (s, 3H, CH_3), 2.33 (s, 3H, Tosyl-CH_3), 2.23 – 2.13 (m, 2H, cyclohexane-CH_2), 2.08 – 1.85 (m, 4H, cyclohexane-CH_2), 1.48 – 1.35 (m, 2H, cyclohexane-CH_2), 0.89 (d, *J* = 6.8 Hz, 3H, $NHCHCH_3$), 0.83 (s, 9H, *t*-butyl).

^{13}C NMR (101 MHz, $CDCl_3$) δ 163.1, 144.3, 143.8, 138.2, 134.9, 129.5, 128.1, 106.0, 78.4, 77.2, 56.9, 56.0, 52.5, 34.0, 34.0, 30.8, 30.6, 30.3, 26.3, 21.7, 16.2, 15.3.

IR 3337, 2942, 2864, 2824, 1597, 1555, 1422, 1336, 1157, 1094 cm^{-1}.

5. Chapter 5: Biology Materials and Methods

5.1. Cells and reagents

Human GBM cell line U-87 MG was obtained from the European Collection of Authenticated Cell Cultures (ECACC; Public Health England, Salisbury, UK). RPMI 1640 medium (R0883, Sigma-Aldrich, Dorset, UK). Sodium pyruvate (P5280, Sigma-Aldrich, Dorset, UK). L-glutamine (G5792, Sigma-Aldrich, Dorset, UK). Heat inactivated foetal calf serum (FCS, F2442, Sigma-Aldrich, Dorset, UK). Trypsin-EDTA solution (T4049, Sigma-Aldrich, Dorset, UK). Hanks balanced salt solution (HBSS, Sigma-Aldrich, Dorset, UK). Phosphate Buffered Saline (PBS, Severn Biotech Ltd cat. no. 20-74-05). 3-(4,5-dimethyl thiazol-2-yl)-2,5-diphenyl tetrazolium bromide (MTT, M5655, Sigma-Aldrich, Dorset, UK). Dimethyl sulfoxide (Sigma-Aldrich, Dorset, UK). Molecular Probes^{TM} Fluo-4 NW (no wash) (Invitrogen F36206 starter kit). f-Met-Leu-Phe (fMLF, 47729, Sigma-Aldrich, Dorset, UK). Methyl cellulose (Sigma-Aldrich, Dorset, UK). Calcein AM (C1359, Sigma-Aldrich, Dorset, UK). Sodium Hydroxide (1M NaOH, Sigma-Aldrich, Dorset, UK). Bovine Serum Albumin (A9418, Sigma-Aldrich, Dorset, UK).

5.2. Cell culture

Human GBM cell line U87MG, obtained from the European Collection of Authenticated Cell Cultures (ECACC; Public Health England, Salisbury, UK) and maintained as monolayers in RPMI-1640 supplemented with 10 % (v/v) foetal calf serum, 1mM sodium pyruvate and 2 mM L-glutamine. Cells were grown in 75 cm^2 culture flasks in an atmosphere of 95 % air, 5 % CO_2 at 37 °C and harvested in a solution of trypsin-EDTA at the logarithmic growth

phase. Cell lines were used up to maximum of 5 passages from defrosting before discarding.

5.3. Cell Passaging

Cells in a T75 flask (Corning. Cat. no. 430641U) were washed with 10 ml Phosphate buffer saline then washed again with 3 ml of trypsin-EDTA. The flask containing the cells was then incubated for around 5 min at 37 °C/ 5 % CO_2 until cells became detached and a single cell population was obtained. The cells were then checked for suspension under a light microscope. When cell suspension was confirmed, trypsin was neutralised with 5 ml RPMI 1640 w/FBS (10 % v/v) and transferred to a 20 ml universal tube. The universal tube was then centrifuged at 1000 RPM for 3 min. The pellet was re-suspended in 10 ml of cell culture media, then split between T75 flasks at an average split ration of 1:10. Cells were incubated as above, and the medium replaced 2-3 times a week dependant on growth rate.

5.4. Formation of spheroids by spinner flask method

U-87 MG cells (1 x 10^6 cells/ml) were seeded into a spinner flask (F7690, Techne, Bibby Scientific Limited, Staffordshire, UK) containing 150 ml of complete culture medium, and placed on a magnetic stirrer plate (MCS-104S, Techne, Bibby Scientific Limited, Staffordshire, UK). The medium was stirred at a rate of 55 rpm. Spheroids were grown for 5 days before the medium was first changed and the spheroids diameter measured. Thereafter medium was changed every 24-48 hours as needed.

5.5. Formation of spheroids by hanging drop method

Adherent cells were grown according to cell culture method previously mentioned. Prior to formation of spheroids, the cells were trypsonised and suspended as a single cell population as per the method for cell passaging. Cells were centrifuged followed by washing with PBS. The cells were resuspended in medium containing FCS (10 % v/v) followed by addition and incubation with 1 µl of Calcein AM (4 mM) in DMSO, for 30 min at 37 °C/5 % CO_2. The cell suspension was centrifuged, and the supernatant discarded. The cells were resuspended in culture medium and the cells concentration determined. The cells were then diluted to the desired concentration (8 x 10^4 cells/ml) in culture medium containing methyl cellulose (20 % v/v). The lid of a 60 mm tissue culture dish was inverted, and 5 ml of PBS added to the bottom of the dish. A multi-channelled pipette was used to deposit 25 µl drops (2000 cells) to the base of the lid. The lid was then inverted and placed onto the PBS-filled bottom chamber. The dish was incubated at 95 % air, 5 % CO_2 at 37 °C for 24 h or until spheroids had formed.

5.6. Histology of Spheroids

Fixation: Spheroids were collected from the spinner flasks and transferred to 20 ml universal tubes. Remaining medium was discarded carefully and replaced with Bouin's Solution. The spheroids were left in Bouin's Solution at room temperature for 1 h 15 min. The Bouin's Solution was decanted off and the spheroids washed in 70 % (v/v) ethanol to remove excess fixative. The spheroids were stored in 70 % (v/v) ethanol at room temperature until processing.

Processing: The ethanol was discarded and replaced with 90 % (v/v) ethanol for 1 h at room temperature. 90 % (v/v) ethanol was discarded and replaced with 100 % ethanol for 30 minutes. The ethanol was discarded and replaced with another portion of 100 % ethanol for 30 minutes then repeated once more. The ethanol discarded and replaced with xylene for 30 minutes. The xylene was removed and replaced with fresh xylene for 30 minutes and repeated once more. The spheroids were removed from the tube and placed in an embedding mould with excess xylene carefully pipetted off and discarded. The mould was filled with hot wax. The mould containing the spheroids in wax were left in a warming oven at 68 °C for 30 minutes. The wax was pipetted off and replaced with fresh hot wax. This was repeated two more times before the mould was placed on the cold stage to set.

Sectioning: This method was applied to the sectioning of paraffin embedded spheroids and tissue sections. Blocks to be sectioned were chilled overnight at -20 °C. Using a microtome, 5 µm sections of the paraffin blocks were cut and mounted on Superfrost Plus slides (BDH, Poole, UK). Slides were incubated on a heated slide stage at 37 °C for at least 2 hours to dry and ensure sections were fully adhered to the slide and reduce risk of sections detaching from the slide during processing.

5.7. Haematoxylin and Eosin Staining

Slide mounted paraffin sections were de-paraffinized with xylene (2 x 5 minutes) and rehydrated using a xylene/ethanol (50:50 v/v) solution, followed by 100 % (v/v) ethanol (1 x 5 minutes, 1 x 2 minutes), then subsequently 90 % (v/v) ethanol followed by 70 % (v/v) ethanol (both 2 minutes each) and then

finally distilled water (5 minutes). The sections were then stained with Harris's haematoxylin (HHS128, Sigma-Aldrich, Merck KGaA, Darmstadt, Germany) (1 minute). The sections were washed under running tap water and then immersed in acid alcohol solution (30 seconds) to remove excess haematoxylin staining followed by Scott's Tap Water (60 seconds) to allow the colour to develop. Sections were counterstained with Eosin Y solution (E4009, Sigma-Aldrich, Merck KGaA, Darmstadt, Germany) (1 minute) followed by a final wash in running tap water. Following staining, sections were dehydrated using sequential ethanol (1 x 2 minutes, 2 x 1 minute) and xylene (3 x 1 minute) submersion and slide covers mounted using diphenyl xylene (BDH, Pool, UK).

5.8. Immunohistochemistry

Slide mounted paraffin sections were de-paraffinized with xylene (2x5 minutes) and rehydrated using a xylene/ethanol (50:50 (v/v)) solution, followed by 100 % ethanol (1 x 5 minutes, 1 x 2 minutes), then subsequently 90 % (v/v) ethanol followed by 70 % (v/v) ethanol (both 2 minutes each) and then finally distilled water (5 minutes). When necessary, antigen retrieval was carried out by heating slides in antigen retrieval solution in a microwave for a specified length of time followed by cooling. Slides were washed with PBS followed by blocking of endogenous peroxidase activity by incubation in hydrogen peroxide solution in methanol (3 % v/v) for 10 minutes at room temperature. Slides were washed with PBS then further blocking steps performed dependant on the primary antibody to be used. The sections were incubated with the primary antibody diluted in antibody diluent in a humidified chamber under the conditions specified in Table 9. After incubation, the sections were

washed with PBS before the application of a labelled polymer-HRP secondary antibody and incubation (30 minutes) at room temperature. Following this step, slides were washed, and antibody staining was achieved using the Vectastain ABC kit (PK-4001, Vector Laboratories, Peterborough, UK) followed by addition of the peroxidase substrate 3,3-diaminobenzidine (DAB, DAKO North America Inc, CA, USA) until desired staining intensity was achieved. Sections were washed under running tap water (5 minutes) before being counterstained using Harris's haematoxylin (30 seconds), rinsed in tap water, submerged in acid alcohol (5 seconds), followed by Scott's Tap Water for a further 60 seconds. The sections were given a final wash in tap water (60 seconds). Following staining, sections were dehydrated using sequential ethanol (1 x 2 minutes, 2 x 1 minute) and xylene (3 x 1 minute) submersion and slide covers mounted using diphenyl xylene (BDH, Pool, UK). A list of all antibodies used, and specific conditions used for IHC are presented in Table 9.

Table 9 List of all the antibodies and the specific conditions used for antigen retrieval, blocking, dilution of primary antibody, incubation, and secondary antibody for immunohistochemistry.

Primary Antibody	Antigen Retrieval	Blocking Reagents	Dilution	Incubation	Secondary Antibody
anti-FPR1 antibody (Rabbit polyclonal to FPR1, ab113531, Abcam)	None	H_2O_2 (3% v/v in methanol), 10 min. Normal Goat Serum (1:200 in PBS), 20 min.	1:150 – 1:250	Overnight (o/n) at 4 °C	Biotinylated Goat anti-Rabbit from Vectastain ABC Kit (PK-4001, Vector Labs)
Anti-HIF-1-alpha antibody (Rabbit monoclonal to HIF-1-alpha, ab51608, Abcam)	15 min, Citrate Buffer (pH 6.04, 10 mM)	H_2O_2 (3% v/v in methanol), 10 min. Normal Goat Serum (1:200 in PBS), 20 min.	1:100	o/n at 4 °C	Biotinylated Goat anti-Rabbit from Vectastain ABC Kit (PK-4001, Vector Labs)
Anti-Ki67 antibody (Rabbit monoclonal to Ki67, ab92742, Abcam)	15 min, Citrate Buffer (pH 6.04, 10 mM)	H_2O_2 (3% v/v in methanol), 10 min. Normal Goat Serum (1:200 in PBS), 20 min.	1:1000	o/n at 4 °C	Biotinylated Goat anti-Rabbit from Vectastain ABC Kit (PK-4001, Vector Labs)
Anti-Annexin A1 antibody (Rabbit polyclonal to Annexin A1, ab33061, Abcam)	None	H_2O_2 (3% v/v in methanol), 10 min. Normal Goat Serum (1:200 in PBS), 20 min.	1:50	o/n at 4 °C	Biotinylated Goat anti-Rabbit from Vectastain ABC Kit (PK-4001, Vector Labs)
Anti-GFAP antibody (Rabbit polyclonal to GFAP, ab7260, Abcam)	15 min, Citrate Buffer (pH 6.04, 10 mM)	H_2O_2 (3% v/v in methanol), 10 min. Normal Goat Serum (1:200 in PBS), 20 min.	1:500	30 min at 37 °C	Biotinylated Goat anti-Rabbit from Vectastain ABC Kit (PK-4001, Vector Labs)

5.9. Immunofluorescence

U-87 MG cells (2 x 10^4 cells/ml) were seeded onto coverslips within 6 well plates with 2 ml of RPMI 1640 containing 10% (v/v) FCS. After cells had adhered to the coverslip surface, the media was removed and discarded and replaced with 2 ml of ice-cold methanol to fix the cells. The methanol was removed and 2 ml of 2 % (w/v) BSA in PBS added to block non-specific binding, the slides were incubated at room temperature (60 minutes). Coverslips were washed in 2 ml PBS (2 x 5 minutes). To each coverslip was added (except the control slips) 200 µl of rabbit anti-FPR1 antibody (Rabbit polyclonal to FPR1, ab113531, Abcam) diluted 1:250 with 2 % (w/v) BSA in PBS and incubated at room temperature (30 minutes). The coverslips were then washed in PBS (2 x 5 minutes) followed by the application of the fluorescently labelled secondary antibody (Alexa Fluor® 546, goat anti-rabbit, IgG; Invitrogen, Camarillo, CA, USA, 2mg/mL) diluted 1:50 in 2 % (w/v) BSA in PBS. The cover slips were incubated at room temperature with the secondary antibody for 30 minutes followed by washing in PBS (2 x 5 minutes). The coverslips were then mounted using a hard-set mounting medium containing DAPI (H-1500, VECTASHIELD hard set mounting medium with DAPI, Vector Labs) and kept away from light sources at 4 °C until examination.

5.10. Flow Cytometry to analyse FPR1 expression after cellular stress

U-87 MG cells were grown in T25 flasks containing RPMI 1640 medium supplemented either 10 % (v/v) FCS or 0.1 % (v/v) FCS for the starved population. Cells were incubated under normal condition (95 % Air/ 5 % CO_2) and under hypoxic conditions to simulate hypoxia. After 24 hours of incubation

under the specific conditions (normoxia, serum starvation, hypoxia), the medium was removed, the cells were trypsonised and suspended as a single cell population as per the method for cell passaging. Cells were centrifuged followed by washing with PBS. The cells were resuspended in PBS/BSA to remove any remaining cellular debris. The cells were centrifuged again, and the supernatant discarded, the cells were resuspended in fresh PBS/BSA, and the cell concentration determined by cell counting with a haemocytometer. The cell concentration was diluted with cold (4 °C) PBS/BSA to a concentration of 1 x 10^7 cells/ml. The cell suspension was aliquot (100 µl) into an Eppendorf, and to the suspension was added 1 µl of the fluorescently conjugated primary antibody phycoerythrin (PE) conjugated anti-human FPR1 antibody (R&D Systems, FAB3744P) or the corresponding isotype matched control antibody Mouse IgG2A PE-conjugated Antibody (R&D Systems, IC003P) as a control. After incubation for 30 minutes at 4 °C (in the dark) the cells were centrifuged, washed with cold (4 °C) PBS/BSA, centrifuged again and the resulting supernatant discarded. The cells were resuspended in cold (4 °C) PBS (200 µl) and analysed by Flow Cytometry using a FACSCalibur (BD Biosciences).

5.11. Cytotoxicity (MTT) Assay

Into each well of the 96 well plates, 180 µl of U-87 MG cell suspensions were seeded at a concentration of 5 x 10^4 cells/ml. 20 µl of the compound solution for testing increasing concentrations were also added, and each concentration carried out in quadruplicate. Plates were incubated at 37 °C, 5% CO_2, for 24-96 hours. Upon completion of the incubation time of 24-96 hours, the growth medium was aspirated and replaced with MTT solution and

incubated at 37 °C, 5 % CO_2 for 4 hours. After the incubation period, the MTT was carefully removed and DMSO added to dissolve the (MTT) crystals. The absorbance of the 96 well plates were measured at 540 nm using a Multiscan Ex 96 well microplate reader (Thermo Electron Corporation, United Kingdom).

5.12. Calcium mobilisation assay (Agonist mode)

4 x 10^4 U-87 MG cells were seeded into each well of a tissue culture treated 96-well black polystyrene assay plate (Corning, VWR, 734-1609). After 24 h, the growth medium was removed and replaced with 100µl of the dye loading solution (Molecular Probes™ Fluo-4 NW (no wash), Invitrogen F36206). The plates were incubated at 37 °C for 30 min. 20 µL of plain assay buffer was added to each well and the plate was incubated at 37 °C for 30 minutes. The plate was transferred into a Fluoroskan Ascent FL instrument (Thermo Scientific) and the fluorescence in response to the addition of 20 µL of the given concentration of the agonist was measured at 37 °C (Ex 485 nm, Em 538 nm). EC_{50} is calculated as the concentration of the agonist required to give half the maximal response.

5.13. Preparation of necrotic supernatant

A suspension of ~50 x 10^4 cells/mL of U-87 MG cells in PBS was subjected to 5 cycles of rapid freezing at -80 °C and thawing at room temperature. The mixture was centrifuged, and the supernatant was filtered to remove any debris.

5.14. Calcium mobilisation assay (Antagonist mode)

4 x 10^4 U-87 MG cells were seeded into each well of a tissue culture treated 96-well black polystyrene assay plate (Corning, VWR, 734-1609). After 24 h,

the growth medium was removed and replaced with 100 µl of the dye loading solution (Molecular Probes™ Fluo-4 NW (no wash), Invitrogen F36206). The plates were incubated at 37 °C for 30 minutes. 20 µL of a given concentration of the antagonist in assay buffer, or plain assay buffer as control was added to each well and the plate was incubated at 37 °C for 30 minutes. The plate was transferred into a Fluoroskan Ascent FL instrument (Thermo Scientific) and the fluorescence in response to the addition of 20 µl the given concentration of the agonist was measured at 37 °C (Ex 485 nm, Em 538 nm). IC_{50} is calculated as the concentration of the antagonist required to half the maximal response to the given agonist.

5.15. U-87 MG Boyden Well two-chamber Chemotaxis assay

The chemotaxis assay was performed using 24-well chemotaxis chamber inserts (Corning, Product code: 3415). The filters were coated with collagen type-I solution from rat tail (Sigma, C3867). To the lower chamber was added RPMI 1640 (no serum) containing either no agonist for controls or fMLF. To the upper compartment were added U87MG cells (106 cells/mL). After incubation for 15 hours, the medium was removed and replaced with 70% (v/v) ethanol to fix the cells. Using a cotton bud, the non-migrated cells in the top compartment were gently removed from the membrane. The porous membrane was air dried and then was removed using a scalpel. The membrane was mounted onto a slide using mounting medium containing DAPI (Vector Labs, VECTASHIELD hard set mounting medium with DAPI). The mounted slides were viewed under a fluorescent microscope with a camera attached. At least 5 images from varying fields at a 20x magnification were

taken. The number of migrated cells were counted in each field and the averages calculated.

5.16. U-87 MG 3D Collagen Invasion Assay

U-87 MG spheroids were formed using the hanging drop method 24 hours before the experiment set up (section 4.5). Serial drug dilutions were prepared prior to setting the assay up. Collagen (Corning, Collagen I, Rat Tail, 354236) prepared according to the guidelines provided with the product; on ice, to PBS 5x (2 ml) was added sodium hydroxide solution (1 M, 108.33 µl), sterilised and distilled H_2O (3.56 ml) and collagen-I (4.33 ml); all solutions were sterile/sterilised and chilled before addition. The resulting Collagen I mix was kept on ice until use. The Collagen mix was divided between Eppendorf's and the agonist/antagonist dilutions added and gently pipetted to homogenise the resultant mixture. The wells of a 96-well clear-bottomed black plate were loaded with 40 µl Collagen mix which after warming to room temperature, formed a gel. Single spheroids either untreated or pre-treated with antagonist were loaded into each well containing a layer of collagen gel. Another 40 µl Collagen mix was loaded over the top of each spheroid to ensure the spheroid was encased in collagen gel. On top of the final layer of collagen gel was added RPMI 1640 (50 µl) without serum to prevent the spheroids/gel from drying out. Images were taken at 0 hours and 39 hours using a LumaScope 500 and the green fluorescence function to detect the preloaded Calcien AM within the cells. The images were analysed using ImageJ software.[237]

5.17. *In vivo* Experiments

Balb/c immunodeficient nude mice (Envigo, Loughborough, U.K.), between the ages of 6 and 8 weeks were used. Throughout the study, all mice were housed in air-conditioned rooms in facilities approved by the United Kingdom Home Office to meet all current regulations and standards. All procedures were carried out under a Project Licence (PPL 40/3670) issued by the UK Home Office according to government legislation, following approval of the work by the local Animal Welfare Ethics Review Board at the University of Bradford, and in accordance with the UK National Cancer Research Institute Guidelines for the Welfare of Animals.[252]

5.17.1. *In vivo* small molecule tissue distribution

Mice bearing xenografted U-87 MG tumours were administered a single dose of ICT12028 **(60)** (20 mg/kg) in DMSO/mineral oil *via* intraperitoneal injection and divided into groups for time points. At each time point, tissues and plasma were collected and snap frozen at -80 °C until analysis.

Tissue extraction: For each tissue, the weight of the tissue was recorded, and the tissue transferred to a tube containing 3 equivalents (w/v) of chilled PBS. The tissue sample was homogenised, and the homogenate (100 µl) added to an Eppendorf with chilled methanol (300 µl). After thorough mixing, the homogenate/methanol mix was centrifuged at 10000 rpm for 5 minutes at 4 °C. The supernatant was collected and transferred to a mass spectrometry sample vial and kept chilled (-20 °C) until analysis.

Plasma Extraction: To the plasma sample (100 µl) was added chilled methanol (300 µl) and mixed thoroughly. The sample was centrifuged at 10000

rpm for 5 minutes at 4 °C. The supernatant was collected and transferred to a mass spectrometry sample vial and kept chilled (-20 °C) until analysis.

Calibration: Serial dilutions of the drug to be analysed (ICT12028 **(60)**) were made up in methanol. The serial dilutions were added to plasma of untreated mice. To each plasma drug dilution was added chilled methanol (300 µl) and mixed thoroughly. The sample was centrifuged at 10000 rpm for 5 minutes at 4 °C. The supernatant was collected and transferred to a mass spectrometry sample vial and kept chilled (-20 °C) until analysis.

HPLC-MS analysis: The samples were analysed using an Alliance Waters 2695 HPLC linked to a Waters Quattro Ultima Mass Spectrometer (Waters). The column used was the Phenomonex Luna C18 5 µ 250mm x 2mm (00G-4252-E0). Mobile phase A was 90 % distilled H_2O; 9.9 % methanol; 0.1 % formic acid (v/v). Mobile phase B was 9.9 % distilled H_2O; 90 % methanol; 0.1 % formic acid (v/v). The gradient set up is shown in Table 10. The experiment was run, and the data collected and analysed using MassLynx Mass Spectrometry Software (Waters).

*Table 10 The gradient set up parameters used for analysis of ICT12028 **(60)** by HPLC-MS*

Time (min)	A (%)	B (%)	Flow rate (ml/min)	Curve
0	30	70	0.4	1
15	0	100	0.4	6
30	0	100	0.4	6
31	30	70	0.4	6
45	30	70	0.4	6

5.17.2. *In vitro* liver metabolism

Sample preparation: Mouse liver sample weight was recorded, and the tissue transferred to a tube containing 3 equivalents (w/v) of chilled PBS. The

tissue sample was homogenised and to the homogenate (990 µl) was added ICT12028 **(60)** (10 µl) at 1 mg/ml in methanol to a final concentration in liver homogenate of 10 µg/ml. The sample was incubated at 37 °C, and at each time point 100 µl of homogenate was extracted and added to an Eppendorf with chilled methanol (300 µl). After thorough mixing, the homogenate/methanol mix was centrifuged at 10000 rpm for 5 minutes at 4 °C. The supernatant was collected and transferred to a mass spectrometry sample vial and kept chilled (-20 °C) until analysis. Samples were analysed as per the same procedure used for *in vivo* tissue distribution (section 4.16.1).

5.17.3. Tumour xenograft studies

Under brief general inhalation anaesthesia 2 to 3 mm^3 fragments of U87MG human tumour xenografts were implanted subcutaneously in the abdominal flank of the mice. Once tumour volumes reached approximately 32 mm^3 (as measured by callipers), this was designated as Day 0, and mice were randomised into two groups (n=8). One group received ICT12035 **(11)** administered intraperitoneally at 100 mg/kg/dose on days 0, 1, 2, 3 and 4. For comparison, the other group was left untreated. Tumour volume was measured using callipers and animal body weight were recorded through the experiment and normalised to the respective volume on the initial day of treatment (day 0). Mann-Whitney U tests were conducted to determine the statistical significance of any differences in growth rate (based on tumour volume doubling time) between control and treated groups.

5.18. Statistical analysis

For *in vitro* data where statistical analysis is shown, a minimum of 3 independent biological repeats were analysed using the student's t-test (two tailed, equal variance) and expressed as mean ± SD. One biological repeat comprised a minimum of at least 3 technical replicates. Approximate normal distribution of data was assumed. For xenograft tumour analysis, the Mann-Whitney U-test was used (two tailed). The significance was calculated using the log-rank test. P values of ≤ 0.05 were considered significant (*) and P values of ≤ 0.01 were considered highly significant (**).

Bibliography

1. Ahmet, D.S., H.A. Basheer, A. Salem, D. Lu, A. Aghamohammadi, P. Weyerhäuser, A. Bordiga, J. Almeniawi, S. Rashid, P.A. Cooper, S.D. Shnyder, V. Vinader, and K. Afarinkia, *Application of small molecule FPR1 antagonists in the treatment of cancers.* Scientific Reports, 2020. **10**(1): p. 17249.
2. Ahmet, D.S., M.V. Vinader, S. Shnyder, X.W. Bian, L.H. Patterson, and K. Afarinkia, *Targeting the formylpeptide receptor-1 for treatment of glioma*, in *Yorkshire Cancer Research Annual Meeting*. 2013: Harrogate.
3. Ahmet, D.S., M.V. Vinader, S. Shnyder, X.W. Bian, L.H. Patterson, and K. Afarinkia, *Targeting the formylpeptide receptor-1 for treatment of glioma*, in *RSC North East Section Annual Meeting*. 2014: Hull, UK.
4. Ahmet, D.S., M.V. Vinader, S. Shnyder, X.W. Bian, L.H. Patterson, and K. Afarinkia, *Targeting the formylpeptide receptor-1 for treatment of glioma*, in *Gordon Research Council Conference (Chemotactic Cytokines)*. 2014: West Dover Vermont USA.
5. Holland, E.C., *Glioblastoma multiforme: the terminator.* Proceedings of the National Academy of Sciences of the United States of America, 2000. **97**(12): p. 6242-6244.
6. Schwartzbaum, J.A., J.L. Fisher, K.D. Aldape, and M. Wrensch, *Epidemiology and molecular pathology of glioma.* Nat Clin Pract Neurol, 2006. **2**(9): p. 494-503.

7. Pope, W.B., J. Sayre, A. Perlina, J.P. Villablanca, P.S. Mischel, and T.F. Cloughesy, *MR imaging correlates of survival in patients with high-grade gliomas.* AJNR Am J Neuroradiol, 2005. **26**(10): p. 2466-2474.
8. Binello, E., S. Green, and I.M. Germano, *Radiosurgery for high-grade glioma.* Surg Neurol Int, 2012. **3**(Suppl 2): p. S118-S126.
9. Louis, D.N., H. Ohgaki, O.D. Wiestler, W.K. Cavenee, P.C. Burger, A. Jouvet, B.W. Scheithauer, and P. Kleihues, *The 2007 WHO classification of tumours of the central nervous system.* Acta Neuropathologica, 2007. **114**(2): p. 97-109.
10. Hadziahmetovic, M., K. Shirai, and A. Chakravarti, *Recent advancements in multimodality treatment of gliomas.* Future Oncology, 2011. **7**(10): p. 1169-1183.
11. *Cancer Statistics for the UK 2015.* [cited 2018 September]; Cancer Statistics for the UK]. Available from: https://www.cancerresearchuk.org/health-professional/cancer-statistics-for-the-uk.
12. Hanahan, D. and R.A. Weinberg, *The hallmarks of cancer.* Cell, 2000. **100**(1): p. 57-70.
13. Hanahan, D. and R.A. Weinberg, *Hallmarks of cancer: the next generation.* Cell, 2011. **144**(5): p. 646-674.
14. Arruebo, M., N. Vilaboa, B. Saez-Gutierrez, J. Lambea, A. Tres, M. Valladares, and A. Gonzalez-Fernandez, *Assessment of the evolution of cancer treatment therapies.* Cancers, 2011. **3**(3): p. 3279-3330.
15. Heidelberger, C., N.K. Chaudhuri, P. Danneberg, D. Mooren, L. Griesbach, R. Duschinsky, R.J. Schnitzer, E. Pleven, and J. Scheiner,

Fluorinated pyrimidines, a new class of tumour-inhibitory compounds. Nature, 1957. **179**(4561): p. 663-666.

16. Ling, Y.H., J.W. Chen, S.H. Wen, C.Y. Huang, P. Li, L.H. Lu, J. Mei, S.H. Li, W. Wei, M.Y. Cai, and R.P. Guo, *Tumor necrosis as a poor prognostic predictor on postoperative survival of patients with solitary small hepatocellular carcinoma.* BMC Cancer, 2020. **20**(1): p. 607.
17. Bredholt, G., M. Mannelqvist, I.M. Stefansson, E. Birkeland, T.H. Bo, A.M. Oyan, J. Trovik, K.H. Kalland, I. Jonassen, H.B. Salvesen, E. Wik, and L.A. Akslen, *Tumor necrosis is an important hallmark of aggressive endometrial cancer and associates with hypoxia, angiogenesis and inflammation responses.* Oncotarget, 2015. **6**(37): p. 39676-39691.
18. Lotfi, R., C. Kaltenmeier, M.T. Lotze, and C. Bergmann, *Until Death Do Us Part: Necrosis and Oxidation Promote the Tumor Microenvironment.* Transfus Med Hemother, 2016. **43**(2): p. 120-132.
19. Muz, B., P. de la Puente, F. Azab, and A.K. Azab, *The role of hypoxia in cancer progression, angiogenesis, metastasis, and resistance to therapy.* Hypoxia (Auckland, N.Z.), 2015. **3**: p. 83-92.
20. Monteiro, A.R., R. Hill, G.J. Pilkington, and P.A. Madureira, *The Role of Hypoxia in Glioblastoma Invasion.* Cells, 2017. **6**(4): p. 45.
21. Hsieh, C.H., C.H. Lee, J.A. Liang, C.Y. Yu, and W.C. Shyu, *Cycling hypoxia increases U87 glioma cell radioresistance via ROS induced higher and long-term HIF-1 signal transduction activity.* Oncol Rep, 2010. **24**(6): p. 1629-1636.
22. Das, B., R. Tsuchida, D. Malkin, G. Koren, S. Baruchel, and H. Yeger, *Hypoxia enhances tumor stemness by increasing the invasive and*

tumorigenic side population fraction. Stem Cells, 2008. **26**(7): p. 1818-1830.

23. Emami Nejad, A., S. Najafgholian, A. Rostami, A. Sistani, S. Shojaeifar, M. Esparvarinha, R. Nedaeinia, S. Haghjooy Javanmard, M. Taherian, M. Ahmadlou, R. Salehi, B. Sadeghi, and M. Manian, *The role of hypoxia in the tumor microenvironment and development of cancer stem cell: a novel approach to developing treatment.* Cancer Cell Int, 2021. **21**(1): p. 62.
24. Papale, M., M. Buccarelli, C. Mollinari, M.A. Russo, R. Pallini, L. Ricci-Vitiani, and M. Tafani, *Hypoxia, Inflammation and Necrosis as Determinants of Glioblastoma Cancer Stem Cells Progression.* Int J Mol Sci, 2020. **21**(8): p. 2660.
25. Yao, M., S. Li, X. Wu, S. Diao, G. Zhang, H. He, L. Bian, and Y. Lu, *Cellular origin of glioblastoma and its implication in precision therapy.* Cell Mol Immunol, 2018. **15**(8): p. 737-739.
26. Alcantara Llaguno, S.R. and L.F. Parada, *Cell of origin of glioma: biological and clinical implications.* Br J Cancer, 2016. **115**(12): p. 1445-1450.
27. Fan, X., Y. Xiong, and Y. Wang, *A reignited debate over the cell(s) of origin for glioblastoma and its clinical implications.* Front Med, 2019. **13**(5): p. 531-539.
28. Cahill, D. and S. Turcan, *Origin of Gliomas.* Semin Neurol, 2018. **38**(1): p. 5-10.
29. Visvader, J.E., *Cells of origin in cancer.* Nature, 2011. **469**(7330): p. 314-322.

30. Molnar, C. and J. Gair. *Concepts of Biology - 1st Canadian Edition*. 2015.

31. Edward, M. *Pathology images and text for medical education - WebPath*. 2021 [cited 2021 14/07/2021]; Available from: https://webpath.med.utah.edu/.

32. Charity, T.B.T. *Brain Tumour Prognosis*. 2018 [cited 2018 September]; Glioblastoma statistics survival]. Available from: https://www.thebraintumourcharity.org/understanding-brain-tumours/getting-a-diagnosis/prognosis/prognosis-specific-brain-tumours/.

33. Jeffrey N Bruce, B.K. *Glioblastoma Multiforme Clinical Presentation*. 2018 [cited 2018 September]; Available from: https://emedicine.medscape.com/article/283252-overview.

34. Perry, J., L. Zinman, A. Chambers, K. Spithoff, N. Lloyd, N. Laperriere, G. on behalf of the Neuro-oncology Disease Site, and C. of Cancer Care Ontario's Program in Evidence-Based, *The use of prophylactic anticonvulsants in patients with brain tumours—a systematic review.* Curr Oncol, 2006. **13**(6): p. 222-229.

35. Hanif, F., K. Muzaffar, K. Perveen, S.M. Malhi, and U. Simjee Sh, *Glioblastoma Multiforme: A Review of its Epidemiology and Pathogenesis through Clinical Presentation and Treatment.* Asian Pac J Cancer Prev, 2017. **18**(1): p. 3-9.

36. Davis, M.E., *Glioblastoma: Overview of Disease and Treatment.* Clin J Oncol Nurs, 2016. **20**(5 Suppl): p. S2-S8.

37. Rong, Y., D.L. Durden, E.G. Van Meir, and D.J. Brat, *'Pseudopalisading' necrosis in glioblastoma: a familiar morphologic feature that links vascular pathology, hypoxia, and angiogenesis.* J Neuropathol Exp Neurol, 2006. **65**(6): p. 529-539.

38. Kwock, L., J.K. Smith, M. Castillo, M.G. Ewend, F. Collichio, D.E. Morris, T.W. Bouldin, and S. Cush, *Clinical role of proton magnetic resonance spectroscopy in oncology: brain, breast, and prostate cancer.* Lancet Oncol, 2006. **7**(10): p. 859-868.

39. Zhu, X.P., K.L. Li, I.D. Kamaly-Asl, D.R. Checkley, J.J. Tessier, J.C. Waterton, and A. Jackson, *Quantification of endothelial permeability, leakage space, and blood volume in brain tumors using combined T1 and T2* contrast-enhanced dynamic MR imaging.* J Magn Reson Imaging, 2000. **11**(6): p. 575-585.

40. Swanson, K.R., C. Bridge, J.D. Murray, and E.C. Alvord, Jr., *Virtual and real brain tumors: using mathematical modeling to quantify glioma growth and invasion.* J Neurol Sci, 2003. **216**(1): p. 1-10.

41. Mandonnet, E., J.Y. Delattre, M.L. Tanguy, K.R. Swanson, A.F. Carpentier, H. Duffau, P. Cornu, R. Van Effenterre, E.C. Alvord, Jr., and L. Capelle, *Continuous growth of mean tumor diameter in a subset of grade II gliomas.* Ann Neurol, 2003. **53**(4): p. 524-528.

42. Gupta, M., A. Djalilvand, and D.J. Brat, *Clarifying the Diffuse Gliomas.* Am J Clin Pathol, 2005. **124**(5): p. 755-768.

43. Bellail, A.C., S.B. Hunter, D.J. Brat, C. Tan, and E.G. Van Meir, *Microregional extracellular matrix heterogeneity in brain modulates glioma cell invasion.* Int J Biochem Cell Biol, 2004. **36**(6): p. 1046-1069.

44. Brat, D.J., A. Castellano-Sanchez, B. Kaur, and E.G. Van Meir, *Genetic and biologic progression in astrocytomas and their relation to angiogenic dysregulation.* Adv Anat Pathol, 2002. **9**(1): p. 24-36.

45. Onishi, M., T. Ichikawa, K. Kurozumi, and I. Date, *Angiogenesis and invasion in glioma.* Brain Tumor Pathol, 2011. **28**(1): p. 13-24.

46. Sun, H., D. Guo, Y. Su, D. Yu, Q. Wang, T. Wang, Q. Zhou, X. Ran, and Z. Zou, *Hyperplasia of pericytes is one of the main characteristics of microvascular architecture in malignant glioma.* Plos One, 2014. **9**(12): p. e114246.

47. Wang, Y. and T. Jiang, *Understanding high grade glioma: molecular mechanism, therapy and comprehensive management.* Cancer Lett, 2013. **331**(2): p. 139-146.

48. Lara-Velazquez, M., R. Al-Kharboosh, S. Jeanneret, C. Vazquez-Ramos, D. Mahato, D. Tavanaiepour, G. Rahmathulla, and A. Quinones-Hinojosa, *Advances in Brain Tumor Surgery for Glioblastoma in Adults.* Brain Sci, 2017. **7**(12): p. 166.

49. De Bonis, P., C. Anile, A. Pompucci, A. Fiorentino, M. Balducci, S. Chiesa, L. Lauriola, G. Maira, and A. Mangiola, *The influence of surgery on recurrence pattern of glioblastoma.* Clin Neurol Neurosurg, 2013. **115**(1): p. 37-43.

50. Milano, M.T., P. Okunieff, R.S. Donatello, N.A. Mohile, J. Sul, K.A. Walter, and D.N. Korones, *Patterns and timing of recurrence after temozolomide-based chemoradiation for glioblastoma.* Int J Radiat Oncol Biol Phys, 2010. **78**(4): p. 1147-1155.

51. Rapp, M., J. Baernreuther, B. Turowski, H.J. Steiger, M. Sabel, and M.A. Kamp, *Recurrence Pattern Analysis of Primary Glioblastoma.* World Neurosurg, 2017. **103**: p. 733-740.

52. Baskar, R., J. Dai, N. Wenlong, R. Yeo, and K.W. Yeoh, *Biological response of cancer cells to radiation treatment.* Front Mol Biosci, 2014. **1**: p. 24.

53. Gzell, C., M. Back, H. Wheeler, D. Bailey, and M. Foote, *Radiotherapy in Glioblastoma: the Past, the Present and the Future.* Clin Oncol, 2017. **29**(1): p. 15-25.

54. Mann, J., R. Ramakrishna, R. Magge, and A.G. Wernicke, *Advances in Radiotherapy for Glioblastoma.* Front Neurol, 2017. **8**(748): p. 748.

55. Shukla, G., G.S. Alexander, S. Bakas, R. Nikam, K. Talekar, J.D. Palmer, and W. Shi, *Advanced magnetic resonance imaging in glioblastoma: a review.* Chin Clin Oncol, 2017. **6**(4): p. 40.

56. Nie, S., Y. Zhu, J. Yang, T. Xin, S. Xue, X. Zhang, J. Sun, D. Mu, Y. Gao, Z. Chen, X. Ding, J. Yu, and M. Hu, *Determining optimal clinical target volume margins in high-grade glioma based on microscopic tumor extension and magnetic resonance imaging.* Radiat Oncol, 2021. **16**(1): p. 97.

57. Price, S.J., R. Jena, N.G. Burnet, P.J. Hutchinson, A.F. Dean, A. Pena, J.D. Pickard, T.A. Carpenter, and J.H. Gillard, *Improved delineation of glioma margins and regions of infiltration with the use of diffusion tensor imaging: an image-guided biopsy study.* AJNR Am J Neuroradiol, 2006. **27**(9): p. 1969-1974.

58. Stupp, R., M.E. Hegi, W.P. Mason, M.J. van den Bent, M.J. Taphoorn, R.C. Janzer, S.K. Ludwin, A. Allgeier, B. Fisher, K. Belanger, P. Hau, A.A. Brandes, J. Gijtenbeek, C. Marosi, C.J. Vecht, K. Mokhtari, P. Wesseling, S. Villa, E. Eisenhauer, T. Gorlia, M. Weller, D. Lacombe, J.G. Cairncross, R.O. Mirimanoff, R. European Organisation for, T. Treatment of Cancer Brain, G. Radiation Oncology, and G. National Cancer Institute of Canada Clinical Trials, *Effects of radiotherapy with concomitant and adjuvant temozolomide versus radiotherapy alone on survival in glioblastoma in a randomised phase III study: 5-year analysis of the EORTC-NCIC trial.* Lancet Oncol, 2009. **10**(5): p. 459-466.

59. Lee, S.Y., *Temozolomide resistance in glioblastoma multiforme.* Genes Dis, 2016. **3**(3): p. 198-210.

60. Yoshimoto, K., M. Mizoguchi, N. Hata, H. Murata, R. Hatae, T. Amano, A. Nakamizo, and T. Sasaki, *Complex DNA repair pathways as possible therapeutic targets to overcome temozolomide resistance in glioblastoma.* Front Oncol, 2012. **2**: p. 186.

61. Liu, G., X. Yuan, Z. Zeng, P. Tunici, H. Ng, I.R. Abdulkadir, L. Lu, D. Irvin, K.L. Black, and J.S. Yu, *Analysis of gene expression and chemoresistance of CD133+ cancer stem cells in glioblastoma.* Mol Cancer, 2006. **5**(1): p. 67.

62. Pistollato, F., S. Abbadi, E. Rampazzo, L. Persano, A. Della Puppa, C. Frasson, E. Sarto, R. Scienza, D. D'Avella, and G. Basso, *Intratumoral hypoxic gradient drives stem cells distribution and MGMT expression in glioblastoma.* Stem Cells, 2010. **28**(5): p. 851-862.

63. Beier, D., P. Hau, M. Proescholdt, A. Lohmeier, J. Wischhusen, P.J. Oefner, L. Aigner, A. Brawanski, U. Bogdahn, and C.P. Beier, *CD133(+) and CD133(-) glioblastoma-derived cancer stem cells show differential growth characteristics and molecular profiles.* Cancer Res, 2007. **67**(9): p. 4010-4015.

64. Beier, D., S. Rohrl, D.R. Pillai, S. Schwarz, L.A. Kunz-Schughart, P. Leukel, M. Proescholdt, A. Brawanski, U. Bogdahn, A. Trampe-Kieslich, B. Giebel, J. Wischhusen, G. Reifenberger, P. Hau, and C.P. Beier, *Temozolomide preferentially depletes cancer stem cells in glioblastoma.* Cancer Res, 2008. **68**(14): p. 5706-5715.

65. Gramatzki, D., P. Roth, E.J. Rushing, J. Weller, N. Andratschke, S. Hofer, D. Korol, L. Regli, A. Pangalu, M. Pless, J. Oberle, R. Bernays, H. Moch, S. Rohrmann, and M. Weller, *Bevacizumab may improve quality of life, but not overall survival in glioblastoma: an epidemiological study.* Ann Oncol, 2018. **29**(6): p. 1431-1436.

66. Westphal, M., C.L. Maire, and K. Lamszus, *EGFR as a Target for Glioblastoma Treatment: An Unfulfilled Promise.* CNS Drugs, 2017. **31**(9): p. 723-735.

67. Nakada, M., D. Kita, T. Watanabe, Y. Hayashi, and J. Hamada, *Mechanism of chemoresistance against tyrosine kinase inhibitors in malignant glioma.* Brain Tumor Pathol, 2014. **31**(3): p. 198-207.

68. Prados, M.D., S.M. Chang, N. Butowski, R. DeBoer, R. Parvataneni, H. Carliner, P. Kabuubi, J. Ayers-Ringler, J. Rabbitt, M. Page, A. Fedoroff, P.K. Sneed, M.S. Berger, M.W. McDermott, A.T. Parsa, S. Vandenberg, C.D. James, K.R. Lamborn, D. Stokoe, and D.A. Haas-

Kogan, *Phase II study of erlotinib plus temozolomide during and after radiation therapy in patients with newly diagnosed glioblastoma multiforme or gliosarcoma.* J Clin Oncol, 2009. **27**(4): p. 579-584.

69. Weller, M., N. Butowski, D.D. Tran, L.D. Recht, M. Lim, H. Hirte, L. Ashby, L. Mechtler, S.A. Goldlust, F. Iwamoto, J. Drappatz, D.M. O'Rourke, M. Wong, M.G. Hamilton, G. Finocchiaro, J. Perry, W. Wick, J. Green, Y. He, C.D. Turner, M.J. Yellin, T. Keler, T.A. Davis, R. Stupp, J.H. Sampson, and A.I.t. investigators, *Rindopepimut with temozolomide for patients with newly diagnosed, EGFRvIII-expressing glioblastoma (ACT IV): a randomised, double-blind, international phase 3 trial.* Lancet Oncol, 2017. **18**(10): p. 1373-1385.
70. Peereboom, D.M., D.R. Shepard, M.S. Ahluwalia, C.J. Brewer, N. Agarwal, G.H. Stevens, J.H. Suh, S.A. Toms, M.A. Vogelbaum, R.J. Weil, P. Elson, and G.H. Barnett, *Phase II trial of erlotinib with temozolomide and radiation in patients with newly diagnosed glioblastoma multiforme.* J Neurooncol, 2010. **98**(1): p. 93-99.
71. Chaichana, K.L., H. Zaidi, C. Pendleton, M.J. McGirt, R. Grossman, J.D. Weingart, A. Olivi, A. Quinones-Hinojosa, and H. Brem, *The efficacy of carmustine wafers for older patients with glioblastoma multiforme: prolonging survival.* Neurol Res, 2011. **33**(7): p. 759-764.
72. Attenello, F.J., D. Mukherjee, G. Datoo, M.J. McGirt, E. Bohan, J.D. Weingart, A. Olivi, A. Quinones-Hinojosa, and H. Brem, *Use of Gliadel (BCNU) wafer in the surgical treatment of malignant glioma: a 10-year institutional experience.* Ann Surg Oncol, 2008. **15**(10): p. 2887-2893.

73. Reithmeier, T., E. Graf, T. Piroth, M. Trippel, M.O. Pinsker, and G. Nikkhah, *BCNU for recurrent glioblastoma multiforme: efficacy, toxicity and prognostic factors.* BMC Cancer, 2010. **10**: p. 30.

74. Belhadj, Z., C. Zhan, M. Ying, X. Wei, C. Xie, Z. Yan, and W. Lu, *Multifunctional targeted liposomal drug delivery for efficient glioblastoma treatment.* Oncotarget, 2017. **8**(40): p. 66889-66900.

75. Ozdemir-Kaynak, E., A.A. Qutub, and O. Yesil-Celiktas, *Advances in Glioblastoma Multiforme Treatment: New Models for Nanoparticle Therapy.* Front Physiol, 2018. **9**: p. 170.

76. Abbott, N.J., L. Ronnback, and E. Hansson, *Astrocyte-endothelial interactions at the blood-brain barrier.* Nat Rev Neurosci, 2006. **7**(1): p. 41-53.

77. Oberoi, R.K., K.E. Parrish, T.T. Sio, R.K. Mittapalli, W.F. Elmquist, and J.N. Sarkaria, *Strategies to improve delivery of anticancer drugs across the blood-brain barrier to treat glioblastoma.* Neuro Oncol, 2016. **18**(1): p. 27-36.

78. Liu, H.L., C.H. Fan, C.Y. Ting, and C.K. Yeh, *Combining microbubbles and ultrasound for drug delivery to brain tumors: current progress and overview.* Theranostics, 2014. **4**(4): p. 432-444.

79. Li, J., C. Di, A.K. Mattox, L. Wu, and D.C. Adamson, *The future role of personalized medicine in the treatment of glioblastoma multiforme.* Pharmgenomics Pers Med, 2010. **3**: p. 111-127.

80. Weller, M., R. Stupp, M. Hegi, and W. Wick, *Individualized targeted therapy for glioblastoma: fact or fiction?* Cancer J, 2012. **18**(1): p. 40-44.

81. Domanska, U.M., R.C. Kruizinga, W.F. den Dunnen, H. Timmer-Bosscha, E.G. de Vries, and A.M. Walenkamp, *The chemokine network, a newly discovered target in high grade gliomas.* Crit Rev Oncol Hematol, 2011. **79**(2): p. 154-163.

82. Huang, J., K. Chen, J. Chen, W. Gong, N.M. Dunlop, O.M. Howard, Y. Gao, X.W. Bian, and J.M. Wang, *The G-protein-coupled formylpeptide receptor FPR confers a more invasive phenotype on human glioblastoma cells.* Br J Cancer, 2010. **102**(6): p. 1052-1060.

83. Huang, J., K. Chen, W. Gong, Y. Zhou, Y. Le, X. Bian, and J.M. Wang, *Receptor "hijacking" by malignant glioma cells: a tactic for tumor progression.* Cancer Lett, 2008. **267**(2): p. 254-261.

84. Liu, M., J. Zhao, K. Chen, X. Bian, C. Wang, Y. Shi, and J.M. Wang, *G protein-coupled receptor FPR1 as a pharmacologic target in inflammation and human glioblastoma.* Int Immunopharmacol, 2012. **14**(3): p. 283-288.

85. Yang, Y., Y. Liu, X. Yao, Y. Ping, T. Jiang, Q. Liu, S. Xu, J. Huang, H. Mou, W. Gong, K. Chen, X. Bian, and J.M. Wang, *Annexin 1 released by necrotic human glioblastoma cells stimulates tumor cell growth through the formyl peptide receptor 1.* Am J Pathol, 2011. **179**(3): p. 1504-1512.

86. Zhou, Y., X. Bian, Y. Le, W. Gong, J. Hu, X. Zhang, L. Wang, P. Iribarren, R. Salcedo, O.M. Howard, W. Farrar, and J.M. Wang, *Formylpeptide receptor FPR and the rapid growth of malignant human gliomas.* J Natl Cancer Inst, 2005. **97**(11): p. 823-835.

87. Galluzzi, L., I. Vitale, S.A. Aaronson, J.M. Abrams, D. Adam, P. Agostinis, E.S. Alnemri, L. Altucci, I. Amelio, D.W. Andrews, M. Annicchiarico-Petruzzelli, A.V. Antonov, E. Arama, E.H. Baehrecke, N.A. Barlev, N.G. Bazan, F. Bernassola, M.J.M. Bertrand, K. Bianchi, M.V. Blagosklonny, K. Blomgren, C. Borner, P. Boya, C. Brenner, M. Campanella, E. Candi, D. Carmona-Gutierrez, F. Cecconi, F.K. Chan, N.S. Chandel, E.H. Cheng, J.E. Chipuk, J.A. Cidlowski, A. Ciechanover, G.M. Cohen, M. Conrad, J.R. Cubillos-Ruiz, P.E. Czabotar, V. D'Angiolella, T.M. Dawson, V.L. Dawson, V. De Laurenzi, R. De Maria, K.M. Debatin, R.J. DeBerardinis, M. Deshmukh, N. Di Daniele, F. Di Virgilio, V.M. Dixit, S.J. Dixon, C.S. Duckett, B.D. Dynlacht, W.S. El-Deiry, J.W. Elrod, G.M. Fimia, S. Fulda, A.J. Garcia-Saez, A.D. Garg, C. Garrido, E. Gavathiotis, P. Golstein, E. Gottlieb, D.R. Green, L.A. Greene, H. Gronemeyer, A. Gross, G. Hajnoczky, J.M. Hardwick, I.S. Harris, M.O. Hengartner, C. Hetz, H. Ichijo, M. Jaattela, B. Joseph, P.J. Jost, P.P. Juin, W.J. Kaiser, M. Karin, T. Kaufmann, O. Kepp, A. Kimchi, R.N. Kitsis, D.J. Klionsky, R.A. Knight, S. Kumar, S.W. Lee, J.J. Lemasters, B. Levine, A. Linkermann, S.A. Lipton, R.A. Lockshin, C. Lopez-Otin, S.W. Lowe, T. Luedde, E. Lugli, M. MacFarlane, F. Madeo, M. Malewicz, W. Malorni, G. Manic, J.C. Marine, S.J. Martin, J.C. Martinou, J.P. Medema, P. Mehlen, P. Meier, S. Melino, E.A. Miao, J.D. Molkentin, U.M. Moll, C. Munoz-Pinedo, S. Nagata, G. Nunez, A. Oberst, M. Oren, M. Overholtzer, M. Pagano, T. Panaretakis, M. Pasparakis, J.M. Penninger, D.M. Pereira, S. Pervaiz, M.E. Peter, M. Piacentini, P. Pinton, J.H.M. Prehn, H. Puthalakath, G.A.

Rabinovich, M. Rehm, R. Rizzuto, C.M.P. Rodrigues, D.C. Rubinsztein, T. Rudel, K.M. Ryan, E. Sayan, L. Scorrano, F. Shao, Y. Shi, J. Silke, H.U. Simon, A. Sistigu, B.R. Stockwell, A. Strasser, G. Szabadkai, S.W.G. Tait, D. Tang, N. Tavernarakis, A. Thorburn, Y. Tsujimoto, B. Turk, T. Vanden Berghe, P. Vandenabeele, M.G. Vander Heiden, A. Villunger, H.W. Virgin, K.H. Vousden, D. Vucic, E.F. Wagner, H. Walczak, D. Wallach, Y. Wang, J.A. Wells, W. Wood, J. Yuan, Z. Zakeri, B. Zhivotovsky, L. Zitvogel, G. Melino and G. Kroemer, *Molecular mechanisms of cell death: recommendations of the Nomenclature Committee on Cell Death 2018.* Cell Death Differ, 2018. **25**(3): p. 486-541.

88. Majno, G., M. La Gattuta, and T.E. Thompson, *Cellular death and necrosis: chemical, physical and morphologic changes in rat liver.* Virchows Arch Pathol Anat Physiol Klin Med, 1960. **333**: p. 421-465.

89. Page, A.R. and R.A. Good, *A clinical and experimental study of the function of neutrophils in the inflammatory response.* Am J Pathol, 1958. **34**(4): p. 645-669.

90. Rock, K.L. and H. Kono, *The inflammatory response to cell death.* Annu Rev Pathol, 2008. **3**: p. 99-126.

91. Liu, Z.X., D. Han, B. Gunawan, and N. Kaplowitz, *Neutrophil depletion protects against murine acetaminophen hepatotoxicity.* Hepatology, 2006. **43**(6): p. 1220-1230.

92. Romson, J.L., B.G. Hook, S.L. Kunkel, G.D. Abrams, M.A. Schork, and B.R. Lucchesi, *Reduction of the extent of ischemic myocardial injury by neutrophil depletion in the dog.* Circulation, 1983. **67**(5): p. 1016-1023.

93. Scaffidi, P., T. Misteli, and M.E. Bianchi, *Release of chromatin protein HMGB1 by necrotic cells triggers inflammation.* Nature, 2002. **418**(6894): p. 191-195.

94. Martin, P. and S.J. Leibovich, *Inflammatory cells during wound repair: the good, the bad and the ugly.* Trends Cell Biol, 2005. **15**(11): p. 599-607.

95. Balkwill, F. and A. Mantovani, *Inflammation and cancer: back to Virchow?* Lancet, 2001. **357**(9255): p. 539-545.

96. Coussens, L.M. and Z. Werb, *Inflammation and cancer.* Nature, 2002. **420**(6917): p. 860-867.

97. Rakoff-Nahoum, S., *Why cancer and inflammation?* Yale J Biol Med, 2006. **79**(3-4): p. 123-130.

98. Munger, K. and P.M. Howley, *Human papillomavirus immortalization and transformation functions.* Virus Res, 2002. **89**(2): p. 213-228.

99. Hussain, S.P., L.J. Hofseth, and C.C. Harris, *Radical causes of cancer.* Nat Rev Cancer, 2003. **3**(4): p. 276-285.

100. Coussens, L.M., W.W. Raymond, G. Bergers, M. Laig-Webster, O. Behrendtsen, Z. Werb, G.H. Caughey, and D. Hanahan, *Inflammatory mast cells up-regulate angiogenesis during squamous epithelial carcinogenesis.* Genes Dev, 1999. **13**(11): p. 1382-1397.

101. Dvorak, H.F., *Tumors: wounds that do not heal. Similarities between tumor stroma generation and wound healing.* N Engl J Med, 1986. **315**(26): p. 1650-1659.

102. Bergers, G., R. Brekken, G. McMahon, T.H. Vu, T. Itoh, K. Tamaki, K. Tanzawa, P. Thorpe, S. Itohara, Z. Werb, and D. Hanahan, *Matrix*

metalloproteinase-9 triggers the angiogenic switch during carcinogenesis. Nat Cell Biol, 2000. **2**(10): p. 737-744.

103. Proskuryakov, S.Y. and V.L. Gabai, *Mechanisms of tumor cell necrosis.* Curr Pharm Des, 2010. **16**(1): p. 56-68.

104. Raza, S.M., F.F. Lang, B.B. Aggarwal, G.N. Fuller, D.M. Wildrick, and R. Sawaya, *Necrosis and glioblastoma: a friend or a foe? A review and a hypothesis.* Neurosurgery, 2002. **51**(1): p. 2-13.

105. Noch, E. and K. Khalili, *Molecular mechanisms of necrosis in glioblastoma: the role of glutamate excitotoxicity.* Cancer Biol Ther, 2009. **8**(19): p. 1791-1797.

106. Liu, S., Y. Wang, K. Xu, Z. Wang, X. Fan, C. Zhang, S. Li, X. Qiu, and T. Jiang, *Relationship between necrotic patterns in glioblastoma and patient survival: fractal dimension and lacunarity analyses using magnetic resonance imaging.* Sci Rep-UK, 2017. **7**(1): p. 8302.

107. Wippold, F.J., 2nd, M. Lammle, F. Anatelli, J. Lennerz, and A. Perry, *Neuropathology for the neuroradiologist: palisades and pseudopalisades.* AJNR Am J Neuroradiol, 2006. **27**(10): p. 2037-2041.

108. Rong, Y. and D.J. Brat, *Vaso-occlusive Mechanisms that Intiate Hypoxia and Necrosis in Glioblastoma: The Role of Thrombosis and Tissue Factor*, in *CNS Cancer*, E.G. Meir, Editor. 2009, Humana Press: Totowa, NJ. p. 507-528.

109. Brat, D.J. and E.G. Van Meir, *Vaso-occlusive and prothrombotic mechanisms associated with tumor hypoxia, necrosis, and accelerated growth in glioblastoma.* Lab Invest, 2004. **84**(4): p. 397-405.

110. Brat, D.J., A.A. Castellano-Sanchez, S.B. Hunter, M. Pecot, C. Cohen, E.H. Hammond, S.N. Devi, B. Kaur, and E.G. Van Meir, *Pseudopalisades in glioblastoma are hypoxic, express extracellular matrix proteases, and are formed by an actively migrating cell population.* Cancer Res, 2004. **64**(3): p. 920-927.

111. Inoue, A., H. Takahashi, H. Harada, S. Kohno, S. Ohue, K. Kobayashi, H. Yano, J. Tanaka, and T. Ohnishi, *Cancer stem-like cells of glioblastoma characteristically express MMP-13 and display highly invasive activity.* Int J Oncol, 2010. **37**(5): p. 1121-1131.

112. Wang, F., P. Zhang, L. Yang, X. Yu, X. Ye, J. Yang, C. Qian, X. Zhang, Y.H. Cui, and X.W. Bian, *Activation of toll-like receptor 2 promotes invasion by upregulating MMPs in glioma stem cells.* Am J Transl Res, 2015. **7**(3): p. 607-615.

113. Mayr, M.T., I.R. Crocker, E.K. Butker, H. Williams, G.A. Cotsonis, and J.J. Olson, *Results of interstitial brachytherapy for malignant brain tumors.* Int J Oncol, 2002. **21**(4): p. 817-823.

114. Charfen, C.O., P.K. Sneed, W.M. Wara, D.A. Larson, T.L. Phillips, M.D. Prados, K.A. Weaver, M. Malec, P. Acord, K.R. Lamborn, S.A. Lamb, B. Ham, and P.H. Gutin, *High activity iodine-125 interstitial implant for gliomas.* Int J Radiat Oncol Biol Phys, 1992. **24**(4): p. 583-591.

115. Pisetsky, D., *Cell death in the pathogenesis of immune-mediated diseases: the role of HMGB1 and DAMP-PAMP complexes.* Swiss medical weekly, 2011. **141**: p. w13256.

116. Lin, J.C., J.T. Tsai, T.Y. Chao, H.I. Ma, and W.H. Liu, *Musashi-1 Enhances Glioblastoma Migration by Promoting ICAM1 Translation.* Neoplasia (New York, N.Y.), 2019. **21**(5): p. 459-468.

117. Alieva, M., A.S. Margarido, T. Wieles, E.R. Abels, B. Colak, C. Boquetale, H. Jan Noordmans, T.J. Snijders, M.L. Broekman, and J. van Rheenen, *Preventing inflammation inhibits biopsy-mediated changes in tumor cell behavior.* Sci Rep-UK, 2017. **7**(1): p. 7529.

118. Alieva, M., J. van Rheenen, and M.L.D. Broekman, *Potential impact of invasive surgical procedures on primary tumor growth and metastasis.* Clinical & experimental metastasis, 2018. **35**(4): p. 319-331.

119. *Brain tumours (primary) and brain metastases in adults - NICE guideline [NG99]*. 2018 29/01/2021 [cited 2021 30/07/2021]; Available from: https://www.nice.org.uk/guidance/ng99/chapter/Recommendations.

120. Siu, A., J.J. Wind, J.B. Iorgulescu, T.A. Chan, Y. Yamada, and J.H. Sherman, *Radiation necrosis following treatment of high grade glioma--a review of the literature and current understanding.* Acta Neurochir (Wien), 2012. **154**(2): p. 191-201.

121. Reinhold, H.S., W. Calvo, J.W. Hopewell, and A.P. van der Berg, *Development of blood vessel-related radiation damage in the fimbria of the central nervous system.* Int J Radiat Oncol Biol Phys, 1990. **18**(1): p. 37-42.

122. Zhao, W. and M.E. Robbins, *Inflammation and chronic oxidative stress in radiation-induced late normal tissue injury: therapeutic implications.* Curr Med Chem, 2009. **16**(2): p. 130-143.

123. Barker, F.G., 2nd, R.L. Davis, S.M. Chang, and M.D. Prados, *Necrosis as a prognostic factor in glioblastoma multiforme.* Cancer, 1996. **77**(6): p. 1161-1166.

124. Hammoud, M.A., R. Sawaya, W. Shi, P.F. Thall, and N.E. Leeds, *Prognostic significance of preoperative MRI scans in glioblastoma multiforme.* J Neurooncol, 1996. **27**(1): p. 65-73.

125. Lacroix, M., D. Abi-Said, D.R. Fourney, Z.L. Gokaslan, W. Shi, F. DeMonte, F.F. Lang, I.E. McCutcheon, S.J. Hassenbusch, E. Holland, K. Hess, C. Michael, D. Miller, and R. Sawaya, *A multivariate analysis of 416 patients with glioblastoma multiforme: prognosis, extent of resection, and survival.* J Neurosurg, 2001. **95**(2): p. 190-198.

126. Quail, D.F. and J.A. Joyce, *The Microenvironmental Landscape of Brain Tumors.* Cancer Cell, 2017. **31**(3): p. 326-341.

127. De Vleeschouwer, S. and G. Bergers, *Glioblastoma: To Target the Tumor Cell or the Microenvironment?*, in *Glioblastoma*, S. De Vleeschouwer, Editor. 2017, Codon Publications

128. Manini, I., F. Caponnetto, A. Bartolini, T. Ius, L. Mariuzzi, C. Di Loreto, A.P. Beltrami, and D. Cesselli, *Role of Microenvironment in Glioma Invasion: What We Learned from In Vitro Models.* Int J Mol Sci, 2018. **19**(1): p. 147.

129. Xiao, W., A. Sohrabi, and S.K. Seidlits, *Integrating the glioblastoma microenvironment into engineered experimental models.* Future Sci OA, 2017. **3**(3): p. FSO189.

130. Bizzarro, V., R. Belvedere, V. Migliaro, E. Romano, L. Parente, and A. Petrella, *Hypoxia regulates ANXA1 expression to support prostate cancer cell invasion and aggressiveness.* Cell Adh Migr, 2017. **11**(3): p. 247-260.

131. Jensen, R.L., *Brain tumor hypoxia: tumorigenesis, angiogenesis, imaging, pseudoprogression, and as a therapeutic target.* J Neurooncol, 2009. **92**(3): p. 317-335.

132. Terasaki, M., Y. Sugita, F. Arakawa, Y. Okada, K. Ohshima, and M. Shigemori, *CXCL12/CXCR4 signaling in malignant brain tumors: a potential pharmacological therapeutic target.* Brain Tumor Pathol, 2011. **28**(2): p. 89-97.

133. Couturier, C.P., S. Ayyadhury, P.U. Le, J. Nadaf, J. Monlong, G. Riva, R. Allache, S. Baig, X. Yan, M. Bourgey, C. Lee, Y.C.D. Wang, V. Wee Yong, M.C. Guiot, H. Najafabadi, B. Misic, J. Antel, G. Bourque, J. Ragoussis, and K. Petrecca, *Single-cell RNA-seq reveals that glioblastoma recapitulates a normal neurodevelopmental hierarchy.* Nat Commun, 2020. **11**(1): p. 3406.

134. Dirkse, A., A. Golebiewska, T. Buder, P.V. Nazarov, A. Muller, S. Poovathingal, N.H.C. Brons, S. Leite, N. Sauvageot, D. Sarkisjan, M. Seyfrid, S. Fritah, D. Stieber, A. Michelucci, F. Hertel, C. Herold-Mende, F. Azuaje, A. Skupin, R. Bjerkvig, A. Deutsch, A. Voss-Bohme, and S.P. Niclou, *Stem cell-associated heterogeneity in Glioblastoma results from intrinsic tumor plasticity shaped by the microenvironment.* Nat Commun, 2019. **10**(1): p. 1787.

135. Burrell, R.A., N. McGranahan, J. Bartek, and C. Swanton, *The causes and consequences of genetic heterogeneity in cancer evolution.* Nature, 2013. **501**(7467): p. 338-345.

136. Auffinger, B., D. Spencer, P. Pytel, A.U. Ahmed, and M.S. Lesniak, *The role of glioma stem cells in chemotherapy resistance and glioblastoma multiforme recurrence.* Expert review of neurotherapeutics, 2015. **15**(7): p. 741-752.

137. Iwadate, Y., *Plasticity in Glioma Stem Cell Phenotype and Its Therapeutic Implication.* Neurologia medico-chirurgica, 2018. **58**(2): p. 61-70.

138. Cancer Genome Atlas Research, N., *Comprehensive genomic characterization defines human glioblastoma genes and core pathways.* Nature, 2008. **455**(7216): p. 1061-1068.

139. Verhaak, R.G., K.A. Hoadley, E. Purdom, V. Wang, Y. Qi, M.D. Wilkerson, C.R. Miller, L. Ding, T. Golub, J.P. Mesirov, G. Alexe, M. Lawrence, M. O'Kelly, P. Tamayo, B.A. Weir, S. Gabriel, W. Winckler, S. Gupta, L. Jakkula, H.S. Feiler, J.G. Hodgson, C.D. James, J.N. Sarkaria, C. Brennan, A. Kahn, P.T. Spellman, R.K. Wilson, T.P. Speed, J.W. Gray, M. Meyerson, G. Getz, C.M. Perou, D.N. Hayes, and N. Cancer Genome Atlas Research, *Integrated genomic analysis identifies clinically relevant subtypes of glioblastoma characterized by abnormalities in PDGFRA, IDH1, EGFR, and NF1.* Cancer Cell, 2010. **17**(1): p. 98-110.

140. Wang, Q., B. Hu, X. Hu, H. Kim, M. Squatrito, L. Scarpace, A.C. deCarvalho, S. Lyu, P. Li, Y. Li, F. Barthel, H.J. Cho, Y.H. Lin, N. Satani,

E. Martinez-Ledesma, S. Zheng, E. Chang, C.G. Sauve, A. Olar, Z.D. Lan, G. Finocchiaro, J.J. Phillips, M.S. Berger, K.R. Gabrusiewicz, G. Wang, E. Eskilsson, J. Hu, T. Mikkelsen, R.A. DePinho, F. Muller, A.B. Heimberger, E.P. Sulman, D.H. Nam, and R.G.W. Verhaak, *Tumor Evolution of Glioma-Intrinsic Gene Expression Subtypes Associates with Immunological Changes in the Microenvironment.* Cancer Cell, 2017. **32**(1): p. 42-56.

141. Gill, B.J., D.J. Pisapia, H.R. Malone, H. Goldstein, L. Lei, A. Sonabend, J. Yun, J. Samanamud, J.S. Sims, M. Banu, A. Dovas, A.F. Teich, S.A. Sheth, G.M. McKhann, M.B. Sisti, J.N. Bruce, P.A. Sims, and P. Canoll, *MRI-localized biopsies reveal subtype-specific differences in molecular and cellular composition at the margins of glioblastoma.* Proceedings of the National Academy of Sciences of the United States of America, 2014. **111**(34): p. 12550-12555.

142. Teo, W.Y., K. Sekar, P. Seshachalam, J. Shen, W.Y. Chow, C.C. Lau, H. Yang, J. Park, S.G. Kang, X. Li, D.H. Nam, and K.M. Hui, *Relevance of a TCGA-derived Glioblastoma Subtype Gene-Classifier among Patient Populations.* Sci Rep-UK, 2019. **9**(1): p. 7442.

143. Singh, S.K., C. Hawkins, I.D. Clarke, J.A. Squire, J. Bayani, T. Hide, R.M. Henkelman, M.D. Cusimano, and P.B. Dirks, *Identification of human brain tumour initiating cells.* Nature, 2004. **432**(7015): p. 396-401.

144. Galli, R., E. Binda, U. Orfanelli, B. Cipelletti, A. Gritti, S. De Vitis, R. Fiocco, C. Foroni, F. Dimeco, and A. Vescovi, *Isolation and*

characterization of tumorigenic, stem-like neural precursors from human glioblastoma. Cancer Res, 2004. **64**(19): p. 7011-7021.

145. Vescovi, A.L., R. Galli, and B.A. Reynolds, *Brain tumour stem cells.* Nat Rev Cancer, 2006. **6**(6): p. 425-436.

146. Kang, M.K. and S.K. Kang, *Tumorigenesis of chemotherapeutic drug-resistant cancer stem-like cells in brain glioma.* Stem Cells Dev, 2007. **16**(5): p. 837-847.

147. Rycaj, K. and D.G. Tang, *Cancer stem cells and radioresistance.* Int J Radiat Biol, 2014. **90**(8): p. 615-621.

148. Arnold, C.R., J. Mangesius, Skvortsova, II, and U. Ganswindt, *The Role of Cancer Stem Cells in Radiation Resistance.* Front Oncol, 2020. **10**(164): p. 164.

149. Bao, S., Q. Wu, R.E. McLendon, Y. Hao, Q. Shi, A.B. Hjelmeland, M.W. Dewhirst, D.D. Bigner, and J.N. Rich, *Glioma stem cells promote radioresistance by preferential activation of the DNA damage response.* Nature, 2006. **444**(7120): p. 756-760.

150. Chen, J., Y. Li, T.S. Yu, R.M. McKay, D.K. Burns, S.G. Kernie, and L.F. Parada, *A restricted cell population propagates glioblastoma growth after chemotherapy.* Nature, 2012. **488**(7412): p. 522-526.

151. Alves, A.L.V., I.N.F. Gomes, A.C. Carloni, M.N. Rosa, L.S. da Silva, A.F. Evangelista, R.M. Reis, and V.A.O. Silva, *Role of glioblastoma stem cells in cancer therapeutic resistance: a perspective on antineoplastic agents from natural sources and chemical derivatives.* Stem Cell Res Ther, 2021. **12**(1): p. 206.

152. Luecken, M.D. and F.J. Theis, *Current best practices in single-cell RNA-seq analysis: a tutorial.* Mol Syst Biol, 2019. **15**(6): p. e8746.

153. Bedard, P.L., A.R. Hansen, M.J. Ratain, and L.L. Siu, *Tumour heterogeneity in the clinic.* Nature, 2013. **501**(7467): p. 355-364.

154. Khalafallah, A.M., S. Huq, A.E. Jimenez, R. Serra, C. Bettegowda, and D. Mukherjee, *"Zooming in" on Glioblastoma: Understanding Tumor Heterogeneity and its Clinical Implications in the Era of Single-Cell Ribonucleic Acid Sequencing.* Neurosurgery, 2021. **88**(3): p. 477-486.

155. Meng, Q., Y. Zhang, G. Li, Y. Li, H. Xie, and X. Chen, *New insights for precision treatment of glioblastoma from analysis of single-cell lncRNA expression.* J Cancer Res Clin Oncol, 2021. **147**(7): p. 1881-1895.

156. Lv, D., S.C. Yu, Y.F. Ping, H. Wu, X. Zhao, H. Zhang, Y. Cui, B. Chen, X. Zhang, J. Dai, X.W. Bian, and X.H. Yao, *A three-dimensional collagen scaffold cell culture system for screening anti-glioma therapeutics.* Oncotarget, 2016. **7**(35): p. 56904-56914.

157. Fallica, B., G. Makin, and M.H. Zaman, *Bioengineering approaches to study multidrug resistance in tumor cells.* Integr Biol (Camb), 2011. **3**(5): p. 529-539.

158. Birgersdotter, A., R. Sandberg, and I. Ernberg, *Gene expression perturbation in vitro--a growing case for three-dimensional (3D) culture systems.* Semin Cancer Biol, 2005. **15**(5): p. 405-412.

159. Abbott, A., *Cell culture: biology's new dimension.* Nature, 2003. **424**(6951): p. 870-872.

160. Zanoni, M., F. Piccinini, C. Arienti, A. Zamagni, S. Santi, R. Polico, A. Bevilacqua, and A. Tesei, *3D tumor spheroid models for in vitro*

therapeutic screening: a systematic approach to enhance the biological relevance of data obtained. Sci Rep-UK, 2016. **6**: p. 19103.

161. Huang, J., K. Chen, J. Huang, W. Gong, N.M. Dunlop, O.M. Howard, X. Bian, Y. Gao, and J.M. Wang, *Regulation of the leucocyte chemoattractant receptor FPR in glioblastoma cells by cell differentiation.* Carcinogenesis, 2009. **30**(2): p. 348-355.

162. Migeotte, I., D. Communi, and M. Parmentier, *Formyl peptide receptors: a promiscuous subfamily of G protein-coupled receptors controlling immune responses.* Cytokine Growth F R, 2006. **17**(6): p. 501-519.

163. Chesler, D.A., M.S. Berger, and A. Quinones-Hinojosa, *The potential origin of glioblastoma initiating cells.* Front Biosci (Schol Ed), 2012. **4**: p. 190-205.

164. Sung, S.Y., C.L. Hsieh, D. Wu, L.W. Chung, and P.A. Johnstone, *Tumor microenvironment promotes cancer progression, metastasis, and therapeutic resistance.* Curr Probl Cancer, 2007. **31**(2): p. 36-100.

165. Huang, J., J. Hu, X. Bian, K. Chen, W. Gong, N.M. Dunlop, O.M. Howard, and J.M. Wang, *Transactivation of the epidermal growth factor receptor by formylpeptide receptor exacerbates the malignant behavior of human glioblastoma cells.* Cancer Res, 2007. **67**(12): p. 5906-5913.

166. Heimberger, A.B., R. Hlatky, D. Suki, D. Yang, J. Weinberg, M. Gilbert, R. Sawaya, and K. Aldape, *Prognostic effect of epidermal growth factor receptor and EGFRvIII in glioblastoma multiforme patients.* Clinical Cancer Research, 2005. **11**(4): p. 1462-1466.

167. Yang, X.J., W. Cui, A. Gu, C. Xu, S.C. Yu, T.T. Li, Y.H. Cui, X. Zhang, and X.W. Bian, *A novel zebrafish xenotransplantation model for study of glioma stem cell invasion.* PLoS One, 2013. **8**(4): p. e61801.

168. Dorward, D.A., C.D. Lucas, G.B. Chapman, C. Haslett, K. Dhaliwal, and A.G. Rossi, *The role of formylated peptides and formyl peptide receptor 1 in governing neutrophil function during acute inflammation.* Am J Pathol, 2015. **185**(5): p. 1172-1184.

169. Ye, R.D. and F. Boulay, *Structure and Function of Leukocyte Chemoattractant Receptors*, in *Adv Pharmacol*. 1997. p. 221-289.

170. Rabiet, M.J., E. Huet, and F. Boulay, *The N-formyl peptide receptors and the anaphylatoxin C5a receptors: an overview.* Biochimie, 2007. **89**(9): p. 1089-1106.

171. Mills, J.S., H.M. Miettinen, D. Cummings, and A.J. Jesaitis, *Characterization of the binding site on the formyl peptide receptor using three receptor mutants and analogs of Met-Leu-Phe and Met-Met-Trp-Leu-Leu.* J Biol Chem, 2000. **275**(50): p. 39012-39017.

172. Jacoby, E., R. Bouhelal, M. Gerspacher, and K. Seuwen, *The 7 TM G-protein-coupled receptor target family.* ChemMedChem, 2006. **1**(8): p. 761-782.

173. Yi, L., H. Xiao, M. Xu, X. Ye, J. Hu, F. Li, M. Li, C. Luo, S. Yu, X. Bian, and H. Feng, *Glioma-initiating cells: a predominant role in microglia/macrophages tropism to glioma.* Journal of Neuroimmunology, 2011. **232**(1-2): p. 75-82.

174. Yao, X.H., Y.F. Ping, J.H. Chen, C.P. Xu, D.L. Chen, R. Zhang, J.M. Wang, and X.W. Bian, *Glioblastoma stem cells produce vascular*

endothelial growth factor by activation of a G-protein coupled formylpeptide receptor FPR. Journal of Pathology, 2008. **215**(4): p. 369-376.

175. Boer, J.C., D.M. van Marion, J.V. Joseph, N.M. Kliphuis, H. Timmer-Bosscha, J.A. van Strijp, E.G. de Vries, W.F. den Dunnen, F.A. Kruyt, and A.M. Walenkamp, *Microenvironment involved in FPR1 expression by human glioblastomas.* J Neurooncol, 2015. **123**(1): p. 53-63.
176. Allen, M., M. Bjerke, H. Edlund, S. Nelander, and B. Westermark, *Origin of the U87MG glioma cell line: Good news and bad news.* Sci Transl Med, 2016. **8**(354): p. 354re3.
177. Neska-Matuszewska, M., J. Bladowska, M. Sasiadek, and A. Zimny, *Differentiation of glioblastoma multiforme, metastases and primary central nervous system lymphomas using multiparametric perfusion and diffusion MR imaging of a tumor core and a peritumoral zone-Searching for a practical approach.* Plos One, 2018. **13**(1): p. e0191341.
178. Groothuis, D.R., J.F. Pasternak, J.M. Fischer, R.G. Blasberg, D.D. Bigner, and N.A. Vick, *Regional measurements of blood flow in experimental RG-2 rat gliomas.* Cancer Res, 1983. **43**(7): p. 3362-3367.
179. Brem, S., R. Cotran, and J. Folkman, *Tumor Angiogenesis: A Quantitative Method for Histologic Grading<xref ref-type="fn" rid="FN2">2</xref>.* JNCI-J Natl Cancer I, 1972. **48**(2): p. 347-356.
180. Carmeliet, P. and R.K. Jain, *Angiogenesis in cancer and other diseases.* Nature, 2000. **407**(6801): p. 249-257.

181. Das, S. and P.A. Marsden, *Angiogenesis in glioblastoma.* N Engl J Med, 2013. **369**(16): p. 1561-1563.

182. Folkman, J., *Angiogenesis in cancer, vascular, rheumatoid and other disease.* Nature Medicine, 1995. **1**(1): p. 27-31.

183. Benjamin, L.E. and E. Keshet, *Conditional switching of vascular endothelial growth factor (VEGF) expression in tumors: induction of endothelial cell shedding and regression of hemangioblastoma-like vessels by VEGF withdrawal.* Proceedings of the National Academy of Sciences of the United States of America, 1997. **94**(16): p. 8761-8766.

184. Yao, X.H., Y.F. Ping, J.H. Chen, D.L. Chen, C.P. Xu, J. Zheng, J.M. Wang, and X.W. Bian, *Production of angiogenic factors by human glioblastoma cells following activation of the G-protein coupled formylpeptide receptor FPR.* J Neurooncol, 2008. **86**(1): p. 47-53.

185. Christian, F., E.L. Smith, and R.J. Carmody, *The Regulation of NF-kappaB Subunits by Phosphorylation.* Cells, 2016. **5**(1): p. 12.

186. Huang, G., H. Yan, S. Ye, C. Tong, and Q.L. Ying, *STAT3 phosphorylation at tyrosine 705 and serine 727 differentially regulates mouse ESC fates.* Stem Cells, 2014. **32**(5): p. 1149-1160.

187. Kietzmann, T., D. Mennerich, and E.Y. Dimova, *Hypoxia-Inducible Factors (HIFs) and Phosphorylation: Impact on Stability, Localization, and Transactivity.* Front Cell Dev Biol, 2016. **4**: p. 11.

188. Soubannier, V. and S. Stifani, *NF-kappaB Signalling in Glioblastoma.* Biomedicines, 2017. **5**(2): p. 29.

189. Chang, N., S.H. Ahn, D.S. Kong, H.W. Lee, and D.H. Nam, *The role of STAT3 in glioblastoma progression through dual influences on tumor*

cells and the immune microenvironment. Mol Cell Endocrinol, 2017. **451**: p. 53-65.

190. Schittenhelm, J., K. Trautmann, G. Tabatabai, C. Hermann, R. Meyermann, and R. Beschorner, *Comparative analysis of annexin-1 in neuroepithelial tumors shows altered expression with the grade of malignancy but is not associated with survival.* Mod Pathol, 2009. **22**(12): p. 1600-1611.

191. Schittenhelm, J., K. Trautmann, G. Tabatabai, C. Hermann, R. Meyermann, and R. Beschorner, *Comparative analysis of annexin-1 in neuroepithelial tumors shows altered expression with the grade of malignancy but is not associated with survival.* Modern Pathology, 2009. **22**(12): p. 1600-1611.

192. Hsieh, C.H., H.T. Chang, W.C. Shen, W.C. Shyu, and R.S. Liu, *Imaging the impact of Nox4 in cycling hypoxia-mediated U87 glioblastoma invasion and infiltration.* Mol Imaging Biol, 2012. **14**(4): p. 489-499.

193. Huang, B.C., D.Y. Geng, C.S. Zee, Y.M. Ji, H.X. Cheng, and Y.M. Dai, *A unique magnetic resonance imaging feature of glioblastoma multiforme: the 'pseudopalisade' sign.* J Int Med Res, 2010. **38**(2): p. 686-693.

194. Van den Eynde, M., J.F. Baurain, F. Mazzeo, and J.P. Machiels, *Epidermal growth factor receptor targeted therapies for solid tumours.* Acta Clinica Belgica, 2011. **66**(1): p. 10-17.

195. Kuracinova, K., A. Janegova, P. Janega, and P. Babal, *Expression of epidermal growth factor receptor in soft tissue tumours.* Virchows Archiv, 2013. **463**(2): p. 190.

196. Adam, P., S. Hahner, M. Hartmann, B. Heinrich, M. Quinkler, H.S. Willenberg, W. Saeger, S. Sbiera, S. Schmull, H.U. Voelker, P. Strobel, B. Allolio, and M. Fassnacht, *Epidermal growth factor receptor in adrenocortical tumors: analysis of gene sequence, protein expression and correlation with clinical outcome.* Mod Pathol, 2010. **23**(12): p. 1596-1604.

197. Yung, W.K.A., G.E. Gallick, M.D. Waterfield, R.P. Moser, and P.A. Steck, *Expression of Epidermal Growth-Factor Receptor in Cultured Human-Brain Tumor-Cells.* Journal of Neuro-Oncology, 1986. **4**(1): p. 98-98.

198. Moch, H., G. Sauter, N. Buchholz, T.C. Gasser, L. Bubendorf, F.M. Waldman, and M.J. Mihatsch, *Epidermal growth factor receptor expression is associated with rapid tumor cell proliferation in renal cell carcinoma.* Human Pathology, 1997. **28**(11): p. 1255-1259.

199. Huang, J., Y. Zhou, X. Bian, Y.Y. Le, W. Gong, K. Chen, and J.M. Wang, *The formylpeptide receptor FPR exploits the function of the epidermal growth factor receptor to promote the progression of glioblastoma.* Faseb Journal, 2008. **22**.

200. Fenstermaker, R.A., J. Capala, R.F. Barth, A. Hujer, H.J. Kung, and D.M. Kaetzel, Jr., *The effect of epidermal growth factor receptor (EGFR) expression on in vivo growth of rat C6 glioma cells.* Leukemia, 1995. **9 Suppl 1**: p. S106-S112.

201. Gemperle, C., M. Schmid, M. Herova, J. Marti-Jaun, S.J. Wuest, C. Loretz, and M. Hersberger, *Regulation of the formyl peptide receptor 1*

(FPR1) gene in primary human macrophages. Plos One, 2012. **7**(11): p. e50195.

202. Snapkov, I., C.O. Oqvist, Y. Figenschau, P. Kogner, J.I. Johnsen, and B. Sveinbjornsson, *The role of formyl peptide receptor 1 (FPR1) in neuroblastoma tumorigenesis.* BMC Cancer, 2016. **16**: p. 490.

203. Dorward, D.A., C.D. Lucas, M.K. Doherty, G.B. Chapman, E.J. Scholefield, A. Conway Morris, J.M. Felton, T. Kipari, D.C. Humphries, C.T. Robb, A.J. Simpson, P.D. Whitfield, C. Haslett, K. Dhaliwal, and A.G. Rossi, *Novel role for endogenous mitochondrial formylated peptide-driven formyl peptide receptor 1 signalling in acute respiratory distress syndrome.* Thorax, 2017. **72**(10): p. 928-936.

204. Cheng, T.Y., M.S. Wu, J.T. Lin, M.T. Lin, C.T. Shun, K.T. Hua, and M.L. Kuo, *Formyl Peptide receptor 1 expression is associated with tumor progression and survival in gastric cancer.* Anticancer Res, 2014. **34**(5): p. 2223-2229.

205. Derian, C.K., H.F. Solomon, J.D. Higgins, 3rd, M.J. Beblavy, R.J. Santulli, G.J. Bridger, M.C. Pike, D.J. Kroon, and A.J. Fischman, *Selective inhibition of N-formylpeptide-induced neutrophil activation by carbamate-modified peptide analogues.* Biochemistry, 1996. **35**(4): p. 1265-1269.

206. Edwards, B.S., C. Bologa, S.M. Young, K.V. Balakin, E.R. Prossnitz, N.P. Savchuck, L.A. Sklar, and T.I. Oprea, *Integration of virtual screening with high-throughput flow cytometry to identify novel small molecule formylpeptide receptor antagonists.* Mol Pharmacol, 2005. **68**(5): p. 1301-1310.

207. Young, S.M., C.M. Bologa, D. Fara, B.K. Bryant, J.J. Strouse, J.B. Arterburn, R.D. Ye, T.I. Oprea, E.R. Prossnitz, L.A. Sklar, and B.S. Edwards, *Duplex high-throughput flow cytometry screen identifies two novel formylpeptide receptor family probes.* Cytometry A, 2009. **75**(3): p. 253-263.

208. de Paulis, A., A. Ciccarelli, G. de Crescenzo, R. Cirillo, V. Patella, and G. Marone, *Cyclosporin H is a potent and selective competitive antagonist of human basophil activation by N-formyl-methionyl-leucyl-phenylalanine.* J Allergy Clin Immunol, 1996. **98**(1): p. 152-164.

209. Wenzel-Seifert, K. and R. Seifert, *Cyclosporin H is a potent and selective formyl peptide receptor antagonist. Comparison with N-t-butoxycarbonyl-L-phenylalanyl-L-leucyl-L-phenylalanyl-L- leucyl-L-phenylalanine and cyclosporins A, B, C, D, and E.* J Immunol, 1993. **150**(10): p. 4591-4599.

210. Stenfeldt, A.L., J. Karlsson, C. Wenneras, J. Bylund, H. Fu, and C. Dahlgren, *Cyclosporin H, Boc-MLF and Boc-FLFLF are antagonists that preferentially inhibit activity triggered through the formyl peptide receptor.* Inflammation, 2007. **30**(6): p. 224-229.

211. Schepetkin, I.A., A.I. Khlebnikov, L.N. Kirpotina, and M.T. Quinn, *Antagonism of human formyl peptide receptor 1 with natural compounds and their synthetic derivatives.* Int Immunopharmacol, 2016. **37**: p. 43-58.

212. Yan, P., M. Nanamori, M. Sun, C. Zhou, N. Cheng, N. Li, W. Zheng, L. Xiao, X. Xie, R.D. Ye, and M.-W. Wang, *The Immunosuppressant Cyclosporin A Antagonizes Human Formyl Peptide Receptor through*

Inhibition of Cognate Ligand Binding. J Immunol, 2006. **177**(10): p. 7050.

213. Sklar, L.A., *Probe Report: Formylpeptide Receptor Antagonist*. University of New Mexico.

214. Unitt, J., M. Fagura, T. Phillips, S. King, M. Perry, A. Morley, C. MacDonald, R. Weaver, J. Christie, S. Barber, R. Mohammed, M. Paul, A. Cook, and A. Baxter, *Discovery of small molecule human FPR1 receptor antagonists.* Bioorg Med Chem Lett, 2011. **21**(10): p. 2991-2997.

215. Morley, A.D., A. Cook, S. King, B. Roberts, S. Lever, R. Weaver, C. Macdonald, J. Unitt, M. Fagura, T. Phillips, R. Lewis, and M. Wenlock, *Discovery of pyrazoles as novel FPR1 antagonists.* Bioorg Med Chem Lett, 2011. **21**(21): p. 6456-6460.

216. Morley, A.D., S. King, B. Roberts, S. Lever, B. Teobald, A. Fisher, T. Cook, B. Parker, M. Wenlock, C. Phillips, and K. Grime, *Lead optimisation of pyrazoles as novel FPR1 antagonists.* Bioorg Med Chem Lett, 2012. **22**(1): p. 532-536.

217. Postma, B., M.J. Poppelier, J.C. van Galen, E.R. Prossnitz, J.A.G. van Strijp, C.J.C. de Haas, and K.P.M. van Kessel, *Chemotaxis Inhibitory Protein of Staphylococcus aureus Binds Specifically to the C5a and Formylated Peptide Receptor.* J Immunol, 2004. **172**(11): p. 6994.

218. Frasinyuk, M.S., N.V. Gorbulenko, and V.P. Khilya, *Chemistry of the heteroanalogs of isoflavones. 20. Benzimidazole analogs of isoflavones.* Chem Heterocyc Compd, 1997. **33**(9): p. 1078-1085.

219. McKinnon, D.M., P. Spevack, and G. Tipples, *Conversion of some azaheterocyclic-acetic esters and -acetonitriles into fused heterocycles.* Can J Chem, 1988. **66**(9): p. 2339-2344.

220. Schepetkin, I.A., L.N. Kirpotina, A.I. Khlebnikov, N. Cheng, R.D. Ye, and M.T. Quinn, *Antagonism of human formyl peptide receptor 1 (FPR1) by chromones and related isoflavones.* Biochem Pharmacol, 2014. **92**(4): p. 627-641.

221. Carpino, L.A., *1-Hydroxy-7-azabenzotriazole. An efficient peptide coupling additive.* J Am Chem Soc, 2002. **115**(10): p. 4397-4398.

222. Carpino, L.A., H. Imazumi, A. El-Faham, F.J. Ferrer, C. Zhang, Y. Lee, B.M. Foxman, P. Henklein, C. Hanay, C. Mugge, H. Wenschuh, J. Klose, M. Beyermann, and M. Bienert, *The uronium/guanidinium Peptide coupling reagents: finally the true uronium salts.* Angew Chem Int Ed Engl, 2002. **41**(3): p. 441-445.

223. Brown, N.F., T.J. Carter, D. Ottaviani, and P. Mulholland, *Harnessing the immune system in glioblastoma.* Br J Cancer, 2018. **119**(10): p. 1171-1181.

224. Moraes, L.A., P.B. Ampomah, and L.H.K. Lim, *Annexin A1 in inflammation and breast cancer: a new axis in the tumor microenvironment.* Cell Adh Migr, 2018. **12**(5): p. 417-423.

225. Sheikh, M.H. and E. Solito, *Annexin A1: Uncovering the Many Talents of an Old Protein.* Int J Mol Sci, 2018. **19**(4): p. 1045.

226. Wang, L.P., J. Bi, C. Yao, X.D. Xu, X.X. Li, S.M. Wang, Z.L. Li, D.Y. Zhang, M. Wang, and G.Q. Chang, *Annexin A1 expression and its*

prognostic significance in human breast cancer. Neoplasma, 2010. **57**(3): p. 253-259.

227. Achilli, T.M., J. Meyer, and J.R. Morgan, *Advances in the formation, use and understanding of multi-cellular spheroids.* Expert opinion on biological therapy, 2012. **12**(10): p. 1347-1360.

228. Griffith, L.G. and M.A. Swartz, *Capturing complex 3D tissue physiology in vitro.* Nat Rev Mol Cell Biol, 2006. **7**(3): p. 211-224.

229. Berridge, M.J., P. Lipp, and M.D. Bootman, *The versatility and universality of calcium signalling.* Nat Rev Mol Cell Biol, 2000. **1**(1): p. 11-21.

230. Bootman, M.D., T.J. Collins, C.M. Peppiatt, L.S. Prothero, L. MacKenzie, P. De Smet, M. Travers, S.C. Tovey, J.T. Seo, M.J. Berridge, F. Ciccolini, and P. Lipp, *Calcium signalling--an overview.* Semin Cell Dev Biol, 2001. **12**(1): p. 3-10.

231. Ma, Q., L. Ye, H. Liu, Y. Shi, and N. Zhou, *An overview of Ca(2+) mobilization assays in GPCR drug discovery.* Expert Opin Drug Discov, 2017. **12**(5): p. 511-523.

232. Charlton, S.J. and G. Vauquelin, *Elusive equilibrium: the challenge of interpreting receptor pharmacology using calcium assays.* Br J Pharmacol, 2010. **161**(6): p. 1250-1265.

233. Ulrich, T.A., E.M. de Juan Pardo, and S. Kumar, *The mechanical rigidity of the extracellular matrix regulates the structure, motility, and proliferation of glioma cells.* Cancer Res, 2009. **69**(10): p. 4167-4174.

234. Memmel, S., D. Sisario, C. Zoller, V. Fiedler, A. Katzer, R. Heiden, N. Becker, L. Eing, F.L.R. Ferreira, H. Zimmermann, M. Sauer, M. Flentje,

V.L. Sukhorukov, and C.S. Djuzenova, *Migration pattern, actin cytoskeleton organization and response to PI3K-, mTOR-, and Hsp90-inhibition of glioblastoma cells with different invasive capacities.* Oncotarget, 2017. **8**(28): p. 45298-45310.

235. Lefranc, F., J. Brotchi, and R. Kiss, *Possible future issues in the treatment of glioblastomas: special emphasis on cell migration and the resistance of migrating glioblastoma cells to apoptosis.* J Clin Oncol, 2005. **23**(10): p. 2411-2422.

236. Hagemann, C., J. Anacker, S. Haas, D. Riesner, B. Schomig, R.I. Ernestus, and G.H. Vince, *Comparative expression pattern of Matrix-Metalloproteinases in human glioblastoma cell-lines and primary cultures.* BMC Res Notes, 2010. **3**(1): p. 293.

237. Schindelin, J., I. Arganda-Carreras, E. Frise, V. Kaynig, M. Longair, T. Pietzsch, S. Preibisch, C. Rueden, S. Saalfeld, B. Schmid, J.Y. Tinevez, D.J. White, V. Hartenstein, K. Eliceiri, P. Tomancak, and A. Cardona, *Fiji: an open-source platform for biological-image analysis.* Nat Methods, 2012. **9**(7): p. 676-682.

238. Brat, D.J. and E.G. Van Meir, *Glomeruloid microvascular proliferation orchestrated by VPF/VEGF: a new world of angiogenesis research.* Am J Pathol, 2001. **158**(3): p. 789-796.

239. Martinez-Gonzalez, A., G.F. Calvo, L.A. Perez Romasanta, and V.M. Perez-Garcia, *Hypoxic cell waves around necrotic cores in glioblastoma: a biomathematical model and its therapeutic implications.* Bull Math Biol, 2012. **74**(12): p. 2875-2896.

240. Zagzag, D., R. Amirnovin, M.A. Greco, H. Yee, J. Holash, S.J. Wiegand, S. Zabski, G.D. Yancopoulos, and M. Grumet, *Vascular apoptosis and involution in gliomas precede neovascularization: a novel concept for glioma growth and angiogenesis.* Lab Invest, 2000. **80**(6): p. 837-849.

241. Rodriguez-Vita, J. and T. Lawrence, *The resolution of inflammation and cancer.* Cytokine Growth F R, 2010. **21**(1): p. 61-65.

242. Li, S.Q., N. Su, P. Gong, H.B. Zhang, J. Liu, D. Wang, Y.P. Sun, Y. Zhang, F. Qian, B. Zhao, Y. Yu, and R.D. Ye, *The Expression of Formyl Peptide Receptor 1 is Correlated with Tumor Invasion of Human Colorectal Cancer.* Sci Rep-UK, 2017. **7**(1): p. 5918.

243. Khau, T., S.Y. Langenbach, M. Schuliga, T. Harris, C.N. Johnstone, R.L. Anderson, and A.G. Stewart, *Annexin-1 signals mitogen-stimulated breast tumor cell proliferation by activation of the formyl peptide receptors (FPRs) 1 and 2.* Faseb Journal, 2011. **25**(2): p. 483-496.

244. Landry, A.P., M. Balas, S. Alli, J. Spears, and Z. Zador, *Distinct regional ontogeny and activation of tumor associated macrophages in human glioblastoma.* Sci Rep-UK, 2020. **10**(1): p. 19542.

245. Saavedra-Lopez, E., M. Roig-Martinez, G.P. Cribaro, P.V. Casanova, J.M. Gallego, A. Perez-Valles, and C. Barcia, *Phagocytic glioblastoma-associated microglia and macrophages populate invading pseudopalisades.* Brain Commun, 2020. **2**(1): p. fcz043.

246. Yang, S.C., P.J. Chung, C.M. Ho, C.Y. Kuo, M.F. Hung, Y.T. Huang, W.Y. Chang, Y.W. Chang, K.H. Chan, and T.L. Hwang, *Propofol inhibits superoxide production, elastase release, and chemotaxis in formyl*

peptide-activated human neutrophils by blocking formyl peptide receptor 1. J Immunol, 2013. **190**(12): p. 6511-6519.

247. Montana, V. and H. Sontheimer, *Bradykinin promotes the chemotactic invasion of primary brain tumors.* J Neurosci, 2011. **31**(13): p. 4858-4867.

248. Hamadi, A., G. Giannone, K. Takeda, and P. Ronde, *Glutamate involvement in calcium-dependent migration of astrocytoma cells.* Cancer Cell Int, 2014. **14**: p. 42.

249. Chen, J.H., X.W. Bian, X.H. Yao, W. Gong, J. Hu, K. Chen, P. Iribarren, W. Zhao, and X.D. Zhou, *Nordy, a synthetic lipoxygenase inhibitor, inhibits the expression of formylpeptide receptor and induces differentiation of malignant glioma cells.* Biochem Biophys Res Commun, 2006. **342**(4): p. 1368-1374.

250. Sheldrick, G.M., *Crystal structure refinement with SHELXL.* Acta Crystallogr C Struct Chem, 2015. **71**(Pt 1): p. 3-8.

251. Hubschle, C.B., G.M. Sheldrick, and B. Dittrich, *ShelXle: a Qt graphical user interface for SHELXL.* J Appl Crystallogr, 2011. **44**(Pt 6): p. 1281-1284.

252. Workman, P., E.O. Aboagye, F. Balkwill, A. Balmain, G. Bruder, D.J. Chaplin, J.A. Double, J. Everitt, D.A. Farningham, M.J. Glennie, L.R. Kelland, V. Robinson, I.J. Stratford, G.M. Tozer, S. Watson, S.R. Wedge, and S.A. Eccles, *Guidelines for the welfare and use of animals in cancer research.* Br J Cancer, 2010. **102**(11): p. 1555-1577.